FOCUSED ELECTRON- AND ION-BEAM INDUCED PROCESSES: *IN SITU* MONITORING, ANALYSIS AND MODELING

THÈSE N^{O} 4036 (2008)

PRÉSENTÉE LE 29 FÉVRIER 2008
À LA FACULTÉ DES SCIENCES ET TECHNIQUES DE L'INGÉNIEUR
LABORATOIRE D'OPTIQUE APPLIQUÉE
PROGRAMME DOCTORAL EN SCIENCE ET GÉNIE DES MATÉRIAUX

ÉCOLE POLYTECHNIQUE FÉDÉRALE DE LAUSANNE

POUR L'OBTENTION DU GRADE DE DOCTEUR ÈS SCIENCES

PAR

Vinzenz FRIEDLI

ingénieur en microtechnique diplômé EPF
de nationalité suisse et originaire de Rohrbach (BE)

acceptée sur proposition du jury:

Prof. J. Lemaître, président du jury
Dr P. Hoffmann, Dr I. Utke, directeurs de thèse
Prof. P. Boggild, rapporteur
Prof. H. Brune, rapporteur
Dr K. Edinger, rapporteur

EPFL
ÉCOLE POLYTECHNIQUE
FÉDÉRALE DE LAUSANNE
Suisse
2008

To my family.

I arise today
Through the strength of heaven;
Light of the sun,
Splendor of fire,
Speed of lightning,
Swiftness of the wind,
Depth of the sea,
Stability of the earth,
Firmness of the rock.

Saint Patrick, "The Lorica"

Abstract

Focused electron- and ion-beam induced processing are well established techniques for local deposition and etching that rely on decomposition of precursor molecules by irradiation. These high-resolution nanostructuring techniques have various applications in nanoscience including attach-and-release procedures in nanomanipulation and fabrication of sensors (magnetic, optical and thermal) for scanning probe microscopy. However, a complete physical and chemical understanding of the process is hampered by the lack of suitable means to monitor and to access the numerous interrelated and time-varying process parameters (deposition and etch rate, yield, molecule flux and adsorption/desorption).

This thesis is a first attempt to fill this gap. It is based on experimental and simulative approaches for the determination of process conditions and mechanical properties of deposited materials:

i) Mass and force sensors: The use of tools merging micromechanical cantilever sensors and scanning electron microscopy was demonstrated for *in situ* monitoring and analysis. A cantilever-based resonant mass sensing setup was developed and used for real-time mass measurements. A noise level at the femtogram-scale was achieved by tracking the resonance frequency of a temperature stabilized piezoresistive cantilever using phase-locking. With this technique the surface coverage and residence time of $(CH_3)_3PtCpCH_3$ molecules, the mass deposition rate, the yield, and the material density of corresponding deposits were measured. *In situ* cantilever-based static force sensing and mechanical modal vibration analysis were employed to investigate the Young's modulus and density of individual high aspect ratio deposits from the precursor $Cu(hfac)_2$.

ii) Precursor supply simulations and experiments: A prerequisite to understand and quantify irradiative precursor chemistry is the knowledge of the local flux of molecules impinging on the substrate. Therefore, Monte Carlo simulations of flux distributions were developed and gas flows injected into a vacuum chamber were analyzed experimentally for the precursors $Co_2(CO)_8$, (hfac)CuVTMS, and $[(PF_3)_2RhCl]_2$.

The process parameters extracted from the mentioned approaches are valuable input for numerical focused electron- and ion-beam induced process models (Monte Carlo, continuum). We evaluated the precursor surface diffusion coefficient and the electron impact dissociation cross-section by relating deposit shapes to a continuum model.

Keywords – focused electron- and ion-beam induced processes, process parameters, cantilever-based *in situ* mass and force sensing, precursor gas flow, adsorption rate equation

Kurzfassung

Lokales Abscheiden und Ätzen basierend auf fokussierten Elektronenstrahl- und Ionenstrahl-induzierten Prozessen sind etablierte Techniken, die auf der Strahlungszersetzung von Precursormolekülen beruhen. Diese hochauflösenden Nanostrukturierungstechniken finden eine Vielzahl von Anwendungen in der Nanotechnologie, unter anderem für Fixier- und Ablöseverfahren in der Nanomanipulation und zur Fabrikation von Sensoren (magnetisch, optisch und thermisch) für die Rastersondenmikroskopie. Allerdings verhindert das Fehlen von geeigneten Messmethoden zur Kontrolle und Bestimmung der zahlreichen von einander abhängigen und zeitlich variierenden Prozessparametern (Abscheide- und Ätzgeschwindigkeit, Effizienz, Molekülfluss und Adsorption/Desorption) ein umfassendes physikalisches und chemisches Verständnis der Prozesse.

Diese Doktorarbeit ist eine erste Bestrebung diese Lücke zu schliessen. Sie beruht auf experimentellen und simulierenden Ansätzen zur Bestimmung der Prozessbedingungen und der mechanischen Eigenschaften der abgeschiedenen Materialien:

i) Masse- und Kraftsensoren: Die Nutzung von mikromechanischen Kantileversensoren, integriert in ein Rasterelektronenmikroskop, wurde für *in situ* Beobachtungen und Analysen demonstriert. Ein Massesensor basierend auf einem in Resonanz oszillierenden Kantilever wurde aufgebaut und für Echtzeit-Massemessungen angewandt. Ein Rauschuntergrund im Femtogramm-Bereich wurde erreicht durch phasenstarre Verfolgung der Resonanzfrequenz eines temperaturstabilisierten piezoresistiven Kantilevers. Diese Technik erlaubte die Messung der Oberflächenbedeckung und Verweilzeit von $(CH_3)_3PtCpCH_3$ Molekülen, der Masseabscheiderate, der Prozesseffizienz und der Materialdichte von entsprechenden Abscheidungen. Kantilever basierte statische Kraftmessungen und mechanische Vibrationsanalysen wurden angewandt für *in situ* Bestimmungen des Elastizitätsmoduls und der Dichte von langen Säulen abgeschieden von $Cu(hfac)_2$.

ii) Simulationen und Experimente der Precursorzufuhr: Die Kenntnis des lokal eintreffenden Molekülflusses auf das Substrat ist eine Voraussetzung zum Verständnis und zur Quantifizierung der strahlungsinduzierten Precursorchemie. Monte Carlo Simulationen der Flussdichteverteilung wurden entwickelt und der Gasfluss in eine Vakuumkammer wurde für die Precursor: $Co_2(CO)_8$, (hfac)CuVTMS und $[(PF_3)_2RhCl]_2$ experimentell analysiert.

Die mit den genannten Methoden bestimmten Prozessparameter liefern wertvolle Eingangswerte für numerische Modelle (Monte Carlo, Kontinuum) der fokussierten Elektronenstrahl- und Ionenstrahl-induzierten Prozesse. Über den Vergleich von Formen von Abscheidungen mit einem Kontinuummodel wurde der Oberflächendiffusionskoeffizient sowie der Dissoziationswirkungsquerschnitt des Moleküls für eintreffenden Elektronen bestimmt.

Schlüsselwörter – fokussierte Elektronenstrahl- und Ionenstrahl-induzierte Prozesse, Prozessparameter, *in situ* Masse- und Kraftmessungen mit Kantilevern, Precursor Gasfluss, Adsorptionsratengleichung

Acknowledgements

I gratefully acknowledge the Research Commission of the Swiss Federal Laboratories for Materials Testing and Research (EMPA) for creating such a stimulating research environment and for funding this Ph.D. project.

This thesis presents the results of four years of research carried out at the Laboratory for Mechanics of Materials and Nanostructures at EMPA in Thun, Switzerland. These results were possible thanks to support from many people in numerous discussions and collaborations. I would like to express my gratitude to all the people who contributed to this scientific and human adventure in one way or another.

First of all, I'd like to express my gratitude to Patrik Hoffmann, the director of my thesis and head of the Nanostructuring Research Group at EPFL, who supported me with constructive ideas and scientific advice during the past four years. I warmly thank Johann Michler who initiated the collaboration between the nanostructuring labs at EMPA and EPFL as well as Lukas Rohr for giving me the opportunity of carrying out my project under excellent conditions in their laboratory. I specially thank my supervisor Ivo Utke, the co-director of my thesis, for sharing his immense knowledge in the field of electron and ion beam induced processing, for always being available for discussions sometimes stretching beyond scientific questions, for thoughtful criticism, and overall for his constantly positive spirit, which has tremendously helped me in times of doubts.

My next thoughts go to the many people who have contributed to this project. I thank Christian Santschi who assisted in the mass sensing experiments performed in the dual beam microscope at EPFL for his personal efforts and the many scientific discussions we had. Many thanks go to Gerhard Bürki who introduced me to the world of electron microscopy and provided valuable assistance in the lab with his large experience of the technical aspects involved. I thank Thomas Sidler who helped with various aspects related to electronic and mechanical equipment and contributed through many discussions and Victor Callegari who was always available for questions related to focused ion beams.

My acknowledgments also go to Jörg Rychen and his collaborators at Nanonis who advised me with details in the fields of scanning probe microscopy and cantilever-based sensing. My project was brought to a next level through their control system providing high flexibility and reliability.

Many thanks go to Anton Böll for his excellent job in the metal workshop. He was always willing to push the limits of his equipment to provide us with small parts. I also acknowledge Ronald Gianotti and Claude Amendola who provided support in electronics and Laser cutting and Heinz Altorfer who assisted me with the design and construction of the vacuum chamber built for the thermal decomposition experiments.

My thanks also go to all the colleagues at EPFL. Among them I would like to mention Tristan Bret who left a thesis full of ideas and open questions, which served as a starting point and inspiration source in my research and Alexandre Perentes whom I thank for the encouraging discussions during the last period of thesis writing.

People come and go at EMPA Thun, creating a very dynamic and fascinating environment from both a scientific and human perspective. First of all, I warmly thank my collaborators Samuel and Fredrik, who were a constant source of help and inspiration in the lab as well as in everyday life. I'm grateful to all the people who created an enjoyable and open atmosphere at EMPA Thun, where one could always count on the help of the others. Many thanks to Adrien, Hiroyuki, Kilian, Jong-Wong, Benedikt, Karolina, Stephan, Laurent, Simona, Philippe, Christian, Laetitia, Mikhael, Jaques, Elisa and all the other group members for sharing many unforgettable moments in- and outside EMPA Thun. Furthermore, I thank all the students for their interest in our work as well as for their fresh and unbiased ideas. Thank you Ulf, Olivier, Pablo and Chong.

I would also like to acknowledge all the help with the administrative aspects of this project from Katrin Gurtner and Eveline Straubhaar at EMPA and Yvette Bernhard and Erika Menamkat at EPFL.

My final and warmest thoughts go to my friends who shared this experience with me from the “backstage”. Finally, I'm greatly thankful for all the love and encouragement I got during the last four years from my family and from Ursina, who could not be of better support.

Contents

Chapter 1

Introduction

The ongoing scaling down of structures and devices far below the micrometer scale has pushed the development of a large variety of novel fabrication methods. Among one of those, focused electron- and ion-beam (FEB/FIB) induced processing is especially attractive for prototyping tasks due to its high flexibility. This direct-write nanofabrication technique relies on a spatially confined chemical vapor deposition (CVD) process based on the decomposition of adsorbed precursor molecules by electron or ion irradiation. Deposition results from non-volatile dissociation products whereas etching occurs when a reaction of dissociation products with the substrate leads to the formation of volatile species.

1.1 The scope of this work: Objectives and Approach

This thesis evaluates mainly three approaches which contribute to advance the field of FEB/FIB induced processing: the development of tools for *in situ* monitoring of the process, the *in situ* analysis of the deposited materials and the detailed characterization of the precursor supply into the vacuum chamber. The proposed methods are interesting for both FEB and FIB induced processing. Most of our experimental results were, however, obtained for FEB induced deposition. This particular process is most commonly abbreviated EBID or FEBID and occasionally EB-CVD or FEB-CVD in the literature. Using ions instead of electrons introduces fundamental physical differences, such as the ion sputtering action, while most aspects of the process description remain equivalent. The etching process is very similar to deposition in terms of the relevant process parameters, it is, however, not addressed in detail within this work.

Although a large number of experimental data on FEB/FIB induced deposition and etching is reported in the literature, the difficulty to identify the resolution- and rate-limiting process parameters prevails at the current state of research. Full control over the outcome of FEB/FIB induced processes for fabrication and applications in micro- and nanodevices requires further understanding of the fundamental physics underlying the process. This was the main driving force of this work.

The final objective of this thesis comprises the advancement of the predictive power of model descriptions of FEB/FIB nanofabrication. The developed methods aim to extract process parameters and material properties by complementary experiments and simulations. The knowledge of these parameters, previously difficult to access, confine the multi-variable space of model descriptions.

1.2 Thesis Outline

In Chapter 2, the background on FEB/FIB induced processing is given focusing on the instrumentation (electron/ion microscopes and gas injection systems), principles, historical overview and applications of the technique. We summarize the state of the art of numerical process models and of experimental methods to monitor the process and to analyze mechanical properties of the deposited materials.

The experimental setup based on a Hitachi S-3600N scanning electron microscope (SEM) hosting a homemade gas injection system is described in Chapter 3. The integration and operation of micromechanical *in situ* characterization tools employed for mass and force measurements inside the SEM is outlined. The *ex situ* characterization equipment for high-resolution observation and material compositional analysis of nanostructures are presented.

After a review of the basic theoretical foundations of static and dynamic mechanics of cantilever beams, Chps. 4 and 5 report the results of *in situ* mass and force sensing experiments. *In situ* mass sensing is applied for process monitoring of FIB sputtering and FEB/FIB induced deposition and for the determination of material densities of deposits fabricated therewith. *In situ* force sensing (bending and tensile tests) and modal vibration analysis are employed for the mechanical analysis and the density determination of FEB deposits.

To support the characterization and design considerations of local precursor supply by gas injection systems (GISs) into vacuum chambers the relevant formalisms of rarefied gas dynamics are summarized in the first part of Chapter 6. Precursor flux distributions impinging on the substrate were simulated using Monte Carlo simulations for typical conditions in FEB/FIB induced processing systems. The shaping of rarefied flow by gas effusion from a tube into a vacuum chamber is analyzed based on the prevailing gas flow regime. Experimental measurements of flux distributions on the substrate for several precursors are compared to the simulations. The optimization of the arrangement and geometry of tube nozzle-based GISs as well as two alternative GIS designs are analyzed and discussed.

In Chapter 7 the continuum process model based on the adsorption rate equation is described and numerical solutions for an electron beam with Gaussian profile are presented. The parameters which have been measured and simulated using the methods developed in this work serve as the bases for model calculations of FEB deposit rate and resolution. Experimentally determined deposit shapes are fitted using the model.

The work is concluded in Chapter 8 with a summary of the contributions of this thesis and the future perspectives.

Chapter 2

Background

2.1 Instrumentation

Electron and ion microscopes are the host instruments to perform focused electron-/ion-beam (FEB/FIB) nanofabrication. A precursor supply is the essential add-on to an electron/ion microscope which enables additive and subtractive surface processing. The basic setup for both, FEB and FIB induced processing is presented in Fig. 2.1.

2.1.1 Electron microscope

Most commonly, scanning electron microscopes (SEMs) are used due to their availability in research facilities.[185] Environmental scanning electron microscopes (ESEMs) have proved to be an interesting option since they allow for an increased pressure in the sample chamber.[85] FEB induced processing has also been investigated in transmission electron microscopes (TEMs)[55] and scanning transmission electron microscopes (STEMs)[272,274].

Electrons are emitted from a source, accelerated to energies up to 30 keV in SEMs and 200-300 keV in TEMs, and focused onto the sample by an electron optical system composed of electromagnetic lenses and apertures for spatial filtering. Usually, all microscopes are classified according to their power of resolution. In FEB induced processing, both, the probe size, which is related to the resolution, and the current density of the focused beam in the sample plane are of interest. Different types of electron emitters impose a limit on the achievable probe size d_p and current I_p by the brightness β which is constant on the axis throughout the optical system. The brightness is a measure of the current per area normal to the beam direction and per element of solid angle:[246]

$$\beta = \frac{4I_p}{(\pi d_p \alpha_p)^2} \tag{2.1}$$

where α_p is the beam divergence angle. For thermionic electron emitters $\beta \simeq j_e E/(\pi \Delta E)$ with kinetic electron energy $E = eV$, where V is the acceleration voltage, and emission current density j_e, i.e. for thermionic W filament electron emitters ~ 3 A cm^{-2} and for LaB$_6$ emitters $\sim 20 - 50$ A cm^{-2}. The energy spread ΔE of the electrons from these sources is about $\sim 1 - 3$ eV. Field emission guns (FEG) can reach $j_e \sim 10^5$ A cm^{-2} and have energy

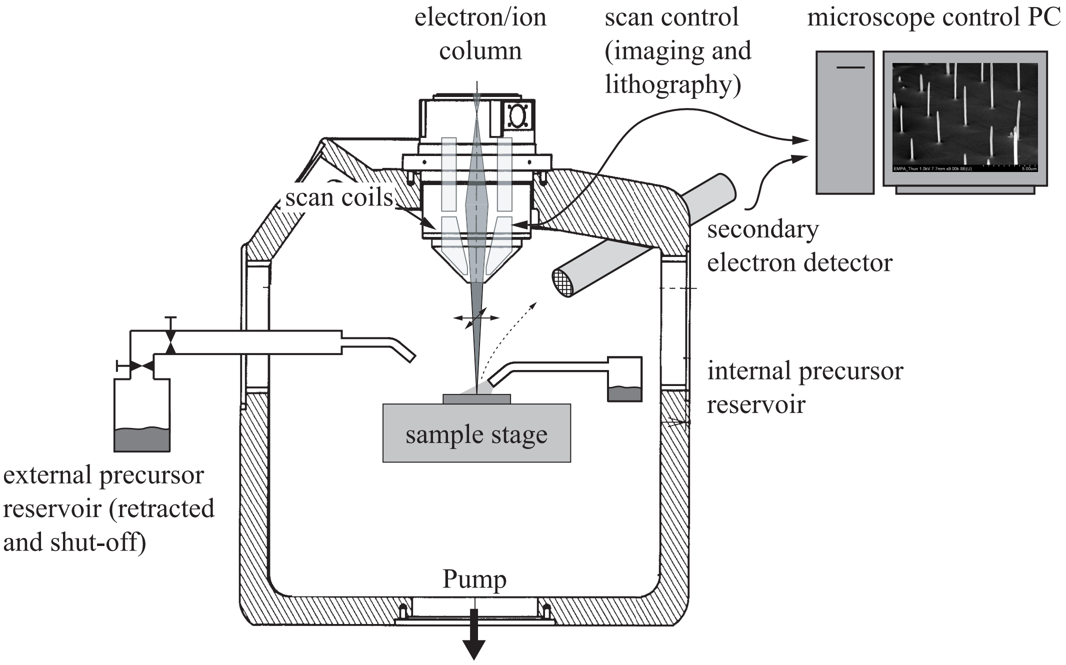

Figure 2.1: *Schematics of FEB and FIB nanofabrication systems. Precursor supply with external and internal precursor reservoirs are shown. The computer monitor shows FEB deposited pillars in tilt view.*

spreads $\Delta E < 0.5$ eV which results in substantially higher emitter brightness and thus, strongly reduced probe size at a given probe current. In practice the probe size is limited by aberrations in the optical system.

The imaging principle relies on raster scanning the beam over the sample, while the intensity of different signals produced by the electron interaction with the sample, i.e. secondary and backscattered electrons (SEs and BSEs), are acquired on a point-to-point bases and reconstructed as a two-dimensional grayscale image. In ESEMs imaging is done by detecting the current in a weak cascade discharge to the detector. Besides raster scan imaging, in standard SEM control systems rectangle, line and spot irradiation geometries are available. Lithography scan control systems are used to write complex patterns with varying irradiation dwell times.

For further details on electron microscopy, we refer to standard literature, e.g. by Goldstein *et al.*[108] that contains a thorough review of electron microscopes and their applications, or by Reimer[246] who outlines the theoretical aspects involved.

2.1.2 Ion microscope

Scanning ion microscopes (SIMs) are assembled similarly as their electron counterparts but use other interaction mechanisms with the sample surface. Most SIMs today use liquid Ga sources being available since the late 1980s. The Ga wets a W filament and an electric field

$> 10^8$ V cm^{-1} causes the formation of a sharp tip (Taylor cone) where field emission of Ga ions occurs. These are accelerated to an energy of $5-50$ keV, and focused onto the sample by electrostatic lenses. As for SEMs, imaging of samples is done by raster scanning and detection of emitted secondary electrons from the beam impact location. Unlike an electron beam, the FIB is inherently destructive to the sample. Impinging Ga ions, being $\sim 10^5$ times heavier than electrons, are able to sputter atoms from the surface. Re-impingement of these sputtered surface atoms on the sample can lead to redeposition, e.g. high aspect-ratio drilling typically results in clogged holes.[210] A fraction of the Ga atoms are also implanted into the top few nanometers of the surface, and the surface might be damaged. In Si an amorphous zone can be created, while in metals dislocations are introduced. For a more detailed description of SIMs we refer to standard literature[222] and for their use as micro-/nanofabrication instruments to recent review articles.[61,162,247,289]

2.1.3 Precursor supply

Precursor supply arrangements have been based on subchambers introduced into the vacuum chamber containing the sample[184] or on nozzle-based gas injection systems (GISs)[268]. In subchamber configurations the FEB or FIB can access the sample through a small hole with diameter ~ 1 mm acting as a differential pumping aperture. Biasing the subchamber relative to the sample potential permits to extract low-energy electrons and thus imaging of the sample through the hole.[217] A uniform precursor flux to the sample is established by feeding precursor gas into the subchamber which rises the pressure at a tolerable level via an injection line. The vacuum outside of the subchamber is maintained at high vacuum conditions to limit electron/ion gas phase scattering and to reduce the pressure load for the vacuum system. In nozzle-based systems the precursor is supplied as a molecular flux effusing from a nozzle onto the substrate. The pressure is increased locally above the sample substrate. This system is preferred to subchambers in most of today's setups. It allows the processing of large samples and facilitates the sample transfer.

Solid and liquid precursors are sublimated in the precursor reservoir. Their volatility is characterized by the vapor pressure which determines the source pressure maintained in the reservoir.[153] The vapor pressure can be controlled by the reservoir temperature, however, condensation of sublimated molecules on tubing surfaces which have a lower temperature than the precursor reservoir can reduce the flux.

A limited number of studies have been performed that investigate the injection of precursor gas onto the sample substrate in both FEB and FIB induced processing. Kohlmann *et al.* suggested a basic model which predicts the gas covered area based on the calculation of the intersection between a flow expansion cone from a GIS tube nozzle and the substrate.[146] This model does not include the strong non-uniform distribution within this area. However, it could be concluded that at a minimal distance between the tube and the substrate the flux is maximal which was observed experimentally by a maximum deposition rate and using a simple micromechanical pressure sensor. A conical tube finish was suggested to reduce the tube-substrate height. Blauner *et al.* measured the precursor pressure on the substrate in average across an aperture of 1 mm diameter as a function of the vertical tube nozzle distance using a stagnation tube (Pitot tube) connected to a capacitance manometer.[19] In order to calibrate

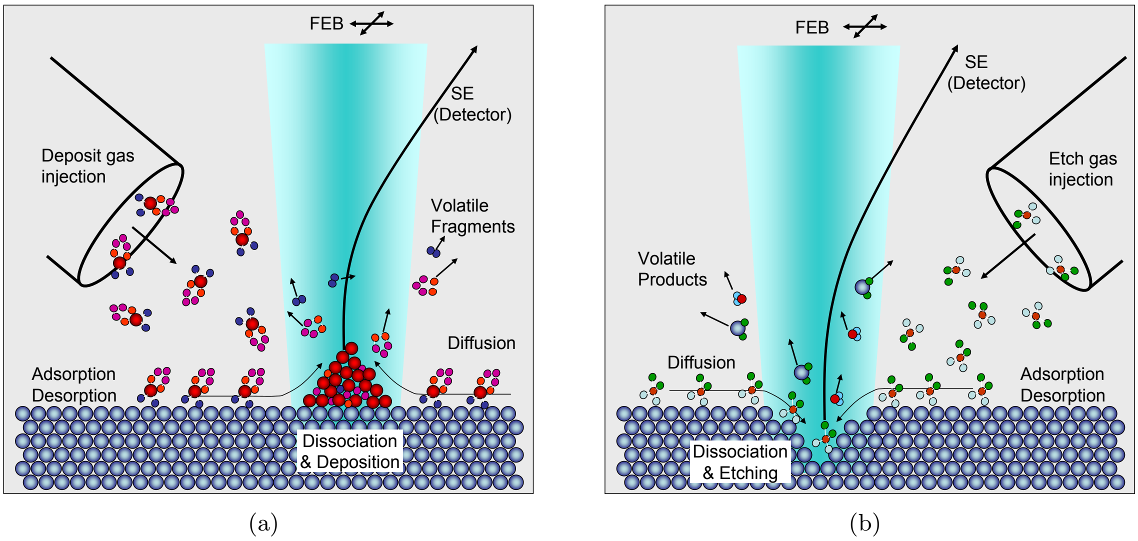

(a) (b)

Figure 2.2: *(a) Principle of FEB induced deposition: Molecules adsorb at the surface of the solid substrate and are dissociated under electron impact. Volatile fragments are pumped away and a deposit grows coaxially to the beam. Here molecules are injected by a tube nozzle-based gas injection system. (b) Principle of FEB induced etching: The surface adsorbed molecules dissociate under electron impact into reactive species and form volatile compounds with the substrate material.*

the total flux of metal carbonyls impinging on the substrate, the condensation of precursor molecules was measured on a quartz crystal microbalance (QCM) cooled to -40 °C.[265] The flux was revealed to have an exponential dependence on the precursor reservoir temperature which is due to the exponential temperature dependence of the vapor pressure as is predicted by the Clausius-Clapeyron relation.[6] The deposit topography of condensed impinging water molecules representing the impinging flux distribution was measured on a cryo-cooled substrate and modeled solving numerically the continuum Navier-Stokes equation.[80] Model and experiments of the lateral distribution deviated by nearly a factor of two.

Some attempts were made to optimize the GIS nozzle geometry which lead to the proposition of alternative nozzle geometries.[245] However, no experimental characterization can be found in the literature. It was further proposed that surfaces which are intercepting the gas flow can act as reflectors and serve to increase the local gas flux.[94] In some setups, the precursor flux has been increased and homogenized by arrangements of two symmetrically arranged tube nozzles.[220]

2.2 FEB induced deposition and etching

2.2.1 Principle

The principle of FEB induced deposition and etching is shown in Fig. 2.2. During deposition and etching surface-adsorbed gas molecules are decomposed by electron irradiation and form either a stable deposit and gaseous by-products or volatile reaction products with the substrate. FEB induced processing can be conceptually described by basic steps that occur simultaneously during deposition or etching:

1. Basic interaction of the FEB with the solid,
2. transport of precursor to the FEB interaction region,
3. primary decomposition step (and secondary decomposition of intermediate reaction products), and
4. transport of volatile precursor fragments away from the interaction region.

Each of these steps may be complex and vary in time, i.e. with ongoing evolution of the deposit shape and material or the etched pit. Some of these steps are currently not well characterized for most precursors and material systems.

In step 1 the impinging primary electrons are scattered in the bulk of the solid substrate material. The electron trajectory results from elastic collisions with the electric field of substrate atom nuclei and inelastic collisions with the electric field of substrate atom electrons each of which is characterized by an energy-dependent collision cross-section describing the probability of the event. The corresponding electron mean free path λ between two subsequent scattering events presented in Fig. 2.3 in Al and Cu is calculated according to the models described by Hagen *et al.*[114]. An impinging electron gradually looses energy caused by the occurrence of multiple scattering events. As a consequence, the electrons have a finite interaction range described by R (Fig. 2.4 (a)).

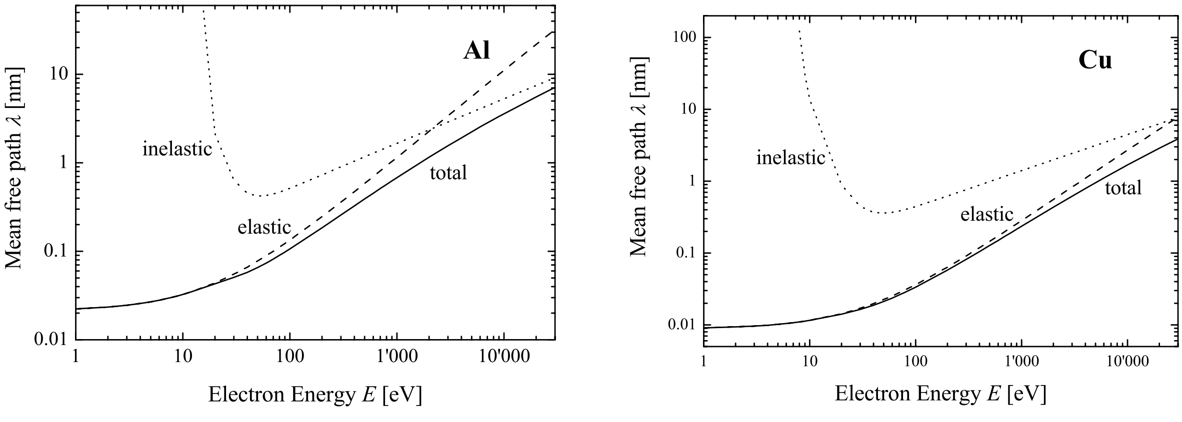

(a) (b)

Figure 2.3: *The mean free path λ of electrons in a solid at a given energy E. The elastic mean free path, λ_e, is calculated based on the Rutherford scattering model[138]. The inelastic mean free path, λ_i, corresponds to the empirical expression of Seah and Dench[267] based on a compilation of experimental results. The total mean free path is $\lambda_t^{-1} = \lambda_e^{-1} + \lambda_i^{-1}$. (a) Al and (b) Cu.*

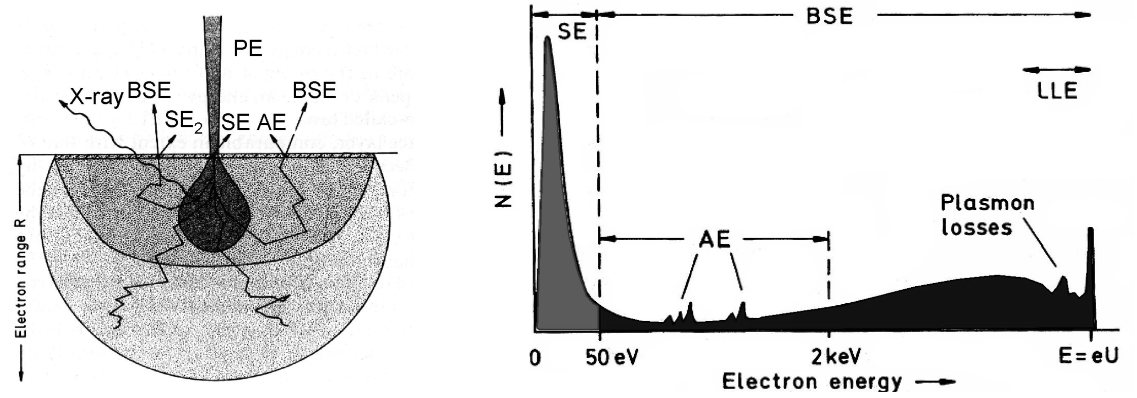

(a) (b)

Figure 2.4: *(a) FEB - solid interaction indicating the origin and escape depth of secondary electrons (SEs), backscattered electrons (BSEs), Auger electrons (AEs) and X-rays in the interaction volume of electron range R for normal incidence of a primary electron (PE) beam. (b) Typical electron emission energy spectrum produced by the FEB - solid interaction. By convention, electrons with exit energies* > 50 *eV are called BSEs and those with* < 50 *eV SEs. Emitted AEs produce characteristic peaks in the spectrum.*[246]

In elastic collisions negligible energy transfer occurs between the electron and the solid, the scattering angle distribution from these interactions mainly determines the electrons trajectory within the solid. The elastic scattering angle is a function of the substrate material parameters such as density, atomic number/weight and the electron energy along its trajectory. The inelastic events are responsible for the decay of the electron energy. A typical energy spectrum of electrons which escape from the bulk by overcoming the work function at the substrate-vacuum surface is shown Fig. 2.4 (b). The BSE part of the spectrum is characteristic for the substrate material while it is relatively insensitive to the PE energy in qualitative terms. Along the trajectory of a scattered electron in the bulk material atomic excitation/relaxation mechanisms from inelastic collisions lead to the formation of SEs. SEs are highly susceptible to elastic and inelastic scattering and travel limited distances in the order of a few nanometers before all their energy is transferred to the substrate. In Fig. 2.4 (b) a distinct emission peak of SEs is observed at energies < 50 eV. This corresponds to reduced energy losses at low electron energies as is qualitatively predicted by the strongly increasing mean free path between inelastic collision events in Fig. 2.3. To simulate the electron escape depths as shown in Fig. 2.4 (a) a full treatment of the FEB - solid interaction based on Monte Carlo simulations is required. This common approach includes the simulation of the gradual electron energy diminution as well as the simulation of the electron trajectories governed by energy-dependent elastic and inelastic angular scattering distributions.[138] Such simulations rely on the energy-dependent elastic and inelastic mean free path (Fig. 2.3).

Step 2 describes the gas transport of precursor molecules to the site of FEB interaction region at the substrate surface. As in CVD, this can be a rate-limiting step. The local molecular surface coverage results from a balance of molecule depletion by dissociation induced by the electron irradiation and molecule replenishment which is governed by adsorption, desorption, and diffusion. An important parameter is the average molecule residence time τ, which is related to the thermal energy at the surface and can be expressed by[218]

$$\tau = \frac{1}{\nu} \exp\left(\frac{E_\mathrm{d}}{kT}\right) \tag{2.2}$$

where ν is the vibrational frequency of a molecule adsorbed on the surface, E_d is the desorption energy, and k is the Boltzmann constant. The incident electron beam can stimulate non-dissociative desorption.[179,243]

During the primary decomposition step 3, interactions between electrons and precursor molecules occur. Irradiation induced chemical reactions leading to deposition and etching mainly take place at the solid surface. This is supported by the evidence that the substrate temperature has a major effect on the process rate.[166] PEs, BSEs and SEs all have the ability to decompose precursor molecules adsorbed on the substrate.[5] Several decomposition channels are likely to occur which, however, are rarely known for the precursor molecules used for FEB induced processing. Typically, an overall energy dependent cross-section describing the electron-induced decomposition probability of surface adsorbed molecules is defined, which can be modeled based on available experimentally determined data for simple organic molecules.[87,275] More specific, for FEB induced deposition post-irradiative decomposition or polymerization of intermediate reaction products, i.e. trapped molecule fragments, occurs by scattered electrons in the bulk of the growing structure. Such "dose" effects scale with the PE energy having an energy-dependent interaction depth, R, in the solid (Fig. 2.4 (a)). In most cases, the interactions of the FEB with the surface adsorbed precursor molecules produces deposited materials with chemical compositions including the desired atoms and undesired impurities, such as C, O, and H, originating from incorporated partially decomposed molecular fragments. Residual contamination in the microscope vacuum chamber, composed of mainly hydrocarbon and water molecules, influence the deposition results.[298] While carbonaceous contaminants may be incorporated in the deposit limiting the obtained purity,[184] electron beam irradiation in presence of water may lead to etching of carbon.

Transport of reaction products, i.e. ligands or fragments of decomposed precursor molecules, from the deposition site in step 4 include the diffusion and desorption of volatile molecules from the surface. This step is related to step 2 and 3: Adsorbed fragments may influence the surface coverage of undecomposed precursor molecules and may eventually be trapped inside the deposit leading to increased contamination.

All physico-chemical processes contribute to the final shape and resolution of deposits and etch pits. Comprehensive overviews of the fundamentals of FEB induced processing are found in.[23,46,47,244,298]

2.2.2 Historical overview

Electron-induced deposition was observed in the context of sample contamination during imaging since the construction of the first electron microscopes in the 1930's.[33,150,189,216,307] In early works it was concluded that under electron irradiation adsorbed hydrocarbon molecules lead to carbonaceous contamination deposits. Sources of hydrocarbon molecules in the vacuum system of SEMs and TEMs were identified to come from pump oil vapors, outgasing materials and from the contamination on the sample itself.[82] Reduction of contamination was achieved by sample heating,[81,156] injection of air into the chamber,[72,122,151,305] liquid N_2 coldtraps,[149,318] and fixation by electron irradiation prior to imaging[10,57,242,319].

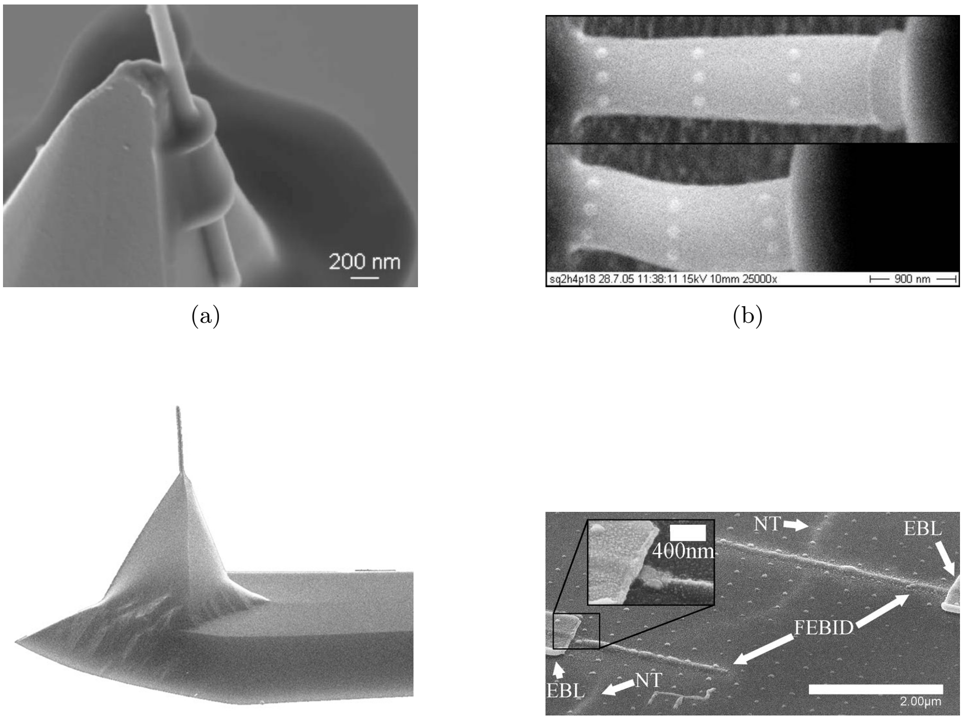

(a) (b)

(c) (d)

Figure 2.5: *Examples of FEB deposits. (a) FEB clamp deposit to fix nanowire to a cantilever tip from a Paraffin precursor.*[63] *(b) FEB marker deposits from contamination for strain detection during compression experiment of micropillars.*[199] *(c) AFM sensor functionalized with a magnetic tip deposit used for magnetic force microscopy.*[292] *(d) FEB contacts to a CNT using a gold-containing precursor.*[29]

Historically regarded as an unwanted side effect, contamination deposition has proved very useful in various applications, such as attaching nanostructures to cantilevers and as a marker technique for surface strain quantification detection (Fig. 2.5 (a) and (b)). Obviously, the reproducibility of "contamination" attachments strongly depends on the contamination level of the sample and the microscope. Organic,[23,26] organometallic (e.g. carbonyls,[152,292] metal-alkyls,[225] and acetylacetonates[176]), and inorganic (e.g. phosphines[8,228,291]) precursor molecules have been supplied into the microscope chamber which allowed to influence deliberately the deposit composition and deposition rate. The resulting deposits typically are a nanocomposite of metal nanocrystals embedded in a carbonaceous matrix.[197,293] In such deposits the metal content varies according to the precursor chemistry and deposition conditions. One advantage of FEB-induced deposition is that tuning between mechanical stability and functionality, e.g. electrical conductivity, of deposits can be performed using adapted precursor molecules (Fig. 2.5 (c) and (d)). Variation of the ion/electron or the precursor flux was shown to have a strong influence on the FEB/FIB deposition rates and yields.[171] Recent results highlight the influence of the H_2O rest-gas partial pressure which largely dominates the background pressure in SEMs.[225] Higher metal contents are deposited when beam heating effects occur.[293,294] Electrical characterization of materials deposited from organometallic precursors typically results in resistivities about 100-1000 times higher than the corresponding metallic bulk value.[20,148,152] Post-treatment of the deposits allows to increase the metal content and to decreased the resistivity.[21] Depositions of low resistivity Au contacts comparable to standard Au liftoff techniques were achieved with an inorganic gold precursor $AuClPF_3$[29] and a mixture of $(CH_3)_2$-Au-$C_5H_7O_2$ and H_2O gas[181] without the need for post-treatment.

Coburn *et al.* reported that Si etches rapidly when it is subjected to electron-beam irradiation in the presence of XeF_2.[53] Its use as FEB induced etching precursor has been reviewed in detail.[244] Carbon etching gases comprise H_2O[123,147] and O_2[139]. Water vapor attacks carbon under electron irradiation and cutting of CNTs has been demonstrated.[324] By switching between a deposition gas and an etching gas, one can use the technique as an attach-and-release tool to/from a nanomanipulator or sensor.

2.2.3 Applications

Recent research has spent tremendous efforts on the systematic creation of functional nanoscale deposits by means of FEBs and FIBs. FEB/FIB nanofabrication has many applications in tailored device prototyping covering fields of nanoelectronics,[12,60] nanophotonics,[165,202,211,226,258] functionalization of scanning probe sensors (magnetic, thermal, and optical),[39,86,292] nanomechanics,[321] and biology[56,212]. For electrical contacts to carbon nanotubes (CNTs) or nanowires (NWs), FEB induced deposition is frequently used as a soldering technique.[29,92,93,109]

In recent years industrial applications of FEB induced deposition and etching have evolved in the field of photomask repair[209] and fabrication of scanning probe supertips[207].

2.3 Modeling

Because of the complexity of the process, the reported studies have usually treated only a few of the conceptual process steps described in detail in Sect. 2.2.1, while treating the others only approximately.

2.3.1 Continuum models

Christy published the first continuum model in the field of electron-induced deposition in 1960.[44] His model was extended by Ling[167] to include the surface coverage of adsorbed molecules, and by Fritzsche[91] to take into account polymerization by radical formation and pulsed beams. A two-stage decomposition model was proposed which considers the decomposition and fixation as two coupled processes with independent cross-sections.[129,130] Zhdanov[325,326] and Müller[201] included surface diffusion as contribution which allowed to describe the formation of contamination donut structures produced by a stationary FEB. Müller's model for FEB induced deposition, which was later adapted by Haraichi *et al.*[117] to ion-beam induced etching, takes the key processes of surface diffusion, dissociation, desorption, and adsorption via an adsorption rate equation into account. He used a flat-top beam distribution which allowed to solve the differential equation analytically and to show interesting trends. However, these solutions have limited practical applicability. Recently, the rate equation has been numerically solved for Gaussian beam profiles and scaling laws for resolution have been formulated.[297] Toth *et al.*[287] explored a model approach by comparing competitive deposition and etching processes based on the precursor pressure, dissociation cross-sections, substrate temperature and the electron distribution. Surface diffusion processes were analyzed by numerically solved transport equations on curved surfaces.[255]

2.3.2 Dynamic Monte Carlo simulations

Several groups have developed Monte Carlo simulations to model dynamically the FEB induced deposition process. Such dynamic simulations adapt the topography and material composition of the deposit with the ongoing process. For a point electron beam Silvis-Cividjian *et al.*[273,275] and Hagen *et al.*[114] concluded from dynamic Monte Carlo simulations that the ultimate lateral process resolution depends on the emitted secondary electron distribution. They used the idealization of permanent monolayer coverage of the adsorbed molecules in the irradiated area. The importance of a detailed treatment of the precursor supply has been recognized in further developed dynamic Monte Carlo simulations taking into account the processes which govern the molecular coverage. Fowlkes *et al.* developed a three-dimensional Monte Carlo simulation which included the precursor supply described by Langmuir adsorption, but neglected surface diffusion.[87] A similar simulation was developed by Liu *et al.*.[173,174,194] In recent Monte Carlo simulations the full treatment of the balance of molecular adsorption, desorption and diffusion is included.[278]

2.3.3 Model limitations

The main limitations to the currently existing models of FEB induced processing are:

- FEB-solid interaction: Scattering of electrons in the deposited material is related to the unknown material density, composition, substructures and possibly charging.
- Precursor supply: The precursor coverage in the area of FEB-solid interaction can only roughly be approximated due to poorly known parameters, such as the directly impinging precursor flux, molecule residence time, sticking probability and surface diffusion coefficient.
- Irradiation chemistry: The decomposition and fixation paths of precursor molecules are manifold and rarely understood. The modeling of relevant energy dependent dissociation cross-sections relies on fundamental assumptions based on very few measurements in the gas phase. Residual gases, such as water and hydrocarbon molecules should be accounted for in the models.

This list is non exhaustive and has the goal to point out that there is a lack of knowledge of the fundamental parameters which influence the process rate and resolution as well as the composition and properties of deposited materials.

2.4 *In situ* monitoring

In situ monitoring of FEB/FIB induced processing means the correlation of real-time observations to the process parameters.

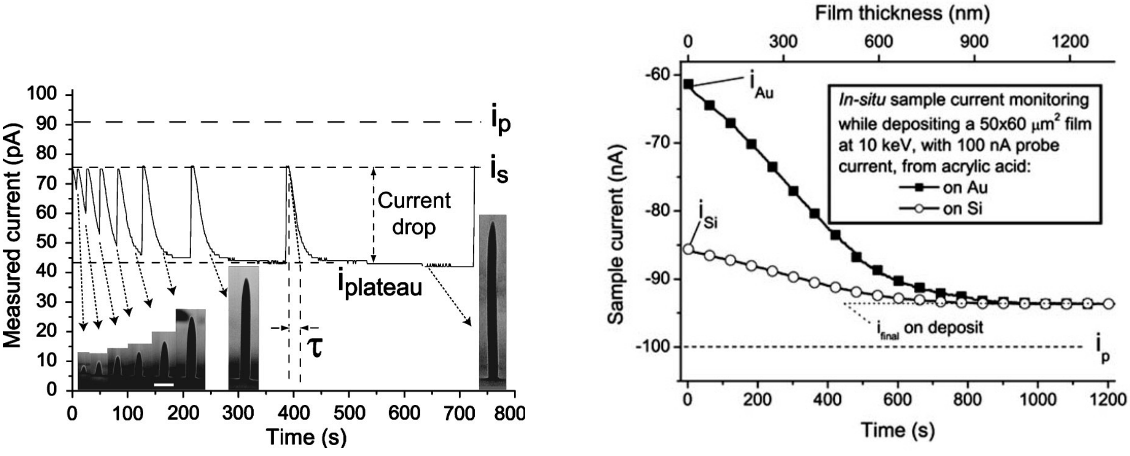

(a) (b)

Figure 2.6: *(a) Current monitoring for eight successive deposits from [$(PF_3)_2RhCl$]$_2$ at $I_p = 91$ pA. Inset: SEM 75°-tilt images of resulting tips. From left to right, respectively grown in: 10, 20, 30, 40, 60, 120, 240, and 480 s, corresponding to the current curves (scale bar = 625 nm).*[24] *(b) In situ sample current monitoring during the growth of large-area carbon films.*[28]

An easy accessible real-time measurement is based on the analysis of the current absorbed in the sample, I_s, and/or the secondary electron signal during processing. The techniques rely on the change of the SE yield, δ, and the BSE yield, η, with varying structure shape and material. The relation of the sample current to the SE and BSE yields is revealed by the current balance:

$$I_s = I_p(1 - \delta - \eta), \tag{2.3}$$

where I_p is the probe current. Both η and δ are strongly sensitive on the FEB incidence angle to the sample surface which leads to edge effects: The PEs incident on a sample edge or ridge produce more SEs than upon normal incidence, e.g. resulting in brighter edges in SEM images. Furthermore, electron scattering is characteristic for the sample material density and atomic number which makes η and δ material sensitive. In stationary spot irradiations, the change of the deposited pillar geometry is the main information contained in the sample current monitoring signal (Fig. 2.6 (a)). In large area scan irradiations the material change of the deposits within the electron-sample interaction volume with increasing film thickness is the main information content (Fig. 2.6 (b)). In FEB induced deposition the method is used for continuous shape monitoring and for process reproducibility.[24,240] Systematic sample current monitoring allowed to develop a more detailed model of electron scattering.[28]

In FIB milling the same approach is conventionally used for end-point detection during processing of thin films or multilayer structures. Besides the use of the sample current[119] and SE signal,[121] the use of secondary ion mass spectroscopy has been reported[118].

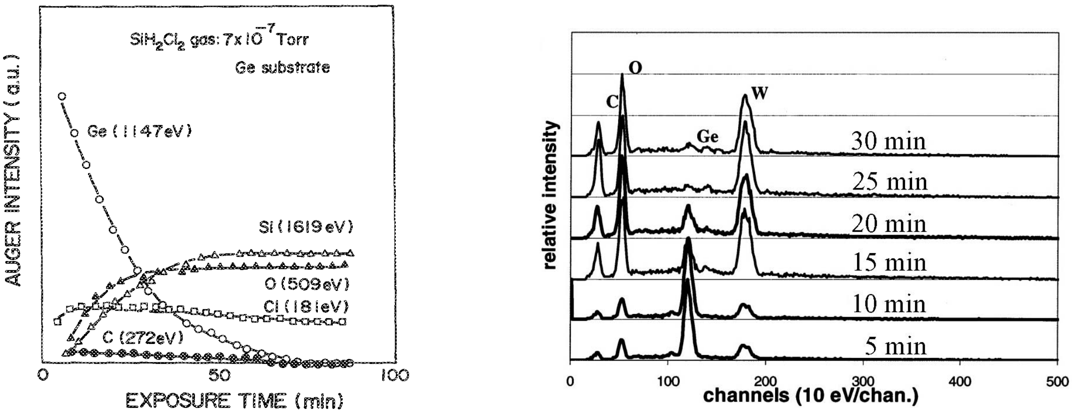

(a) (b)

Figure 2.7: *(a) AES intensity evolution during FEB induced deposition using the precursor* SiH_2Cl_2 *on a Si substrate.*[183] *(b) EDX spectra during FEB induced deposition in* 2.5×2.5 μm^2 *scan areas using the precursor* $W(CO)_6$ *on a Ge substrate.*[241]

During FEB induced deposition, several attempts were made to monitor the signals from AEs and X-rays emitted in the relaxation mechanisms of core-shell ionizations of the sample atoms upon incident electrons. Spectra of both signals represent a characteristic fingerprint of the irradiated material which forms the bases of microanalysis, i.e. the compositional analysis by energy-dispersive X-ray (EDX) spectroscopy and Auger electron spectroscopy (AES). While AES is surface sensitive with typical depths in the order of 2-5 nm, EDX averages the material composition within the electron-sample interaction volume (Fig. 2.4 (a)). The electron range is material and electron energy dependent, e.g. extending to several micrometer depth for 20 keV electrons impinging on a Si substrate. *In situ* AES observations were performed in a modified AE spectrometer using a cylindrical mirror analyzer during FEB induced deposition from the precursors WF_6 and SiH_2Cl_2 (Fig. 2.7 (a)).[183,186] The method allowed to determine the growth rates and the evolution of material composition of the growing film by a 1 μA electron probe defocused to roughly 30 μm. An EDX spectrometer mounted to a FEG-SEM was used to monitor *in situ* the evolution of the material composition during FEB induced depositions in scanned areas using the precursor $W(CO)_6$ (Fig. 2.7 (b)).[241] The substrate signal was observed to decrease and the deposited material signal increased as a function of deposit thickness. Probably, the high complexity involved in modeling quantitative EDX signals[246] influenced by the substrate geometry prevented this method to investigate in detail the process in further studies.

Interesting results have recently been obtained for FEB induced deposition with $W(CO)_6$ in a STEM.[300] Monitoring of the annular dark field (ADF) transmission intensity, having a strong Z-contrast component, allowed to observe the material deposition at the initial growth stage within a few seconds. The ADF signal incorporated in a feedback control loop was used to correct for proximity effects. This monitoring method is limited to electron transparent samples, it offers, however, insight into the growth process of individual nanometer-sized deposits.

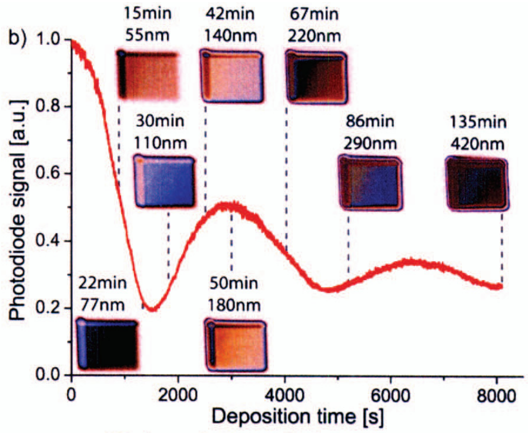

Figure 2.8: *Reflectometry curves as function of time for FEB induced deposition from* $Si(OCH_3)_4$. *Insets are optical-microscope images of the deposits with corresponding deposition time and thickness. Deposit dimensions:* 140×120 μm^2.[227]

By *in situ* real-time laser reflectometry the evolution of optical thickness of transparent materials deposited by FEB has been measured.[227] From the periodic intensity variations due to interference effects as function of deposit thickness the complex-refractive index of deposits from $Si(OCH_3)_4$ was found to be higher than that of pure SiO_2 due to carbon contamination (Fig. 2.8). The optical thickness measurements monitor the growth rate for homogeneous materials and in addition the evolution in composition during growth.

The invention of the QCM in 1959 introduced a method to sensitively detect the growth of thin films by mass changes at the nanogram-scale.[263] FEB carbon contamination depositions at electron energies of 10 eV to 4 keV were measured on a Ni-coated QCM.[158] Correlation between SE emission and the film growth rate were revealed from their similar temporal evolution and energy dependence. Low temperature FEB assisted autocatalytic CVD from the metal-carbonyls $Fe(CO)_5$ and $Cr(CO)_6$ on Si has been observed by QCM mass measurements.[157] Metal nuclei were supplied as autocatalyst by breaking the adsorbed molecules with electrons. QCM-based process monitoring was employed in an extended study on thin film depositions within square millimeters by defocused Ar^+ ion beams using the precursor $(CH_3)_2Au(hfac)$, $C_7H_7F_6O_2Au$.[68] The deposition rate was measured as a function of ion current, gas pressure, and substrate temperature. The rate variations with the precursor pressure (Fig. 2.9 (a)) and with the substrate temperature could be attributed to precursor coverage variations depending on adsorption-desorption kinetics.[69] The ion yield was proportional to the precursor

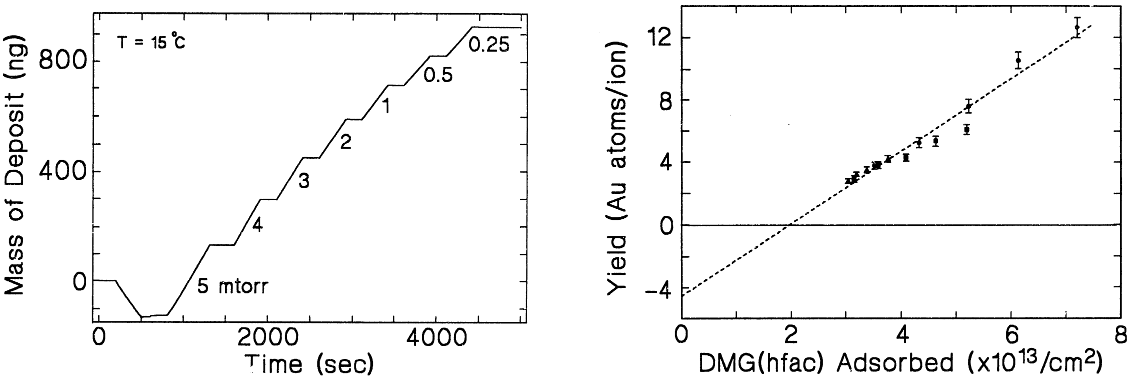

(a)

(b)

Figure 2.9: *(a) Frequency and corresponding mass response evolution measured by QCM monitoring during an ion-beam deposition run in which the* $(CH_3)_2Au(hfac)$ *pressure in the subchamber was varied as indicated for each sloped region where the beam irradiated the substrate. The substrate was kept at 15 °C. (b) The ion yield plotted against the* $(CH_3)_2Au(hfac)$ *coverage.*[67]

surface coverage (Fig. 2.9 (b)). An interesting result was the evidence of $(CH_3)_2$Au(hfac) chemisorption on clean surfaces which was independent on the substrate temperature between -0.9 °C and 14.9 °C. Results from these QCM monitoring experiments allowed an atomistic energy transfer model to be developed.[71] From similar QCM-based monitoring experiments from the precursor (hfac)CuVTMS a phenomenological surface kinetic model describing the adsorption, deposition, reaction product desorption, and sputtering steps involved in ion-beam induced deposition for the particular precursor was formulated.[42] The surface kinetic model was sufficient to describe the deposition rate, deposit composition, and precursor coverage in agreement with experimental measurements.

In microscopes equipped with both, an electron and ion column, termed dual beam microscopes, continuous visualization of FIB processing is achieved with live FEB imaging. The method was applied to control gap reduction down to 5 nm between Pt containing electrodes.[102] Fabrication of multi-electrode structures by depositing three closely spaced free-standing pillar electrodes in three dimensions further demonstrated the flexibility of this hybrid FIB-FEB approach.

2.5 Mechanical analysis of FEB/FIB deposited materials

Both, static and dynamic mechanical test methods have been used for many years to characterize composite materials and structures at the macromechanical level, and the same approaches are proving to be effective for characterizing materials at the micro- and nanomechanical levels.[237] Static bending, tensile and compression experiments and modal vibration analysis are increasingly employed to measure the mechanical properties of one-dimensional nanostructures such as CNTs and NWs.

Static methods rely on physical interaction with the sample object typically achieved with the tip of an AFM cantilever used as the force sensor. Adhesion forces and molecule binding forces have been extensively studied using this technique.[35,155,215] CNTs and NWs have been bent, stretched (Fig. 2.10 (a)), or compressed with nanometer positioning accuracy inside SEMs and TEMs, while performing measurements with nano- to millinewton force resolution.[64,84,106,127,128,141,223]

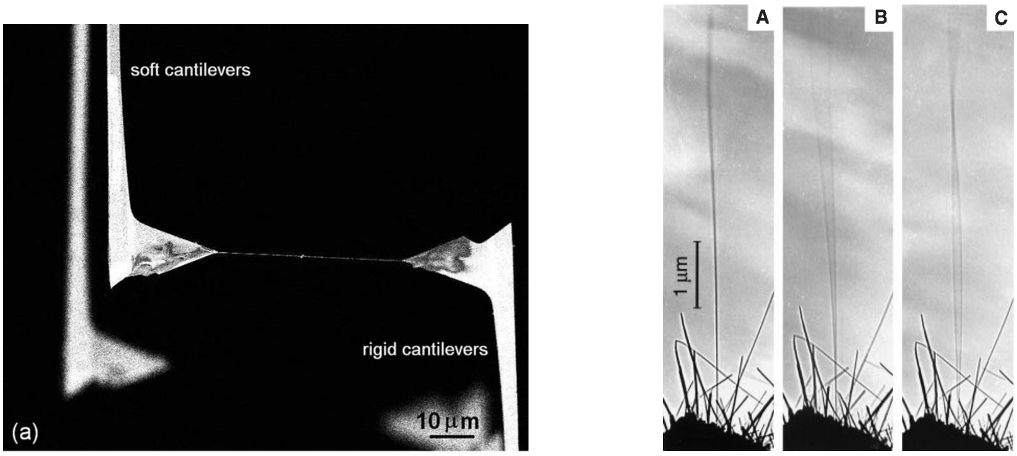

(a) (b)

Figure 2.10: *(a) A boron NW clamped between two AFM cantilever tips under a tensile load. FEB induced contamination deposition was used to bond the NWs to the tips.[64] (b) CNT response to resonant alternating applied potentials. (A) Thermally induced spontaneous vibration. (B) Excitation at the resonance frequency of the fundamental mode of vibration, (C) and at the second harmonic.[235]*

In modal vibration analysis the sample structure is excited at one of its resonance modes. The resonance frequency is related to the structure size and its mechanical properties. Resonance experiments relying on thermal energy as the excitation have been performed on CNTs.[7,288] Electric field excitation has been used by Poncharal *et al.* to drive multiwall CNTs while observing resonance in a TEM (Fig. 2.10 (b)). From the driving frequency at resonance the Young's modulus of the CNT was determined.[235] The method was extensively used in recent research studies to characterize, e.g. ZnO NWs,[271,322] B NWs,[64] amorphous SiO_2 NWs,[62] and WO_3 NWs[172]. Vibration monitoring by field emission from the structure under test was used to observe resonance frequencies of multiwall CNTs in the MHz range.[238]

In a number of recent studies *in situ* mechanical analyzes have been performed on structures fabricated by FEB and FIB induced deposition. Amorphous carbon Ga^+ FIB depositions from the precursor Phenanthrene, $C_{14}H_{10}$, have been analyzed in spiral spring[203] and pillar[94] structures. The combination of bending tests and vibration experiments was employed to determine both, the density and Young's modulus of vertically FIB deposited pillars.[95,133] The material tends to become stiffer with decreasing growth rate which varied with the impinging precursor flux (Fig. 2.11 (a)). The material density did not show a clear dependence on growth

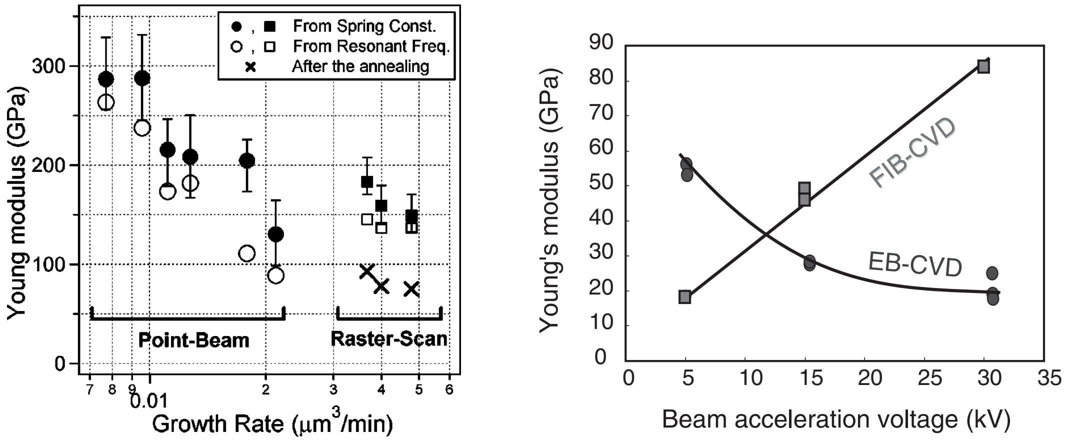

(a) (b)

Figure 2.11: *Mechanical analysis of amorphous carbon pillar deposits from the precursor Penathrene. (a) The Young's moduli derived from the spring constant (solid symbols) and the resonant frequency (open symbols) are compared. The Young's moduli were obtained for pillars fabricated by point-beam (circles) or raster-scan (squares), and after annealing at 600℃ (crosses).*[132] *(b) Dependence of Young's modulus on the acceleration voltage of FEB (circles) and Ga^+ FIB (squares).*[96]

rate.[132] Mechanical analysis of Ga^+ FIB deposits from $W(CO)_6$ showed the same trends.[133]

The opposing dependence of Ga^+ FIB and FEB deposited material stiffness on the acceleration voltage as shown in Fig. 2.11 (b) was qualitatively explained by variations in the deposited energy dose due to the differing interaction volume of FIB and FEB in the pillar structure.[96,221]

Post-treatment with oxygen plasma increased the Young's modulus of amorphous carbon pillars.[96] The measurements could be explained by a core-shell morphology model of the pillars with a Ga-rich core, from implantation during the fabrication, and an amorphous carbon shell as was experimentally verified by EDX. Since the plasma reduced the pillar diameter by etching the shell it was concluded that the Young's modulus of the core exceeds the Young's modulus of the shell.

Density measurements have been performed from direct measurements of the mass and volume of FEB induced deposits. A cantilever-based mass sensor in a conventional AFM setup was used to determine *ex situ* the density of FEB deposited pillars grown in varying conditions.[296] Relations between the chemical deposit composition and deposit density were established and irradiation dose effects measured. The density of deposits from the precursors $Co_2(CO)_8$ and $[(PF_3)_2RhCl]_2$ predicted from their chemical composition related well to the measured values. From the measurements of deposit densities using the precursors Tetramethoxysilane (TMOS) and (hfac)CuVTMS two coupled decomposition mechanisms were identified: irradiative decomposition causing bond breaking and matrix reticulation as well as thermal dissociation. The latter was identified to mainly increase the copper content in the deposits (Fig. 2.12). It was concluded that the ratio of impinging electrons per deposited

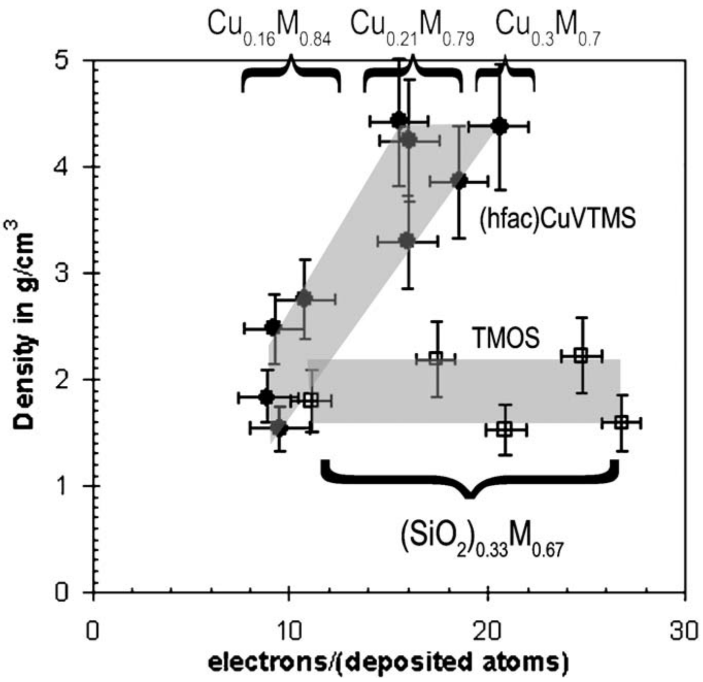

Figure 2.12: *Deposit density plotted in function of the number of electrons per deposited atom. Deposit compositions are given in generalized form, where M stands for the carbonaceous matrix. The two precursors used were: TMOS, tetramethoxysilane, and (hfac)CuVTMS, hexafluoroacetylacetonato-Cu(I)-vinyltrimethylsilane.*[296]

atom, beam heating, and thermal stability of the precursor molecule determine the density and composition in FEB induced deposits.

Recently, CNT resonators for *in situ* mass sensing of material grown at the tube extremity by FEB induced deposition from hydrocarbon and $W(CO)_6$ precursor molecules were presented.[213,214,264] Material densities of 0.29 to 0.8 g cm^{-3} for the carbon deposits and 1.4 to 2.7 g cm^{-3} for the W containing deposits were determined. The sensor response could only be approximately calibrated from the resonance frequency, dimensions and material properties of the CNT. The CNT-based mass sensing approach offered a very high mass sensitivity and a resolution at the attogram-scale.

Chapter 3

Setup and methods

3.1 FEB/FIB induced processing setup

3.1.1 Electron microscope Hitachi S3600-N

FEB induced deposition was performed inside a Hitachi S-3600N thermal W emitter SEM (Fig. 3.1). The large vacuum chamber, intended for samples with diameters up to 10 inch, with five horizontal and three inclined accessory ports for various feedthroughs was ideally suited for integration tasks, e.g. of bulky micromechanical testing setups. Samples were positioned by a fully motorized stage and were hold in place on the sample holder by stainless steel clamps or by silver glue. The range of acceleration voltage in this instrument is 0.5 to 30 kV and electron probe currents up to 10 nA were routinely achieved. The microscope was equipped with an Everhart-Thornley SE detector and a BSE detector for imaging. An analogue PC card was used to acquire SE video image sequences. A picoammeter[140] connected to the sample stage was used to adjust the FEB current absorbed in a Faraday cup and to monitor the sample current.

Extended control of the beam movement is achieved by a lithography system[312] which enables the writing of complex shapes and provides exposure dwell times $\tau > 200$ ns and control over the beam-blanking unit mounted in the electron column.

Experimental determination of FEB parameters

The electron probe radial current density in the focal plane shows approximately a Gaussian distribution[246]

$$j_p(r) = j_0 \exp(-r^2/2a^2) \tag{3.1}$$

with a full width at half maximum of the peak FWHM $= d_{1/2} = a2\sqrt{2\ln 2}$.

In Fig. 3.2 (a) results of the probe size and resolution measurements of the Hitachi S-3600N SEM are summarized. Knife edge measurements[249] based on either the intensity edge profile of sample current or the SE detector signal differ insignificantly within their level of accuracy. The measurements indicate that the probe size is considerably larger than the resolution values predicted by the Fourier transform image analysis method.

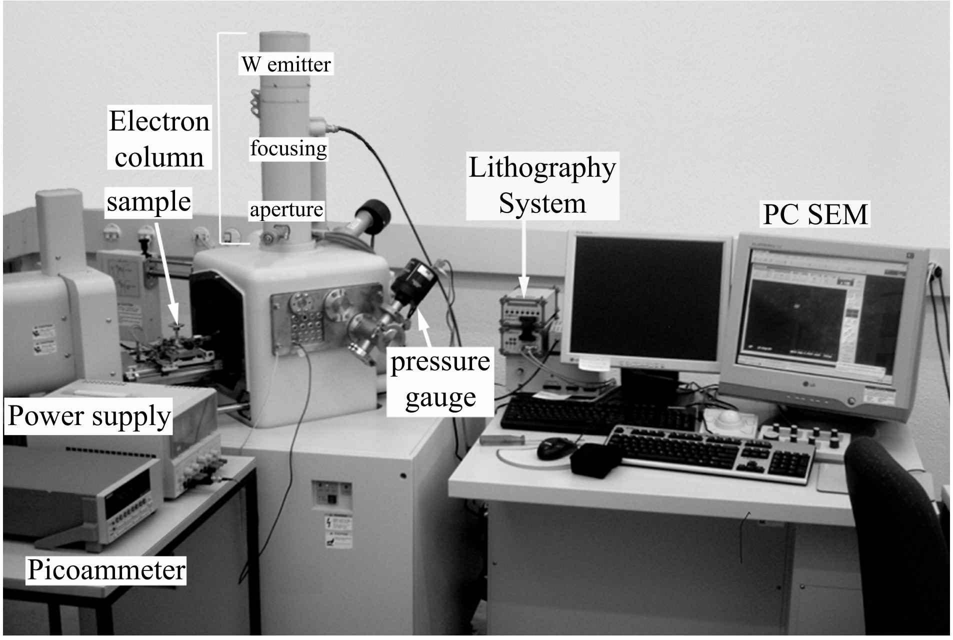

Figure 3.1: *Hitachi S-3600N SEM for FEB induced processing with lithography software for beam control. Sample current monitoring was performed using the picoammeter.*

As outlined in Fig. 3.2 (b), the probe size has been measured from a knife edge method performed on membranes. These methods largely avoided edge effects due to the limited interaction volume produced by the primary electrons in 30-50 nm thick membranes. The limited measurement speed of the picoammeter required to perform slow line scans across the membrane edge which resulted in considerable contamination deposition and falsified the probe size measurement. Injecting a carbon etch gas, i.e. H_2O, avoided the contamination on SiO_2 membranes.[123] Alternatively, the membrane edge was conventionally imaged at high scan rates limiting the irradiation dose and thus, contamination. The SE profile was subsequently extracted from the acquired image. In the measured profiles the rise-distance $d_{25-75\%}$ of points corresponding to 25% and 75% of the signal base level are related to the FWHM according to

$$\mathrm{FWHM} = 1.745\ d_{25-75\%}. \tag{3.2}$$

The resolution of the Hitachi S-3600N SEM was also measured from the Fourier transform of an image of sputtered gold particles on a carbon plate. The intensity of the two-dimensional Fourier transform of an image represents its frequency contents plotted radially as a function of the spatial frequency, with the DC (zero frequency) component at the origin of the transform. Essentially, the noise contribution in the Fourier transform is a uniform (high-frequency) background signal. The background cut-off frequency is used to determine the level of the maximum spatial frequency in the image containing information. Since the signal to noise ratio falls toward unity at the resolution limit the boundary between signal information and noise is poorly defined and its exact position must be defined on the basis of arbitrary choices

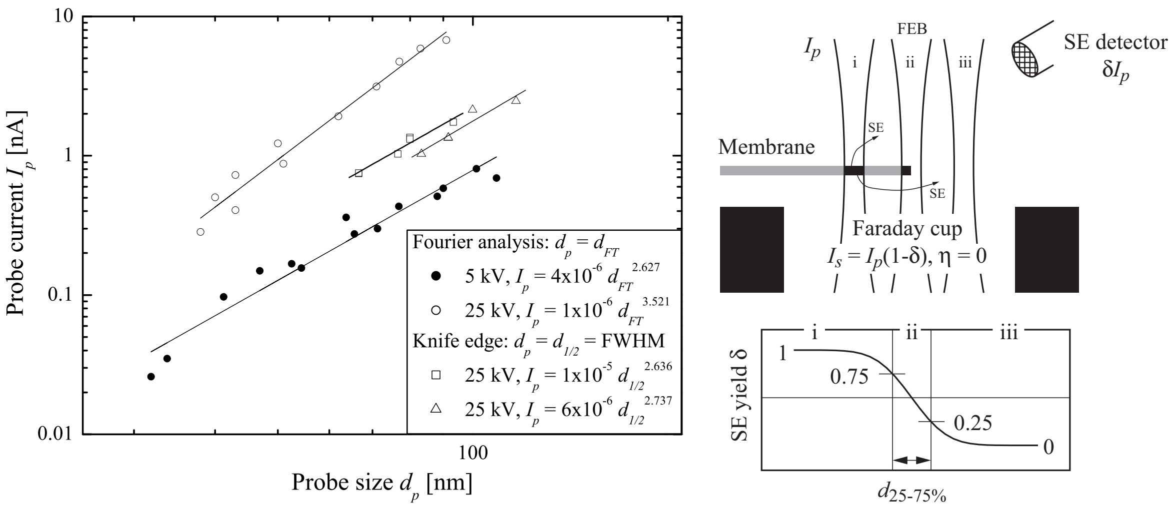

(a) (b)

Figure 3.2: *(a) Probe current as a function of the resolution and the probe size at acceleration voltages of 5 kV and 25 kV with an aperture size of* 50 *µm and at a working distance of 10 mm. Other SEM parameters were chosen to yield best resolution. (b) Experimental determination of the probe size by the membrane knife edge method. The sample current I_s, measured in a Faraday cup located below the membrane, and the SE signal δI_p are recorded while scanning the beam across the edge of a thin membrane. The calculated SE yield profile, depicted in the lower part of the figure, corresponds to the integrated Gaussian profile. From the determination of* $d_{25\text{-}75\%}$ *the beam FWHM is determine by Eq. 3.2.*

made by the operator.[135] In this method the measured resolution depends not only on the FEB probe size but also on the sample structure due to edge effects in the secondary electron signal.

3.1.2 Microtube gas injection system

A homemade gas injection system (GIS) for solid and liquid precursors was mounted to the Hitachi S-3600N SEM. The GIS consisted of four main parts: i) The precursor reservoir, ii) the tubing which connects the reservoir to iii) the nozzle and, vi) the positioning unit which supported the GIS attached to the objective lens.

An internal GIS setup was entirely enclosed inside the vacuum chamber and an external GIS setup had the precursor reservoir outside the vacuum chamber. Both, the external and internal GIS setups are schematically depicted in Fig. 2.1. Modular GIS tubings, reservoirs and nozzles were assembled from standard components conventionally used for medical applications.[290] All components are easily interchangeable which allowed to conveniently switch the GIS nozzle while keeping the rest of the assembly. Nozzle tubes were modified by manual grinding and in some cases by drilling of additional holes using Laser cutting. Further details of the used GIS nozzles are discussed in Sect. 6.9.2. The short tubing components in the

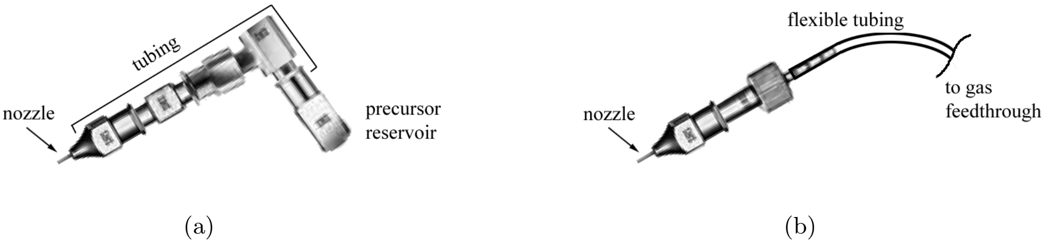

Figure 3.3: *The (a) internal and (b) external tube nozzle GIS assembly employed for FEB induced deposition in this work.*

internal GIS (Fig. 3.3 (a)) can provide a sufficiently high gas flux to the sample for precursors with low and medium vapor pressures at room temperature, e.g. Cu(hfac)$_2$, [(PF$_3$)$_2$RhCl]$_2$, Co$_2$(CO)$_8$. High vapor pressure precursors and gases such as molecular oxygen can be injected through a vacuum feedthrough connected to a flexible silicon tube fitted to the GIS nozzle head (Fig. 3.3 (b)). Individual sets of GIS components were used for each precursor. Standard vacuum feedthroughs, fittings and valves have been employed for tubing outside of the vacuum chamber.

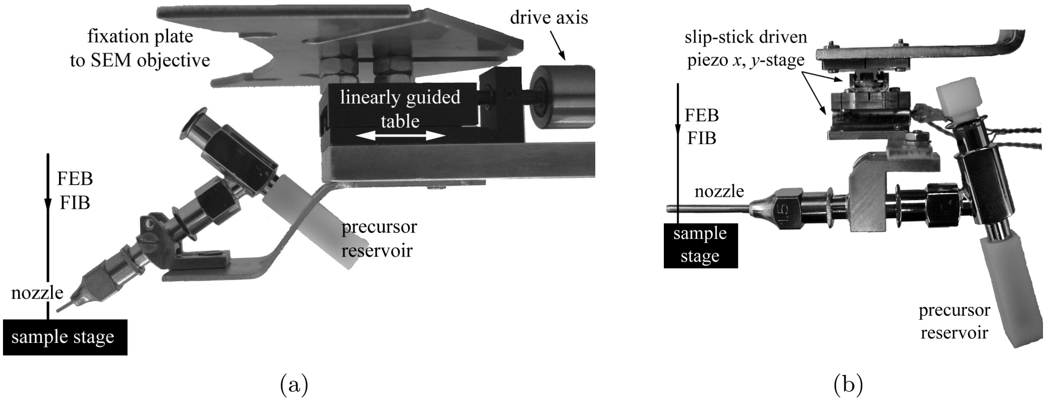

Figure 3.4: *Homemade mobile nozzle-based GISs with internal precursor reservoirs. (a) First generation mobile GIS with a linearly guided table driven by a DC-motor. (b) Second generation mobile GIS with two slip-stick driven piezo x, y-stages*[276].

The position of the nozzle relative to the FEB was controlled by vacuum-compatible positioning units. Motorized GIS positioning avoided the need for an accurate manual adjustment while the vacuum chamber was open. Two generations of mobile GISs were integrated in the Hitachi S-3600N SEM in the framework of this thesis (Fig. 3.4). These systems were used with internal and external precursor reservoirs using the mentioned assemblies (Fig. 3.3). The SEM stage provided x, y, z, rotation and tilt positioning of the sample below the GIS nozzle.

Precursors which are sensitive to oxygen and/or humidity were transfered from their storage containers into the reservoir under inert atmosphere inside a glove box. The reservoirs were sealed vessels from either stainless steel or PTFE (internal), or glass (external). The supplied throughput Q (in molecules per time) and the corresponding flux J_{tot} (in molecules per area-time) from the nozzle-based GIS with exit aperture radius r, was experimentally determined by measurements of the mass loss Δm, using a precision balance with sub-milligram resolution after the injection period Δt:

$$J = \frac{Q}{\pi r^2} = \frac{\Delta m}{\Delta t}\frac{N_a}{M}\frac{1}{\pi r^2}, \tag{3.3}$$

where N_a is Avogadro's constant and M the molecular mass.

Vacuum system and background pressure

The vacuum chamber and electron column of the Hitachi S-3600N SEM were differentially pumped with an oil-diffusion pump backed by a rotary pump to a chamber pressure of $1 \ldots 5 \times 10^{-3}$ Pa in standard imaging mode.

Injection of precursor gas at a rate Q leads to an increased background pressure by the amount of the partial precursor pressure P_b which is depending on the pumping speed S (in volume per time)[i] according to $P_b = kTQ/S$. The background flux contribution for an ideal gas at rest to the substrate is found using

$$J_b = P_b \left(2\pi mkT\right)^{-1/2}, \tag{3.4}$$

where m is the molecule mass. A cold cathode ionization Penning-type pressure gauge was used to monitor the pressure in the high-vacuum range.

Gas flux characterization setup

A custom-built vacuum chamber (Fig. 3.5) was used for characterization experiments of local precursor flux distributions by thermal decomposition on a substrate. Transparent windows allowed to observe and measure the distance and angle between the nozzle and the substrate using an optical microscope (Leica MZ16 A Stereomicroscope[164]). Positioning was done by a three-axes sample stage with micrometer resolution. The chamber was evacuated by a turbo-molecular pump backed by a rotary pump and background pressures in the order of $3 \ldots 5 \times 10^{-3}$ Pa were routinely reached. A pyrolytic boron nitride resistive heating element[103] was mechanically attached to a heat sink which was kept at room temperature by a circulating water flow. Substrate samples with a typical size of 2×2 cm^2 were hold in place by a stainless steel spring sheet on a polished stainless steel or copper plate which was in direct contact with the heater. The intermediate metal piece increased the thermal contact to the substrate and homogenized temperature gradients. The substrate temperature was measured by a thermocouple (type K) which was mechanically clamped to the substrate by a spring sheet. The heating unit typically allowed to reach substrate temperatures of 200 °C within some minutes and manual adjustment of the heating current permitted to limit temperature fluctuations to within ±5 °C.

---

[i] Specified to 570 l s^{-1} for the oil-diffusion pump. The pump speed is depending on the molecular weight, i.e. heavier molecules are pump more efficiently.[160]

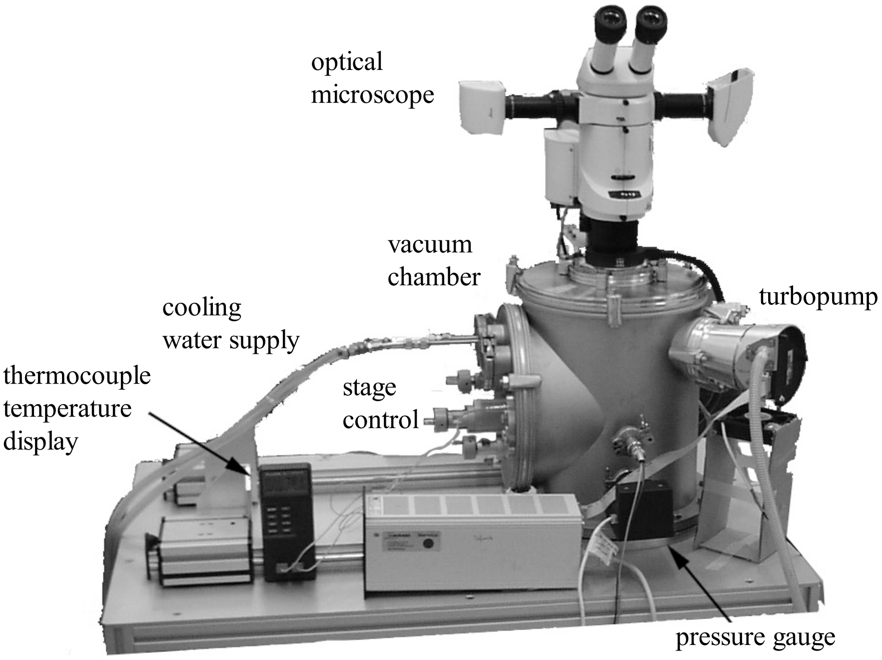

Figure 3.5: *Setup for thermal decomposition experiments for precursor flux distribution measurements. In situ observation of the process is provided by an optical microscope.*

3.2 *In situ* characterization tools

For *in situ* handling and testing of micro- and nanostructures high-resolution displacement units driven by piezoelectric slip-stick actuators were used. Such devices provide nanometer resolution and several centimeters traveling range at a relatively high velocity (typically 5 mm/s).[22] Using microfabricated tools for nanomanipulation and characterization requires at least two manipulation units: one to move the tool and one to move the sample.

In the SEM, a short working distance will usually provide high resolution and limit the drift due to stray fields, which is important for these setups with many electrically driven devices. It is also important to avoid obscuring the sample for the detector to work efficiently.

3.2.1 Positioning and scanning units

Two different systems for the manipulation and characterization of nano-scale objects have been developed and integrated into the Hitachi S-3600N SEM to solve different tasks described in Chps. 4, 5 and 7: i) A scanning probe microscopy (SPM) setup and, ii) a six-axes Cartesian nanomanipulator.

The SPM setup can be used in scanning, i.e. AFM imaging, and manipulation mode. It is composed of two different manipulators (Fig. 3.6 (a)). The sample is mounted on a three-axes Cartesian nanopositioning stage with integrated capacitive position sensors (P-620 series[233]). Piezoelectric actuators and a flexure guiding system provide a travel range of 50 μm for each axis and sub-nanometer resolution. For coarse positioning towards the sample, the sensor or manipulation tool is mounted on a three-axes nanomanipulator with two rotational and one linear degree of freedom (MM3A[142]). The manipulator is driven by piezo actuators with sub-nanometer precision. Operating the actuators in slip-stick mode, a working range of more than 100 cm^3 can be achieved. The whole setup is mounted inside the SEM such that the sample is normal or at an angle up to 60° with the FEB. With the SEM sample stage, the sample's area of interest can be moved into the field of view. This setup was used for nanomanipulation task related to cantilever calibration, for *in situ* bending experiments using cantilever-based force sensors and for *in situ* frequency modulation AFM.

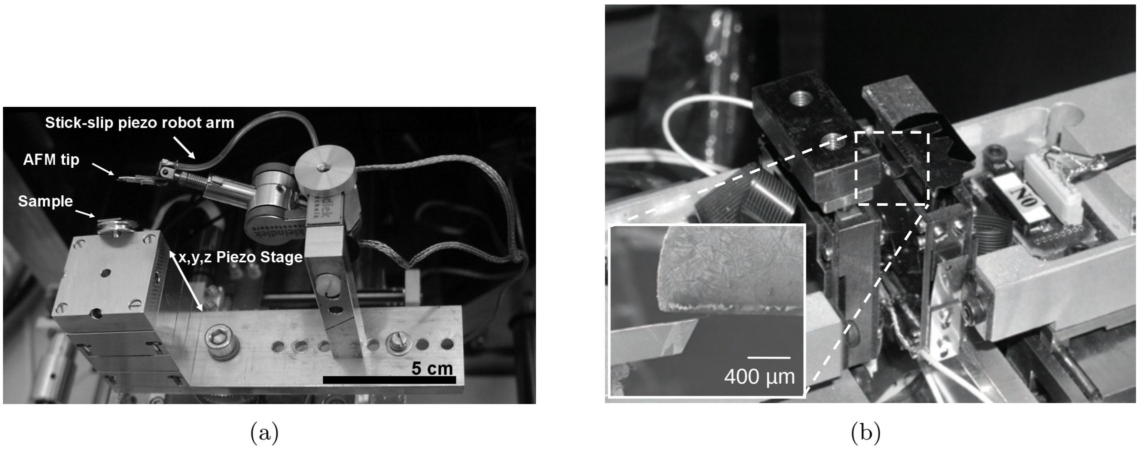

(a) (b)

Figure 3.6: *(a) Scanning probe microscopy setup. (b) Six-axes Cartesian nanomanipulator. The inset shows a close-up view of a cantilever manipulating nanotubes at the edge of a Si substrate.*[83] *The cantilever and the substrate both have three orthogonal degrees of freedom.*

The second system is based on a six-axes Cartesian nanomanipulator (Fig. 3.6 (b)). The nanomanipulator is driven by piezoelectric actuators combined with a stick-slip motion principle. Two three-axes Cartesian positioning stages have been combined into a nanomanipulator with six axes and three degrees of freedom. Each positioning stage is built of an x, y, z-stage. The z-stage has especially been designed for operation inside a SEM.[187] The piezo actuator is shielded avoiding electromagnetic interferences with the electron beam and the correct choice of material makes it compatible with the SEM environment (non-magnet and low outgassing materials). By implementing a pre-load mechanism, thrust forces of 1.6 N in vertical direction could be realized. The travel range of the nanomanipulator is 10 mm in x and y, and 8 mm in z direction. Incremental optical encoders with a grating pitch of 20 μm are embedded into each axis. A 50-fold interpolation yields a final resolution of 100 nm. This setup was used for *in situ* tensile strength experiments.

3.2.2 Mass sensor setup

Two generations of mass sensors based on AFM cantilevers with piezoresistive deflection read-out have been implemented within this work. A first prototype (Fig. 3.7 (a)) showed the feasibility of the employed actuation principle using 1 mm thick piezoelectric plates with Ni electrodes on their flat surfaces.[190] The contacts from the built-in piezoresistors were bonded directly to an IC chip holder. A more elaborated second generation setup (Fig. 3.7 (b)) offered the possibility for convenient exchanging of the piezoresistive cantilever sensor bonded previously to a patterned ceramic base plate. The sensor was mounted to a PTFE piece with contact clamps. It had been recognized from experiments using the setup in Fig. 3.7 (a) that thermally induced drifts are a major problem in mass sensing applications in vacuum using piezoresistive sensors. This issue had been addressed by thermally stabilizing the sensor and the cables which are connected to it. Best results were achieved if the cantilever chip was directly contacted to the stabilized heat sink by a copper wire. Good thermal contacts were established either by soldering or using silver paint.

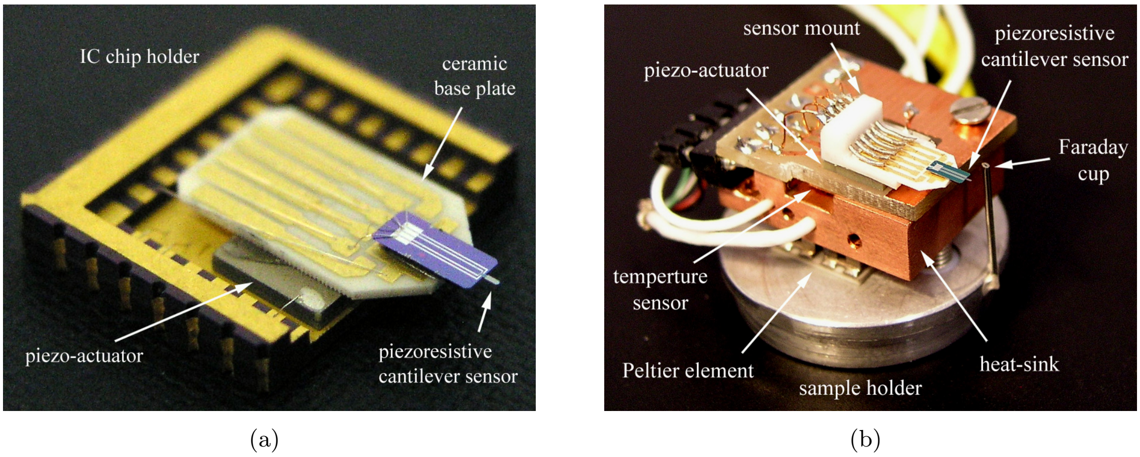

(a) (b)

Figure 3.7: *(a) First generation mass sensor setup without temperature stabilization mounted into a standard IC chip holder. (b) Second generation mass sensor setup with temperature stabilization by a closed-loop controlled Peltier element-heat sink with an integrated temperature sensor.*

3.2.3 Cantilever-based sensors

The microfabricated cantilever devices presented in Fig. 3.8 have been selected for different applications in view of their characteristics in terms of sensitivity and deflection read-out principle. Si cantilevers with spring constants of 45 N m^{-1} or 2.8 N m^{-1}, as specified by the manufacturer, have been used for *in situ* nanomanipulation tasks and mechanical tests on FEB deposits (Fig. 3.8 (a)). The protruding AFM tip permits to observe the location of the tip-sample interaction. Piezoresistive Si cantilevers with spring constants in the range of 20 – 400 N m^{-1} and with built-in Wheatstone bridge circuitry by four piezoresistors located

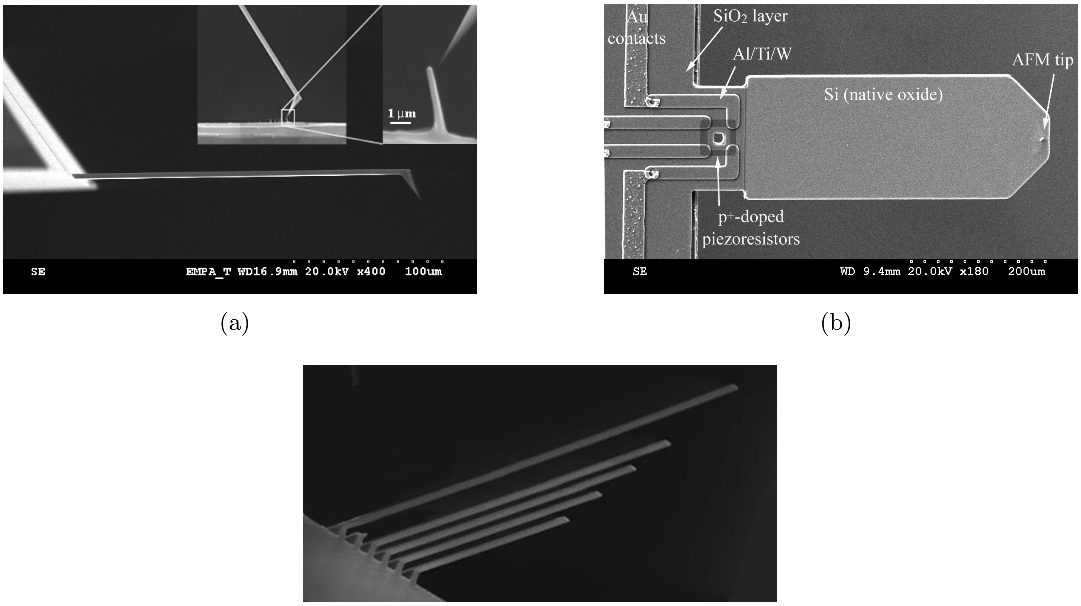

(a) (b)

(c)

Figure 3.8: *(a) Si cantilever with protruding AFM tip (AdvancedTEC™[205]). The insets show a bending test on a freestanding FEB deposited pillar. (b) Piezoresistive Si cantilever used for mass sensing.[208] (c) SiO_2 cantilever beams used for bending tests.[196]*

on the cantilever have been used for *in situ* mass sensing (Fig. 3.8 (b)). SiO_2 cantilever arrays with spring constants in the range of $0.01 \ldots 1$ N m^{-1} have been used for bending tests on FEB deposits (Fig. 3.8 (c)).

3.2.4 *In situ* AFM

AFM is routinely used for accurate shape determination of nanostructured features.[309] The accurate topography data is useful to extract precisely the volume of the FEB/FIB grown or etched material. This is of interest for the determination of process rates and yields at the initial phase of growth and for material density measurements when correlated to mass measurements. AFM performed inside a SEM allows for observing a sample using the electron beam and investigating the local topography by AFM. The advantages of the standalone techniques are combined: The SEMs field-of-view of up to several square millimeters provides greater operating convenience than the relatively small one of the AFM. This advantage, coupled with the SEMs high scan rate - providing images at TV rate (50 Hz) - and large depth of field, simplifies the survey process required to locate specific surface features for analysis by the AFM. *In situ* AFM measurements in contact mode of FEB deposits from the precursor $W(CO)_6$ to analyze the deposit shape and deposition rate were reported.[11]

In this work a sensor consisting of a self-sensing and -actuating cantilever probe based on a quartz tuning fork (Fig. 3.9 (a)),[2] was integrated into the vacuum chamber of the SEM

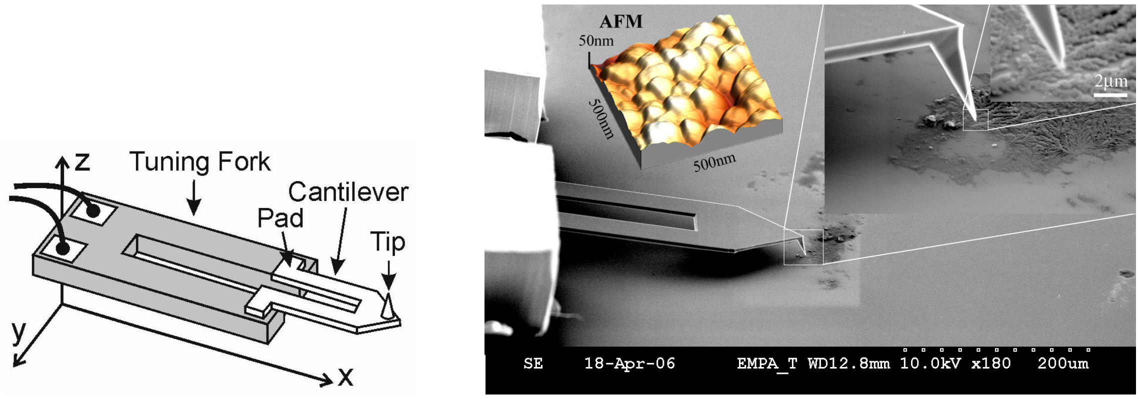

(a) (b)

Figure 3.9: *(a) Scheme of the self-sensing and -actuating sensor combining a Si cantilever mounted to a quartz tuning fork (Akiyama-Probe[206]) used for in situ frequency modulation AFM. (b) Illustration of the AFM operated in a SEM. The AFM image (inset) corresponds to the position of the cantilever tip shown in the SEM images.*

combined with the SPM setup described in Sect. 3.2.1. These sensors combine the advantages of the tuning fork's extremely stable frequency driving the tip vibration with the Si cantilever's softer force constant and thus, higher sensitivity. Frequency modulation AFM was performed to investigate *in situ* the topography of nanostructures produced by FEB induced deposition. The AFM was controlled using a control system for SPMs described below. Figure 3.9 (b) shows the benefit of the 3D image capabilities of measurements performed with our *in situ* AFM when compared to secondary electron images.

3.2.5 Control system

A scanning probe microscopy (SPM) control system from Nanonis[204] was used to perform frequency modulated AFM and to measure and control the response of mechanical resonators, e.g. for mass sensing applications and modal vibration analysis.

The oscillation control software consists of modules that are running on a real-time processor (time-critical operations) and on a National Instruments FPGA card as well as on the host computer running the graphical user interface. This system features oscillation control for dynamic mode measurements and control of mechanical resonators based on a digital phase-locked loop (PLL) and proportional-integral control loops. The hardware interface basically provides a fast D/A converter and a fast A/D converter to output an excitation signal and to input the oscillation signal of the resonator, respectively. In order to cope with the large dynamic range of these signals, the hardware also provides low noise signal conditioning, filters, preamplifiers and dividers. Additionally, analog input and output signals are provided which allow simultaneous data acquisition during oscillation measurements and control.

3.3 *Ex situ* characterization tools

3.3.1 Cold field emitter SEM

High-resolution SEM observation was done in a Hitachi S-4800 cold FEG-SEM. The microscope is equipped with a “through the lens” (in-lens) SE detector and a BSE detector. The software allows controlled signal mixing from pure SE to pure BSE images. Image artifacts due to charging effects can be reduced by filtering the low energy BSE content. The microscope is further equipped with a EDAX Sapphire Si(Li) detector for EDX spectroscopy.

3.3.2 Optical profilometry

Two-dimensional topography measurements were performed to determine thickness profiles of thermally decomposed precursor flux patterns by vertical scanning optical profilometry. These patterns had lateral dimensions in the order of $1 \ldots 2$ mm and thickness < 100 μm. An InfiniteFocus™ profilometer[4] with a working principle based on the determination of the varying focal plane by image processing and a Wyko™ NT1100 profilometer[301] with a working principle based on white light interferometric microscopy were used. The reliability of optical measurements and base-plane corrections were verified by contact mode stylus profiles.

Chapter 4

Cantilever-based mass sensor

In this chapter, the extension of the range of applications of cantilever-based mass sensors when integrating them in FEB and FIB nanostructuring systems is presented. We successfully explored *in situ* process monitoring by absolute mass changes from FIB sputtering, FEB/FIB deposition and precursor adsorption. In the first part of the Chapter (Sect. 4.2) the dynamic properties of cantilevers are outlined specifically for their use as mass sensing devices in vacuum conditions. It is shown that the sensitivity increases with increasing cantilever resonance frequency and decreasing cantilever mass. The detection limits are related to the frequency selectivity of the resonance peak. The relevant aspects of the setup integration and operation, such as the piezoresistive deflection read-out, the frequency tracking, the temperature stability and the cantilever calibration are outlined in Sect. 4.3. Carefully designed experiments allowed for mass measurements with a noise level of 1. . . 10 fg $\mathrm{Hz}^{-1/2}$ by tracking the resonance frequency of a temperature stabilized piezoresistive cantilever using phase locking. The achieved femtogram mass resolution allows to detect minimum deposit volumes of 2×10^{-4} $\mu\mathrm{m}^3$ assuming a density of 5 g cm^{-3}, which corresponds to a half-sphere volume with a radius $r = 36$ nm. The cantilever-based mass sensor enables to measure FEB/FIB induced processes in standard nanofabrication conditions, i.e. on a plane Si substrate. Measurements of precursor surface coverage, molecular residence time, mass deposition rates, yields, and deposit density are presented (Sect. 4.4). The methods and results presented herein have partly been reported in a textbook chapter.[90]

4.1 Introduction

In vacuum thin film deposition machines mass sensing based on QCMs has been standard measurement technology for many decades to monitor film thickness. These sensors are based on the fact that the resonance frequency of a vibrating structure, i.e. a quartz crystal, depends on external stimuli, such as mass loading. Other applications use QCMs to detect monolayers of molecules or arrays of biopolymers distributed over an active sensor area of typically $\sim$ 1 cm^2. This technology offers absolute mass resolution in the range of nano- to picograms. However, the resolution of QCMs is insufficient to measure typical mass changes of deposited or removed material by a FEB or FIB. Such features with dimensions at the micrometer-and ultimately at the nanometer-scale[299] have masses in the order of picograms (10^{-12} g) to zeptograms (10^{-21} g). This range of mass resolution is reached by reducing the mass of the vibrating sensor structure which is achieved in micro- and nanoelectromechanical systems (MEMs and NEMs).

The progress in microsystem fabrication originally triggered the development of micromechanical cantilever beams for use in AFMs. In parallel the sensing potential of cantilevers and similar MEMs and NEMs was exploited in various other applications.[279] These systems are generally operated in either the static deflection mode, where unbalanced surface stress results in a measurable deflection, or the dynamic, resonant mode, where mass changes on the vibrating structure alter the resonance frequency. Cantilevers functionalized with organic or inorganic adhesion coatings favor uptake of adsorbates inducing surface stress response by several orders of magnitude. Simultaneous measurement of the resonance frequency and cantilever static bending allows differentiating the response from mass loading and surface stress.[9,188] Comprehensive reviews which focus on both principles have been presented by Thundat,[285] Lavrik *et al.*,[163] Ziegler,[327] Carrascosa *et al.*,[38] and Waggoner *et al.*[303].

Using standard AFM cantilevers and equipment the group of Thundat started to observe mass changes induced by adsorption of molecules on the cantilever surfaces.[40,284,302] Further development has lead to sensor arrays for the discrimination of volatile organic compounds[115,161] and cells of Escherichia coli bacteria have been selectively detected with antibody surface coated cantilever beams[131]. Another wide application field of cantilever-based mass sensors is process control, e.g. weight change due to chemical or biological reactions occurring on the cantilever surface. Berger *et al.* demonstrated *in situ* measurements of surface stress changes and kinetics during the formation of self assembled monolayers[14] and thermally induced mass changes[15].

4.2 Fundamentals of resonant cantilever sensors

4.2.1 Cantilever rigidity

The cantilever rigidity expressed by the static force constant k_c crucially determines both, the static and dynamic operation of cantilever beams. In static operation, the force F applied to the cantilever causing a vertical deflection Δz at the loading point is calculated by Hooke's law, $F = k_c \Delta z$. The force constant for forces acting vertically on the cantilever end $x = l$ is given by

$$k_c = \frac{3EI}{l^3}, \tag{4.1}$$

in terms of the geometrical moment of inertia I. In the case of a uniform cantilever with rectangular cross-section (Fig. 4.1) the moment of inertia is $I = wh^3/12$. The cantilever deflection Δz can either be directly read out from the output of the deflection sensing system or from SEM images in *in situ* experiments. For non-uniform cantilever shapes, e.g. the piezoresistive cantilever in Fig. 4.5 (a), Eq. 4.1 doesn't hold. For absolute measurements the cantilever needs to be calibrated (Sect. 4.3.4).

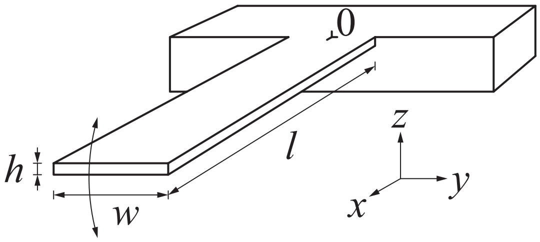

Figure 4.1: *Cantilever with length l, width w and thickness h. A rectangular cantilever generally fulfills: $l \gg w \gg h$.*

4.2.2 Modal analysis

The equation of motion for the flexural vibrations of a freely oscillating and undamped cantilever can be approximated by the Euler-Bernoulli equation for small vibration amplitudes[308]

$$EI\frac{\partial^4 z(x,t)}{\partial x^4} + \frac{m_c}{l}\frac{\partial^2 z(x,t)}{\partial t^2} = 0, \tag{4.2}$$

where z is the cantilever displacement at the position $x \in [0, l]$ along the cantilever at time t, E is the Young's modulus, and m_c/l is the cantilever mass per unit length l. In the case of a clamped-free cantilever beam, the boundary conditions imposed are zero displacement and slope at the clamped end, $Z(x=0) = Z'(x=0) = 0$, and vanishing external torque and shear forces at the free end, $Z''(x=l) = Z'''(x=l) = 0$. They lead to the stationary modal shapes given by

$$Z_n(x) = \frac{A_c}{2}\left((\cos\beta_n x - \cosh\beta_n x) - \frac{\cos\beta_n l + \cosh\beta_n l}{\sin\beta_n l + \sinh\beta_n l}(\sin\beta_n x - \sinh\beta_n x)\right), \tag{4.3}$$

where $Z_n(x)$ is the n^{th} eigenmode of Eq. 4.2 and $A_c = Z_n(l)$ is the vibration amplitude at the free cantilever end.

The boundary conditions further result in the characteristic equation

$$\cos\beta_n l \cosh\beta_n l = -1 \Rightarrow \begin{cases} \beta_1 l = 1.87510 \\ \beta_2 l = 4.69409 \\ \beta_3 l = 7.85476 \\ \vdots \\ \beta_n l \simeq (n - 1/2)\pi \quad \text{for n} > 3, \end{cases} \tag{4.4}$$

wherefrom the dimensionless eigenvalue $\beta_n l$ of the n^{th} flexural resonance mode can be numerically calculated.

The resonance frequencies for flexural vibrations in the cantilever are obtained from Eq. 4.2

using the stationary solutions of Eq. 4.3:

$$f_n = \frac{(\beta_n l)^2}{2\pi}\sqrt{\frac{EI}{l^3 m_c}} \tag{4.5}$$

$$= \frac{(\beta_n l)^2}{2\pi}\frac{h}{l^2}\sqrt{\frac{E}{12\rho}}, \tag{4.6}$$

where the second relation is only valid for rectangular cantilevers having $I = wh^3/12$.

The point-mass model

The complexities of the cantilever vibrations have given rise to models that simplify the dynamics considerably. In the point-mass model (also called the first mode approximation), the cantilever is approximated by a one-degree-of-freedom mass-spring model, such that the higher-order flexural modes are neglected. The distributed cantilever mass is replaced by an effective point mass m^* attached to a massless spring with stiffness k_c (Fig. 4.2). m^* is chosen such that the fundamental resonance frequency f_1 of the free cantilever equals the point-mass resonance frequency:[239]

$$f_0 = 1/2\pi\sqrt{k_c/m^*}, \tag{4.7}$$

where $m^* = n_e m_c$ with n_e being the normalized effective mass. For rectangular beams n_e is obtained from the comparison of Eqs. 4.6 and 4.7 by setting $n = 1$:

$$n_e = 3/(\beta_1 l)^4 = 0.2427. \tag{4.8}$$

It is noted that $n_e = 33/140 = 0.2357$ is sometimes used in literature. This approximation is derived by assuming a static cantilever deflection curvature and results in a systematic error of 3%.

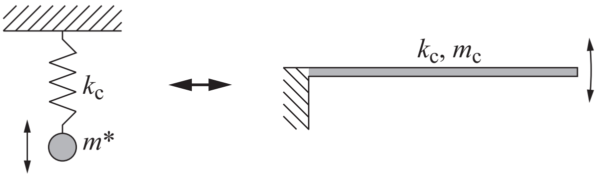

Figure 4.2: *The point-mass attached to a spring (left) models the clamped-free cantilever with distributed mass. (Here without damping.)*

Dissipation - Quality factor

As we will see later, dissipation has a crucial influence on the ability to resolve small shifts in resonance frequency. Operating the cantilever sensors inside the vacuum chamber of a SEM/SIM implicates low damping and thus, low dissipation working conditions which is favorable for high resolution mass sensing.

In the model of the harmonic oscillator, dissipation can be included in the system by introducing the dimensionless quality factor Q of the resonator which is a description of the total damping. The quality factor of a resonator is inversely proportional to the damping coefficient and is defined as[182]

$$Q = 2\pi \frac{W_0}{\Delta W} \tag{4.9}$$

where W_0 is the stored vibrational energy and ΔW is the total energy lost per oscillation cycle. The dissipation channels that contribute to ΔW can be divided into internal damping due to the physical structure of the micromechanical resonator, dissipation via coupling to the support structure (clamping loss) and internal friction,[78,317] and external damping caused by molecular, viscous and turbulent flow of the surrounding media or acoustic radiation. In high vacuum conditions, $P < 10^{-1}$ Pa, external damping is negligible.

While the modal shape solutions $Z_n(x)$ (Eq. 4.3) are independent on damping the dispersion relation giving the damped eigenfrequencies f_0' in terms of the undamped frequencies f_0 is[257]

$$f_0' = f_0 \sqrt{1 - \frac{1}{4Q^2}}. \tag{4.10}$$

The cantilever sensors used in this work typically had quality factors greater than 10'000 in high vacuum conditions, thus, damping induced shifts are predicted to be negligible.

The steady-state solution of the equation of motion for the driven damped harmonic oscillator leads to the following expressions for amplitude A_c and phase ϕ of the oscillations as function of the drive amplitude A_d and the excitation frequency ω_d:

$$A_c = \frac{A_d \omega_0^2}{\sqrt{\left(\omega_0 \omega_d / Q\right)^2 + \left(\omega_0^2 - \omega_d^2\right)^2}} \tag{4.11}$$

$$\phi = \arctan\left(\frac{\omega_0 \omega_d}{Q\left(\omega_0^2 - \omega_d^2\right)}\right). \tag{4.12}$$

It is clear from Eqs. 4.11 and 4.12 that if $Q \gg 1$, the amplitude maximum is reached at the frequency where the oscillation has a 90° phase-lag relative to the excitation. The frequency is, however, shifted according to Eq. 4.10 at high damping conditions (in air and water).

In practice the quality factor is either determined from the full width at half maximum (FWHM) of the squared amplitude peak or from the phase variation $d\phi/df$ at resonance according to

$$Q \simeq \frac{f_0}{\mathrm{FWHM}} = \frac{f_0}{2} \left|\frac{d\phi}{df}\right|_{f_0}. \tag{4.13}$$

It is important to note that in low damping conditions the drive amplitude A_d is a direct measure of relative changes in quality factor, since from Eq. 4.11, $A_d/A_c = Q^{-1}$ at $\omega_d = \omega_0$.

4.2.3 Mass loading

In general, resonant mass sensing is performed by observing a shift in resonance frequency Δf due to the added mass Δm. We will consider two extreme cases (Fig. 4.3), homogenous surface coverage loading: $f_0 \pm \Delta f = (2\pi)^{-1}\sqrt{k_c/(n_e(m_c \mp \Delta m))}$, and point mass loading: $f_0 \pm \Delta f = (2\pi)^{-1}\sqrt{k_c/(n_e m_c \mp \Delta m)}$.

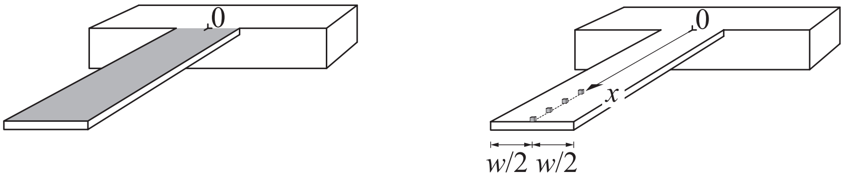

(a) (b)

Figure 4.3: *(a) Homogenous surface loading. (b) Point mass loading at position x.*

Homogenous mass loading

Assuming that the added mass Δm is a small fraction of the cantilever mass m_c the frequency response of the fundamental mode upon homogeneous surface loading R_h is approximately linear and can be written as

$$R_h = \frac{\Delta f}{\Delta m} = -2\pi^2 n_e \frac{f_0^3}{k_c} = -\frac{1}{2}\frac{f_0}{m_c}. \tag{4.14}$$

This expression assumes that the cantilever stiffness EI, surface stress, and damping are not significantly affected by the added mass. This still holds if the added species form a film, which has insignificant intra cross-linking and is not rigidly bonded to the cantilever surface. In practice, for physisorption (van der Waals interaction) of molecules on the sensor surface these assumptions are valid. It is noted that Eq. 4.14 is analogous to the Sauerbrey equation[263] but here written in terms of the absolute mass rather than the mass density of the added species. Hence, it is noted that the frequency response given by Eq. 4.14 upon homogenously loaded mass is dependent on the active sensor area.

Point mass loading

Particle beam induced processes modify the cantilever surface at the micro-/nanometer length scale with the positioning accuracy inherent to the SEM/SIM. The imaging capabilities do further allow to determine the location of added or removed mass on the cantilever, e.g. from loaded nanoparticles or wires.

We consider here the response of the cantilever sensor upon loading of mass at a specific location on the cantilever in a small area wherein the mass responsivity can be considered as constant. Upon loading of such a point mass at the free cantilever end the responsivity of the fundamental mode becomes

$$R_p = \frac{\Delta f}{\Delta m} = -2\pi^2 \frac{f_0^3}{k_c} = -\frac{1}{2n_e}\frac{f_0}{m_c}. \tag{4.15}$$

Using the approach of equality of the kinetic energy of the system with distributed mass $m\,(x)$ and with effective mass m^*, a position depending formulation of mass responsivity along the x axis of a rectangular cantilever can be derived. An integral formulation for the effective mass in terms of the transverse mode shape $Z_1\,(x)$ is given by[192]

$$m^* = \frac{1}{l}\int_0^l m_c\,(x)\left(\frac{Z_1(x)}{A_c}\right)^2 dx. \tag{4.16}$$

As can be seen from this relation the mass $m_c(x)$ along the cantilever contributes to the effective mass m^* weighted by a factor $(Z_1(x)/A_c)^2$. Accordingly, a small mass Δm added at the position x is also weighted by the same factor and thus,[270]

$$R_p(x) = R_p \cdot \left(\frac{Z_1(x)}{A_c}\right)^2 \tag{4.17}$$

A useful approximative relation $R_p(x) = R_p \cdot (x/l)^3$ was proposed by Sader[257], which replaces the trigonometric and hyperbolic functions in the modal shape expression $Z_1(x)$ (Eq. 4.3). The third-order position dependency deviates less than 2% from Eq. 4.17 for $x > 2/3l$. Equations 4.15 and 4.17 were both obtained by assuming that the load position lies in the axis of symmetry of the cantilever. For cantilevers with large length to width ratio, the application of an off-axis load only produces a small deviation from the on-axis value (<2%).[257] The position dependent responsivity of the fundamental mode given in Eq. 4.17 was experimentally verified as shown later in Fig. 4.9. Comparison with finite element simulations and experimental values[65] show that Eq. 4.17 can be extended to higher-order modes, $n > 1$, by replacing $Z_1(x)$ by $Z_n(x)$ given in Eq. 4.3. Mass sensing at higher-order modes increases the mass responsivity due to increased resonance frequency as seen from Eq. 4.6: $f_n/f_1 = (\beta_n l/\beta_1 l)^2$. This corresponds to a gain in responsivity of a factor of 6.3 and 17.5 for the second and third mode, respectively. It is noted that the positioning sensitivity in point mass loading is stronger for higher-order modes. An analytic distributed mass model was formulated,[73,239] wherefrom the dynamic response to various tip-sample contact mechanisms and mass loading at variable positions along the beam can be derived including all higher modes. Within this work we focused on mass sensing at the fundamental resonance mode.

4.2.4 Detection limits

Noise

In any actual implementation noise and drift sources are imposed by the measuring system as well as by the environment, such as the temperature instability. From an engineering point of view these noise and drift contributions can be minimized in a carefully designed measurement setup. The fundamental limits of resonating cantilever sensors are determined by the ratio of their responsivity to the level of intrinsic noise. Accordingly, the minimum resolvable frequency shift $\delta f_{\min}$ determines the minimum resolvable mass change as $\delta m_{\min} = \delta f_{\min} R^{-1}$. The ultimate fundamental limits are set by the thermomechanical noise. The minimal detectable relative frequency shift is then given by[3]

$$\frac{\delta f}{f_0} = \frac{1}{A_c}\sqrt{\frac{2k_BTB}{f_0 k_c Q}}, \tag{4.18}$$

where k_BT is the thermal energy and B the measurement bandwidth. From Eq. 4.18 it is seen that the thermomechanical frequency noise is depending on the dissipation $1/Q$. Combining Eqs. 4.15 and 4.18 and using Eq. 4.7 the minimum resolvable point mass change at the free end of the cantilever becomes

$$\delta m = -\frac{1}{\pi A_c}\sqrt{\frac{2k_BTBn_em_c}{f_0^3Q}}. \tag{4.19}$$

An implication of Eq. 4.19 is that the point mass noise can be minimized when driving the cantilever sensor at the maximum acceptable deflection amplitude A_c. The measurement bandwidth is determined by trading-off the minimum noise level and the maximum available measurement response.

Sensor improvements

Sensor scaling Pushing down the detection limit by design considerations of rectangular cantilever sensors is discussed in terms of size and material. In Table 4.1 the dependence on dimensions and material properties of the force constant, resonance frequency, responsivity, and the minimum detectable mass at the thermomechanical noise limit are compiled.

Table 4.1: *Scaling laws of rectangular cantilever mass sensors for point mass loading. For homogenous loading, the responsivity R must be divided by the active area.*

Spring constant (Eq. 4.1)	$k_c \propto l^{-3}wh^3 \cdot E$
Resonance frequency (Eq. 4.6)	$f_0 \propto l^{-2}h \cdot \sqrt{E\rho^{-1}}$
Responsivity (Eqs. 4.14 and 4.15)	$R \propto l^{-3}w^{-1} \cdot \sqrt{E\rho^{-3}}$
Minimum detectable mass at the thermomechanical noise limit (Eq. 4.19)	$\delta m \propto \sqrt{l^7wh^{-2}} \cdot \sqrt{E^{-3/2}\rho^{5/2}}$

If the size of a cantilever is reduced proportionally in all dimensions by the scaling factor a ($a < 1$), according to Table 4.1 the responsivity increases by a factor a^{-4} and the minimum detectable mass at the thermomechanical noise limit decreases by a factor of a^{-3}. Furthermore, in the case of a reduction of the cantilever length to bl ($b < 1$) and an increase of its thickness to ch ($c > 1$), the responsivity increases by a factor b^{-3} and the minimum detectable mass at the thermomechanical noise limit decreases by a factor $b^{7/2}c^{-1}$. These examples illustrate that besides overall size reduction the l/h ratio should be minimized to obtain the best sensing capabilities.[49] At the same time, a proportional size reduction and a reduction of the l/h ratio increase the resonance frequency by a factor a^{-1} and $b^{-2}c$, respectively.

For homogenous mass loading the conclusion on size reduction and l/h ratio minimization is similar to the case of point mass loading.

Besides cantilever size reduction the material choice influences the sensing capabilities. A comparison of conventional materials used in microfabrication reveals that mono- and polycrystalline Si have an outstanding high stiffness to density ratio making them ideal materials for high resolution cantilever mass sensors.

Development of advanced surface machining techniques and the integration of nanowires and -tubes into NEMs allow for the realization of resonators with minuscule masses in conjunction with excellent mechanical properties. This translates into opportunities for unprecedented mass resolution at the zeptogram-scale as demonstrated in recent experiments.[316]

Sensor quality Central to attaining high resolution resonant mass sensing is the achievement of devices with high quality factors Q. From an applications point of view, dissipation ($\sim 1/Q$) within a vibrating mechanical structure sets the level of fluctuations that degrade its spectral purity.

In ambient conditions viscous damping is dominating the loss mechanisms in most cases responsible for reduction of quality factors by a few orders of magnitude. Operation in vacuum conditions at $< 10^{-1}$ Pa eliminates viscous damping and reveals other mechanisms such as surface and clamping (support) loss.[45] There is overwhelming experimental evidence that upon shrinking the volume of the sensors the surface damping become particularly important related to the increase in surface to volume ratio.[78] Energy dissipation in MEMS/NEMS operated in vacuum conditions is an interesting problem of fundamental importance on its own which is currently extensively discussed in the literature.[78]

Other issues, such as additional intrinsic noise sources, the integration of a sensitive read-out system and the device fabrication must be taken into account for the optimization of high resolution mass sensing devices.[49,50,79]

4.3 Integration and operation of the mass sensor

We integrated a Si cantilever with piezoresistive deflection read-out for mass sensing inside SEMs/SIMs equipped with a GIS. The arrangement of the cantilever mass sensor and the GIS which locally supplies the volatile precursor into the vacuum chamber of the SEM/SIM is shown in Fig. 4.4. Note that for illustrative convenience the microtube GIS is scaled down, in this figure. All processing is restricted to a small area of constant responsivity at the extremity of the cantilever where the sensor responsivity is maximal.

4.3.1 Piezoresistive deflection read-out

The most common cantilever deflection read-out system is the well known optical lever.[193] This technique uses a collimated light beam emitted from a laser diode which is reflected-off from the cantilever and projected onto a segmented photodiode which detects sensitively changes in the cantilever slope and thus in its deflection. A typical sensing head incorporating such a system has dimensions of several centimeters in width and length. This is clearly a disadvantage when a cantilever sensor is integrated in a SEM or SIM, because in many of these instruments severe size constraints are imposed by the available space between objective and microscope sample stage. For these reasons, for its ease of operation with no alignment required (as for all optical detection systems), and no disturbance of the FEB/FIB due to large electric fields applied (as for capacitive detection systems) piezoresistive deflection read-out was considered to be most favorable for integration into the vacuum chamber of the SEM/SIM.

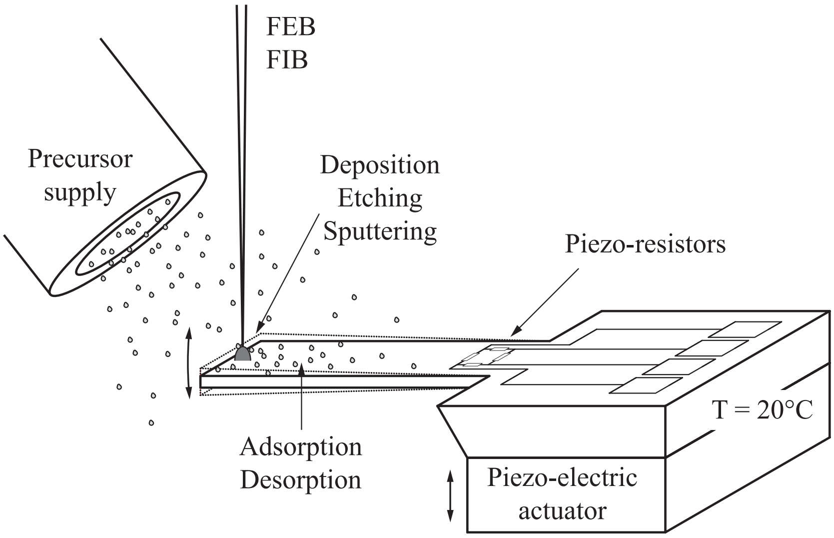

Figure 4.4: *Schematics of a cantilever mass sensor with piezoresistive read-out which allows the measurement of precursor adsorption/desorption, FEB/FIB deposition and etching, and FIB milling. The precursor supply tube is not at scale.*

Built-in piezoresistive elements measure the variation in film resistance with respect to cantilever deflection as a consequence of a surface-stress change. Piezoresistivity is a material property where the bulk resistivity of a material is influenced by the mechanical stress applied to the material.[143] For piezoresistivity to be observable, the electrical conductivity along the thickness of the cantilever has to be asymmetric, which is often accomplished by a differential doping of the material to form embedded piezoresistors.[180]

Cantilever sensors with piezoresistive deflection read-out have mainly been implemented in two ways, by integrating a thin piezoresistive layer on one side of a cantilever which is typically U-shaped or by placing piezoresistors in the zone of maximum surface stress close to the clamped end of the cantilever. The first approach was proposed and implemented for AFM with atomic resolution by Tortonese *et al.*.[286] For accomplishment of the resistivity measurement in the detection system, four resistors, wherefrom one or two are sensing deflection and the others are passive, are connected to form a Wheatstone bridge. The alternative design employs a single cantilever containing four piezoresistors connected in a Wheatstone bridge arrangement (Fig. 4.5).[168] To improve the sensitivity of this design, the cantilever was perforated at the center of the Wheatstone bridge which increases the mechanical strain in the material next to the hole where the resistors are located.[169] The sensitivity and noise of piezoresistive cantilever sensors can be tailored by optimizing the dimensions of the integrated piezoresistors.[116] However, for a cantilever with piezoresistive detection the minimum detectable frequency shift is in most cases limited by the Johnson noise at high frequency and the $1/f$ noise at low frequencies of the piezoresistors.[323]

A SEM image of a typical cantilever with built-in piezoresistors used for *in situ* mass sensing in this work is depicted in Fig. 4.5 (a). The built-in Wheatstone bridge, schemati-

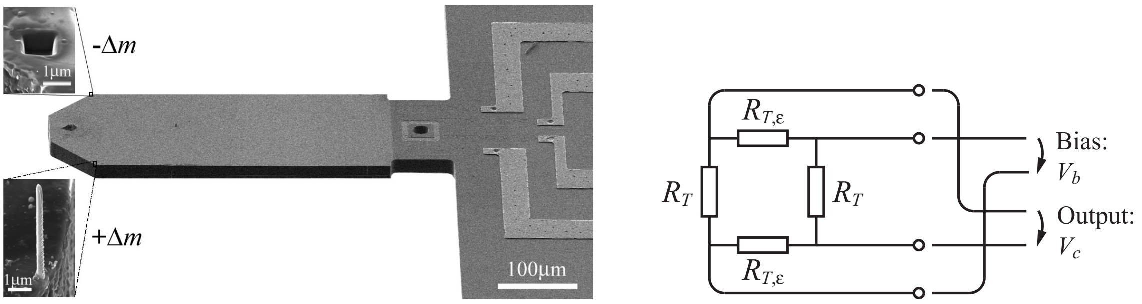

(a) (b)

Figure 4.5: *(a) SEM image of a piezoresistive Si cantilever with built-in Wheatstone bridge*[208] *used as in situ resonating mass sensor. The insets show FIB milling and FEB deposition on the cantilever surface. (b) Scheme of the symmetric built-in Wheatstone half-bridge. The two opposite resistors aligned along the cantilever are strain active (index ϵ). The cantilever deflection is sensed by the bridge output voltage V_c which is amplified by the bridge bias V_b.*

cally depicted in Fig. 4.5 (b), consists of four nominally equivalent piezoresistors with $R = 1.2 \ldots 1.8$ kΩ. For a 10 μm thick cantilever a typical bridge output $V_c/A_c \simeq 50$ μV nm^{-1} at a bias voltage $V_b = 1$ V was measured by SEM imaging. However, this value strongly varies between different cantilevers and needs to be measured for each device if a precise calibration is required. The symmetric Wheatstone half-bridge responses to the resistance change γR_ϵ according to $V_c/V_b = -0.5\gamma(1+\gamma/2)^{-1}$. The bridge output is thus amplified by $-V_b/2$ and produces a relative non-linearity of $\gamma/2$. For $A_c = 500$ nm the active resistors of the above calibrated cantilever change by $\gamma \sim 0.05$ which results in a 2.5% non-linearity error. With decreasing deflection amplitude this error is further reduced.

The symmetric Wheatstone half-bridge arrangement with all resistors being at the same temperature compensates for the influence of thermal drifts on the detection system. However, in practice small differences in the resistance values unbalance the bridge and may introduce slight temperature dependencies in the output signal. The power dissipated in piezoresistive devices tends to heat up the cantilever and the setup at a rate depending on the input power and the thermal resistance of the device.[116] As a consequence, the resonance frequency is subject to thermally induced drifts as discussed in Sect. 4.3.3.

4.3.2 Frequency measurements

One of the simplest methods to continuously sense resonance frequency shifts, which was originally employed for AFM, involves the excitation of the cantilever at a fixed frequency close to its resonance. A resonance frequency shift is measured by the corresponding amplitude change in the off resonance slope of the resonance peak. Upon a sudden change in resonance frequency the oscillation amplitude settles with a time constant of $\tau = Q(\pi f)^{-1}$ to the new steady-state value. Operation in vacuum conditions with high Q produces transients which can last up to seconds and thus limit the available bandwidth $B = (2\pi\tau)^{-1}$ and the dynamic linear sensing range.[100]

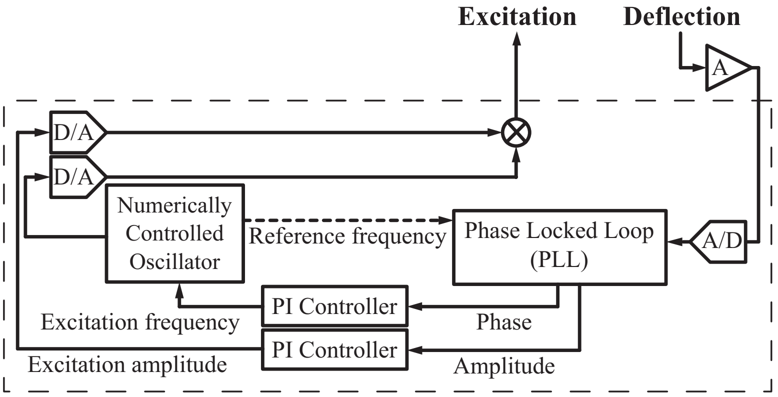

Figure 4.6: *Scheme of oscillation control used for cantilever-based mass sensing. The resonance frequency is tracked in a closed loop implementation with feedback from the amplitude and phase signals measured by the PLL. The phase loop ensures a proper phase relation between the excitation signal and the measured deflection response such that the oscillation frequency is exactly at the peak of the resonance curve (phase-controlled oscillator). The amplitude loop adjusts the excitation amplitude keeping the deflection amplitude at its setpoint.*

To overcome this severe limitation in measurement speed, we employed a closed loop implementation where the cantilever acts as resonator in an active feedback circuit (Fig. 4.6) which makes Q and B independent of each other and further enables the separation of the response from conservative stimuli (e.g. mass loading) and dissipative interactions (e.g. damping).[3,74] The cantilever was continuously driven at its momentary resonance frequency accomplished by generating the excitation signal through a feedback loop which adjusts the phase shift between driving and cantilever vibration signal to 90°. A second feedback loop controlled the amplitude of the driving signal A_d to maintain the deflection amplitude A_c constant. Both, the phase shift and amplitude were detected by the PLL. The desired demodulation bandwidth was set by adjusting the parameters of the PI feedback loops for the oscillation amplitude and phase. The calculated parameters were optimal in terms of feedback stability.[107]

Drifts in the reference clock signal incorporated in the control circuit directly enter in the measured frequency value. An "oven controlled crystal oscillator" with a specified long-term frequency stability of $50 \times 10^{-9} f$ was used in our setup which limited this drift source to ± 2.5 mHz at 50 kHz. This value is in the order of the achieved noise values in our measurements. However, such long-term drifts are not influencing relative frequency measurements during typical experiments of a few minutes.

To amplify the small signals at the output of the built-in piezoresistive Wheatstone bridge, we used homebuilt preamplifiers mounted directly to the SEM vacuum chamber to avoid noise pickup on long cables. Using differential vacuum feedthroughs eliminated ground loops.

It is seen from Eq. 4.18 that it is essential to limit the bandwidth of the measurement system to minimize the noise level from thermomechanical noise and from other contributions, such as the noise of the piezoresistors and preamplifier. The measured rms-noise in the close loop frequency signal of a piezoresistive cantilever at resonance for different demod-

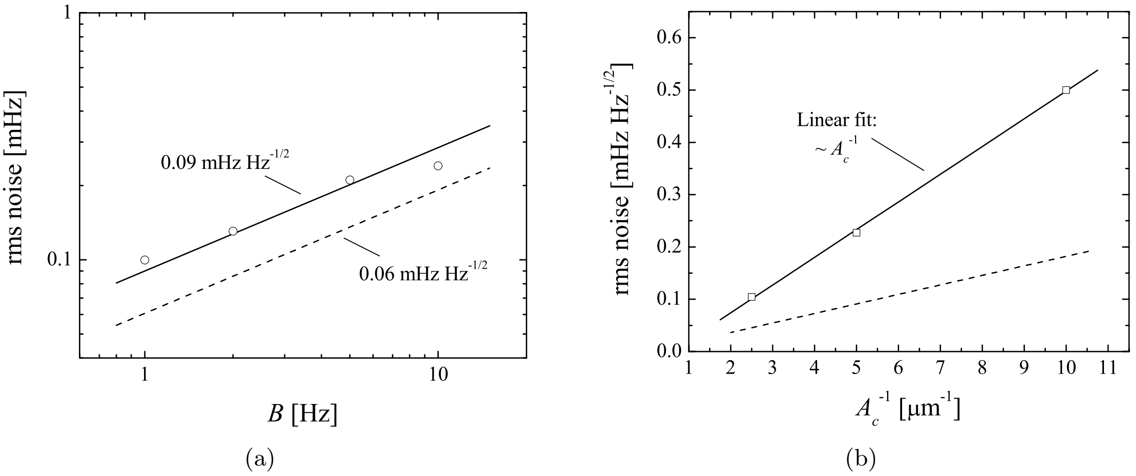

Figure 4.7: *Noise performance of a piezoresistive cantilever with fundamental resonance mode at* $f_0 = 32.5$ *kHz, a force constant* $k_c = 13.5$ *N* m^{-1} *and quality factor* $Q \sim 60'000$ *at* 10^{-3} *Pa measured in the mass sensing setup. The dashed line indicates the thermomechanical frequency noise limit. (a) Noise vs. demodulation bandwidth for* $A_c = 0.3$ μm *and* $V_b = 1$ *V. (b) Noise vs. cantilever vibration amplitude for* $V_b = 1$ *V.*

ulation bandwidths and cantilever vibration amplitudes is shown in Fig. 4.7. The noise is related to the bandwidth as $\propto B^{-1/2}$ and as $\propto A_c^{-1}$ which is in accordance with the thermomechanical noise predicted by Eq. 4.18. There is a noise contribution from piezoresistors and from the preamplifier which is manifested by the offset of the noise relative to the calculated thermomechanical noise limit. The noise in these measurements was in the order of 3 ppb Hz$^{-1/2}$. A trade-off between measurement speed and noise reduction appropriate for the actual experiment determined the bandwidth.

4.3.3 Temperature stability

Operation of the cantilever mass sensor inside the vacuum chamber of a SEM/SIM strongly suffered from long-term drifts due to thermal stabilization of the setup over a time scale of hours. This is mainly due to the fact that in vacuum conditions heat evacuation is dominated by thermal conductance through the microscope stage and electrical connections wired to the setup, while stabilization by thermal convection is negligibly small compared to ambient conditions. Power dissipation in electrical components, e.g. piezoresistive sensors as discussed in Sect. 4.3.1, and temperature changes of the sample stage are significant sources of temperature instabilities.

A change in temperature influences the resonance frequency of a cantilever made from a single material in two ways. The geometrical dimensions and the mechanical properties are changed according to the materials thermal expansion and the temperature dependence of Young's modulus, respectively. The resonance frequency, Eq. 4.6, of the cantilever beam is accordingly modeled by[15]

$$f_0 = \frac{(\beta_n l)^2}{2\pi}\sqrt{\frac{E(T)w(T)h(T)^3}{12l(T)^3 m}}. \tag{4.20}$$

At the temperature T' (the prime is used for values at T') the relative change of resonance frequency with temperature results in

$$\frac{1}{f_0'}\frac{\partial f_0}{\partial T} = \frac{1}{2}\left(3\frac{1}{h'}\frac{\partial h}{\partial T} - 3\frac{1}{l'}\frac{\partial l}{\partial T} + \frac{1}{w'}\frac{\partial w}{\partial T} + \frac{1}{E'}\frac{\partial E}{\partial T}\right) = \frac{1}{2}(\alpha_{\text{th}} + \beta_{\text{th}}), \tag{4.21}$$

where α_{th} is the thermal expansion coefficient, assumed to be isotropic along l, w, and h, and β_{th} is the temperature coefficient of Young's modulus. For Si at room temperature these coefficients are approximately $\alpha_{\text{Si}} = 2.6 \times 10^{-6}$ K^{-1} and $\beta_{\text{Si}} = -90 \times 10^{-6}$ K^{-1}[180], thus, the temperature dependence of the resonance frequency of a Si cantilever is dominated by the variation of Young's modulus. The expected relative frequency temperature dependence is -43.7 ppm K^{-1}. Since the mass loading responsivity $R \propto f_0$ (see Eqs. 4.14 and 4.15), the relative temperature dependence of f_0 and R are equivalent. As a consequence, the mass sensor setup operated in vacuum must be kept at a constant temperature.

The mass sensor device used in this work was mounted on a Peltier-element heat sink (Fig. 3.7 (b)) which stabilized the temperature of the cantilever at a constant value close to room temperature. The temperature of the heat sink consisting of a copper piece measured by a resistive thermal sensor was incorporated in a feedback loop. A proper thermal connection between the heat sink and the cantilever chip was assured by wiring the mass of the built-in Wheatstone bridge circuit to the heat sink. The heat due to dissipation of the applied bias power in the bridge is compensated for and long-term temperature fluctuations by conductive heat transfer through the microscope stage and the electrical connections are avoided.

For a Si cantilever with approximately rectangular shape as the one shown in Fig. 4.5 (a), we measured a relative temperature dependent frequency of -23 ppm K^{-1} of the fundamental resonance mode which translates to a frequency shift of -1 Hz K^{-1} for the resonance frequency of f_0 = 43.4 kHz (Fig. 4.8). This value is clearly smaller than the expected value derived above from the material properties. The deviation might be mainly attributed to the oxide layer of several hundred nanometer thickness which protects the piezoresistive strain sensors at the bases extending to one sixth of the cantilever length. Since this layer is covering the clamping region it has a large impact, since the mechanical properties in the transition from the cantilever to the chip determine disproportionately the cantilever dynamic properties owing to the maximum cantilever curvature in this region. The presence of this double-layer structure indicates that stress-stiffening effects as well as the positive temperature coefficient of the Young's modulus of thermally grown SiO_2 compensate partly for the temperature dependence of the Young's modulus of Si.[259]

Alternative techniques to account for thermal instability have been proposed in the literature. It was shown that by recording difference signals from two cantilever sensors one of which acts as a reference sensor can effectively remove environmental disturbances including temperature induced drifts[161]. A second approach is to adjust the sensor design, e.g. it was demonstrated that composite Si/SiO_2 cantilevers strongly reduce the temperature-dependent frequency response depending on the SiO_2 film to Si thickness ratio.[191]

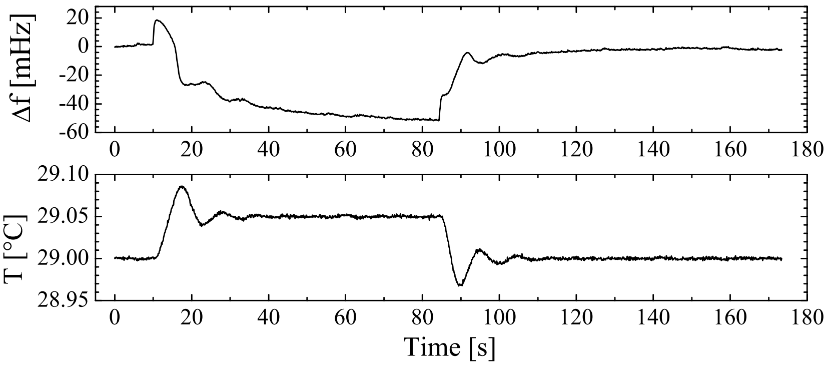

Figure 4.8: *Temperature cycle with sudden temperature setpoint steps of* $\Delta T = 50$ *mK and the corresponding cantilever frequency response for the fundamental mode at* $f_0 = 43.4$ *kHz. The frequency stabilized within* ~ 1 *minute upon an applied step. The temperature of the aluminium heat sink was measured with a platinum resistor temperature sensor with 100 Ω nominal resistance and was closed loop controlled by adjusting the current through a Peltier-element in contact with the heat sink. The feedback control parameters in this measurement produced oscillations in the transients of the heat sink and the frequency upon the temperature setpoint jumps.*

4.3.4 Cantilever calibration

Any quantitative force and mass measurement using cantilever-based sensors relies on the precise knowledge of the cantilever force constant (Eq. 4.1). Evaluation of cantilever force constants can be performed using a number of complementary approaches. For a critical discussion of force constant calibration methods in terms of their simplicity, reliability and precision, the reader is referred to a number of review articles.[32,52,105,256]

Experiments show that theoretically calculated force constants often differ significantly from values which are determined based on a supporting experimental approach.[34,257] Practical shortcomings such as the strong dependence of the force constant on a precise measurement of the cantilever thickness, $k_c \propto h^3$, and variable stoichiometry found in microfabricated cantilever materials[256,304] restrict the applicability of these theoretical calculations.

A convenient way of calibrating rectangular cantilevers relying on material properties but avoiding a measurement of the cantilever thickness enables a rough estimation. The approach is based on the determination of its fundamental mode resonance frequency. This method is straightforward in the *in situ* cantilever mass sensor setup where the plane view dimensions, width w and length l, can be determined by SEM imaging. Combining Eq. 4.1 and Eq. 4.6 leads to

$$k_c = \frac{2578}{(\beta_n l)^6} w (l f_n)^3 \sqrt{\frac{\rho^3}{E}}, \tag{4.22}$$

From an error analysis, the inaccuracy of the method is estimated to 25% due to measurement inaccuracy of the cantilever dimensions, $\Delta w/w = 5\%$ and $\Delta l/l = 5\%$, and the variations of Young's modulus of Si, $\Delta E/E = 10\%$.

The "dynamic add-mass" approach proposed by Cleveland *et al.*[51] is more general and

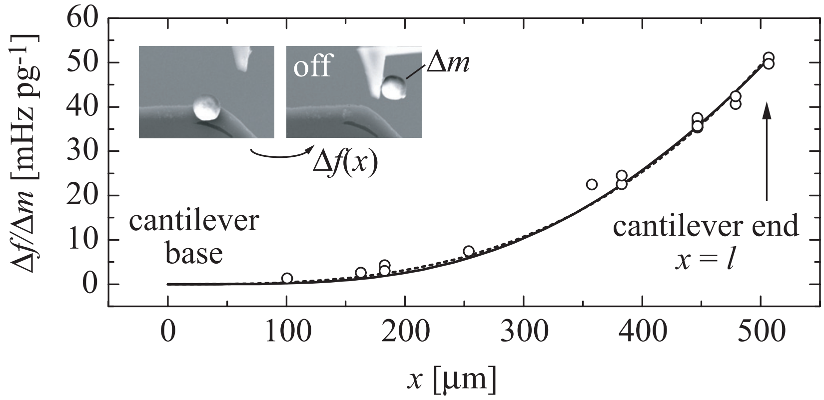

Figure 4.9: *Experimental measurement of the point mass loading response of a nearly rectangular Si cantilever (Fig. 4.5 (a)) with a fundamental mode resonance at 92 kHz. The responsivity,* $R_p(x) = \Delta f(x)/\Delta m$*, was measured by adding and removing micrometer sized copper spheres with mass* $\Delta m = V\rho_{Cu}$ *at the position* x *along the cantilever (see inset). The experimental data (circles) is fitted using Eq. 4.17 (solid) and a third-order approximation*[257] *(dashed). The maximum responsivity at the cantilever end (*$l = 507$ *µm) is 50 mHz* pg^{-1}*.*

reliable than Eq. 4.22 since it is independent on the cantilever shape and material. The shift Δf in resonance frequency due to the loading of a known mass Δm reveals the force constant using

$$k_c = \frac{(2\pi)^2\Delta m}{1/(f_0-\Delta f)^2 - 1/f_0^2} \simeq -2\pi^2 f_0^3 \frac{\Delta m}{\Delta f}, \tag{4.23}$$

where the second relation is linearized (Eq. 4.15) and holds for $\Delta m \ll m_c$. The add-mass is typically a spherical metal particle adhered to the end of the cantilever. The particle mass is calculated by measuring its radius and using the bulk density of the material. To adhere the particle from our experience no glue is necessary, the adhesion is sufficient and the method is non-destructive. In the literature the precision of this method is claimed to be <10-20%.[105,256] As outlined in Sect. 4.2.3 and presented experimentally in Fig. 4.9 the accuracy of this calibration is very sensitive to the loading position of the particles. Spring constant values from off-end loaded particles can however be corrected using $k_c = k_c'(x) \cdot (Z_1(x)/A_c)^2 \simeq k_c'(x) \cdot (x/l)^3$, where $k_c'(x)$ is the force constant found from Eq. 4.23 with the mass Δm loaded at the position x along the beam. Performing such experiments inside the SEM using a nanomanipulator allows for a very precise control of the load position and determination of the particle size. Comparing with experiments conventionally performed under an optical microscope the measurement precision achieved in the SEM relaxes the influence of these two main error sources and a precision of <5% can be achieved. The mass response calibration data presented in Fig. 4.9 evaluates to a force constant of 307 ± 15 N m^{-1} for the mass attached at the cantilever free end using Eq. 4.23. For the same cantilever a force constant of 352 ± 88 N m^{-1} was evaluated using Eq. 4.22. The manipulation procedures to add and remove particles from the cantilever is very time-consuming and requires elaborated *in situ* positioning equipment.

An *in situ* calibration technique of the mass sensor's force constant was established in this work based on Cleveland's method, which relies on the capabilities of removing material by FIB sputtering instead of the cumbersome particle manipulation.[89] The resonance frequency shift of the cantilever sensor is recorded during milling of a defined structure by a focused Ga^+ ion beam at the free end of the cantilever. Ga implantation adds mass during sputtering which can be accounted for by an estimation assuming a value of 6×10^{16} cm^{-2} (at 30 kV acceleration voltage) residual Ga at the bottom of the sputtered structure.[224] If the volume of the sputtered material is sufficiently large the implanted mass is negligible, e.g. a pit of $1 \times 1 \times 1$ μm^3 consists of 2.3 pg Si while the added mass due to implantation is estimated to $m_{\mathrm{Ga}} = 70$ fg, which is 3% of the Si mass. Eventually, redeposition of back-sputtered Si atoms occurs at the sidewalls of pits having aspect ratio > 1. While redeposition lowers the sputter rate the calibration is insensitive since the volume of the removed material is subsequently determined by SEM. The uncertainty of this *in situ* calibration is dominated by the visual determination of depth which allows for a precision $< 5\%$.

4.4 *In situ* mass sensing experiments

The cantilever-based sensor was used to determine the absolute processing rate of FIB milling and FEB/FIB induced deposition from the precursors: $(CH_3)_3PtCpCH_3$ (heated to 45 ℃) and $Cu(hfac)_2$. The evolution of the deposition rate was measured during the growth of pillars in the stationary spot mode and thin films by scanning the beam in a rectangular area. Experiments were conducted in a dual beam Nova 600 NanoLab instrument from FEI Company equipped with a liquid Ga ion and a Schottky field electron emitter as well as in the Hitachi S-3600N SEM.

During the typical experimental procedure a frequency spectrum of the amplitude and phase response at resonance was recorded to determine the location of the amplitude peak and the quality factor (Fig. 4.10). Subsequently, the oscillation tracking circuit was initialized by starting the phase and amplitude feedback loops running at the desired demodulation bandwidth. In this controlled state, the reference phase was swept and the resonance frequency set to the value which ensured that the excitation amplitude is minimal. This assured that the cantilever is excited precisely at resonance. The cantilever amplitude was set by adjusting the vibration amplitude setpoint. All experiments were done at the fundamental mode resonance frequency of the cantilever sensor. Running the PLL at demodulation bandwidths of $1 \ldots 5$ Hz allowed to follow mass changes in FEB/FIB induced processes at a controller response time of $(2\pi B)^{-1} \simeq 30 \ldots 200$ ms, which was acceptable in all cases. The deflection amplitude was set to the maximal tolerable value, between 100 nm and 500 nm, in the experimental conditions which gives best noise performances revealed by Eq. 4.18. Quality factors of the piezoresistive cantilevers at 10^{-3} Pa were typically >10'000, reaching up to 70'000.

Besides thermal drift, long-term pressure variations in the chamber were measured which are related to the precursor gas flux injected into the vacuum chamber. A stable pressure in the chamber was observed to develop at a time-scale of several minutes after turning on or off the gas flux. In some of the measurements a linear drift correction has been performed in post-analysis.

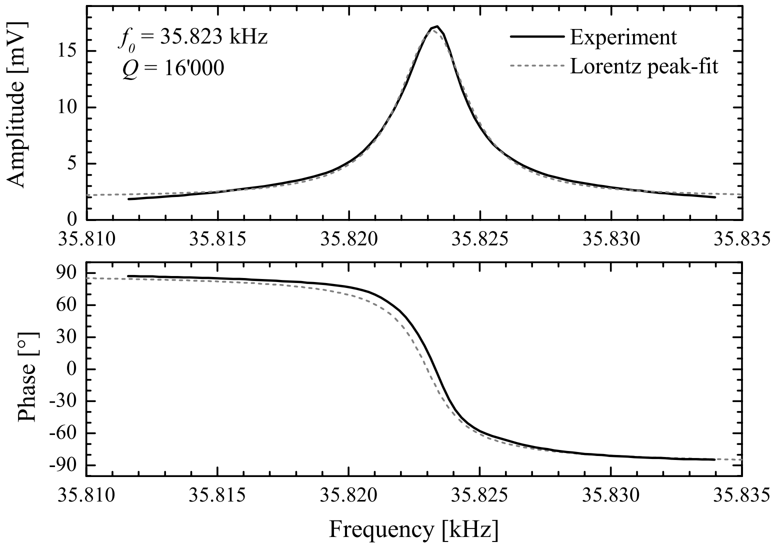

Figure 4.10: *Frequency sweep through the fundamental resonance of a piezoresistive cantilever in vacuum (10^{-3} Pa) used for mass sensing. The excitation amplitude was $V_e = 50$ mV and the Wheatstone bridge bias $V_b = 0.8$ V. The experimental amplitude data is fitted by a Lorentzian peak function (Eq. 4.11); the corresponding phase relation is plotted (Eq. 4.12). The quality factor has been determine from Eq. 4.13.*

4.4.1 FIB milling

The removal of cantilever mass by FIB milling of a 1×1 μm^2 pit is shown in Fig. 4.11. The root-mean-square of the mass noise signal in Fig. 4.11 is 10 fg at a demodulation bandwidth of $B = 1$ Hz. Since the mass of removed Si can be deduced from the pit volume known by SEM imaging, this approach was an elegant way to perform the calibration of the mass sensor response, $\Delta f/\Delta m$ (Sect. 4.3.4). It is noted that the mass due to implanted Ga atoms at the pit bottom has been accounted for.[89]

From this measurement we determined the milling rate in atoms per ion relying on the measured mass removal rate R_{Si} upon irradiation by an ion current I_{Ga} according to

$$Y_{\text{Si}} = \frac{R_{\text{Si}} e N_a}{I_{\text{Ga}} M_{\text{Si}}}, \tag{4.24}$$

where N_a is Avogadro's constant, e is the elementary charge and M_{Si} the molar mass of Si.

Redeposition decreases the measured sputtering yield in high aspect-ratio structures. However, the constant sputter rate observed in Fig. 4.11 indicates that redeposition of ejected Si atoms on the pit sidewalls is insignificant up to the final pit aspect-ratio of ≤ 0.4 explored in this experiment. The measured rate of $R_{\text{Si}} = (29 \pm 1)$ fg s^{-1} (Fig. 4.11) and using Eq. 4.24 evaluates to $Y_{\text{Si}} = (2 \pm 0.2)$ atoms per ion. In the literature the milling rate of Si has been determined several times from experiments.[200,260,313] For a 30 kV Ga ion beam at normal incidence on a Si substrate a value of $2 \ldots 3$ atoms per ion is reported. Using SRIM Monte

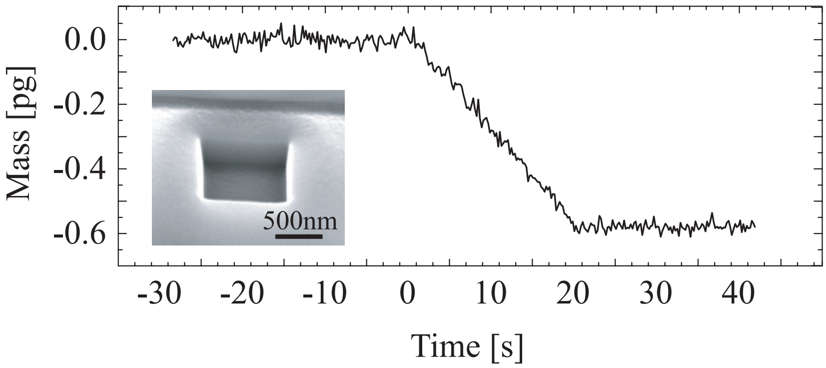

Figure 4.11: *Evolution of the cantilever resonance frequency during FIB (Ga$^+$, 30 kV, 50 pA) milling of a* 1×1 *μm^2 pit. Inset: SEM tilt view (45°) of the sputtered pit.*

Carlo simulations[i] which are based on a quantum mechanical treatment of ion-atom collisions, the milling rate was calculated and results support the range of $2 \ldots 3$ atoms per ion of experimentally found values.[88,247]

4.4.2 FEB/FIB induced deposition from $(CH_3)_3PtCpCH_3$

In Fig. 4.12 the frequency response of the mass sensor is presented during two equivalent deposition experiments using FEB and FIB irradiation which involved the following steps: (A) precursor injection directed to the cantilever, (B) FEB/FIB irradiation, and (C) shutting-off of the precursor flux. The analysis of the frequency shift in parts A and C are subject in the following section. The deposition in part B will be discussed subsequently.

Surface coverage with adsorbed molecules

For FEB/FIB induced processing the GIS supplied the precursor at an average molecule flux at the GIS exit of $J_{\mathrm{tot}} = 3.3 \times 10^{18}$ cm^{-2} s^{-1} measured by mass loss of the precursor reservoir according to Eq. 3.3. The mass change due to adsorption of precursor molecules which impinge homogenously on the topside of the cantilever was detected as a frequency reduction and can be deduced from Eq. 4.14, $\Delta m = \Delta f R_h^{-1}$. Impinging molecules physisorb on the cantilever with a given sticking probability and diffuse on its surface before they eventually desorb after an average residence time. Knowledge of the mass of the time-averaged number of adsorbates and the impinging molecule flux allows deducing the molecule surface coverage and the molecule residence time.

Opening the $(CH_3)_3PtCpCH_3$ precursor reservoir lead to a negative frequency shift due to added mass from adsorption of precursor molecules on the cantilever surface (part A). After several minutes, GIS and vacuum chamber achieved their equilibrium pressure as indicated by a reproducible cantilever frequency shift of ∼150 mHz in Fig. 4.12 (a) and ∼120 mHz in Fig. 4.12 (b). The difference in frequency shift arises from the apparent cantilever area

---

[i] The Stopping and Range of Ions in Matter (SRIM)[328], `www.srim.org`, 2007

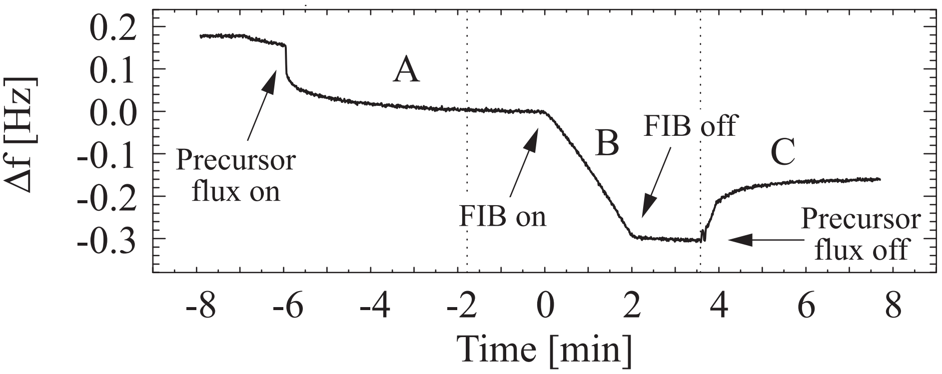

(a)

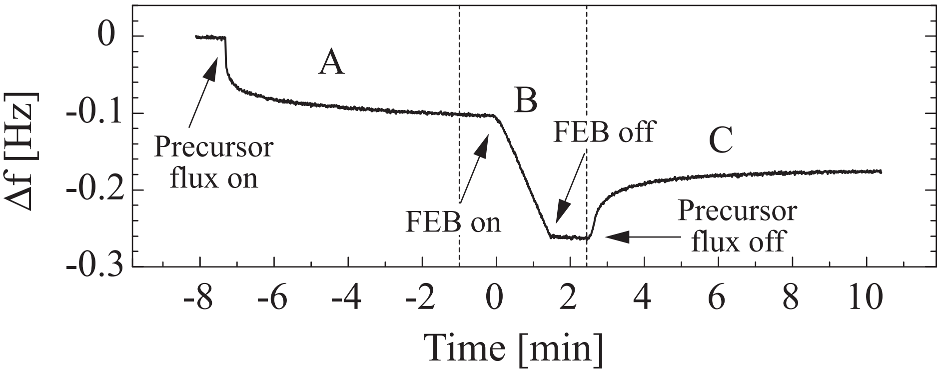

(b)

Figure 4.12: *(a) FIB and (b) FEB induced deposition experiment from the precursor* $(CH_3)_3PtCpCH_3$*: (A) Mass loading due to adsorption and (C) mass loss due to desorption. (B) FEB/FIB exposure of a* 1×1 μm^2 *rectangle.*

exposed to the molecular flux which is larger in the case of normal FIB incidence as compared to the 52° sample tilt for normal FEB incidence. In both cases, the locally increased pressure at the GIS exit lead to higher damping of the cantilever, which is measured as an increase in dissipated excitation energy of 1 %. This has a negligible impact of ~ 1 ppb on the frequency shift calculated by Eq. 4.10, for $Q =$10'000.

The reversibility of the mass loading by desorption of molecules upon closing of the precursor supply is observed in part C. Typically a residual frequency shift of 10-20% was observed in these experiments which could be due to precursor molecules which are chemisorbed to the cantilever.

For the case of the FIB being normally incident onto the cantilever, the Monte Carlo simulated impinging precursor flux distribution, $J(x, y)$, is shown in Fig. 4.13. We refer to Chapter 6 for details of the flux distribution characterization.

Non-dissociative Langmuir adsorption predicts the mass distribution on the cantilever as

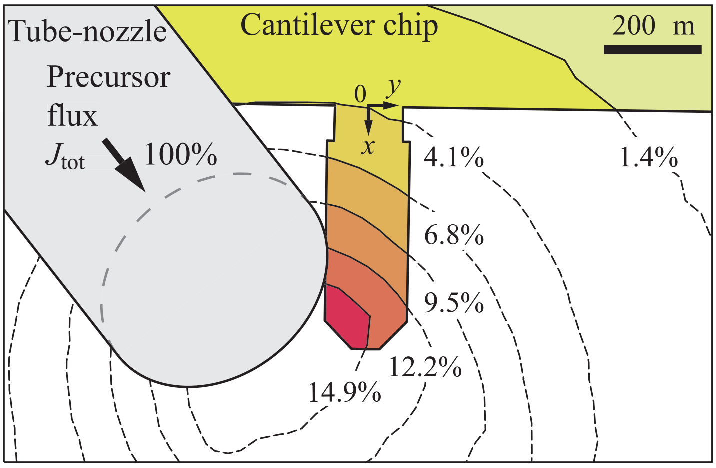

Figure 4.13: *Top-view of cantilever mass sensor and microtube (Fig. 4.4). The microtube is 52° inclined and its exit surface center is at a distance of 600 µm relative to the cantilever chip plane. Monte Carlo simulated precursor isoflux lines show the impinging flux distribution on the cantilever chip (for clarity the contours are extended as dashed lines over the whole plane). Isoflux percentages are indicated ($J_{\text{tot}} = 3.3 \times 10^{18}$ cm^{-2} s^{-1}).*

follows

$$m(x,y) = m_0\Theta(x,y) = m_0 \frac{sJ\tau}{sJ\tau + n_0}, \tag{4.25}$$

where n_0 is the density of a complete monolayer and m_0 the monolayer mass on the cantilever surface, s the sticking probability and τ the surface residence time. For low surface coverage, $\Theta \ll 1$, the mass distribution is expected to be proportional to the flux distribution $m(x,y) \simeq m_0 sJ(x)\tau/n_0$. The frequency shift, Δf, is obtained by integrating the mass distribution and the position depending mass responsivity, $R_p(x)$, along x

$$\Delta f = \frac{1}{l}\int_0^l m(x)R_p(x)\mathrm{d}x \simeq \frac{m_0 s\tau}{n_0 l}\int_0^l J(x)\,\frac{\Delta f}{\Delta m}(x)\,\mathrm{d}x. \tag{4.26}$$

For rectangular cantilevers with $l \gg w$ we have $\Delta f/\Delta m(x) = (\Delta f/\Delta m)_{\text{end}} \cdot (x/l)^3$.[257] From the $(CH_3)_3PtCpCH_3$ molecule size (Appendix A) the 100 % monolayer density is found as $n_0 = 2 \times 10^{14}$ cm^{-2}. The numerical solution of Eq. 4.26 yields $s\tau = 29 \times 10^{-6}$ s. We estimated the precursor coverage in the present GIS configuration at the cantilever end: $\Theta \simeq sJ(l)\tau/n_0 = 7$ % of a monolayer, taking $J(l) = 0.149 J_{\text{tot}}$ from Fig. 4.13. There is currently no data available of the sticking probability. Setting $s = 1$ (100%) results in $\tau = 29$ µs which respresents a minimum value of the surface residence time, since s cannot exceed 100%. This corresponds to the time scale of adsorption/desorption equilibrium on the cantilever surface, which is instantaneous compared to the time scale of pressure variations in the chamber. In this calculation the chamber background flux to the cantilever was neglected which according to Eq. 3.4 was $<$ 5 % of the average GIS-supplied flux to the top side.

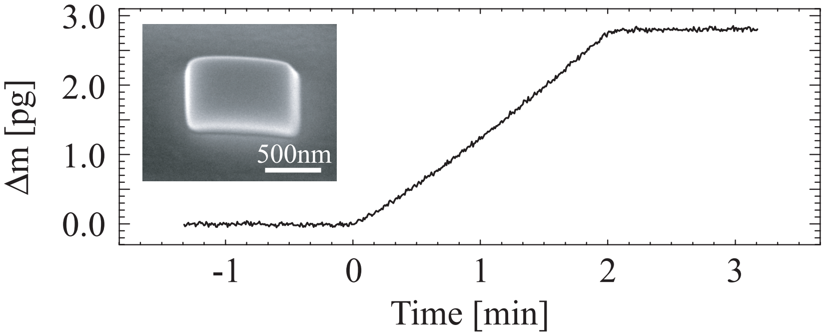

(a)

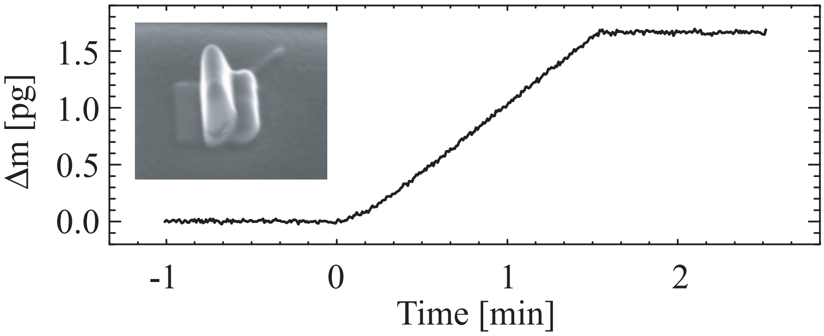

(b)

Figure 4.14: *(a) Evolution of the FIB (30 kV, 5 pA) deposited mass corresponding to part (B) in Fig. 4.12 (a). (b) Evolution of the FEB (5 kV, 800 pA) deposited mass corresponding to part (B) in Fig. 4.12 (b). Insets: SEM tilt view (52°) of the FEB/FIB deposit.*

Deposition rate and yield

As material was added during FEB/FIB induced deposition in part B of Fig. 4.12 (a) and (b) in a 1×1 μm^2 scan area the resonance frequency of the cantilever decreased. Figure 4.14 (a) shows the mass converted FIB deposition sequence with a mass deposition rate of 23 fg s^{-1} in average. A small drift of 1.0 fg s^{-1} was corrected, which is due to the asymptotic approach of chamber pressure to equilibrium after opening the GIS. A deposited material density of $\rho_{\mathrm{Deposit}} = (11.2 \pm 1.1)$ g cm^{-3} was calculated from the total deposited mass of (2.8 ± 0.14) pg and the deposited volume of (0.25 ± 0.01) μm^3 determined from the SEM images. Comparing the deposit density to $\rho_{\mathrm{Pt}} = 21.4$ g cm^{-3} and typical Ga contamination obtained under similar conditions[282] suggests that the material consists of 42 at.% Pt, 29 at.% Ga and 29 at.% carbonaceous matrix. The matrix density was assumed ~ 1.5 g cm^{-3}.[296] The FEB deposition (5 kV, 0.8 nA) presented in Fig. 4.14 (b) resulted in a deposit density of $\rho_{\mathrm{Deposit}} = (4.5 \pm 0.5)$ g cm^{-3}. A Pt content of 15 at.% is estimated assuming the same matrix density as for the FIB deposit. Table 4.2 summarizes data extracted from the FIB and FEB induced deposition experiments.

Table 4.2: *Comparison of FEB and FIB deposition from* $(CH_3)_3PtCpCH_3$ *with an impinging molecule flux of* 5×10^{17} cm^{-2} s^{-1} *(Fig. 4.13): molecule surface coverage* $\Theta = n/n_0$ $(n_0 = 2 \times 10^{14}$ $cm^{-2})$*, adsorbate density* n*, deposit density* $\rho_{Deposit}$*, Pt content, volume deposition yield* Y_V*, mass deposition yield* Y_m*, and deposited Pt atoms yield* Y_{Pt}*. The given error bars take into account the inaccuracy of the mass sensor calibration and the deposit/pit volume determination.*

	FIB (30 kV, 5 pA)[a]	FEB (5 kV, 0.8 nA)[b]
Θ (%)[c]	7.0 ± 0.4	5.6 ± 0.3
n (cm^{-2})[c]	$(1.4 \pm 0.1) \times 10^{13}$	$(1.1 \pm 0.1) \times 10^{13}$
ρ_{Deposit} (g cm^{-3})	11.2 ± 1.1	4.5 ± 0.5
Pt (at.%)	42	15
Y_V (µm^3 nC^{-1})	0.42 ± 0.02	$(4.6 \pm 0.2) \times 10^{-3}$
Y_m (pg nC^{-1})	4.7 ± 0.2	$(21 \pm 1) \times 10^{-3}$
Y_{Pt} (Pt/ion,e$^-$)	1.0 ± 0.1	$(1.5 \pm 0.2) \times 10^{-3}$

[a] dwell time: 0.2 µs, loop time: 5.6 ms
[b] dwell time: 0.2 µs, loop time: 0.36 ms
[c] Without ion/electron irradiation.

Yields are evaluated from the ratio of a deposit quantity, such as the deposit volume or mass to the irradiation dose. Accordingly, the yield in terms of deposited Pt atoms per ion/electron is found as

$$Y_{\mathrm{Pt}} = \frac{x_{\mathrm{Pt}} m_{\mathrm{Deposit}} / m_{\mathrm{Pt}}}{I_p / e \Delta t}, \tag{4.27}$$

where x_{Pt} and m_{Pt} are the Pt content in the deposit and the Pt atom mass, respectively, I_p/e is the ion flux and Δt the irradiation time. From the deposition rate model described in Chp. 7 (Eq. 7.1) it follows that the yield (in "atom per ion/electron") is the product of the adsorbate density in the irradiated zone and the cross-section for irradiative molecule dissociation:

$$Y_{\mathrm{Pt}} = n\sigma. \tag{4.28}$$

This relation points out that Y_{Pt} depends on the specific set of experimental parameters, since n results, besides the adsorption and diffusion kinetics, from the depletion by irradiative dissociation. Therefore, the yield values in Table 4.2 are specific for the deposition conditions.[89] From the presented mass sensing experiments (Fig. 4.12) Eq. 4.28 allows to evaluate the irradiative dissociation cross-section of $(CH_3)_3PtCpCH_3$ molecules for ions and electrons: $\sigma = 7$ nm^2 and $\sigma = 0.014$ nm^2 for the 30 kV FIB and 5 kV FEB irradiation, respectively. However, since the n values in Table 4.2 represent adsorbate densities without ion/electron irradiation (no irradiative depletion) such estimated σ values are lower limits.

4.4.3 FEB induced deposition from Cu(hfac)$_2$

The evolution of FEB induced mass deposition (5 kV, 300 pA) from the precursor Cu(hfac)$_2$ in stationary spot exposure mode is presented in Fig. 4.15 (a). Small signal jumps in the mass response, corresponding to several millihertz in the frequency response, at the start and end of FEB induced deposition are observed. An estimation based on a one-dimensional linear thermal conductance model predicts a temperature rise at x along the cantilever induced by an energy source at the cantilever end according to[246]

$$\Delta T = \frac{V I_p (1-\eta) x}{\kappa w h}, \tag{4.29}$$

where V and I_p are the acceleration voltage and the probe current, η the BSE yield, κ the thermal conductivity and w and h the cantilever width and thickness. The input power term $VI_p(1-\eta)$ induced by the incident electron beam is estimated assuming that the energy of PEs which are not backscattered is lost to the Si crystal lattice. The loss contribution from low energy SEs is neglected. This simple model predicts an average temperature rise (at $x = l/2$) of $\sim$ 1.5 mK in the cantilever with dimensions 508 μm $\times$ 175 μm $\times$ 8 μm with $\kappa_{\mathrm{Si}} = 1.56$ W cm^{-1} K^{-1}[180] and $\eta_{\mathrm{Si}} = 0.2$[136,137]. The measured sensor's frequency dependence on temperature is 1 Hz K^{-1} for the used cantilever with a resonance frequency at $f_0 = 43.4$ kHz, which results in frequency shifts in the order of a few mHz (Eq. 4.21). Thus, we conclude that the observed signal jumps in Fig. 4.15 (a) may be explained by induced FEB heating in the cantilever. It is noted that the effect is more pronounced if the present native oxide layer of 10-30 nm thickness on the Si is taken into account, having a low thermal conductivity $\kappa_{\mathrm{SiO_2}} = 0.014$ W cm^{-1} K^{-1}[180].

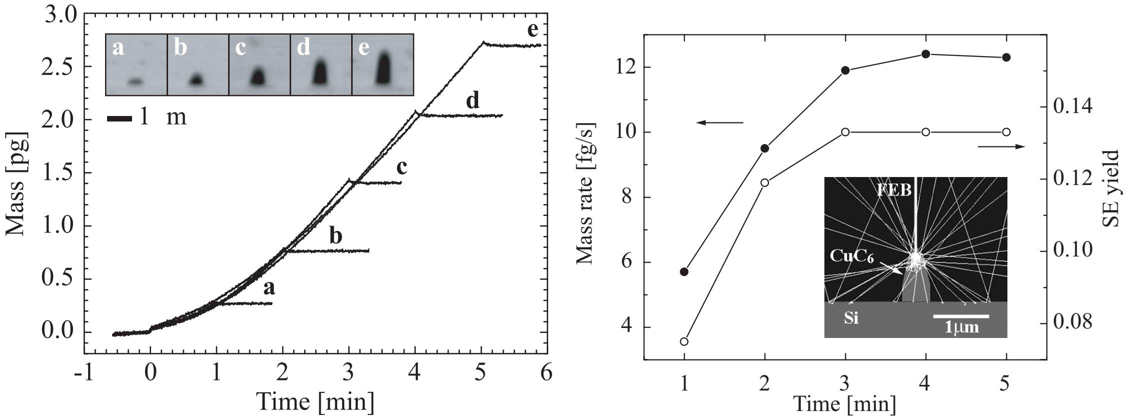

(a) (b)

Figure 4.15: *FEB (5 kV, 300 pA) induced pillar deposition from the precursor Cu(hfac)$_2$ in stationary spot mode irradiation for 1, 2, 3, 4 and 5 minutes. (a) Deposited mass with ongoing deposition. The insets show the corresponding tips in tilted view. (b) Evolution of deposited mass and the corresponding simulated SE yield.*

The absolute mass deposition rate in stationary spot exposure was non-constant (Fig. 4.15 (a)). In terms of deposit height and volume such a behavior is well documented.[25,266] However, in comparison to theses studies the mass measurements include the deposition which occurs on the substrate by forward scattered electrons in the pre-deposited structure. Using the MOCASIM simulation package[246] we computed the SE yield from the growing structures irradiated with a Gaussian beam with a FWHM of 150 nm as determined by knife-edge measurements. The simulation was performed assuming a deposit composition of $\mathrm{Cu}_{0.14}\mathrm{C}_{0.86}$ and an average density of 2 g cm^{-3}. The SE emission is computed based on a parametric model which aims to correctly describe the experimental behavior of SEs without worrying about the details of the processes involved.[138] The two input parameters λ and ϵ can be related to the mean free path of SEs and to the mean energy required to produce a SE, respectively. We used the tabulated data $\lambda_{\mathrm{Si}} = 3$ nm and $\epsilon_{\mathrm{Si}} = 70eV$, and estimated $\lambda_{\mathrm{Cu}_{0.14}\mathrm{C}_{0.86}} = 5.5$ nm and $\epsilon_{\mathrm{Cu}_{0.14}\mathrm{C}_{0.86}} = 80$ eV being typical values for carbon. In Fig. 4.15 (b), the evolution of the mass deposition rate is plotted together with the simulated SE yield. The inset shows the simulated electron trajectories. The mass deposition rate increases with deposition time and reaches a plateau value around 12 fg s^{-1}, simultaneously to the SE yield confirming a strong correlation.[170] The increasing SE yield is due to an extension in apparent surface for SE emission with growing deposit and an increase in FSEs from the deposit which produce SEs on the substrate surface. The forward scattering leads to formation of a halo deposition.[244,296] A constant SE yield is established once the projection relative to the FEB remains the same. These experiments show that the mass deposition rate in stationary spot mode irradiation depends on the shape of the pre-existing deposit. More experimental data is needed to extend the significance of these results.

4.5 Summary

We demonstrated cantilever-based *in situ* mass sensing for monitoring of FEB/FIB induced processes, i.e. FIB milling, FEB/FIB deposition and precursor adsorption, at the femtogram-scale. Cantilevers with piezoresistive deflection read-out have been used for continuous mass measurements based on a phase-locked-loop circuit and amplitude/phase feedback loops which allowed to perform highly sensitive continuous frequency tracking. Calibration of the sensor has been addressed and a simple method to overcome thermal drift problems has been implemented. Absolute mass deposition rates and yields could be extracted and metal/matrix contents estimated without the need for a chemical composition analysis. The measured deposit mass enabled the investigation of the material density by volume determination via imaging using $\rho_{\mathrm{Deposit}} = \Delta m / V_{\mathrm{Deposit}}$. In addition the adsorption of precursor molecules on the cantilever was monitored which served for the determination of the molecular surface coverage and allowed to measure the mean residence time of molecules (assuming a sticking probability of 100%) which characterizes the adsorption/desorption kinetics on the substrate for the actual deposition conditions.

Chapter 5

Mechanical analysis of FEB deposits

We successfully performed *in situ* mechanical experiments to evaluate the Young's modulus, density and tensile strength of FEB deposited materials. The employed experimental methods based on bending (Sect. 5.3.1), resonance (Sect. 5.3.2), and tensile (Sect. 5.4) tests are outlined and discussed. FEB induced deposition from Cu(hfac)$_2$ of pillars with lengths exceeding 30 times their diameter were performed at 5 kV and 20 kV acceleration voltage (Sect. 5.2). The Young's moduli of these pillars measured by *in situ* bending experiments using micromechanical cantilevers were (16 ± 5) GPa (5 kV) and (17 ± 5) GPa (20 kV). From additional modal analysis by vibration experiments the material densities evaluated to (1.9 ± 0.5) g cm^{-3} (5 kV) and (2.9 ± 0.7) g cm^{-3} (20 kV). The measured density values compared well to measurements using the cantilever-based mass sensing approach. The dissipation in the structures had a large scatter revealed by quality factors in the order of 100 to 600 at room temperature in vacuum. *In situ* cantilever-based tensile strength measurements resulted in values of (2 ± 0.5) GPa and (1 ± 0.5) GPa for FEB bonds deposited from W(CO)$_6$ and Co$_2$(CO)$_8$.

5.1 Introduction

With regard to the ability of FEB/FIB induced deposition as a fabrication tool for nanodevice fabrication and as a versatile attachment technique used in nanomanipulation processes inside the SEM, the interest in the mechanical properties such as Young's modulus, hardness and adhesion properties of FEB/FIB deposits has grown in recent research studies. Mechanical properties of FEB and FIB deposits are difficult to predict due to the often composite structure of the deposits, e.g. nanocrystalline grains embedded in a carbonaceous matrix.

5.2 High aspect-ratio pillar growth

For mechanical characterization of FEB deposited materials, high aspect-ratio cylindrical pillars with uniform cross-section were deposited from the precursor Cu(hfac)$_2$. High initial growth rates of up to 90 nm s^{-1} for this precursor having a low vapor pressure of 0.4 Pa at room temperature were achieved by optimization of the GIS. A non-standard nozzle geometry

(Fig. 6.23 (b)) provided a high local flux. The precursor flux arrives uniform from all directions and thus, prevents shadowing effects in vertical pillar growth. A detailed analysis of this nozzle-type is given in Sect. 6.9.2.

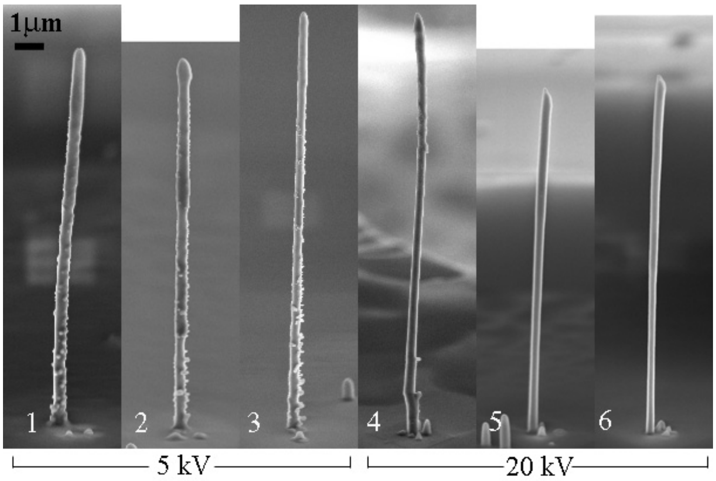

Figure 5.1: *FEB pillar deposits grown normally to the substrate in spot mode for 30 minutes. FEG SEM observation with a substrate tilt of 68°. Deposition conditions: 100 pA, pillars 1-3: 5 kV, pillars 4-6: 20 kV. Precursor: Cu(hfac)$_2$, $J_{tot} = 1.3 \times 10^{17}$ cm^{-2} s^{-1}*

Figure 5.1 shows six pillars all with aspect ratios $l > 30d$, that have been mechanically characterized as outlined in the following sections. The FEB irradiated the substrate at normal incidence and the pillars grew vertically into the stationary beam. All depositions were performed on a Si substrate with a native oxide at a probe current of 100 pA measured in a Faraday cup and at an acceleration voltage of 5 kV (pillars 1-3) and 20 kV (pillars 4-6). The pillars were grown at >10 μm lateral distance on the substrate which avoided pillar bending induced by proximity effects, i.e. due to electrostatic forces induced by charge accumulations during irradiation.[195] It has been experimentally observed that slight bending is induced during post-observation of the pillars in a FEG SEM probably due to surface stress by a deposited contamination layer. To exclude wrong measurements of the length and diameter due to SEM images that are two-dimensional projections of the pillar, they were imaged from two perpendicular directions.

Although the deposition time was 30 min for all pillars, a difference in deposit height is observed which is attributed to focus adjustments between depositions. The cumulative vertical deposition rate, being the ratio of total height to the deposition time, was in the order of 7-9 nm s^{-1} at both 5 and 20 kV.

The 5 kV-pillars show substructures randomly distributed on the whole circumference which are however not present at the pillar top. The pillars grown at 20 kV have smooth surfaces. These phenomena have been reported in the literature several times but are currently not fully understood.[23,240] It is beyond this work to further analyze such structures.

5.3 Mechanical characterization of FEB deposited copper pillars

For the following experiments we assumed an ideal cylindrical pillar shape which allows a treatment based on a basic set of formulations known from classical structural mechanics.[308,320] More complicated geometries could be analyzed using finite element methods. The length and diameter of the samples is measured by FEG SEM imaging of the pillars and average values are given in Table 5.1. An accurate diameter measurement was accomplished by averaging of at least five measurements along the whole pillar.

5.3.1 *In situ* bending tests

Method

In bending test experiments the sample is bent by a calibrated reference cantilever (a force sensor) to measure Young's modulus E of the sample material. There is a maximum tensile and a compressive zone at the sample root which dominantly determines the pillar properties in a bending test.

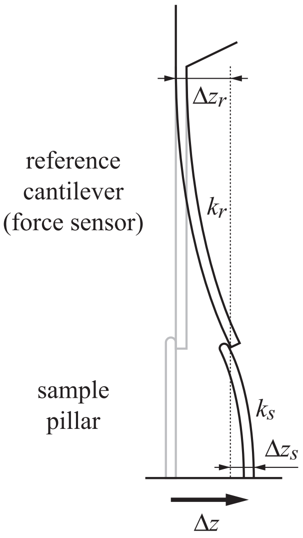

Figure 5.2: *Scheme of bending test arrangement using a reference cantilever as the force sensor with force constant k_r. The applied force is read-out by measuring either the reference or sample deflection $\Delta z_{r,s}$ upon a stage displacement of $\Delta z = \Delta z_r + \Delta z_s$. Applying the force balance at the contact point (Eq. 5.1) leads to the force constant of the sample pillar k_s.*

For the bending experiment in Fig. 5.2 the force balance is

$$F = k_r \Delta z_r = k_s \Delta z_s, \tag{5.1}$$

where F is the force component acting perpendicular to the sample axis, k_r, k_s the force constants and Δz_r, Δz_s the deflections of the reference cantilever and the sample, respectively. Young's modulus of a cylindrical pillar with length l and diameter d is obtained from

$$E = \frac{64}{3\pi} \frac{l^3}{d^4} k_s. \tag{5.2}$$

The error in the determination of Young's modulus using Eq. 5.2 is estimated taking into account the measurement accuracy of the deposit geometry using the SEM and the uncertainty in the determination of k_s which results in

$$\frac{\Delta E}{E} = 3\left|\frac{\Delta l}{l}\right| + 4\left|\frac{\Delta d}{d}\right| + \left|\frac{\Delta k_s}{k_s}\right| . \tag{5.3}$$

The third and forth order dependence on the pillar length and diameter indicates the importance of accurate measurements of the pillar dimensions. The calibration error of the reference cantilever force constant k_r leads to a proportional systematic error in k_s. Off-end position of the contact point between reference cantilever and the pillar can be accounted for by subtracting it from the total pillar length.

Chen *et al.*[41] have investigated the errors originating from the way the sample is attached to the substrate. In the experiments performed on FEB deposits this uncertainty is strongly reduced since the pillars are deposited directly on the substrate and are mechanically adhering.

Experimental method, results and discussion

The bending test on a copper containing FEB deposit (pillar 3 in Fig. 5.1) is summarized in Fig. 5.3. For this experiment a reference cantilever was chosen which had a force constant close to the previously estimated force constant of the sample pillar. This k-matching is required since the measurement accuracy decreases if either the sample or the reference cantilever deflects only marginally upon loading.[104] Figure 5.3 (a) shows the arrangement of reference cantilever and pillar sample. The reference was a microfabricated array of SiO_2 cantilevers with 200 μm length and 10 μm width. These cantilever arrays were fabricated by Kristian Mølhave at the Technical University of Denmark, DTU. *In situ* modal analysis of eight cantilevers on the chip (a description of the frequency measurement setup is given in Sect. 5.3.2) was performed and revealed a fundamental resonance frequency at 21.875 kHz with a narrow standard deviation of ±0.12% between the cantilevers. We evaluated Eq. 4.6 for the cantilever thickness resulting in $h = 0.928$ μm, which is close to the nominal value of 1 μm, assuming a density of 2.2 g cm^{-3} and Young's modulus of 75 GPa[i] of the SiO_2. Equation 4.22 finally results in a calibration of the reference force constant: $k_r = 0.019$ N m^{-1}. This calibration is assumed to be accurate to within 10% due to typical variations in thermally grown thin film SiO_2 properties (with $\Delta E/E = 10\%$, $\Delta\rho/\rho = 3\%$) and measurement inaccuracy of plane dimensions (with $\Delta w = \Delta l = 100$ nm) deduced from the error in Eq. 4.22.

Displacement of the sample was done by a three-axis piezo-stage[233] with closed-loop controlled positioning and sub-nanometer resolution. Displacing the sample stage in positive and negative direction resulted in forth and back deflection of the sample pillar (Fig. 5.3 (b)). Pushing the sample against the force sensor ($+\Delta z$ direction) deflected both the pillar and the cantilever as is observed in part (B). While pulling apart the sample and the cantilever ($-\Delta z$ direction) an adhesive electrostatic force induced by electron-beam charging of the SiO_2 prevented from separation. However, in this case the reference cantilever does not significantly bend as is observed in part (C). This behavior was observed several times, although, some

---

[i] Thermally grown SiO_2, `www.memsnet.org`, 2007

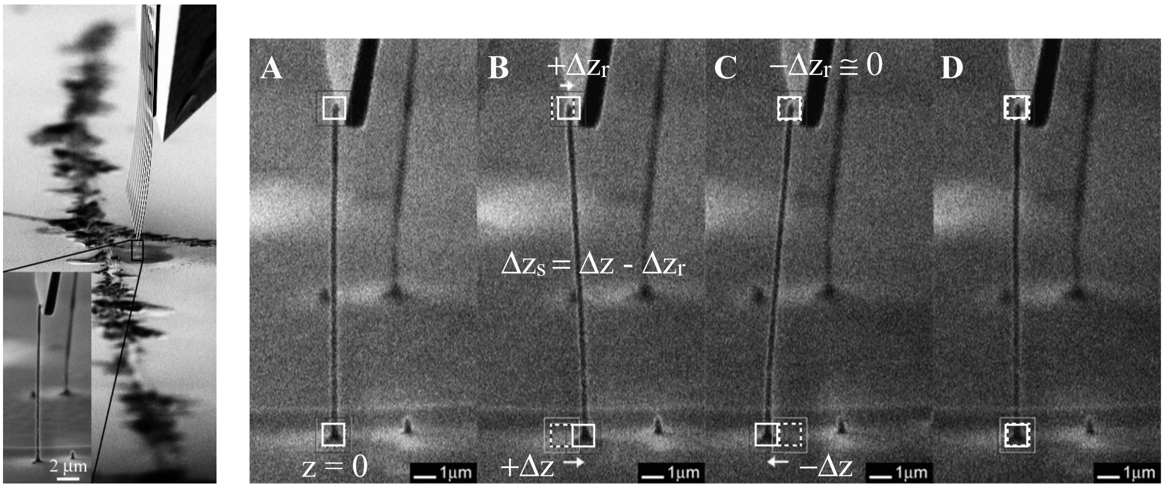

(a) (b)

Figure 5.3: *(a) Arrangement of the reference cantilever array and the sample. The reference force constant was calibrated to* $k_r = 0.019$ *N* m^{-1}*. (b) SEM images of a bending test on pillar 3 in Fig. 5.1. The pillar top and root are tracked by image post-processing and are marked by solid boxes. (A) Initial unstrained contact position of the sample pillar with the reference cantilever; subsequently marked by dashed boxes. (B) The substrate is horizontally shifted by* $+\Delta z$ *resulting in a sample deflection of* $\Delta z_s = \Delta z - \Delta z_r$*. (C) A substrate shift* $-\Delta z$ *bends the sample, however, the reference cantilever remains at its unstrained position. (D) After the bending cycle cantilever and sample are at their initial position.*

of the bending tests revealed a linear deflection response upon pushing and pulling. The observation is not fully understood, however, we believe it is not material dependent and thus consider it to be a measurement artifact. It is speculated that while pulling the electrostatic contact force may have a vertical component which applies compressive forces to the pillar compensating the normally applied force to the reference cantilever by vertical displacement.

In all experiments the deflection Δz_s was kept <10% of the pillar length which is within the elastic bending regime as was confirmed by isolated experiments. The bent pillars flexed back close to their initial unstrained position upon release of the bending force by retracting the reference cantilever.

The quantification of bending tests (e.g. Fig. 5.3 (b)) was performed based on image post-processing of video data captured by SEM imaging during the tests. A cross-correlation algorithm detected the location of a previously defined image detail and the corresponding coordinates were saved in the video time line sequence. Both, the root and the pillar location were tracked using this technique and revealed i) the relative stage displacement Δz and ii) the pillar deflection $\Delta z_s = \Delta z - \Delta z_r$ during the bending test experiment. The data of two experiments presented in Fig. 5.4 shows the measured pillar deflection at the relative stage position. The evolution of the pillar deflection in these tests resulting from a sequence of equivalent stage displacements is plotted in the insets. The reproducibility of cyclic measurements on the same pillar was very high which confirms that the bending within up to 10%

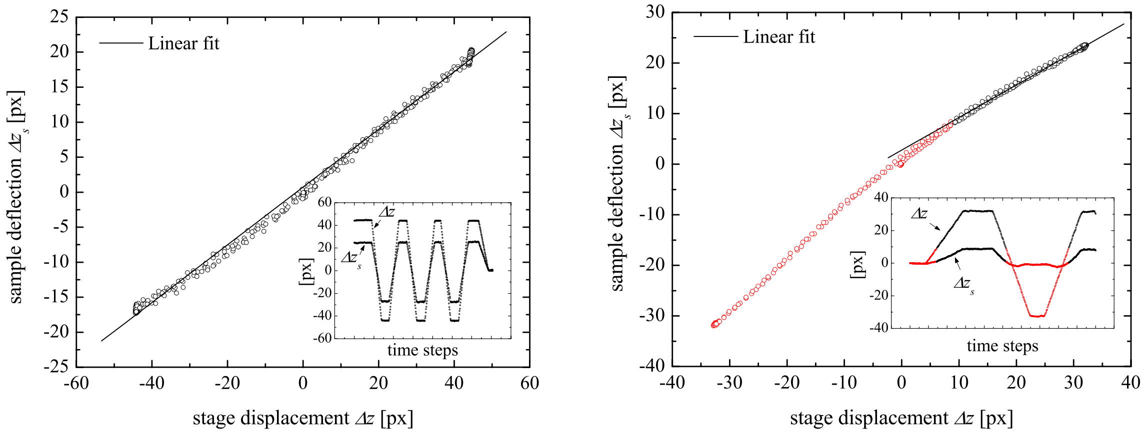

(a) (b)

Figure 5.4: *Pillar deflection Δz_s at sample position Δz from video post-processing of bending tests on the copper containing FEB deposited pillar 2 (a) and 3 (b) in Fig. 5.1. The insets show the corresponding sequence of sample deflection cycles. $\Delta z = 0$ corresponds to zero force applied. (a) The deflection response is linearly fitted to reveal the slope $\Delta z_s/\Delta z = 0.41 \pm 0.0$. (b) The non-linear deflection response while pulling the sample apart from the reference cantilever (in red) is considered as a measurement artifact and linear fitting is performed for the data at $\Delta z > 10$ px which reveals $\Delta z_s/\Delta z = 0.64 \pm 0.0$. Data corresponds to Fig. 5.3 (b).*

deflection does not influence considerably the stiffness of the material and supports that the experiments are performed within the elastic deformation limit.

The displacement noise observed in the post-processed deflection data originating from noisy SEM images is maximally one pixel which corresponds to a position accuracy of 20 nm. For the used reference cantilevers with 0.019 N m^{-1} force constant a force resolution of 0.4 nN results.

Rearranging Eq. 5.1 and expressing the reference cantilever deflection as $\Delta z_r = \Delta z - \Delta z_s$ yields

$$\frac{\Delta z_s}{\Delta z} = \frac{k_r}{k_r + k_s}. \tag{5.4}$$

which corresponds to the slope of the linear regression through the experimental data points in Fig. 5.4 (a). Using Eq. 5.4 we can solve for k_s and from Eq. 5.2 we find:

$$E = \frac{64}{3\pi}\frac{l^3}{d^4}\underbrace{k_r\left[\left(\frac{\Delta z_s}{\Delta z}\right)^{-1} - 1\right]}_{=k_s}. \tag{5.5}$$

If the pillar dimensions as well as the deflections are read out from the SEM, the systematic error in the order of 5% originating from its calibration partly cancels out. As mentioned above the Young's modulus is dominated by the pillar root material, however, it is assumed

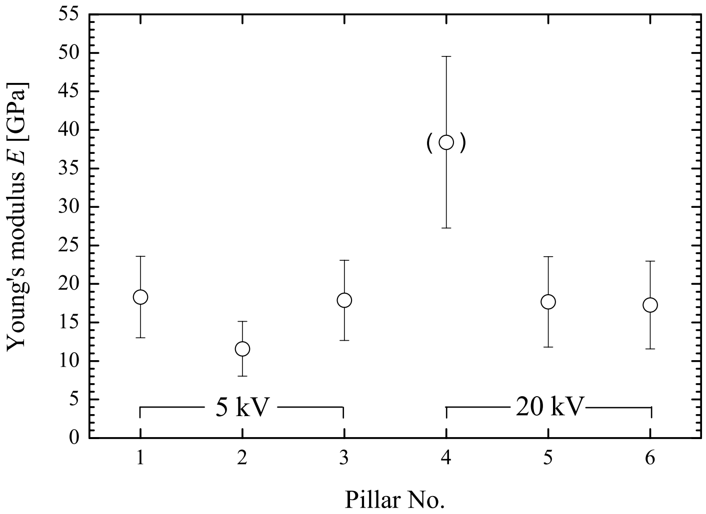

Figure 5.5: *Young's modulus E of copper containing FEB deposited pillars (Fig. 5.1) determined by in situ bending tests. The marked density value of pillar 4 is considered to be an outlier due to a shape irregularity.*

that properties do not strongly vary along the pillar except for the top which was irradiated with a lower electron dose.

The measured Young's moduli of FEB deposited pillars are presented in Fig. 5.5 and the results of the bending tests are compiled in Table 5.1. The error is calculated according to Eq. 5.3 with $\Delta l = 500$ nm, $\Delta d = 20$ nm and, $\Delta k_s = 10\%\ k_s$. A detailed observation of the pillars in Fig. 5.1 reveales that pillar 4 has a distinct shape irregularity at the pillar root. Bearing this in mind we decided to treat the Young's modulus measurement from pillar 4 as an outlier. This demonstrates the sensitivity of the bending method to the shape of the structure to be tested. The influence of geometrical shape irregularities needs to be evaluated in more detail based on further experiments and more significant statistics.

The average Young's modulus for the pillars 1 to 3 grown at 5 kV and for the pillars 5 and 6 grown at 20 kV is found to be (16 ± 5) GPa and (17 ± 5) GPa, respectively. For comparison, Young's modulus of pure copper is in the order of 130 GPa. The stiffness does not significantly change with increasing acceleration voltage. The measurement accuracy of these bending tests is roughly $\pm 30\%$.

Similar measurements on FEB pillar deposits from the precursor Phenathrene have shown that the Young's modulus of these deposits grown at 5 kV and 20 kV was reduced by roughly a factor two (Fig. 2.11 (b)).[221] In a reported study based on nanoindentation on FEB thin film deposits from the precursor Paraffin, the Young's modulus, however, increased by a factor two with increasing acceleration voltage from 3 kV to 20 kV.[63] The inconsistency of these results suggests that the simple model based on the deposited net energy by the FEB in the growing structure[96] needs to be refined, e.g. irradiation induced cross-linking inside the deposit may be a significant source which can lead to higher stiffness. Thus, the electron range which

Table 5.1: *Results from bending and resonance tests on the FEB deposited pillars in Fig. 5.1. The force constant* k_s*, and Young's modulus* E *measured by in situ bending tests, the fundamental mode resonance frequency* f_0*,* $\sqrt{E/\rho}$*, and the fundamental mode quality factor* Q *measured by in situ resonance tests are reported for the pillars with length* l *and diameter* d*.*

				bending test		resonance test		
	pillar	l [μm]	d [nm]	k_s [N m^{-1}]	E [GPa]	f_0 [kHz]	$\sqrt{E/\rho}$ [m s^{-1}]	Q [-]
5 kV	1	14.8	413	0.027	18 ± 5	766	2.9×10^3	154
	2	13.8	354	0.012	12 ± 4	665	2.6×10^3	345
	3	15.7	339	0.010	18 ± 5	600	3.1×10^3	550
20 kV	4	15.5	340	-	-	763	3.9×10^3	358
	5	12.8	305	0.013	17 ± 5	632	2.4×10^3	194
	6	13.2	280	0.008	17 ± 5	566	2.5×10^3	316

increases with increasing acceleration voltage as well as the corresponding local irradiation dose should be taken into account.

5.3.2 *In situ* resonance tests

Method

Another way of measuring Young's modulus are *in situ* resonance experiments in which the sample is excited at its resonance frequency by thermal, piezo, or electrostatic excitation. Vibration amplitude detection is possible with the imaging capabilities of the SEM: the overall modal shape is visualized by normal image scanning and a frequency spectrum is taken by secondary electron (SE) detection with a stationary beam (Fig. 5.6).[31] If the electron beam irradiates the maximum amplitude position, a peak in the integrated SE signal is detected at resonance while sweeping the excitation frequency due to the increasing dwell time of the vibrating sample inside the beam. If the electron beam irradiates the zero amplitude position the resonance manifests as negative SE-peak due to a decreasing dwell time. Employing phase locking of the time-resolved SE and excitation signal allows to extract the amplitude and phase response at resonance from the noisy SE signal. The integrated and time-resolved measurements can be performed simultaneously. The deflection signal acquired by the stationary beam technique is in general not linear with vibration amplitude, whereas the phase does not suffer from this non-linearity.

In our setup excitation was done by a piezo actuator. In comparison to electrostatic actuation principles their use is advantageous due to perturbations of the electron beam by electrical fields inherent to the electrostatic transduction principle.

The modal shape of the flexural vibration modes is given by Eq. 4.3. The resonance frequencies depend on the sample material via $\sqrt{E/\rho}$, the sound velocity in the material, and the sample geometry via the geometric moment of inertia I and the cross section A. From

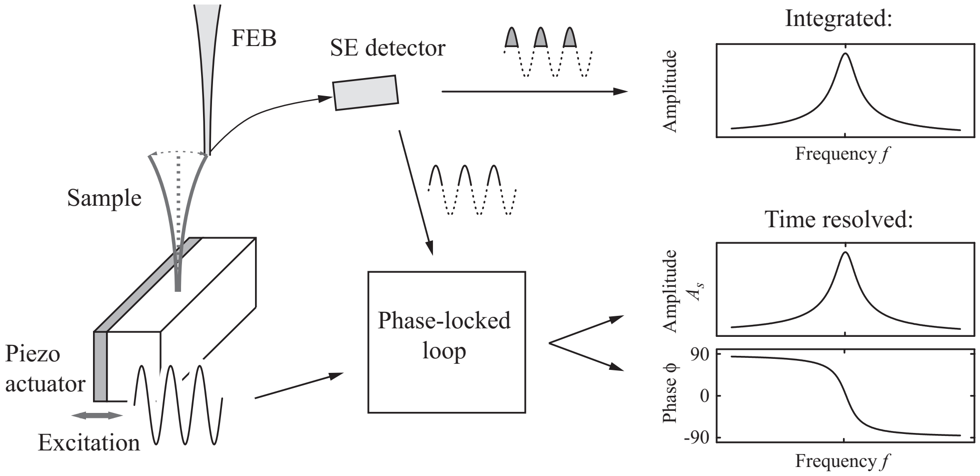

Figure 5.6: *(a) Measurement principle in a piezo-driven resonance experiment based on the stationary beam technique. The time integrated secondary electron (SE) signal is correlated to the interaction dwell time between the stationary electron beam and the vibrating sample. Locking the time-resolved sample deflection signal from the SE detector to the excitation signal in a PLL circuit reveals the deflection amplitude $A_s(f)$ and the phase characteristics $\phi(f)$ at resonance.*

Eq. 4.6 the frequencies for the flexural modes of the sample are

$$f_n = \frac{(\beta_n l)^2}{2\pi l^2}\sqrt{\frac{I}{A}}\sqrt{\frac{E}{\rho}}. \tag{5.6}$$

For cylindrical pillars $(I/A)^{1/2} = d/4$, where $I = d^4\pi/64$. If the pillars have a core-shell morphology with a shell (subscript L) of different material the expression $(EI/A)^{1/2}$ in Eq. 5.6 becomes $EI + E_L I_L/(\rho A + \rho_L A_L)^{1/2}$.[64]

Calabri *et al.* investigated the influence of the presence of intrinsic curvature on the calculated Young's modulus.[36] They suggested a formulation to express the induced fundamental resonance frequency shift as $\Delta f/f \simeq \sqrt{1 + l^2/(ar_c^2)}$, where r_c is the curvature radius and a is a fitting parameter. A finite element modal analysis revealed that the resonance frequency shift imposed by intrinsic curvature in a 10 μm long pillar with 300 nm diameter and consisting of a material having a Young's modulus of 50 GPa and a density of 3 g cm^{-3} is fitted well for $a = 35$. In comparison, Calabri *et al.* found a value of $a = 25$ from finite element analysis for several boron nanowires. For the slight curvatures which were observed in the measured pillars the frequency shift is negligibly small, e.g. for the 10 μm long and 300 nm thick pillar and assuming a curvature radius $r_c \simeq 10$ μm a 1% frequency shift is predicted.

Experimental method, results and discussion

Our *in situ* resonance test setup consisted of a 0.5 mm thick piezoelectric element[190] which was cut to a piece with plane dimensions of about 5×5 mm^2 and glued onto a printed circuit board. Mechanical piezo displacement was excited by applying a voltage across the metallic coatings on the front and backside of the element. The sample was fixed to an intermediate stainless steal angle piece using silver paste. A 10×-amplifier was designed which could drive the ∼ 1 nC capacitive load of the piezo at ±10 V in a bandwidth of 1.2 MHz which limited the overall bandwidth. The bandwidth of the detection system was limited to 2 MHz by the used digital PLL,[204] while the SE detector had a bandwidth > 15.36 MHz which corresponds to the acquisition of 640×480 pixel images at TV mode scan rate (50 Hz). The available overall bandwidth of the setup was sufficient to measure the fundamental resonance mode of the pillars in Fig. 5.1, however, higher modes could not be accessed.

In all the resonance test experiments the excitation amplitude was adjusted to limit the deflection amplitude peak to $< 10\%$ of the pillar length. The distance of the stationary beam relatively to the pillar itself and its peak vibration amplitude crucially determines the amount of "spatial" truncation of small deflection amplitudes. At the maximum tolerable distance, the PLL locks the deflection and excitation signals for a minimum number of data points while sweeping through resonance which allows to determine the amplitude peak value and the slope of the phase curve at f_0. If, on the other hand, the stationary electron beam is positioned very close to the beam rest position, the non-linearities in the amplitude response become very strong. Best results were achieved by slightly defocusing the stationary electron beam which increased the dynamic range of the technique due to a spatially increased interaction between the beam and the vibrating pillar.

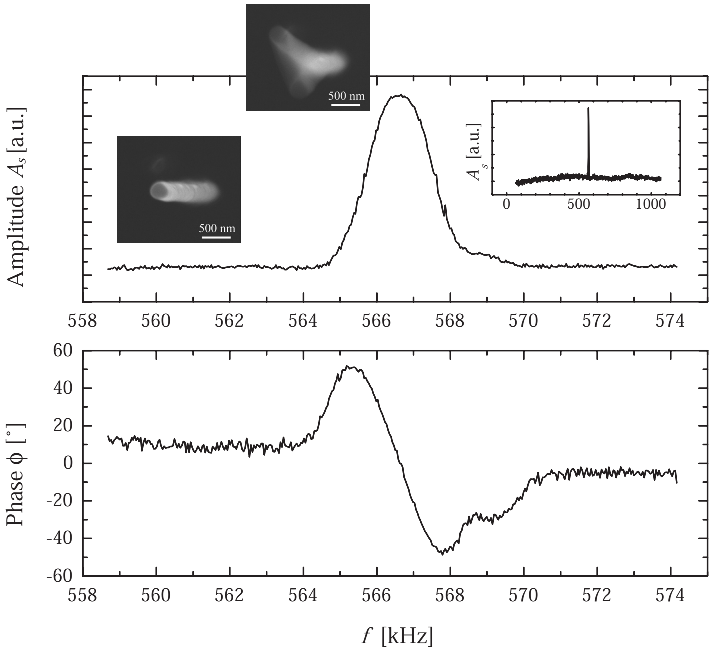

Figure 5.7: *Fundamental mode amplitude and phase response of the pillar 6 in Fig. 5.1 acquired by the stationary beam technique. Top-view SEM images show the slightly tilted pillar off-resonance and at resonance. The PLL locks the deflection to the excitation between 565...568 kHz. The inset (right) shows a wide spectrum of the amplitude response which locates the peak in the vicinity of 566 kHz.*

A typical resonance test experiment is summarized in Fig. 5.7. In a first step an overview spectrum was acquired with the stationary beam technique to roughly locate resonance peaks by sweeping the excitation frequency through the full available frequency range up to 1.2 MHz and measuring the amplitude and phase response. Secondly, close up spectra were acquired at the frequencies of interest. SEM imaging of the pillar at resonance revealed the modal shape and the absolute maximum deflection amplitude for a given excitation amplitude. From the amplitude response the peak position is determined to $f_0 = 566.6$ kHz and from the phase response the slope at resonance: $\phi/\Delta f = 54.7$ ° kHz^{-1}, which evalutates to $Q = 270$ using Eq. 4.13.

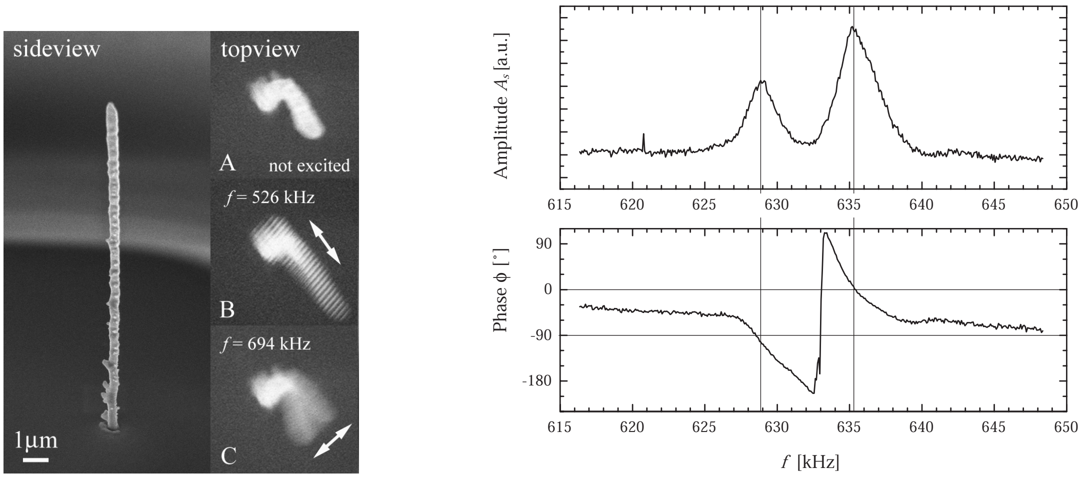

(a) (b)

Figure 5.8: *(a) Orthogonal polarizations of the vibrations of a copper containing FEB deposited pillar grown from the (hfac)CuVTMS. (b) The fundamental mode amplitude and phase response of the pillar 5 in Fig. 5.1 acquired by the stationary beam technique shows a double peak which is due to two orthogonally polarized resonance vibrations. The phase between the two peaks is shifted by 90°.*

In some of the experiments we observed two resonance modes vibrating along the orthogonal principal axes (Fig. 5.8 (a)). This behavior is attributed to both, a non-circular cross-section and intrinsic curvature of the wires.[229] From finite element simulations we found that an intrinsic curvature of a perfectly circular pillar splits up the fundamental resonance modes. Furthermore, theory predicts two fundamental resonance modes for an elliptical pillar with a frequency ratio proportional to the ratio of the two principle diameters. To detect all resonance modes spectra were routinely acquired along two perpendicular directions with the stationary beam technique at top-view incidence. Once, the orthogonal directions of the polarized resonance modes were identified the stationary electron beam was positioned at 45° relative to these directions. This allowed to detect all peaks in a single frequency sweep (Fig. 5.8 (b)). Alternatively, the stationary beam can be positioned at the pillar center which assures that no "spatial" filtering can occur, however, contamination becomes more severe since the electron beam irradiates the pillar during the complete spectrum acquisition.

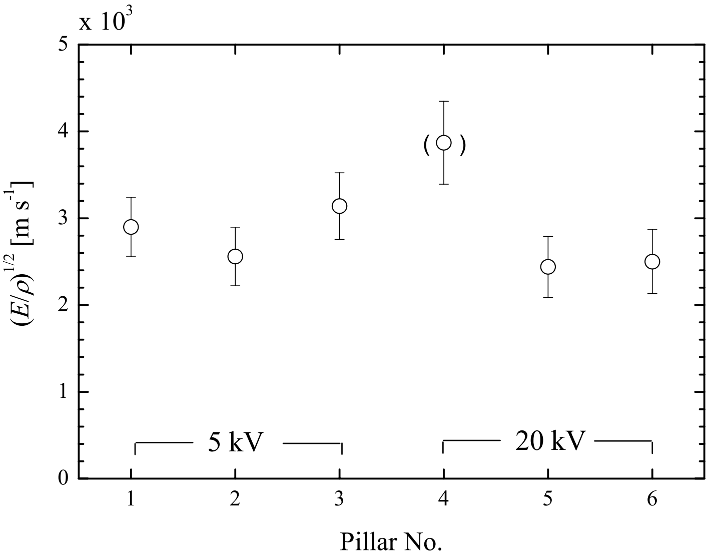

Figure 5.9: *Speed of sound* $\sqrt{E\rho_d}$ *in the copper containing FEB deposited pillars (Fig. 5.1) determined by resonance tests. The marked density value of pillar 4 is considered to be an outlier due to a shape irregularity.*

In Table 5.1 the *in situ* resonance test results of the copper containing pillars (Fig. 5.1) are summarized and in Fig. 5.9 the ratio $\sqrt{E/\rho}$ calculated using Eq. 5.6 with an estimated error $\pm\sqrt{E/\rho}(2\,|\Delta l/l| + |\Delta d/d| + |\Delta f_0/f_0|)$ is presented. If two peaks were observed we used the average frequency to evalute Eq. 5.6 for material characterization. Concerning the result of pillar 4 the same conclusions which were drawn in the bending test are valid, thus, the outlier value is attributed to the shape irregularity at the tip root clearly visible in Fig. 5.1.

5.3.3 Density determination: Combination of bending and resonance tests

Combining Eqs. 5.2 and 5.6 which describe the bending and the resonance experiment the pillar material density is found to be

$$\rho = \frac{(\beta_n l)^4}{3\pi^3}\frac{k_s}{f_0^2 l d^2}. \tag{5.7}$$

The error from Eq. 5.7 is estimated taking into account measurement accuracy of the deposit geometry using the SEM, the uncertainty of the resonance frequency and the force constant which results in:

$$\frac{\Delta\rho}{\rho} = \left|\frac{\Delta l}{l}\right| + 2\left|\frac{\Delta d}{d}\right| + 2\left|\frac{\Delta f_0}{f_0}\right| + \left|\frac{\Delta k_s}{k_s}\right|. \tag{5.8}$$

In Fig. 5.10 the copper containing pillar densities determined from Eq. 5.7 are presented. The reported error (Eq. 5.8) results from $\Delta l = 0.5$ μm, $\Delta d = 20$ nm and, $\Delta k_s = 10\%$ k_s (calibration accuracy of the force sensor). We assumed a negligible error arising from the

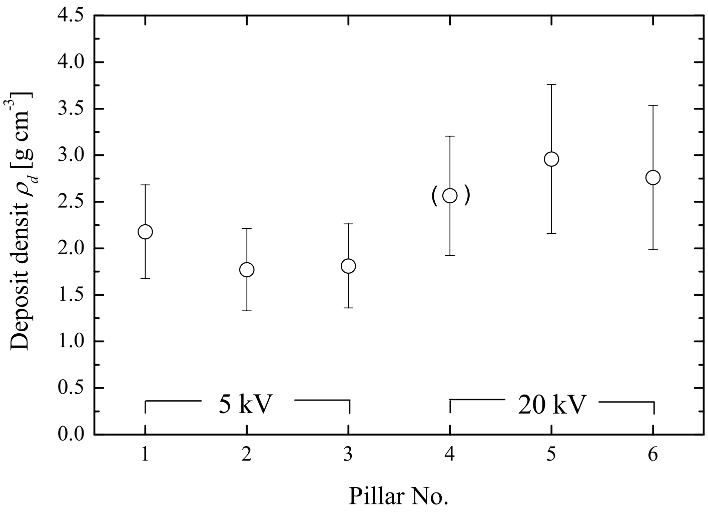

Figure 5.10: *Density ρ_d of copper containing FEB deposited pillars (Fig. 5.1) determined by the combination of bending and resonance tests. The marked density value of pillar 4 is considered to be an outlier due to a shape irregularity.*

determination of the resonance frequency. The estimated error in the measurements in the present work was in the order of 25%. For comparison, from the mass sensing experiments using the piezoresistive cantilever mass sensor described in Chapter 4, the deposit density of FEB/FIB grown deposits could be determined with an error in the order of 10%.[89] The measurements reveal in average that the pillars grown at 5 kV (1-3) have a density of (1.9 ± 0.5) g cm^{-3} while the pillars grown at 20 kV (5 and 6) have a density of (2.9 ± 0.7) g cm^{-3}.

EDX of the pillar deposits revealed that the composition of the material grown at 5 kV was $Cu_{0.06}C_{0.7}O_{0.2}F_{0.04}$ and at 20 kV $Cu_{0.1}C_{0.6}O_{0.22}F_{0.08}$. The deposit density ρ_d can be expressed as a linear combination of the copper density $\rho_{Cu} = 8.96$ g cm^{-3} and carbonaceous (C, O, F, H[ii]) matrix density ρ_M.[296] Accordingly, the matrix densities were determined using $\rho_M = (\rho_d - x\rho_{Cu})/(1 - x)$, where x is the atomic copper content fraction. We found $\rho_M = (1.0 \pm 0.3)$ g cm^{-3} in average for the 5 kV pillars and $\rho_M = (2.3 \pm 0.6)$ g cm^{-3} for the 20 kV pillars. These values compare well to previous studies where the carbonaceous matrix density was measured using an *ex situ* cantilever-based mass sensor.[296]

Dissipation in FEB deposited pillars

As described in Sect. 4.2.2 the quality factor Q quantifies the intrinsic dissipation in the vibration structure and the dissipation to the environment.[78] The latter can be neglected in high vacuum conditions and thus, Q describes intrinsic losses including acoustic clamping losses[54,134,232] and surface losses[306,314,315,317].

The quality factors of the fundamental resonance mode of copper containing FEB deposited

---

[ii] EDX is insensitive to hydrogen. From infrared spectroscopy of organic FEB deposits the hydrogen content can be estimated to be about 2-3 times the oxygen content,[26] thus negligibly affecting the matrix density.

pillars were determined from the slope of the phase curve at resonance using Eq. 4.13 in high-vacuum at room temperature. Results from several measurements on the same pillars are presented in Fig. 5.11. The average Q values of the pillars are compiled in Table 5.1. The phase variation at resonance allows to determine unambiguously the quality factor, whereas the amplitude deflection signal gives erroneous values of Q since the SE signal is not linear with deflection amplitude and thus, the FWHM of the peak does not represent the correct value related to dissipation.

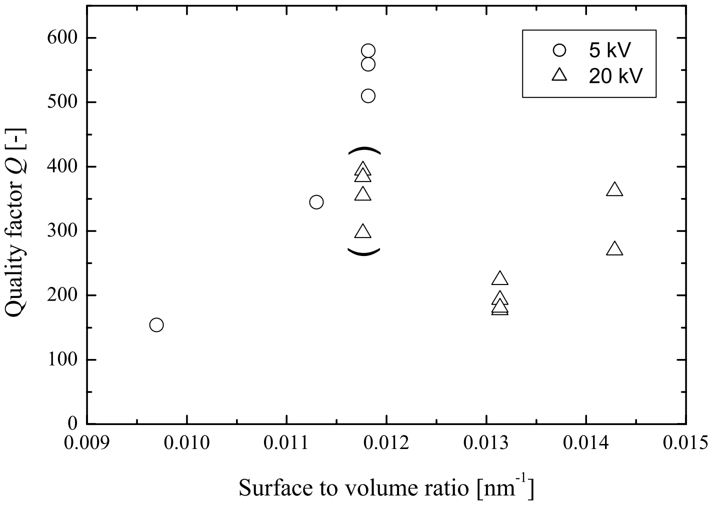

Figure 5.11: *Fundamental resonance mode quality factors Q as a function of the surface to volume ratio of copper containing FEB deposited pillars (Fig. 5.1) in high vacuum (10^{-3} Pa) at room temperature.*

It is known that quality factors strongly depend on the sample volume, the temperature and the clamping of the structure, e.g. single or double clamping. A literature survey shows that published quality factors for micro- and nanomechanical resonators measured at different temperatures in general fall roughly linearly on $Q \simeq 10^6 \sqrt[3]{V}$, where V is the cantilever volume in mm^3.[230] The maximum Q's seem to scale inversely with linear dimension $\sqrt[3]{V}$, i.e. the volume-to-surface ratio, which suggests that surface losses dominate dissipation with shrinking resonator dimensions. Experiments done at room temperature for top-down fabricated double clamped Si cantilevers with surface to volume ratios > 0.01 nm^{-1} similar to our pillars seem to follow the trend. They have, however, Q's which are about one order of magnitude larger than the Q's of our pillars.[37] Due to the large scatter in the measured quality factors shown in Fig. 5.11 and the similar surface to volume ratios of the investigated pillars no specific conclusions can be drawn here. To our knowledge, these are the first investigations on dissipation in FEB deposited pillars.

5.4 Investigation of the bonding strength of W and Co containing FEB deposits

In this section we demonstrate the use of cantilever sensors in the static force mode for *in situ* tensile strength measurements obtained for FEB deposits from $W(CO)_6$ and $Co_2(CO)_8$.

In a tensile test experiment the fracture strain, fracture stress, and Young's modulus are measured. In general, it is preferred over the bending test because the stress distribution is homogeneous throughout the sample. The sample is attached perpendicular to a rigid support and a cantilever force sensor is attached on the free end by FEB/FIB-induced deposition material inside the SEM, as sketched in Fig. 5.12. The sample is then subjected to a tensile stress by either displacing the rigid support or the cantilever. A first approximation of the tensile force F_c necessary to force failure of a perfect, brittle nanostructure in the tensile test experiment can be estimated by

$$F_c \leq \frac{E_s}{10} A, \tag{5.9}$$

where, A denotes the samples cross section and E its Young's modulus. Since E for a nanostructure is not known a priori it is approximated by the known bulk modulus. This can be illustrated for a Si nanowire having a diameter of 100 nm and $E_{\mathrm{Si}(111)} = 188$ GPa, resulting in a critical force of $F_c \simeq 0.1$ mN. For a FEB deposited circular structure with a diameter of 100 nm and an assumed Young's modulus of 20 GPa the critical force is $F_c \simeq 20$ μN.

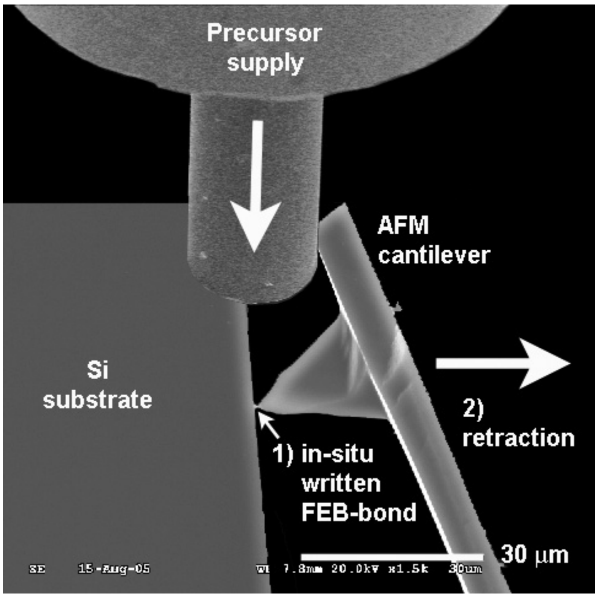

Figure 5.12: *Top-view SEM image of experimental setup with in situ FEB-written bond between AFM cantilever and Si substrate. The precursor supply pointing towards the substrate is not at scale.*

The cantilever's force constant must be tuned to this range in accordance with the Δz increments of the nanopositioning system and the resolution of the deflection measurement.

Let us assume $\Delta z = 100$ nm for such an increment, e.g. for a stick-slip piezo device. After ten incremental steps the maximum error of the actual deflection at failure is reduced to 10%, which gives a total cantilever deflection $\Delta z_{\mathrm{tot}} = 10\Delta z = 1$ μm at failure. The required cantilever force constant k_c follows from the force balance $F_c = k_c \Delta z_{\mathrm{tot}}$; hence, for the Si nanowire $k_c \simeq 100$ N m^{-1} and for the FEB deposit $k_c \simeq 20$ N m^{-1}. If the nanomanipulation system is capable of a better displacement resolution, a stiffer cantilever can be used. This prevents the cantilever from bending too much and therefore helps to minimize offset angle artifacts.[64]

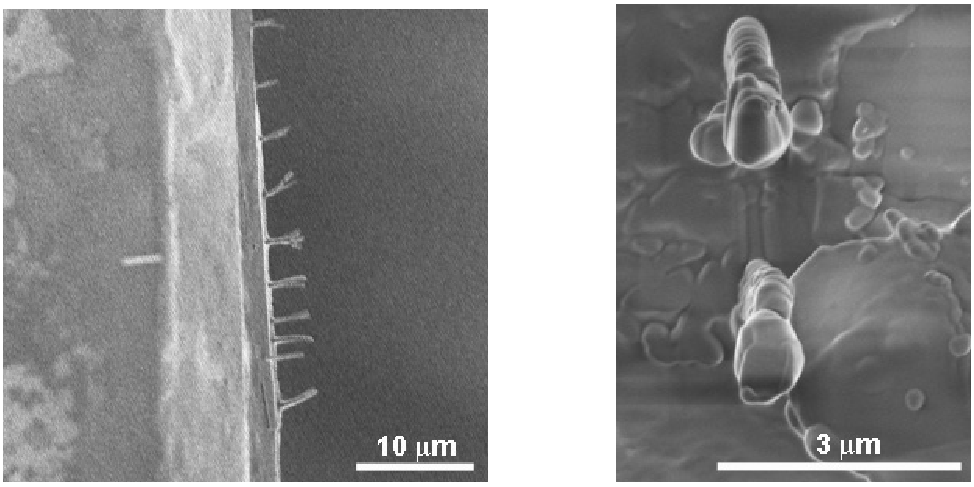

(a) (b)

Figure 5.13: *SEM images of FEB deposited freestanding horizontally grown structures on Si edge. (a) Overview of filaments with FEB incidence as during deposition. (b) Tilt view of separated filaments (two underlying rods).*

Freestanding rods were pre-deposited at the inclined edge of a Si substrate by slow single line scans with the FEB. The scan speed varied from 5 to 40 nm s^{-1}. At low scan speed wall-like structures were obtained which separated into individual freestanding rods with increasing scan speed (Fig. 5.13). This phenomenon further depends on the edge inclination angle, specific nucleation sites, and the penetration depth of high energy electrons (being about 5 μm at 20 kV). For planar substrates a model based on forward scattering of primary electrons is reported.[25]

A tensile strength experiment on an individual freestanding rod is summarized in Fig. 5.14. The cantilever was brought into contact using nanomanipulator stages and then bonded with a thin film FEB deposition (about 100 nm thick) during three minutes at 500 pA probe current and 20 kV. Then a tensile force was generated by retracting the cantilever in 100 nm steps along the rod axis, being equivalent to $k_c \Delta z$, the product of force constant k_c and cantilever deflection Δz. Monitoring the rupture by SEM permitted to read out the cantilever deflection directly and to repeat bonding and tensile tests. Tests were repeated 5 times and yielded reproducible deflection values. For observation of the rupture surface the sample was

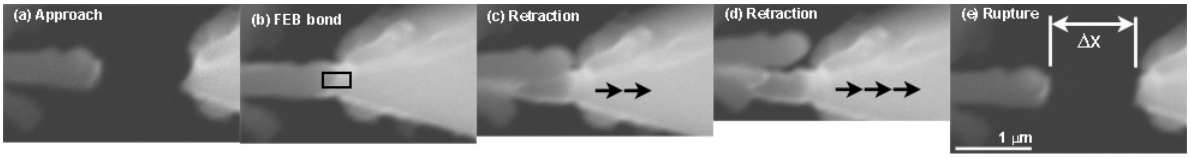

Figure 5.14: *SEM top-view images of tensile strength experiment. (a) The AFM cantilever (right) is approached to a FEB pre-deposited freestanding rod (left). (b) When contact is established, a 100 nm thin FEB bond is written as 200 nm × 400 nm rectangle in TV mode (black rectangle). (c) and (d) Tensile stress is applied to the FEB-bond by retracting the AFM cantilever stepwise to the right. As the cantilever bends a small vertical downward shift is induced and the entire pre-deposited rod structure becomes visible, see also Fig. 5.13 (b). (e) After bond rupture the FEB rod snaps back to its initial position as in (a) and the cantilever resumes its unstrained position. The measured distance Δx is proportional to the rupture force.*

transferred into a high-resolution FEG-SEM as shown in Fig. 5.13 (b). The tensile strength is calculated as $\sigma = k_c \Delta z / A$, A being the rupture surface. Cantilevers with nominal force constants of 45 N m^{-1} (Nanoworld) and 30 N m^{-1} (Nascatec) were used. The experiments revealed tensile strengths of (2 ± 0.5) GPa for $W(CO)_6$ and (1 ± 0.5) GPa for $Co_2(CO)_8$. The error in our measurement mainly evolved from the determination of the rupture areas.

Carbonized nanofibers with 80% sp2 bonds and 20% sp3 bonds were measured to have a tensile strength of 0.64 GPa and show an approximate ratio of tensile strength to elastic modulus $\sigma/E \simeq 0.01$.[329] In amorphous hydrogenated carbon (a-C:H) films the ratio was found to depend strongly on microstructure and reaches values of $\sigma/E \simeq 0.1$ for high sp3 contents ($>$ 70%).[251] The minimum and maximum estimation of the elastic modulus of our deposits from their tensile strengths is thus in the order of 10 GPa and 100 GPa, respectively. These limits compare well with elastic moduli of 30 - 60 GPa of a-C:H FEB film deposits from Paraffin sources[63] and with the results on FEB deposited pillars from $Cu(hfac)_2$ reported in Table 5.1. Together with the small metal content in our deposits these results suggest that mechanical properties are mainly dominated by the carbonaceous matrix.

5.5 Summary

In situ techniques for bending, tensile and vibration tests were used to study the mechanical properties of FEB deposited materials. A positioning setup with nanometer resolution was integrated into a SEM which allowed to manipulate the sample relative to a cantilever-based force sensor. FEB grown pillars were subjected to bending, observing simultaneously the applied force by SEM video image sequences of the calibrated cantilever sensor deflection. Vibrations were induced using mechanical excitation and detected by the varying secondary electron signal through the interaction of the electron beam with the oscillating structure. This approach allowed fast and reliable detection of resonance modes. In combination with the observation by SEM imaging the resonance mode shapes could be identified. Furthermore, top-view imaging of the vibrating structure enabled to conclude on multiple (polarized) resonance modes at frequencies related to each other by elliptical pillar cross-sections and pre-bent pillar shapes. The amplitude *and* phase response at resonance was detected and enabled to unambiguously determine the quality factor from such vibration experiments.

From the combination of bending and vibration tests we deduced Young's moduli and densities of FEB deposited pillars from $Cu(hfac)_2$ at 5 kV and 20 kV acceleration voltage at a probe current of 100 pA. The matrix material seemed to dominate the mechanical properties of the deposits with a Cu content in the order of 10 at.%. While the stiffness remained at a constant level, the density of the pillars tended to increase with increasing FEB voltage. To give a detailed explanation for this, more systematic experiments need to be performed. To increase the accuracy of the bending and vibration tests the deviation from the ideal cylindrical pillar shape can be accounted for using finite element analysis methods.

We presented the first tensile strength measurements of thin FEB-bonds; in particular for bonds obtained from $W(CO)_6$ and $Co_2(CO)_8$.

Although the presented bending and tensile test methods are relatively tedious and time-consuming due to the requirement to establish mechanical contact between the sample and the sensor, they allow to determine directly the Young's modulus and the tensile strength of individual FEB deposits which is not possible by any other method. These measurements are required to validate indirect methods such as the determination of mechanical properties from chemical composition and structural analysis. TEM analysis of the deposits is of interest to correlate the determined mechanical properties to the material morphology, e.g. nanocrystallites and core-shell substructures.

Chapter 6

Precursor supply

This chapter describes investigations of the distribution of impinging precursors supplied via a nozzle-based gas injection system (GIS) to the substrate inside a FEB/FIB nanofabrication system. We successfully compared simulations to experimentally determined local precursor flux. The first part of the chapter (Sects. 6.2 and 6.3) outlines the relevant formalism to describe rarefied precursor gas flow. A case study of precursor flow in GISs indicated that transient and/or molecular flow conditions prevail in the tube nozzle depending on the source pressure. In Sect. 6.4 an implementation of Monte Carlo simulations of three-dimensional precursor flow through tube nozzles is described. Simulation results identified the dependence of transmission probabilities and impinging flux distributions on nozzle parameters and the substrate position in molecular and transient flow conditions (Sects. 6.5 and 6.6). The simulations are validated in Sect. 6.7. A more complex simulation approach yielded improved insight to the flow problem, however, with strongly growing computational cost. For the first time the distribution of precursor flux to the substrate was experimentally analyzed (Sect. 6.8). Deposit thickness topographies produced by thermal decomposition of precursors on the substrate are determined by profilometry or by interference colors. These measurements as well as experimental FEB deposition rates compared well to simulations. In the last part of the chapter (Sect. 6.9) optimization of the local precursor supply by nozzle-based GISs was investigated based on simulations and experiments. The ideal position of the tube nozzle relative to the substrate and the FEB/FIB as well as flux shadowing effects were identified. Alternative nozzle designs are revealed to strongly increase the accessible flux to the FEB/FIB for the same throughput.

6.1 Introduction

The design of a precursor supply into the vacuum chamber of a SEM/SIM processing system aims to provide a controlled local flux to the area of interest at a tolerable pressure load for the vacuum system. Gas phase scattering of the electron beam is minimized by establishing a localized (relative) high-pressure by injecting the gas through a nozzle which is positioned in close proximity to the substrate. In the nozzle gas injection system (GIS) arrangement as outlined in Fig. 6.1 the molecular beam which is reaching the substrate is determined by the final tube nozzle with typical inner diameter in the range of 100 μm - 1 mm. The throughput, Q (in molecules per second), is related to the pressure in the precursor reservoir, P_{vap}, and the duct geometry which bounds the flow.

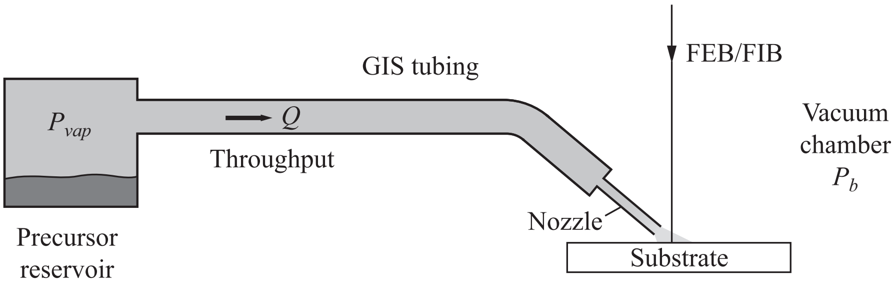

Figure 6.1: *Schematics of a nozzle-based gas injection system (GIS) for FEB/FIB induced processing. The precursor reservoir contains the solid or liquid precursor. Gaseous precursors are supplied through connections to the GIS tubing after considerable pressure reduction.*

6.2 Rarefied gas flow

For the description of gas flow through a GIS nozzle we consider a tube where a large pressure ratio between entrance and exit is preserved and the downstream condition is vacuum. In this flow problem the rarefication (level of dilution) of the gas is a quantity of fundamental importance since it determines the transitions between flow regimes obeying distinct physics. The degree of rarefication can be expressed through the dimensionless Knudsen number Kn: the ratio between the mean free path λ, which is the mean distance traveled by a particle without intermolecular collision, and a characteristic length of the containing region. This length can be some overall dimension of the flow, but a more precise choice is the scale of the gradient of a macroscopic quantity, as for example the pressure $P/\left|\partial P/\partial z\right|$. In a circular tube an obvious choice of Knudsen number is the ratio of the mean free path to the tube diameter:

$$Kn \equiv \lambda/d. \tag{6.1}$$

The Knudsen number distinguishes several flow regimes as illustrated in Fig. 6.2. The different regimes are determined empirically and are therefore only approximate for a particular flow geometry. For an ideal homogeneous gas, modeled as hard (rigid) spheres, at pressure P the average mean free path is:[160]

$$\lambda = \frac{kT}{\sqrt{2}\pi\delta^2 P}, \tag{6.2}$$

where k is the Boltzmann constant, T the temperature, and δ the molecule diameter[i]. In Appendix A the molecule diameter and the mean free path at the vapor pressure of the precursor molecules used in this work are compiled.

---

[i] Molecular size is a quantity that cannot be precisely and uniquely defined and it will be necessary to consider the results from elementary kinetic theory that depend on the molecular “diameter”. The most

As the precursor gas flows down the tube, the pressure and density decrease while the mean free path increases and the Knudsen number correspondingly increases. Conservation of mass requires the flow to accelerate down the constant-area duct, reaching speed of sound (Mach number $Ma = 1$) in the limiting case of choked-flow conditions. For the flow of some precursor gases with relatively high source pressure the slip-flow, transition and molecular regime depicted in Fig. 6.2 may occur in the same duct, and thus, the full description of simple duct flow may in fact manifest a high complexity.

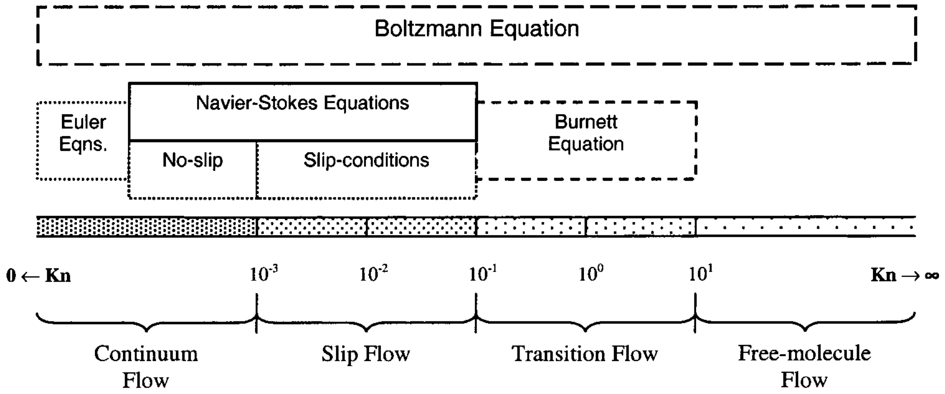

Figure 6.2: *Generally accepted Knudsen regimes and the corresponding mathematical framework.*[253] *The molecular, or free molecular flow can be described by a number of rigorously derived analytical formulations.*[160,269]

6.3 Throughput

The throughput Q in terms of flow conductance C (in volume per second) follows the relation

$$Q = C(P_u - P_d)/(kT), \tag{6.3}$$

where $P_u - P_d$ is the pressure decay between the upstream and downstream pressure of the bounded flow system. The throughput is constant along the entire duct and it is related to the flux according to $J = Q/A$, where A is the tube cross-section. In the case of a flow across a large pressure ratio between the inlet and outlet the throughput is solely controlled by the upstream pressure $Q \simeq CP_u/(kT)$ and is independent on the downstream pressure, i.e. corresponding to choking of the flow. These conditions are typically realized in precursor gas flow through a tube supplied to a vacuum chamber. The downstream pressure P_d is depending on the pumping speed S in the vacuum system. Equation 6.3 can be used to determine the pressure decay within the precursor supply tubing based on measurable quantities: the geometry which

---

important methods are based on experimental measurements of the gas viscosity ν or from the density ρ of the solid or liquid.[160] An alternative way to estimate the molecule size is by a structure analysis based on the covalent (bond lengths) and van der Waals atomic radii.

determines the conductance and the net flux effusing into vacuum. However, the evaluation of the conductance of tubing components requires the knowledge of the prevailing flow regime.

The conductance is conveniently expressed in terms of the transmission probability W of a molecule entering the tube as

$$C = W \underbrace{A\sqrt{RT/(2\pi M)}}_{C_a}, \tag{6.4}$$

where C_a is the conductance of the entrance aperture with area A.

Several tubing components can be regarded as circuit elements connected in series and accordingly their conductances add up as $1/C_{\text{tot}} = 1/C_1 + 1/C_2 + \cdots + 1/C_N$. This expression is valid only if the flow in one component is not affected by the previous or succeeding component, i.e. when a large volume between two successive components establishes vanishing ordered molecular motion. If this condition is not fulfilled, a correction term can be introduced according to Haefer[113] which accounts for the reduced entrance conductance at the crossover to an increased cross-section.

6.3.1 Molecular flow regime

Molecular or free-molecular flow is the limiting case where the flow is controlled solely by wall collisions. In practical situations a flow preserving $Kn \gtrsim 1\ldots10$ can be considered molecular and modeled without taking into account intermolecular collisions is valid, which strongly reduces complexity. The molecules which are transmitted through a tube, with length L, will be made up of a fraction which passes directly through the tube without striking the tube inside-surface and those suffering wall collisions emitted from each element of the inside surface. The total flux J_m through the tube may therefore be written

$$J_m = J_d + \int_0^L J_e(x) P_e(x) \mathrm{d}x, \tag{6.5}$$

where J_d is the direct number flux, $P_e(x)$ is the probability that a molecule reflected from the tube element of length dx at x leaves the tube without striking the tube inside-surface and $J_e(x)$ is the total number flux emitted from this element. The functions J_d and $P_e(x)$ may be found for the cylindrical geometry by straightforward analysis. The solution for J_m can be found by numerical methods assuming that $J_e(x)$ is a linear function of x.[18] This problem was first solved by Clausing.[48]

For circular tubes with radius r of any length a formulation of the transmission probability in molecular flow conditions was derived phenomenologically by Santeler,[261]

$$W_m = \frac{1}{1 + \frac{3}{8}\frac{L_e}{r}}, \tag{6.6}$$

where $L_e = L/\left(3 + 3L/7r\right)$. For long tubes Eq. 6.6 reduces to $W_m = 8r/(3L)$, which is in agreement to other models.[160] In Sect. 6.4.1, Table 6.1, the results from a flow simulation are compared to the values predicted by Eq. 6.6 and agreement within $\sim 1\%$ is found.

6.3.2 Transient flow regime

The conditions where boundary collisions and intermolecular collisions are important ($1 \ldots 10 > Kn > 0.1$) are generally referred to as the transition (transient) flow regime which is referred to as the near-free molecular regime. In these conditions, the gas flow dynamics are intermediate between molecular flow and viscous flow. The transient flux can be described qualitatively by two counteractive effects:[234] on the one hand the transmission probability is reduced by the disruption of molecules having a near axial velocity component by intermolecular collisions and on the other hand the transmission probability is increased by the development of continuum flow properties, known as the inset of a drift velocity. With increasing pressure and thus, decreasing Knudsen number, transient flux conditions may reveal a flux minimum below the molecular level before the transition to the higher continuum fluxes. For short tubes, when l is comparable to d, the two effects may counterbalance each other, and a minimum in conductance would then not be observed, as was confirmed experimentally.[177,178]

Several attempts to empirically model the transmission probability over the extended pressure range covering molecular and transition flow are found in the literature. Knudsen[144] deduced a formula for the transmission probability of long circular tubes in transient flow conditions from a series of measurements which can be written in the form given by Dushman:[75]

$$W_{tr} = 8r/3L \left(0.0736/\bar{Kn} + \frac{1 + 1.254/\bar{Kn}}{1 + 1.548/\bar{Kn}} \right), \tag{6.7}$$

where $\bar{Kn}$ corresponds to the Knudsen number at the average pressure $\bar{P}$ in the tube. At low and high pressures the corresponding result takes values of molecular and viscous transmission probability, respectively. Equation 6.7 was found to predict W_{tr} within 5% over the entire transition range for the flow of air in copper tubes.[75]

According to Eq. 6.7, as the tube length goes to zero the transmission probability becomes infinite which indicates the limit of validity for long tubes. It is difficult to formulate a long tube criteria which specifies the range of validity of Eq. 6.7, due to the lack of experimental data. The issue is discussed in the literature, but no general statement can be given.[160] The tube nozzles used in this work have $l/d = 6 \ldots 30$. Within this range the tubes need to be considered as short tubes and thus, Eq. 6.7 will overestimate the transmission probability.

In choked tube-flow, the flow reaches speed of sound at the tube exit. Choking is established if the pressure ratio of the upstream and downstream pressure fulfills the condition:[160]

$$\frac{P_u}{P_d} > \sqrt{\frac{\gamma + 1}{2}}^{\gamma/(\gamma-1)}, \tag{6.8}$$

where γ is the ratio of the specific heats at constant pressure and volume, which takes typically a value of 1.1 for polyatomic molecules and accordingly, for these molecules an absolute pressure difference across the tube of > 1.7 is sufficient for choking. A description of the transmission probability in choked tube-flow conditions W_c covering the molecular and transient regime weighs the molecular and viscous transmission probability W_m (Eq. 6.6) and W_v according to[160]

$$W_c = \theta W_m + (1-\theta) W_v, \tag{6.9}$$

where $\theta = k_s Kn/(k_s Kn + 1)$ with $k_s = 13.6$ being a fitting parameter related to boundary conditions of a short tube. The laminar viscous transmission probability in choked flow conditions can be found in terms of the ratio of the upstream pressure P_u and the pressure P_{Ma} at Mach number $Ma = 1$ according to $W_v = \sqrt{\pi\gamma(\gamma+1)}\,(P_u/P_{Ma})^{-1}$. The pressure ratio P_u/P_{Ma} can further be expressed in terms of the Mach number at the tube entrance.[175]

There appear to be several approaches to model transitional flow, i.e. throughput, through tubes with arbitrary length based on simple combinations of molecular and viscous models.[160,175] The lack of a well established and generally recognized model covering the whole pressure regime, however, is probably due to the dearth of experimental work in these conditions.

6.3.3 Example: Precursor flux inside a GIS

For solid and liquid precursors a lower bound of the Knudsen number within the GIS (Fig. 6.1) can be determined by $Kn = \lambda_{P_\mathrm{vap}}/d$, where λ_{P_vap} is the mean free path at the vapor pressure and d the diameter of the tubing which supplies gas to the nozzle. For the pressure range of precursors typically used in FEB/FIB induced processing (see Appendix A.1) this regime includes slip- to transient flow. Figure 6.3 exemplifies the Knudsen number at λ_{P_vap} for the precursors, $\mathrm{Cu(hfac)_2}$, $\mathrm{[(PF_3)_2RhCl]_2}$, (hfac)CuVTMS, $\mathrm{Co_2(CO)_8}$, and $\mathrm{CH_2{=}CHCOOH}$ (Acrylic acid) in terms of the characteristic dimension, i.e. the tube diameter. The pressure decay along the tube corresponds to a vertical displacement to higher Knudsen numbers in this plot. In the vacuum chamber of the SEM, where background pressures are typically in the order of $P_b = 10^{-3}$ Pa the mean free path of all five precursors is in the order of 1 m and intermolecular collisions are very rare.

GIS tubing

In the following, a straight tube of length 50 mm with a constant cross-section of diameter 2.7 mm is considered which corresponds reasonably well to the employed GIS tubing components in this work (Sect. 3.1.2) connecting the precursor reservoir with the final beam shaping tube nozzle. For the precursors $\mathrm{Cu(hfac)_2}$ and $\mathrm{Co_2(CO)_8}$ the minimal Knudsen number in this tube is $Kn = \lambda_{P_\mathrm{vap}}/d = 1.76$ and 0.053, respectively. Assuming these conditions along the whole tube, it is found from Eqs. 6.3, 6.4, and 6.7 that for $\mathrm{Cu(hfac)_2}$ the conductance $C_{\mathrm{Cu(hfac)_2}} = 1.1 \times 10^{-5}$ m^3 s^{-1} of this GIS tubing maintains a pressure decay $\Delta P_{\mathrm{Cu(hfac)_2}} = 3.7 \times 10^{-16}$Q. For $\mathrm{Co_2(CO)_8}$ we analogously find $C_{\mathrm{Co_2(CO)_8}} = 3.2 \times 10^{-5}$ m^3 s^{-1} and $\Delta P_{\mathrm{Co_2(CO)_8}} = 1.3 \times 10^{-16}$Q. These values translate in a relative pressure decay $\Delta P/P_\mathrm{vap}$ of 9.3% and 3.0% for typical throughputs $Q_{\mathrm{Cu(hfac)_2}} = 1 \times 10^{14}$ s^{-1} and $Q_{\mathrm{Co_2(CO)_8}} = 3 \times 10^{15}$ s^{-1}, experimentally determined from the precursor mass loss rate in our GIS (Eq. 3.3). This calculation estimates the pressure decay based on two approximations: i) Eq. 6.7 is not valid for the considered "short" tube with aspect ratio $L/d = 18.5$. According to Eq. 6.6 the difference in conductance is $\sim 10\%$ comparing a long and the actual tube in molecular conditions which indicates the order of mangitude of the error. ii) For the evaluation of Eq. 6.7, Kn is assumed

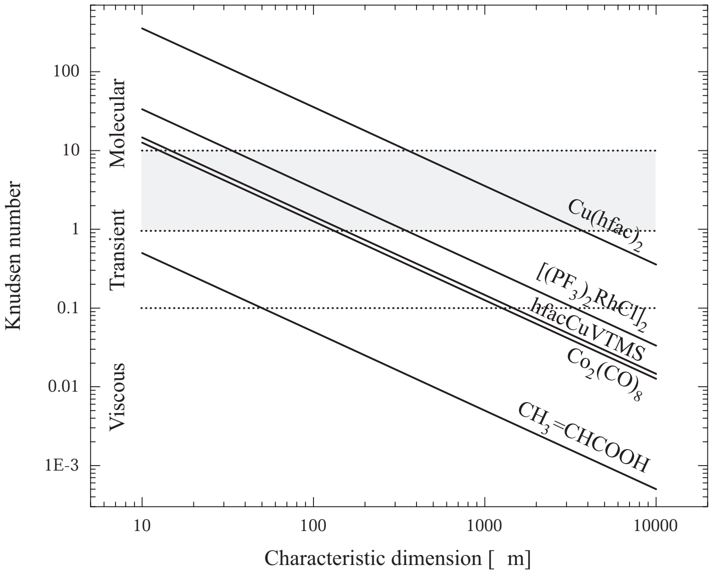

Figure 6.3: *Illustration of the predominant Knudsen regimes for the precursors Cu(hfac)$_2$, [(PF$_3$)$_2$RhCl]$_2$, (hfac)CuVTMS, Co$_2$(CO)$_8$, and CH$_2$=CHCOOH (Acrylic acid) at their vapor pressure in terms of the characteristic dimension, e.g. the tube diameter, in the flow. The indicated transitions at* $Kn = 0.1$ *and 1…10 indicate the flow regime borders.*

to be preserved in the whole tube, neglecting the pressure decay which is a priori unknown. The recalculation of $\Delta P/P_{\text{vap}}$ taking into account the previously found pressure decays results in an error of <1% and <2% for Cu(hfac)$_2$ and Co$_2$(CO)$_8$, respectively. Imposing the limiting case of molecular conditions the pressure decay is obtained without approximations using Eq. 6.6 instead of Eq. 6.7 resulting in 4% lower value of $\Delta P/P_{\text{vap}}$ for Cu(hfac)$_2$ and thus, transient effects are not dominating. The same calculation for Co$_2$(CO)$_8$ yields that the molecular pressure decay is 60% larger than the value given by Eq. 6.7. The Co$_2$(CO)$_8$ flow in this GIS tubing component is thus governed by transient conditions. These observations are expected from Fig. 6.3.

From the above presented estimations of pressure decay within the GIS tubing it is concluded that the conductance of a tubing component of 50 mm length and 2.7 mm diameter can maintain $\gtrsim$ 90% the vapor pressure of typical precursors up to the entrance of the final tube nozzle.

Tube nozzle

According to Eq. 6.8, in the case of vacuum $P \leq 10^{-1}$ Pa on the downstream side and a pressure P_e at the entrance of the tube nozzle close to P_{vap} the flow is always choked. These boundary conditions are present across the final tube in the GIS and thus, the transmission probability in the pressure regime from molecular to continuum (viscous laminar) flow can be found from Eq. 6.9. The Mach number at the entrance of a tube with 6 mm length and 400 μm diameter in choked flow conditions was $\sim$ 0.04 for Co$_2$(CO)$_8$, evaluated from a numerical simulation of the flow (Sect. 6.4.2). These simulations further revealed that in choked flow conditions the entrance Mach number is relatively insensitive to the gas species and the pressure and is mainly determined by the tube geometry. Knowing the entrance Mach number for a given GIS tube geometry allows, thus, to estimate the transmission probability based on Eq. 6.9 in a wide pressure regime for any precursor. Using Eq. 6.9, we found a flow conductance for the considered tube of $C_{\mathrm{Cu(hfac)_2}} = 2.7 \times 10^{-7}$ m^3 s^{-1} and $C_{\mathrm{Co_2(CO)_8}} = 3.4 \times 10^{-7}$ m^3 s^{-1}. In comparison, Eq. 6.7 overestimates the conductance at $\bar{Kn} = \lambda_{0.5P_{\mathrm{vap}}}/d$ by roughly 10% in both cases. The conductance of the tube nozzle is two orders of magnitude smaller than of the tubing component discussed above which cleary indicates that the nozzle is the flux-limiting element in the GIS.

6.4 Probabilistic simulation methods

To describe the flow of rarefied gases leads to the necessity to take into account that the gas is a discrete system composed of individual molecules, being in constant, random motion. The flow of gas is a superimposed ordered motion of molecules. However, at the molecular level, there is no distinction between the random and ordered motion. Probabilistic Monte Carlo simulations are the framework which allow to mathematically model molecular and transient flows.

Within this work two probabilistic simulation methods will be presented in Sect. 6.4.1 and Sect. 6.4.2.

6.4.1 Test-Particle Monte Carlo method

The simulation of molecular and to some extend of transient flow through arbitrary shaped tubing components is ideally suited for a probabilistic simulation called test-particle Monte Carlo (TPMC) method which was first introduced by Davis.[58] A large number of serially generated molecule trajectories are computed which collectively predict the flow problem, i.e. the flow-field describing the macroscopic flow properties in the tube, e.g. number density, angular distributions, flux on a surface inserted into the flow, e.g. spatial flux distributions. The essential limitation of TPMC is that the molecule trajectories are inherently independent of one another. Several authors have proposed and implemented elaborated versions including iterative and grid mapping procedures to evaluate transient flow properties.[97,120] In this work we included intermolecular collisions by imposing a pressure and corresponding mean free path distribution inside and outside the tube.

To evaluate some fundamental aspects in the formation of molecular beams we will concentrate on the simple tube geometry, however, the major advantage of the Monte Carlo approach over a more analytical approach is the ease with which it is able to deal with more complex flow geometries.

A three-dimensional TPMC simulation code[ii] was implemented assuming that molecules enter uniformly over the entrance surface of a circular tube with constant cross-section. A flow

---

[ii] The TPMC program is written in C++ embedded in a graphical user interface developed in the GUI design environment provided with MATLAB™.

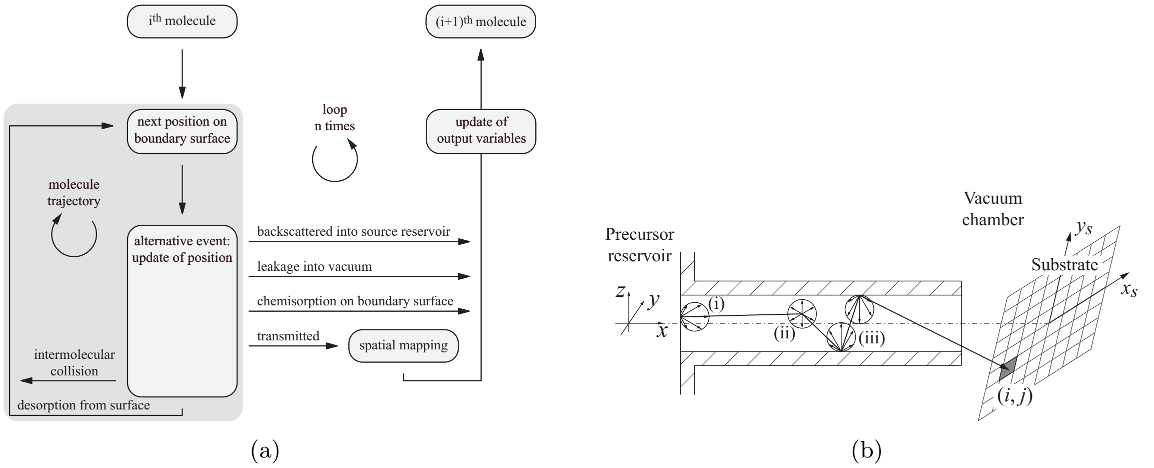

(a) (b)

Figure 6.4: *(a) Flow chart of implemented TPMC simulation of a molecule trajectory inside an arbitrary shaped tubing component. (b) The molecule trajectories through the tube are governed by the following stochastic processes: (i) Cosine point-source at tube entry. (ii) Uniform intermolecular scattering (hard sphere scattering) after having traveled a distance determined by the mean free path* s_λ*. (iii) Diffuse (cosine) tube wall desorption. The substrate is subdivided into a pixel grid denoted by* (i, j)*.*

chart of the procedure to compute a single molecule trajectory and a corresponding schematic drawing is outlined in Fig. 6.4. The trajectory is finished when the molecule escapes from the tube either through the entrance surface into the source reservoir (backscattered), through the exit surface (transmitted) or through an alternative leak into vacuum. No intermolecular collisions are considered outside the tube which is equivalent to molecular conditions in the vacuum chamber. Transmitted molecules are spatially mapped on the substrate surface. The scattering of molecules at the substrate surface and consecutive trajectories inside the vacuum chamber are not taken into account. Individual entrance points were considered to be point-sources producing a cosine angular velocity distribution (Eq. 6.17).[125] The trajectory of the molecule is then generated based on deterministic molecule displacements and stochastic formalisms (Appendix B) to evaluate the angular velocity distribution upon collision with the boundary surface with consecutive desorption and upon an intermolecular collision.

Surface scattering

One of the fundamental assumptions in our TPMC simulations as well as in the theoretical derivations of flow conductance (in the molecular and transition regime) is the diffusive or random scattering (desorption) of molecules from a surface after negligible diffusion on the surface. Diffuse surface scattering has the physical meaning that the desorption direction of the molecule is independent of the direction of incidence and the differential angular velocity probability is described by the cosine law written in terms of the polar and azimuthal angles $(\theta,\ \phi)$ according to[110]

$$\mathrm{d}p_{\cos} = \frac{1}{\pi} \cos\theta \sin\theta \; \mathrm{d}\theta \mathrm{d}\phi. \tag{6.10}$$

The stochastic generation of the angular probability obeying the cosine law is given in Appendix B.

Although the individual processes that result in molecules leaving a surface do not necessarily produce such a velocity distribution, for equilibrium conditions, the overall distribution of molecular flux will obey in most cases the cosine law, e.g. for microscopically rough surfaces the diffuse scattering law is in many cases an adequate description which is well established theoretically and experimentally (for comment and references see the textbook by Lafferty[160]). Thomson and Owens pointed out that a combination of diffuse and specular reflection of the gas from the tube surface in some conditions matches better the experimental results.[283]

Surface uptake

Chemisorption of molecules to the tube boundary surface can be included through an uptake coefficient defined as the probability of removing a molecule from the flow per surface collision. A study based on Monte Carlo simulations of this issue was reported in the literature.[277] The practical importance of chemisorption and decomposition for some precursors inside the GIS was outlined for the gas flow of $Fe(CO)_5$.[124]

Intermolecular collision model

Within the TPMC implementation in this work, molecules are modeled as hard elastic spheres (HS) of diameter δ with a collision cross-section evaluating to $\sigma = \delta^2\pi$. As illustrated in Fig. 6.5, the scatter angle upon an intermolecular HS collision is $\chi = \arccos(b/\delta)$. This results in an angular velocity distribution which is isotropic in all directions seen from the center of mass. The stochastic generation of the isotropic angular distribution is given in Appendix B. Accordingly, the velocity direction after an intermolecular collision is independent on the initial direction of the molecule. It is further noted that colliding molecules depart toward the tube exit or the entrance with a 1:1 probability.

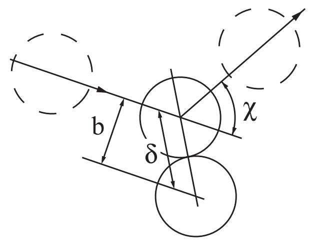

Figure 6.5: *Hard sphere (HS) molecular collision.*

The implementation of the HS model in the TPMC simulation is a non-realistic approach due to the over-simplified model description using a constant cross-section which is independent on the local flow properties. It is, however, valuable to gain insight to the considered flow problem. In view of the random orientation and the large number of collisions that occur it is reasonable to assume a spherically symmetric geometry even for polyatomic molecules. In the literature the modeling of more realistic collision cross-sections is well documented.[18] A useful, though simple approach, referred to as variable hard sphere (VHS) model, takes into account that collision cross-sections are a function of the relative speed between the molecules and thus of the local temperature in the flow. It accounts for a temperature depending "diameter" but uses the deflection angle given by the hard sphere model which is a good approximation.[18] The VHS model will be used in the simulations presented in Sect. 6.4.2.

TPMC implementation

Pressure distribution In the TPMC simulation the molecular path s since the last intermolecular collision is stored, continuously updated and compared to the free path s_λ sampled according to

$$s_\lambda = \lambda \ln Rn^{-1}, \tag{6.11}$$

with the random number Rn being uniformly distributed between 0 and 1. Equation 6.11 describes the free paths at the molecular level.[160] It reproduces a logarithmic distribution with average, λ, defined by Eq. 6.2. If, during a molecular trajectory, the condition $s \geq s_\lambda$ is fulfilled, an intermolecular collision occurs at the location given by s_λ and subsequently sampling of a new value is performed using Eq. 6.11. For simulations in molecular flow conditions $\lambda = \infty$ and this conditional decision is omitted.

The model presented in Fig. 6.6 (a) accounts for the pressure decay along the tube. The decay is implemented by introducing a pressure dependent free path, $s_\lambda(x) \sim \lambda(x)$, which is initialized and adapted according to the pressure distribution $P(x)$ in the tube. From experimental measurements in molecular and transient conditions[159] it is concluded that the decay between the pressure at the tube entrance P_e and at the exit P_x can be linearly modeled in a first approach. This assumption is correct in molecular conditions.[48] At the vacuum side of the tube the molecular flow expands into the chamber and the pressure drops suddenly. In the vicinity of the tube exit we roughly estimate the pressure from its dynamic component, $P_J = J\,(2\pi mkT)^{1/2}$, which arises from the flow J normally transmitting the exit surface plane. Determining P_x from the experimentally measured total flux leaving the tube indicates that the pressure decay between the entrance and exit of the tube is in the order of 80-90%. From simulations shown later in Fig. 6.11 it is seen that P_J overestimates P_x and pressure decays are larger, typically in the order of 95%. We conclude that it is difficult to correctly determine P_x, however, its influence on TPMC simulated flux distributions within the given range of estimation is seen to be small.

In terms of the computational implementation, the adaption of $s_\lambda(x)$ is continuously performed for the forthcoming trajectory piece after a wall or intermolecular collision by an appropriate reduction or extension of $s_\lambda(x)$ depending on the mean pressure in the corresponding tube section. The next intermolecular collision is then evaluate by the condition $s \geq s_\lambda(x)$. This implementation is efficient in the sense of computational cost but only approximately simulates the imposed pressure distribution.

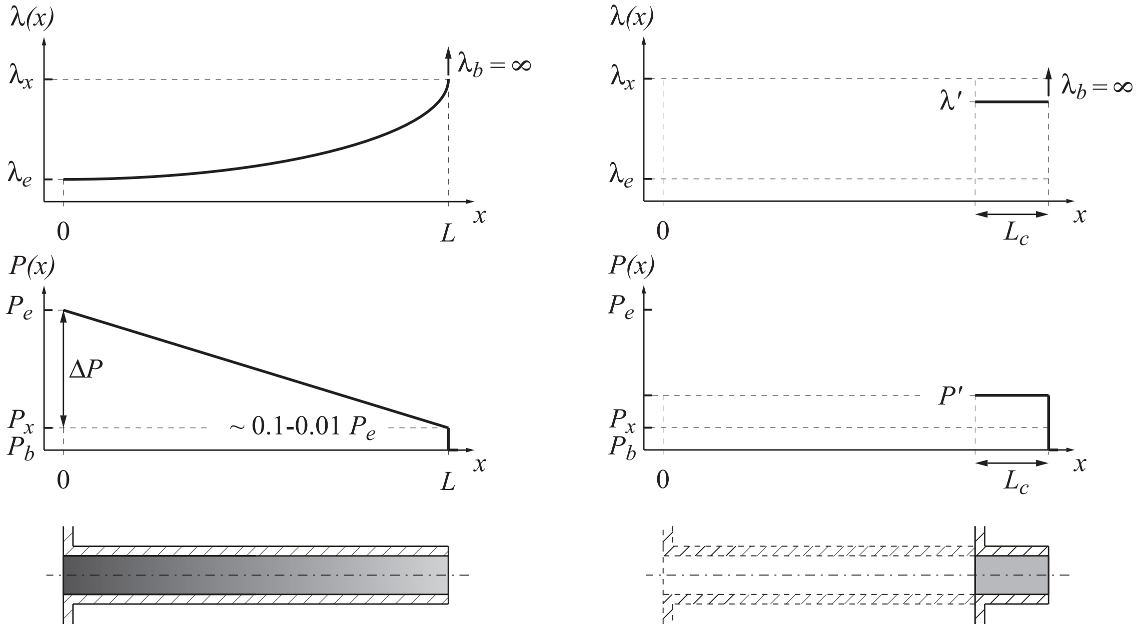

(a) (b)

Figure 6.6: *Pressure models employed for transient TPMC simulations. (a) Pressure decay along the tube. (b) Uniform pressure P' and mean free path λ' in the tube with critical length L_c. P_e and λ_e are the pressure and mean free path at the tube entrance. P_x and λ_x are the pressure and mean free path at the tube entrance. The pressure P_b indicates the vacuum level in the chamber background, where in our TPMC simulations the mean free path λ_b is assumed to be infinitely long (no intermolecular collisions).*

At strongly transient conditions, model Fig. 6.6 (a) is no longer valid. Instead, we use the model in Fig. 6.6 (b) which relies on the estimation of the pressure P' and the mean free path λ' in the last tube section with a critical length $3 - 5\lambda$ (Sect. 6.6.3). The value of P' will be seen as a fitting parameter of the model which can be determined from experiments for the actual flow through the GIS nozzle.

Due to the strong simplifications, e.g. by omitting radial pressure variations, formation of surface boundary layers, and the crude adaption of $s_\lambda(x)$, this TPMC implementation is only a rough reproduction of the pressure distributions within the tube at transient conditions. Although the transmission coefficients are not correctly predicted, the model predicts reasonably well the distribution of impinging molecules on the substrate. This is due to the dominant role of the ratio and the spatial distributions of wall and intermolecular collisions directly before the molecules impinge on the substrate which govern in first order the flux in the downstream of the tube nozzle. The main achievements of the simulations is to reproduce this behavior which resulted in a correct prediction of the impinging rate on the substrate as will be shown in Sect. 6.8. We found from the simulation results that in practical situations the simple model in Fig. 6.6 (b) can also replace the model in Fig. 6.6 (a) in molecular conditions.

Data mapping The value attributed to a pixel (i, j) on the mapping grid, i.e. a grid which subdivides the substrate plane, at a location (x_s, y_s) is incremented upon a "successful" event, i.e. upon an impinging molecule on the substrate (Fig. 6.4 (b)). After a simulation run of n molecule trajectories, the probability map $p_{i,j} = n_{i,j}/n$ is evaluated, where $n_{i,j}$ are the counts of molecules impinging on the pixel i, j. It follows that the local flux in terms of the total flux J_{tot} leaving the tube is

$$J(i, j) = p_{i,j} J_{\mathrm{tot}} \frac{A}{A_{i,j}}, \tag{6.12}$$

where A and $A_{i,j}$ are the cross-section of the tube and the mapped pixel area, respectively.

In an analogous way, this concept is applied for other distributions using an appropriate mapping grid, e.g. of the spatial distribution to the inner tube wall and of the spatial distribution and angular velocity probability of molecules transmitting the exit surface.

Statistical error analysis

To evaluate the reliability and sensitivity of probabilistic simulations it is essential to observe the inherent statistical scatter which is expected in the results.[252] A key feature for the quality of results from such simulations are the characteristics of the employed random number generator. For the Monte Carlo simulations implemented in this work we used the Ecuyer random number generator which has a sequence period of about 2×10^{18}.[236]

The numerical output data generated in Monte Carlo simulations is a random variable X whose expected value is the quantity of interest, e.g. the probability of molecules to impinge on a mapped pixel. For a grid data point (i, j), X either takes the value 0 or 1 which is known as Bernoulli random variable. Several independent simulation runs of n molecule trajectories in the TPMC method, provide n realizations of the random variable all of which are identically distributed and yield in average an estimation, or approximation, of both the mean

$$\bar{X} = \sum_{i=1}^{n} \frac{X_i}{n}, \tag{6.13}$$

and its uncertainty, the standard error,

$$\sigma_{\bar{X}} = \frac{1}{n} \sqrt{\sum_{i=1}^{n} \left(X_i - \bar{X} \right)^2} = \frac{1}{n} \sqrt{\sum_{i=1}^{n} X_i^2 - n\bar{X}^2}, \tag{6.14}$$

which is the standard deviation of the error between simulated and true values. It follows that $\bar{X}$ is a good estimator of the quantity of interest if $\sigma_{\bar{X}}$ is small. From Eq. 6.14 the relative mean error of $p_{i,j}$ is estimated by

$$\frac{\sigma_{\bar{X}}}{p_{i,j}} = \frac{1}{\sqrt{n}} \sqrt{1/p_{i,j} - 1}. \tag{6.15}$$

As an example, if a simulation run revealed that 10% ($p_{i,j} = 0.1$) of $n = 10^6$ calculated molecule trajectories impinge on the grid pixel (i, j) the corresponding local flux value is accurate within a mean error of ±0.3%. The relative mean error of the local flux $J_{i,j}$ translates into $\pm(\sigma_{\bar{X}}/p_{i,j})J_{\text{tot}}(S_{\text{tube}}/S_{i,j})$, using Eq. 6.12. According to Eq. 6.15, the accuracy of output data values in the TPMC simulations increases with $\sqrt{n}$.

A more comprehensible description of the uncertainty of the estimated result is achieved by specifying an interval for which we have a certain degree of confidence that the true value lies within. To do this the distribution of the estimator $\bar{X}$ must be known. From the central limit theorem it follows that the sum of a large number n of independent random variables has approximately a normal distribution. For Bernoulli random variables the "$100(1-\alpha)$ percent confidence interval estimate" of $p_{i,j}$ is

$$p_{i,j} \pm z_{\alpha/2}\sigma_{\bar{X}}, \tag{6.16}$$

where $z_{\alpha/2}$ is obtained from the tabulated standard normal distribution. In the above example with $n = 10^6$ and $p_{i,j} = 0.1$, the scatter was specified as one mean error ($z_{\alpha/2} = 1$) which corresponds to $\alpha = 32\%$ and to a $100(1-0.32) = 68\%$ confidence interval. It is asserted that over the long run the interval $0.1 \pm 0.3\%$ will contain 68% of the simulated values $p_{i,j}$ from other simulation runs (each with $n = 10^6$). This applies of course only if the random number sequence used for the TPMC simulation is different for each run. It is noted that increasing the requested accuracy by choosing $\alpha = 5\%$ results in a 95% confidence interval $p_{i,j} \pm 1.96\sigma_{\bar{X}} = 0.1 \pm 0.6\%$.

6.4.2 Direct Simulation Monte Carlo method

The direct simulation Monte Carlo (DSMC) method relies on a probabilistic model similar to TPMC. The major difference is that the trajectories of a very large number of simulated molecules is followed simultaneously. This approach allows to simulate flows of rarefied gases from the molecular far into the transition regime. However, DSMC simulations cannot be extended to dense gases due to the requirements of molecular chaos and of a diluted gas. A detailed exposition of the method is available in a textbook written by Bird, the pioneer of DSMC.[18]

The essential approximation in the DSMC method is the uncoupling of the molecular motion and the intermolecular collisions over a small time interval or "step". A number of representative molecules are displaced (including the computation of the resulting boundary interactions) over the distances appropriate to this time step, followed by the calculation of a representative set of intermolecular collisions that are appropriate to this interval. The time step should be small in comparison with the mean collision time and, as long as this condition is met, the results are independent of this actual value. The initially imposed flow-field develops with time and after a sufficiently large number of simulation steps steady-state conditions are reached if the flow is stationary.

DSMC implementation

All the DSMC simulations in this work were done using the freely available DS2V program (Version 3.8, October 2006 and Version 4.5, August 2007) developed by Bird[iii]. This implementation of the DSMC method allows the simulation of two-dimensional and axially symmetric

---

[iii] Direct Simulation Monte Carlo Method Visual Programs at GAB Consulting, `gab.com.au`, 2007

flows. The computational parameters are generated automatically by the program, which minimizes the danger of poor calculations being made as a consequence of a poor data set.[16]

The DSMC simulation approach is currently the most reliable way to compute molecular flow in transient conditions more generally applicable than any analytical method.[98] Extensions to include more realistic surface scattering and molecular collision models are established and implemented in the DS2V program but were not exploited in this thesis. The computational cost and the complexity to set up a simulation rises strongly for the extensions to three-dimensions. It is always at least an order of magnitude less effort to calculate a two-dimensional or axially symmetric flow rather than a three-dimensional flow.[17]

6.5 Simulation of transmission probabilities

Table 6.1 shows molecular TPMC results verified against published simulated transmission probabilities W_m in the literature. Complete agreement was found taking into account the scatter of one mean error in our simulations. In Table 6.1 a comparison to the approximative formulation by Santeler (Eq. 6.6) is made which reveals that these values maximally deviate about 1% from TPMC values.

Table 6.1: *Transmission probabilities through circular tubes. Δ indicates the deviation in W_m from Eq. 6.6 and TPMC (100% diffuse desorption). W'_m are TPMC simulations assuming 90% diffuse desorption and 10% specular reflection. All TPMC simulations were performed for $n = 10^6$ transmitted molecules. The given scatter is one standard error, estimated using Eq. 6.15.*

l/d	W_m (diffuse)			Δ	W'_m
	TPMC	Moore[198]	Eq. 6.6		(10% specular)
0.1	$0.90949 \pm 0.030\%$		0.90966	-0.019%	$0.91761 \pm 0.029\%$
1	$0.51415 \pm 0.069\%$	0.51423	0.51428	-0.025%	$0.54773 \pm 0.067\%$
2	$0.35637 \pm 0.080\%$	0.35657	0.35270	1.040%	$0.39022 \pm 0.078\%$
5	$0.19089 \pm 0.089\%$	0.19095	0.18994	0.501%	$0.21701 \pm 0.088\%$
10	$0.10928 \pm 0.094\%$		0.10931	-0.024%	$0.12745 \pm 0.093\%$
20	$0.059467 \pm 0.096\%$		0.05972	-0.423%	$0.07046 \pm 0.096\%$

As mentioned previously depending on the tube surface it is speculated that surface scattering mechanisms result in a mixture of diffuse desorption and specular reflection (angle of incidence equals angle of reflection). Transmission probabilities in molecular flow conditions including 10% specular reflection from tube walls were simulated using TPMC (see Table 6.1). For all tube aspect ratios the transmission probabilities including specular reflections are higher than simulated with pure diffusive desorption. This trend increases for long tubes and saturates at a value of W_m (10% specular)$\simeq$ 120%W_m (diffuse). Besides a change in transmission probability depending on the fraction of specular reflections we expect also the spatial substrate-flux distribution (Sect. 6.6) to be affected. However, the determined experimental flux distributions in Sect. 6.8 matched to simulations with pure diffusive desorption with sufficient agreement for our purposes.

6.6 Simulation of impinging flux distributions

The issue of the locally impinging precursor flux on the substrate supplied by a tube nozzle (Fig. 6.7) has only marginally been addressed in the literature on FEB/FIB induced processing. The simulation of the spatial flux distribution onto the substrate, $J(x, y)$ are envisaged in this work to provide both, the absolute local flux which determines the process regime (Chapter 7) and the spatial flux uniformity within the processing field.

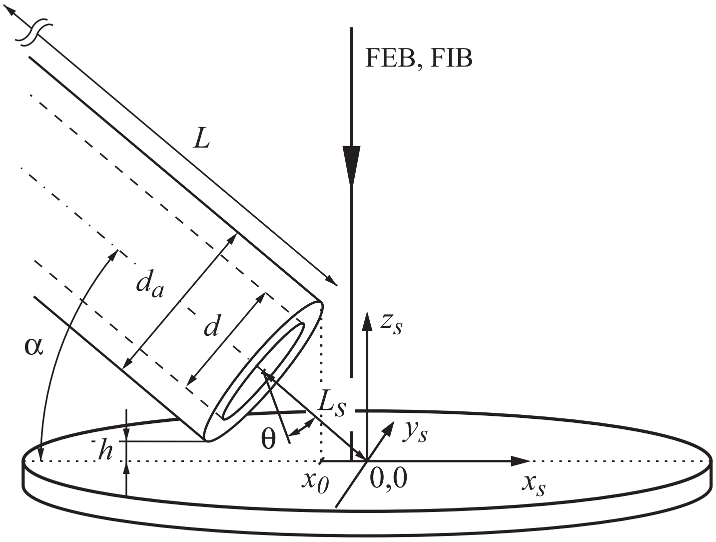

Figure 6.7: *Scheme of a tube nozzle. The origin of the substrate frame of reference* (x_s, y_s, z_s) *is defined by the intersection of the tube axis with the substrate plane. The nozzle position defined by* α *and* L_s*, or by* x_0 *and* h *instead of* L_s*, are controlled by micropositioning units that move the GIS and by the height of the sample stage. The position* x_0 *is defined by the tube upper edge which is accessible to the normally incident FEB/FIB. The polar angle* θ *to the tube axis is used to describe the angular distribution of effusing molecules into the vacuum chamber.*

6.6.1 Point sources - far-field distribution

The molecular flow through an aperture in a infinitesimal thin wall separating a gas source and a vacuum chamber, referred to as a cosine emitter, is described by the cosine law of effusion (Eq. 6.10). It can be written in the form of the differential angular throughput with the polar angle θ[125]

$$\mathrm{d}Q_\theta = \frac{Q}{\pi} \cos\theta \; \mathrm{d}\Theta, \tag{6.17}$$

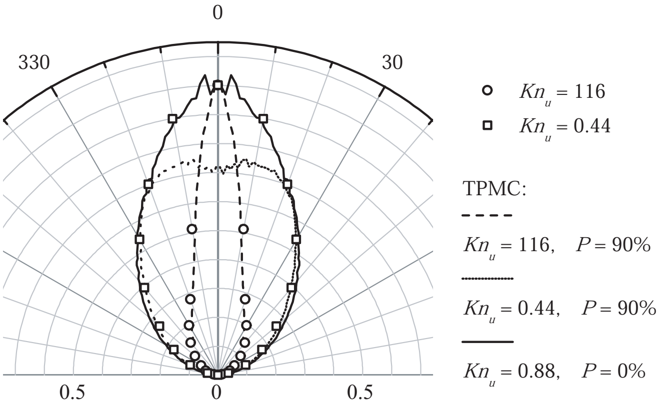

Figure 6.8: *Normalized angular probability distributions for the flow effusing from a tube having* $L = 5.63d$ *in molecular and transient flow conditions. The experimental data (circles) shows experimental results of cesium vapor flowing through stainless steel orifices into vacuum at Knudsen numbers in the upstream gas reservoir of* $Kn_u = 116$ *(molecular flow) and* $Kn_u = 0.44$ *(transient flow).*[280] *Line data are the corresponding TPMC simulations performed with the indicated parameters* Kn_u *and pressure decay* ΔP.

where the solid angle element $\mathrm{d}\Theta = \sin\theta \ \mathrm{d}\theta\mathrm{d}\phi$ and Q the total throughput. We consider the local flux generated by this aperture impinging on a planar substrate placed at a large distance in comparison to the aperture diameter, i.e. the far-field distribution. Such a point source which is incident under an angle α on a substrate plane (normal incidence: $\alpha = 90°$) produces a spatial flux profile which can be calculated by

$$\begin{gathered} J(x_s) = J_0 \left(\frac{\sin(\alpha + \theta(x_s))}{\sin\alpha} \right)^2 \cos\theta(x_s) \sin(\alpha + \theta(x_s)), \\ \theta(x_s) = \arctan(\sin\alpha / (L_s / x_s - \cos\alpha)). \end{gathered} \tag{6.18}$$

This expression is depending on the flux J_0 at the intersection point of the aperture symmetry axis with the substrate, the tilt angle α and the aperture-substrate distance L_s along α. For normal incidence, it follows from Eq. 6.18 that the cosine emitter produces a polar angular probability distribution $J(\theta) = J_0 \cos^4\theta$ and an impinging flux profile of $J(x_s) = J_0 \cos^4\theta(x_s)$. The distribution $J(\theta)$ is obtained by scanning a “point” flux detector radially around the tube exit surface center at a constant azimuth.

For molecular gas flow through tubes, Dayton developed an analytical/numerical solution which predicts the angular probability distribution $J(\theta)$.[59] This solution integrates the distribution across the tube exit surface.

6.6.2 Finite sources - near-field distribution

Since the GIS in FEB/FIB processing systems is located close to the substrate the near-field distribution must be considered. It has been demonstrated that the angular probability distribution is highly non-uniform across the finite tube surface by extending Dayton’s model.[154]

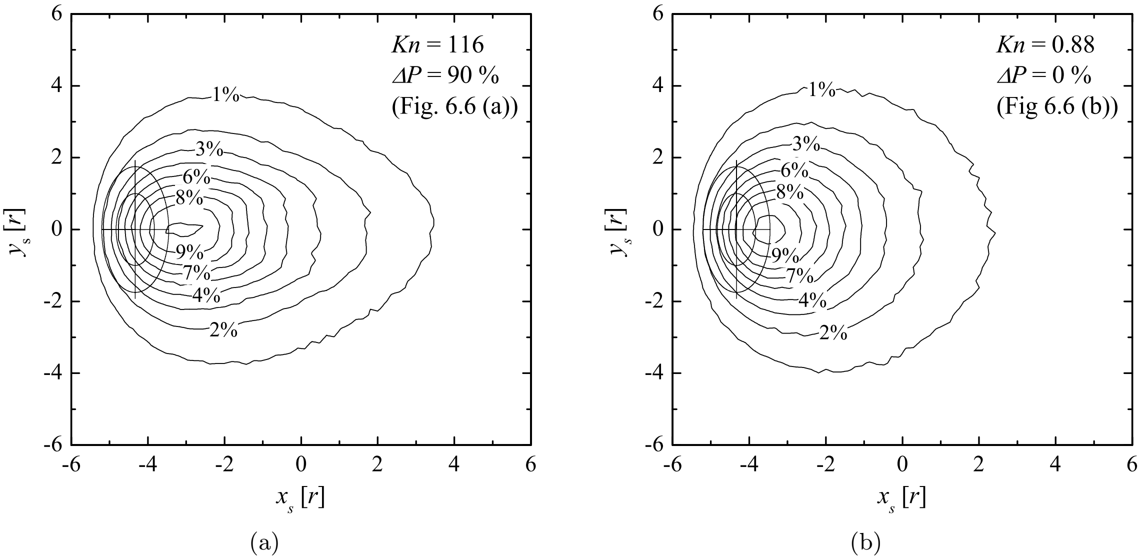

Figure 6.9: *Isoflux contours for the flow effusing from a tube having* $L = 5.63d$ *in (a) molecular:* $Kn_u = 116$, $\Delta P = 90\%$, *and (b) transient:* $Kn_u = 0.88$, $\Delta P = 0\%$, *flow conditions impinging on a plane substrate tilted by* $\alpha = 30°$ *and at a distance of* $L_s = 2.5d$.

This result indicates that an analytical description of the spatial flux distribution becomes very complex in the near-field, and for this reason simulative approaches have been adopted.

The spatial flux profile is composed of the contribution from molecules which are scattered from a surface or from an intermolecular collision (in transient flow conditions) before leaving the tube and from molecules which are transmitted without any collision. The TPMC implementation described above yields results which qualitatively can reproduce experimental results.^{254,280} In Fig. 6.8 TPMC simulated angular probability distributions in molecular and transient conditions are compared to experimental measurements. We found that the TPMC simulation based on the linear pressure decay model Fig. 6.6 (a) predicts a center probability which deviates $\sim 30\%$. The fitting model (Fig. 6.6 (b)), however, allows to match well the experimental data. The influence of the flow regime on the spatial flux distribution in the near-field of the tube is shown in Fig. 6.9. Although the transient flow is more diverging than the molecular flow, Fig. 6.8, the difference in the peak value on the substrate is only 3%. However, the contour plots clearly show a difference in the spatial distributions.

6.6.3 Critical tube length

With increasing tube length the computational effort of TPMC simulations grows strongly due to the decreasing transmission probability. This was overcome by introducing a critical tube length L_c (Fig. 6.6 (b)) which leads to spatial flux distributions being equivalent to results obtained for high aspect ratio tubes.

There are several concerns to be addressed when using a virtual aspect ratio: i) The probability of molecules transmitted through the tube without colliding with the boundary surface, having near-axial velocity components, will increase, which is seen from geometrical considerations. ii) The portion of molecules leaving the tube which are scattered in the "neglected" tube region do not contribute to the resulting distribution.

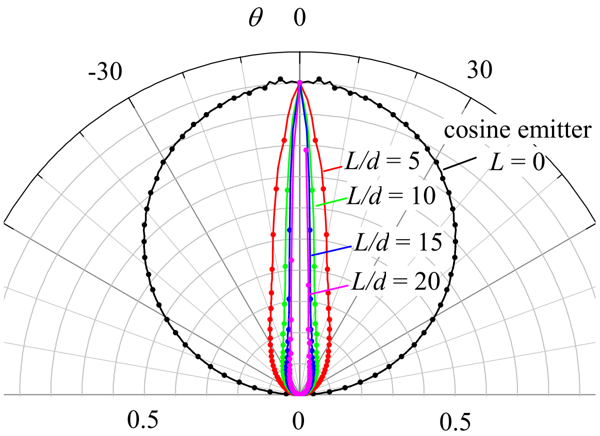

Figure 6.10: *Effect of varying tube aspect ratio on the (normalized) angular probability distribution in molecular flow conditions.*

With increasing tube aspect ratio the number of molecules which are transmitted without a wall collision strongly decays and for an aspect ratio of $L/d = 20$ the portion of directly transmitted molecules reduces to about 1%. A series of simulations with varying tube aspect ratio confirms that the angular probability distribution is insignificiantly altered for tubes having $L/d > 15$ (Fig. 6.10). The angular probability distribution integrated over the exit surface is not necessarily sufficient to unambigousley determine the spatial flux distribution on the substrate. We found, however, that the criterion $L/d > 15$ holds also true for the substrate distribution, since the radial spatial flux density leaving the exit is relatively constant even for short tubes. Accordingly, the critical tube aspect ratio which needs to be computed in molecular flow conditions is $L/d = 15$.

For transient flows the critical tube aspect ratio can be chosen smaller with increasing Knudsen number, since intermolecular collisions have a screening effect for molecules transmitting through the tube. As a rule of thumb derived from our TPMC simulations, the critical tube length is in the order of about $L_c = 3\lambda \ldots 5\lambda$. However, in transient conditions the actual flow and pressure in the tube must be observed in detail and a quantitative evaluation of the critical tube length is possible via trial-and-error simulation runs only.

6.7 Critical examination of TPMC based on DSMC simulations

Two case studies of DSMC simulations using the DS2V program are used to compare to the TPMC simulations and critically examine the assumptions made in the TPMC implemen-

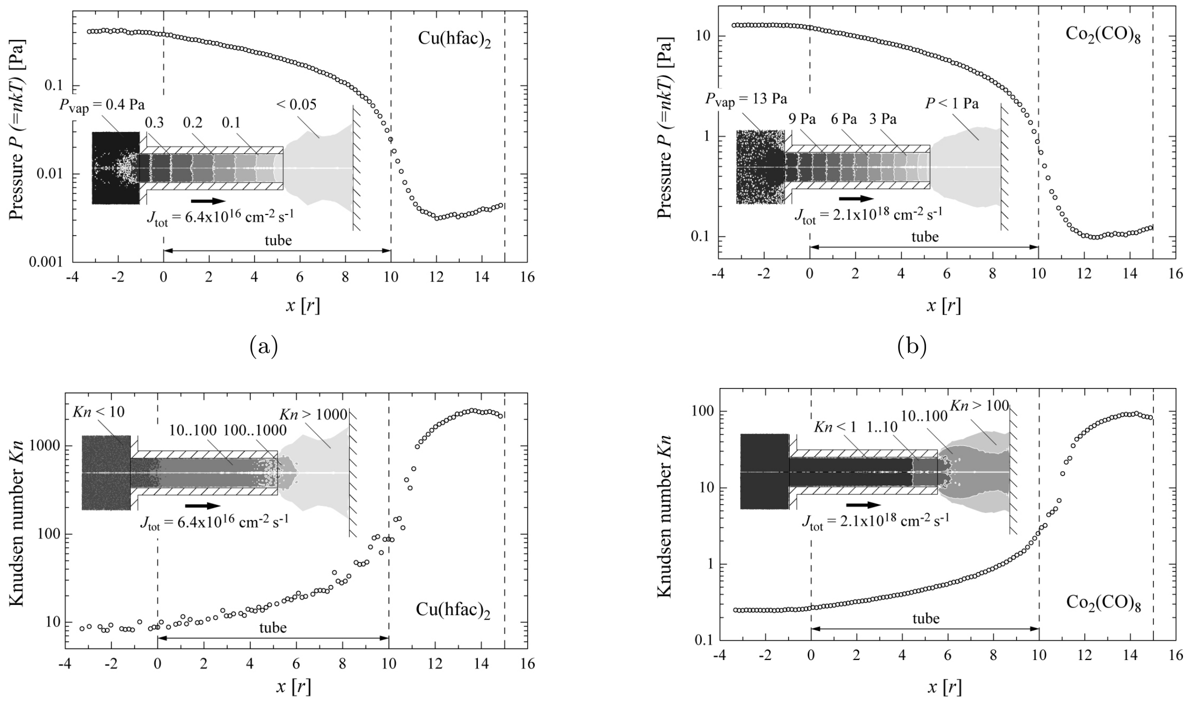

(a) (b)

(c) (d)

Figure 6.11: *$Cu(hfac)_2$ and $Co_2(CO)_8$ precursor flow through a tube with radius $r = 300$ μm and length $L = 3$ mm simulated by DSMC. The tube is normally incident to the substrate located at $x = 15r$. Profile data is taken along the tube axis at $y = 0.3r$ and insets show the simulated axially symmetric tube geometry and the flow in two dimensions. (a),(b) Pressure distribution (nkT, n: molecule number density) and (c),(d) the corresponding Knudsen number ($Kn = \lambda/d$) in the flow. In the radial direction outside of the tube vacuum boundary conditions are employed. The tube upstream pressure P_{vap} is maintained constant at the minimum x boundary. The DSMC simulations were performed including diffuse scattering from the tube and substrate surfaces with full temperature accommodation to 27 °C. DSMC simulation parameters (see Appendix C for details): VHS collision model (viscosity temperature power law: 0.74, number of rotational degrees of freedom: 3, rotational relaxation collision number: 5).*

tation. For the precursor molecules Cu(hfac)$_2$ and Co$_2$(CO)$_8$, the pressure distribution in a tube with an aspect ratio $L/d = 5$ has been simulated using DSMC (Fig. 6.11 (a) and (b)). The tube upstream pressure in these simulations was chosen to be close to the value of the vapor pressure of 0.4 Pa and 13 Pa for Cu(hfac)$_2$ and Co$_2$(CO)$_8$, respectively. For the imposed conditions the simulations yield a total flux of 6.4×10^{16} cm^{-2} s^{-1} for Cu(hfac)$_2$ and 2.1×10^{18} cm^{-2} s^{-1} for Co$_2$(CO)$_8$ molecules which is similar to flux values experimentally measured by the precursor mass loss rate through tubes having similar conductance. The pressure distribution profiles in Fig. 6.11 (a) and (b) reveal an almost linear pressure decay along the tube and an abrupt decay across the tube exit surface. The pressure models used in the TPMC simulations which are presented in Fig. 6.6 compare roughly to these conditions.

It will, however, be demonstrated in Sect. 6.8 that TPMC simulations are a valuable tool to predict substrate flux distributions with good accuracy.

The Knudsen number in these flows is shown in Fig. 6.11 (c) and (d). The definition $Kn = \lambda/d$ allows to demonstrate conveniently the changes in flow regime inside the tube, however, it is noted that outside of the tube the values tend to overestimate the degree of rarefication. A more meaningful definition of the Knudsen number in this region is $Kn = \lambda/L_s$, where L_s is the distance between tube and substrate.

In the case of $Cu(hfac)_2$ the flow is molecular throughout the tube, since $Kn \leq 10$, whereas for $Co_2(CO)_8$ transient conditions are present up to the tube end and molecular conditions establish in the vicinity of the tube exit. From these simulations, it is concluded that transient conditions are relevant for the flux distribution of $Co_2(CO)_8$ extending into vacuum, e.g. the flux distribution impinging on the substrate. Experimental determination of the $Co_2(CO)_8$ spatial flux distribution (Sect. 6.8.1) as well as the predicted regimes in Fig. 6.3 support these findings.

In the molecular and transient flow regime, results of substrate-flux distributions obtained from TPMC and DSMC compare well as illustrated in Fig. 6.12 for normal and 30°-tilted incidence of the tube relative to the substrate. A slight broadening of the DSMC profiles (circular symbols) in Fig. 6.12 (a) and (c) results from a background flux arising from molecules which experience multiple scattering events at surfaces in the vacuum chamber or eventually having re-joined the flow leaving the tube and finally re-impinge on the substrate. This background flux is not taken into account in the TPMC simulations, since trajectories are stopped after the molecules impinge on the substrate. In conclusion, the background flux from the tube itself has a relatively small influence on the prevailing flow regime and, thus, on the spatial substrate-flux distribution at a tube-substrate distance of $L_s = 2.5d$. TPMC simulations which neglect scattering in the vacuum chamber, thus, provide useful results for such configurations. DSMC simulation results at tilted incidence were performed with 100% uptake[iv] to compare with TPMC simulations in Fig. 6.12 (b) and (d).

6.8 Experimental determination of impinging flux distributions

A limited number of measurements of gas flux near-field distributions in rarefied flow conditions can be found in the literature. In these studies diatomic (H_2, N_2, O_2, CO) and noble atoms (He, Ne, Ar, and Kr) are used which can be considered as model gases. These investigations have been motivated by applications of gas beams in molecular beam epitaxy and for the determination of charged particle scattering cross sections employing crossed particle and molecular beams. The experimental methods employed are based on a pressure measurement using an ionization gauge[1,30,254] or a mass spectrometer[112] behind a sub-millimeter-sized en-

---

[iv] The limitation to two-dimensional geometries (axially or plane symmetry) in the DS2V program omitted to simulate the spatial flux profile onto a tilted plane surface. A related substrate geometry was employed instead, based on the superposition of spatial flux profiles on an "open" and a "close" axi-symmetric cone positioned in the tube axis. For this geometry to provide useful results the desorption of molecules after impinging on the substrate was omitted (= 100% uptake).

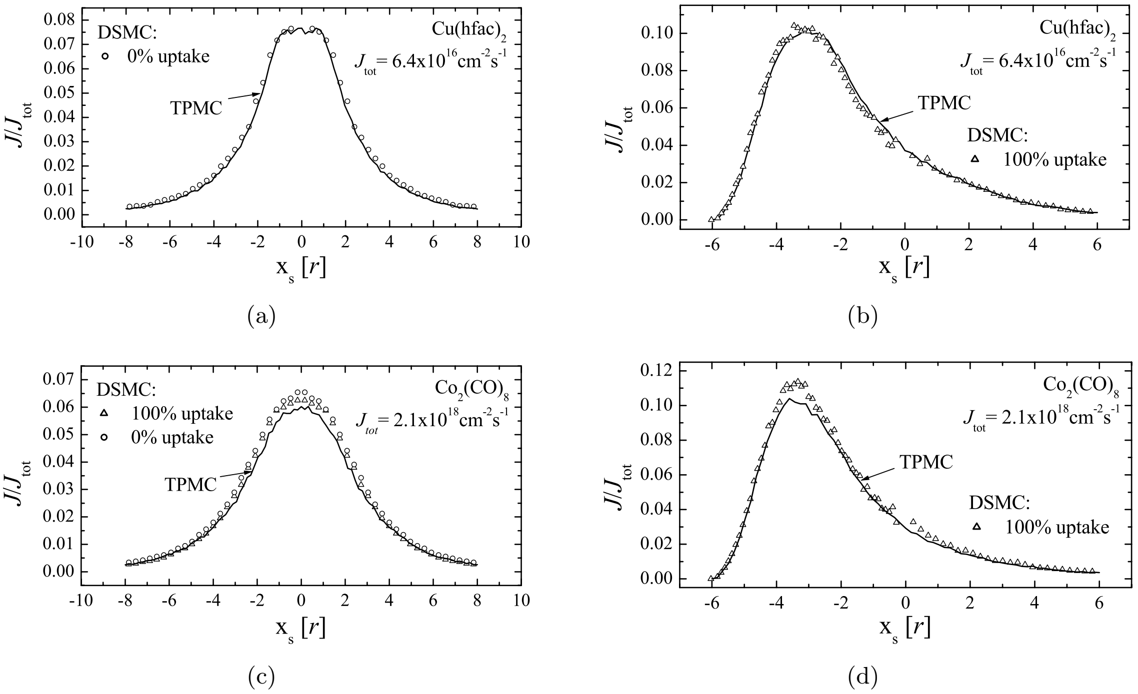

(a) (b) (c) (d)

Figure 6.12: *Spatial substrate-flux profiles produced by Cu(hfac)$_2$ and Co$_2$(CO)$_8$ precursor flow through a tube with radius $r = 300$ µm and length $L = 3$ mm simulated by DSMC (symbols) and TPMC (solid lines). (a),(c) Normal tube incidence ($\alpha = 90°$), and (b),(d) tilted tube incidence ($\alpha = 30°$) with tube-substrate distance of $L_s = 5r$ (see Fig. 6.7). DSMC simulations were performed including diffuse scattering from the tube and substrate surfaces with full temperature accommodation to 27 °C. The simulated substrate uptake is indicated. DSMC simulation parameters (see Appendix C for details): VHS collision model (viscosity temperature power law: 0.74, number of rotational degrees of freedom: 3, rotational relaxation collision number: 5). Molecular TPMC simulations ($Kn = \infty$) predict the Cu(hfac)$_2$ flow. Uniform pressure TPMC simulations (Fig. 6.6 (a)) with $\lambda = 500$ µm ($Kn = 0.8$) predict the Co$_2$(CO)$_8$ flow.*

trance aperture which spatially samples the flux distribution. While these methods are very sensitive, the experimental expense and complexity is relatively large. For some precursor molecules relevant to FEB/FIB induced processing, e.g. Co$_2$(CO)$_8$, the measurement of pressure by ionization is non-reliable since thermal decomposition contaminates the sensor and may alter the signal. In this work we propose a comparatively simple method which allows to experimentally determine the two-dimensional spatial flux distribution of precursor molecules used for FEB/FIB induced processing impinging on a substrate.

6.8.1 Global effusion experiments

The experimental approach for the characterization of the precursor flux distribution relies on the thermal decomposition of impinging precursor molecules on a heated substrate being analogous to chemical vapor deposition (CVD). In the precursor mass-transport limited deposition regime the topography of the deposited material represents the locally impinging flux on the substrate. In the following we refer to the method as local CVD.

Spatial flux distributions of three precursors (properties are summarized in Appendix A) used for FEB induced deposition have been measured under typical injection conditions: First experiments using $[(PF_3)_2RhCl]_2$ and (hfac)CuVTMS showed the feasibility of the method.[295] Further experiments in a more elaborated experimental setup have subsequently been conducted using $Co_2(CO)_8$. The following sections presents the results and their discussion based on the comparison to TPMC simulations for each precursor.

Local CVD from the $[(PF_3)_2RhCl]_2$ and (hfac)CuVTMS precursors

Thermal CVD from the precursors $[(PF_3)_2RhCl]_2$ and (hfac)CuVTMS is reported several times in the literature. $[(PF_3)_2RhCl]_2$ has been known as a volatile precursor for Rh deposition since 1971.[13] This precursor gives high Rh content deposits with low chlorine contamination at 200 °C.[66] Mass transport limited deposition rates from (hfac)CuVTMS were obtained at substrate temperature of 180 - 280 °C.[43] These experiments were performed by vaporizing the precursor in a bubbler and using argon as carrier gas.

Stimulated by the above mentioned studies, local CVD experiments were performed at substrate temperatures in the range of 200 - 300 °C. The depositions have been performed in the high vacuum chamber of a SEM with a conventional high-power resistance employed as the substrate heating element.

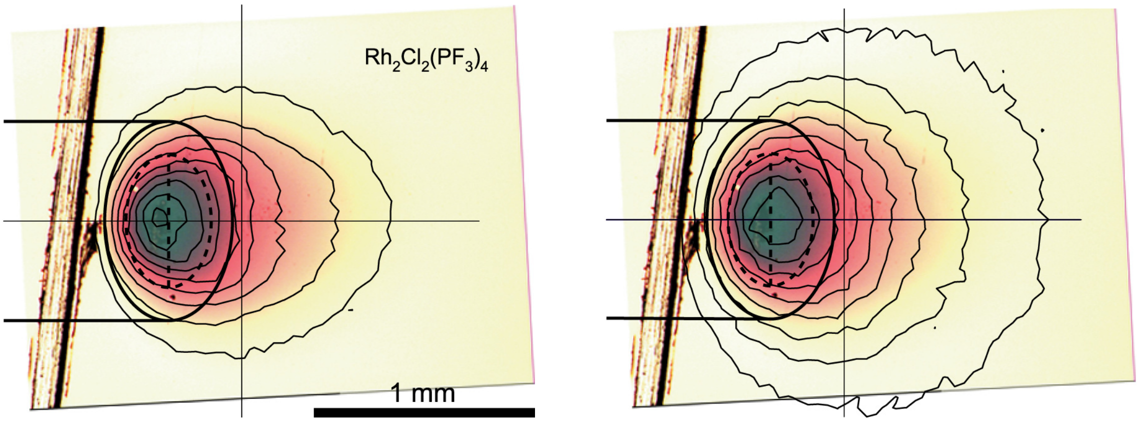

(a) (b)

Figure 6.13: *Top-view interference image superposed with isodensity contour plots of precursor flux obtained from TPMC simulation. The projected view of the tube with inner (dashed) and outer diameter is indicated. (a) Good match is obtained in free molecular flow conditions. (b) Poor match is obtained including molecule collisions (transient flow).*

Fig. 6.13 summarizes the deposition with $[(PF_3)_2RhCl]_2$ on a TiN/Si substrate, where the tube nozzle with L = 6 mm, d = 600 μm, and d_a = 900 μm, was 40° inclined to the substrate at a vertical distance $h = 50$ μm ($L_s = 614$ μm). The resulting deposit shows an interference color contrast in bright field optical microscopy and thus, represents an optical thickness profile. Assuming a homogeneous refractive index, the colors reflect the thickness profile of the deposit. A steady color change from goldish (substrate) to yellow to red to green with increasing deposit thickness towards the tube is observed. This specific color change is attributed to the reflected light spectrum of the underlying TiN/Si substrate. TPMC simulations match the contours of the interference image when free molecular flow conditions are assumed (Fig. 6.13 (a)). A poor match is obtained if transient flow conditions ($Kn = 0.63$), derived from the mean free path of 380 μm at vapor pressure (Fig. 6.3), are simulated along the whole tube (Fig. 6.13 (b)). From these observations it follows, that in this experiment the pressure decay inside the GIS and the tube nozzle was large such that molecular flow conditions are present in the tube end section at the exit into vacuum.

Superposition with the tube geometry in Fig. 6.13 reveals that the position of the precursor flux peak is covered by the tube i.e., it is not accessible to the FEB. From the TPMC simulations it can be calculated that the flux peak in Fig. 6.13 (a) is $0.32 J_{\text{max}}/J_{\text{tot}}$. However, the flux value accessible to the FEB/FIB is $\leq 0.15 J_{\text{max}}/J_{\text{tot}}$.[295]

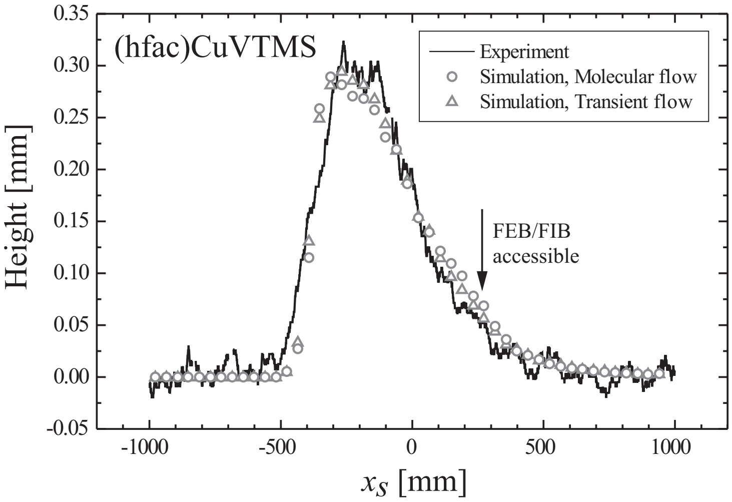

Figure 6.14: *Deposit obtained from (hfac)CuVTMS. Deposit thickness profiles along the tube axis in the center line (y = 0) measured by a stylus profilometer. The origin is defined as the intersection between the tube axis and the substrate. The highest precursor flux value accessible by FEB/FIB is indicated.*

In Fig. 6.14 the thickness profile of a local CVD experiment from (hfac)CuVTMS on a TiN/Si substrate is presented which was measured by a stylus contact profilometer. The tube with $L = 6$ mm, $d = 500$ μm, and $d_a = 710$ μm, was 60° inclined to the substrate. A good match between the experiment and TPMC simulations is obtained for $h = 20$ μm ($L_s = 225$ μm). The short distance between the tube and the substrate in this experiment omits a high sensitivity to observe differences in the divergence of the molecular beam. This results in similar profiles in free molecular and transient flow conditions predicted by the

TPMC simulations and in this case the flow regime cannot be deduced from the spatial flux distribution. From the TPMC simulations it is found that the flux peaks correspond to $0.68 J_{\max}/J_{\mathrm{tot}}$ and the FEB/FEB accessible precursor flux value is $0.18 J_{\max}/J_{\mathrm{tot}}$ in Fig. 6.14.

Local CVD from $Co_2(CO)_8$

These experiments were performed in a dedicated vacuum chamber described in Sect. 3.1.2. A GIS with internal reservoir (Fig. 3.3 (a)) was used to feed the $Co_2(CO)_8$ precursor into the vacuum chamber which was not possible to shut-off. However, substantial deposition (e.g. staining of the substrate seen be eye) occurred only once the GIS tube was brought in close proximity to the substrate.

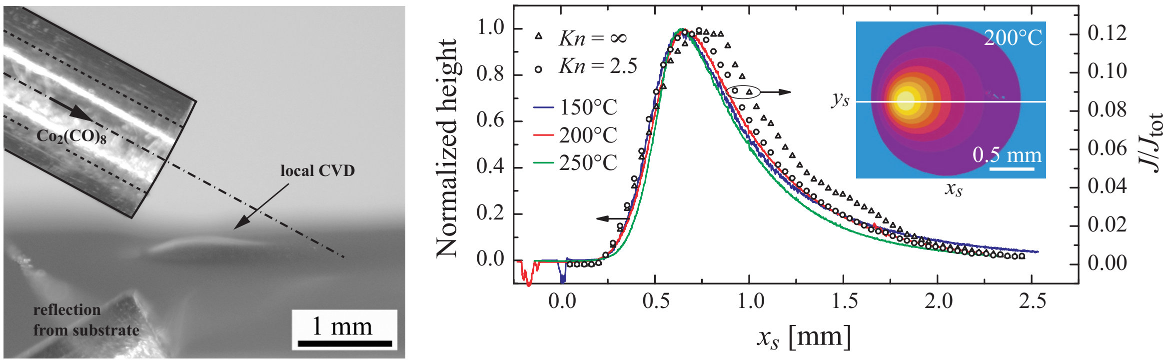

(a) (b)

Figure 6.15: *Microscope image of the of the tube-substrate configuration in side view. The substrate is mounted on a heating stage to thermally decompose all impinging molecules on the entire surface. The scratch (appears sharp only in the focus plane of the microscope) in the substrate below the tube serves as marker to determine the precise tube position relative to the deposition. (b) Deposit profiles (solid lines) grown from* $Co_2(CO)_8$ *at 150, 200, and 250 ℃ substrate temperature using a tube nozzle with* $L = 6 \pm 0.5$ *mm,* $d = 400 \pm 5$ μ*m,* $d_a = 710 \pm 5$ μ*m, at incidence* $\alpha = 33 \pm 1°$ *and a vertical tube-substrate distance of* $h = 190 \pm 5$ μ*m. Superposed are TPMC simulations in molecular flow conditions,* $\lambda = \infty$ *(triangles), and in transient conditions,* $Kn = 2.5$ *uniformly along the tube (circles). The inset shows the deposit topography (200 ℃) in two-dimensions.*

Fig. 6.15 (a) shows an optical image of the tube-substrate configuration in the reactor chamber. The substrate normal and the tube axis are arranged nearly perpendicular to the microscope to allow projection-free distance measurements in the microscope images. A deposit with a height in the order of 100 μm at its maximum elevation is observed on the substrate. The real-time control over the deposit profile allows to stop the deposition process at the moment when a desirable thickness is reached without the need for a deposition rate calibration. The determination of the tube-substrate height and the position of the substrate is possible from the measurement of half the distance between the tube and its reflection in the polished substrate plane.

Deposition shapes from experimentally determined thickness profiles shown as solid lines in Fig. 6.15 (b) with equivalent GIS-substrate configuration at substrate temperatures of 150, 200, and 250 °C were very similar. The distinct deposit topography confirms that the deposition process between 150 - 250 °C substrate temperature occurs in the mass transport limited regime. Transient TPMC simulations (squares) match well the topography shapes, whereas molecular TPMC simulated profiles (circles) deviate considerably. It is noted that the x-position is precisely deduced from the scratch in the substrate which is visible below the tube in Fig. 6.15 (a). Transient TPMC simulations were performed using the uniform pressure model (Fig. 6.6 (a)). Resulting flux distribution contour plots were compared to the two-dimensional topography of the depositions for Knudsen numbers in the range of $Kn = 0.1$ to ∞. Within this range, the simulated substrate flux distributions revealed a strong transition between $Kn = 1 \ldots 10$ and a good match between simulation and experiment was found for $Kn = 2.5$. As discussed in Sect. 6.4.1, this Knudsen number value is a fitting parameter rather than a realistic physical description. However, the magnitude of rarefication in the last tube section predicted by DSMC simulations, supports the validity of an average Knudsen number of 2.5 which determines the spatial flux distribution.

CVD of 99% purity cobalt thin films from $Co_2(CO)_8$ is reported in the temperature range of 150-400 °C.[145] However, also at 60 °C CVD was performed, presumably due to autocatalysis.[310] Experiments in a conventional CVD reactor with a constant $Co_2(CO)_8$ pressure of 50 mTorr in the chamber without carrier gas revealed a maximum deposition rate at 200 °C substrate temperature of ~6 nm min^{-1} on Si substrates as reported in.[248] The authors speculate that at lower substrate temperatures the deposition is reaction limited and at higher substrate temperatures homogeneous gas phase reactions (decomposition into non-volatile particles) take place. In our experiments the deposition rates were one order of magnitude larger. At the position of maximum impinging flux it was 4, 6, and 8 μm min^{-1} at substrate temperatures of 150, 200, and 250 °C, respectively, for a total flux leaving the tube nozzle $J_{\mathrm{tot}} = 2 \times 10^8$ cm^{-2} s^{-1} estimated from the mass loss rate. The unexpected temperature dependence is attributed to an increasing flux related to radiative heating of the precursor reservoir above room temperature in these experiments. We measured a +3.5 °C temperature increase of the GIS within 20 minutes between two successive experiments. This results in an rise of the vapor pressure by a factor ~ 1.5.[101] The ratio of deposition rate and locally impinging flux reveals that the deposition efficiency is similar at 150 and 200 °C and decreases slightly at 250 °C being in accordance with the previously mentioned CVD experiments.[248]

Except for this experiment all the depositions using $Co_2(CO)_8$ were carried out at a constant substrate temperature of 200 °C. Several depositions (maximally three) on the same substrate were made consecutively with no delay. Within such a deposition run the temperature and thus, vapor pressure increase was moderate, which we concluded from the measured deposition rates and distributions which were very similar. The total flux measured by precursor mass loss rate are average values which may underestimate the flux values from several deposition experiments.

Spectroscopy investigations of the compound of $Co_2(CO)_8$ in the literature have shown that already at room temperature decomposition to a condensed phase can occur in vacuo. The disproportionation reactions of $Co_2(CO)_8$ to volatile $Co(CO)_4$ and $Co_4(CO)_{12}$ was identified by mass spectrometry experiments.[101] The total vapor pressure of $Co_2(CO)_8$ is, thus, composed of the partial pressures of the Co-CO mono-, di- and tetramers. Such low temperature was manifested in our experiments by a black coating visible on the metallic parts on the inside of the GIS. However, mass measurements showed that chemisorption is less than 3% which does not result in observable changes in TPMC simulated flux profiles.

The reduction of the Knudsen number due to the undesirably increased vapor pressure inside the GIS at higher substrate temperature with ongoing experiment time may result in the slight narrowing of the flux profile at 250 ℃ in Fig. 6.15 (b) matching better TPMC simulations with $Kn \sim 1$. From the similarity of the profiles it can be concluded that temperature depending secondary effects in the range between 25 to 35 ℃ GIS temperature, such as a change of chemisorption inside the GIS or a change in collision mechanisms don't have a significant impact on the flow patterns in these experiments. Autocatalytic deposition, which was reported for a number of metal carbonyl molecules[157], was not a dominant phenomena since the real-time deposition monitoring showed an immediate onset of growth. The observed constant growth rate with time further rules out the relevance of other effects such as a inhomogeneous growth rate influenced by a reduction of the deposit surface temperature due to a low thermal conductivity of the pre-deposited material. EDX measurements revealed that the deposit composition was in the order of $Co_{0.8}C_{0.1}O_{0.1}$ and from high-resolution FEG SEM images the morphology of the deposits was identified to be porous built up from sheet-like grains.

6.8.2 FEB induced deposition rate dependency on local substrate-flux

We demonstrate the capabilities of TPMC simulated local precursor flux to predict mass transport limited FEB induced growth rates measured by two different *in situ* techniques based on sample current monitoring and cantilever mass sensing (Chapter 5). For each technique a growth rate mapping was performed by varying the distance between the deposition site and the GIs tube nozzle, while all the other process parameters were hold constant.

Relative deposition rate mapping

A spatial mapping of the growth rates of FEB induced carbon deposition from Acrylic acid, $CH_2{=}CHCOOH$, at different distances to the tube nozzle was performed by Bret (Fig. 6.16).[23] Relative deposition rates were measured by monitoring the sample current of 50 μm × 50 μm scanned area deposits which are grown on the same substrate material. During deposition the sample current changes due to the material dependent backscatter and secondary electron yield. The rate of change is correlated to the thickness of the film and saturates when the film thickness exceeds the electron range in the deposited material. Using this technique the relative dependency on probe current, acceleration voltage or precursor flux can be observed *in situ*. From a number of other relative growth rate measurements based on the same current monitoring technique the measurement scatter is estimated to ±5%.[23] Figure 6.16 reveals that the deposition rate decayed with increasing distance to the tube. TPMC simulations were carried out considering a mean free path of 50 μm within the tube which was deduced from an estimation of the pressure at the tube exit to be 10% of the vapor pressure 380 Pa.[23] Superposed TPMC simulations of the local substrate-flux presented by isoflux contours in Fig. 6.16 indicated that the growth rate is a function clearly correlated to the impinging

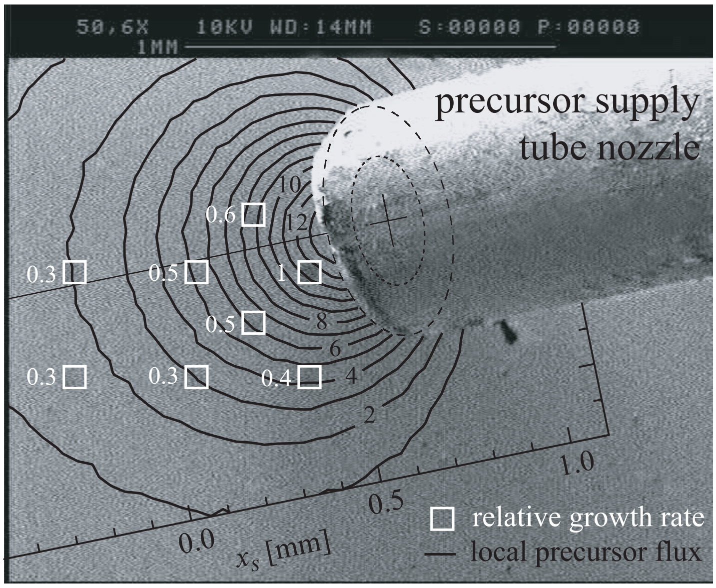

Figure 6.16: *Relative deposition rate measurements*[23] *compared to simulated* ($Kn = 0.14$) *impinging precursor distribution* J/J_{tot} *[%]. FEB: 10 kV,* $I_p = 100$ *nA. Substrate: gold. Precursor: Acrylic acid,* $J_{tot} = 3 \times 10^{19}$ cm^{-2} s^{-1}, *background pressure:* 1.3×10^{-3} *Pa*

precursor flux and thus, the deposition regime is mass transport limited.

The impinging flux simulates the experimental growth rates to within deviations of $< 20\%$. Except for the rates at large distance from the nozzle, with value 0.3, which were measured $40-60\%$ higher than predicted. This deviation may be explained by an increase in the relative contribution of precursor supply by surface diffusion. The tube shape irregularities seen in Fig. 6.16 compared to the simulated perfect geometry may result in slight deviations in the experimental growth rates.

Absolute deposition rate mapping

The absolute mass deposition rate of 1×1 μm^2 scanned areas by FEB induced deposition from Cu(hfac)$_2$ at varying distances relative to the tube nozzle was measured *in situ* by a cantilever mass sensor (Chapter 4). As outlined previously, the Cu(hfac)$_2$ flux is molecular within the nozzle (Fig. 6.3). The mass measurements and the corresponding molecular TPMC simulated local substrate-flux profile are shown in Fig. 6.17. Beside the evaluation of the precursor flux depending mass deposition rates, this approach allows to determine the molecular deposition yield: the ratio of impinging molecules per deposited atom. From this experiment we found that 2 ± 1 molecules impinge per deposited copper atom. This result is based on EDX measurements which revealed a deposit composition containing 30 wt.% copper.

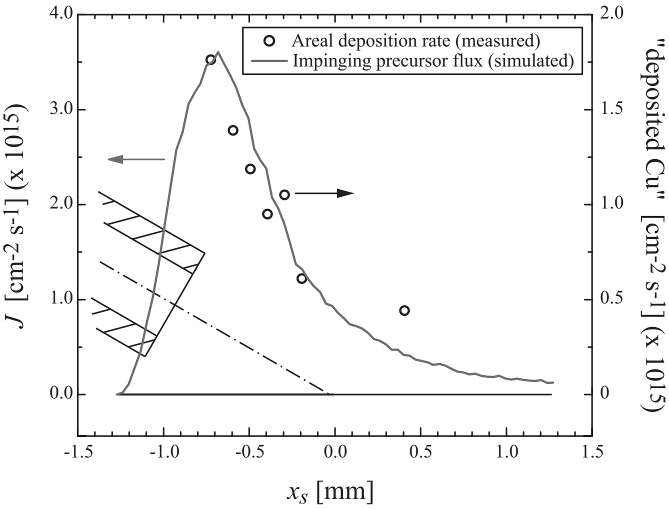

Figure 6.17: *Simulated impinging precursor molecule distribution is fitted to the mass deposition rate measurements of FEB induced 1×1 μm^2 scan field depositions. FEB: 5kV, $i_s = 300$ pA. Substrate: Si with native oxide. Precursor: Cu(hfac)$_2$, $J_{tot} = 6 \times 10^{16}$ cm^{-2} s^{-1}.*

6.9 Precursor supply design optimization

In this section TPMC simulations were employed as predictive tool for the optimization of GISs for FEB/FIB induced processing. The conventional nozzle geometry is studied in detail and subsequently two alternative geometries are discussed based on TPMC simulations and local CVD experiments.

6.9.1 Conventional tube nozzle geometry

Nozzle-substrate position

The divergent molecular beam effusing into vacuum produces a maximum flux impinging onto the substrate if the substrate is located at a minimal distance to the tube nozzle, however, the peak flux may be inaccessible to the FEB/FIB. Molecular TPMC simulations have been performed for a tube nozzle with $L = 7.5d$, exceeding the critical length (Sect. 6.6.3), to evaluate guidelines for the optimum position of the tube relative to the substrate in terms of maximal accessible precursor flux and uniformity within the processing field. In Fig. 6.18 two-dimensional isoflux contour patterns are presented at vertical tube-substrate distance of $h = 0.25d$ and $0.75d$ for a tube incidence of $\alpha = 60,\ 45,\ 30,\ 15,\ 0°$. The tube with $d_a = 1.75d$ obscures the region at $x_s < x_0$, $y_s = 0$ for the FEB/FIB. It can readily be deduced that at large tube incidence angles the flux peak is inaccessible for the FEB/FIB. The flux profiles along the tube axis in the range between the projection of the tube upper edge $x_s = x_0$, extending to $x_s = x_0 + d$ are summarized in Fig. 6.19. Close to the tube, a maximum flux is produced for large incidence angles, whereas at low incidence the flux level is strongly reduced even for the flux peaks at $x_s > x_0$. Within the presented range for $h = 0.25d \ldots 0.75d$ the

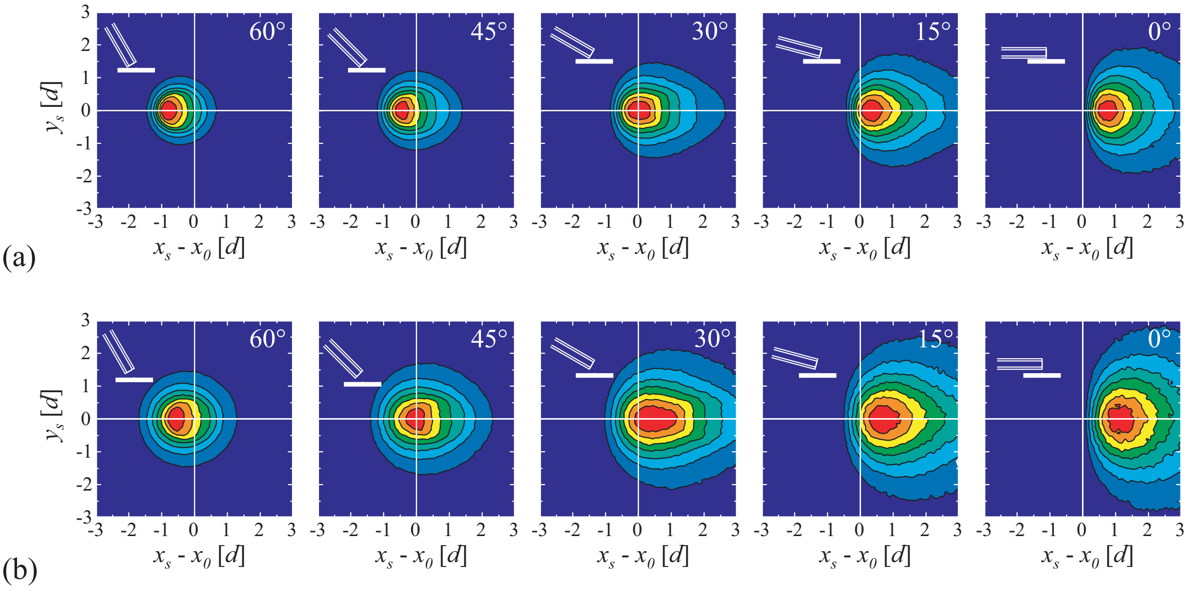

Figure 6.18: *Molecular TPMC simulated isoflux contours of the spatial flux distribution at varying incidence angles and vertical distance. The tube obscures the substrate at $x_s < x_0$ for the FEB/FIB normally incident to the substrate plane. Tube dimensions: $L = 7.5d$, $d_a = 1.75d$. Vertical tube-substrate distance: (a) $h = 0.25d$, (b) $h = 0.75d$. For a tube nozzle with $d = 400$ µm ($d_a = 700$ µm) this results in a length $L = 4$ mm and $h = 100/300$ µm. For the absolute flux scale see Fig. 6.19.*

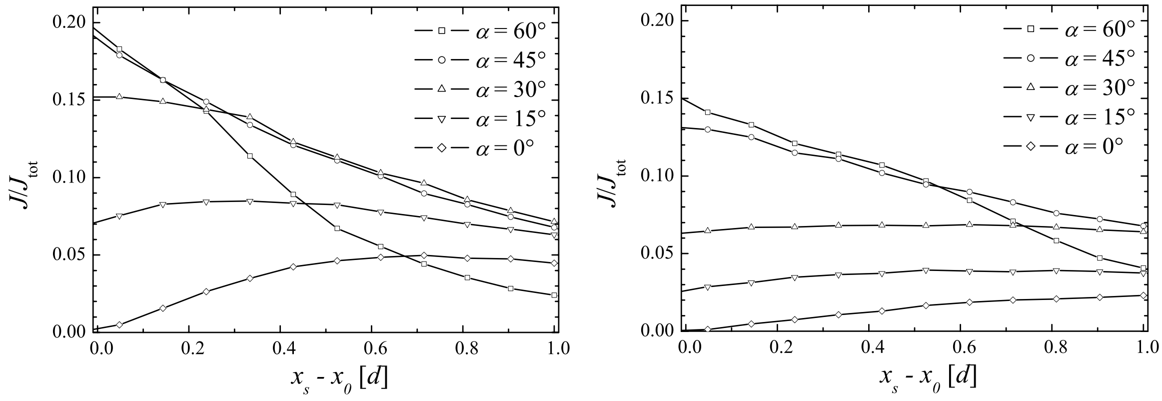

(a) (b)

Figure 6.19: *Normalized molecular impinging flux profiles on substrate along $y = 0$ of the simulations in Fig. 6.18. J_{tot} is the total flux effusing from the tube exit surface. Values at $x_s < x_0$ are not shown, since these locations are not accessible by the FEB/FIB. Tube dimensions: $L = 7.5d$, $d_a = 1.75d$. Vertical tube-substrate distance: (a) $h = 0.25d$, (b) $h = 0.75d$.*

accessible peak flux is maximal for 60° incidence, while it has the strongest non-uniformity. Optimum uniformity at high flux levels is predicted at $15\ldots30°$ incidence depending on h. At incidence $\alpha \rightarrow 0°$ a lower flux level results which is again strongly non-uniform within the simulated range.

In conclusion, if a uniform flux within a field of view of $x_0 < x_s < x_0 + d$ is to be assured, a tube incidence angle around 15° to 30° is favorable in the molecular flow regime at $h = 0.25d \ldots 0.75d$. These results are scalable with tube dimensions as long as molecular conditions prevail. In transient conditions case specific simulations need to be performed. In transient conditions the same qualitative trend is predicted by TPMC simulations, however, simulations are case specific due to the non scalable Knudsen number.

Shadowing effects

Precursor flux obscured by obstacles on the substrate can lead to reduced deposition rates on the shaded surfaced due to a reduced molecular coverage. It has been evidenced that during FEB induced deposition of three-dimensional micro- and nanostructures, different growth rates are obtained when scanning the beam towards different directions relative to the impinging flux[27] and it was speculated that shadowing effects by pre-deposited structures can account for these observations. From thermal decomposition of the impinging $Co_2(CO)_8$ flux on the substrate we observed shadow effects by obscuring features as shown in Fig. 6.20 (a).

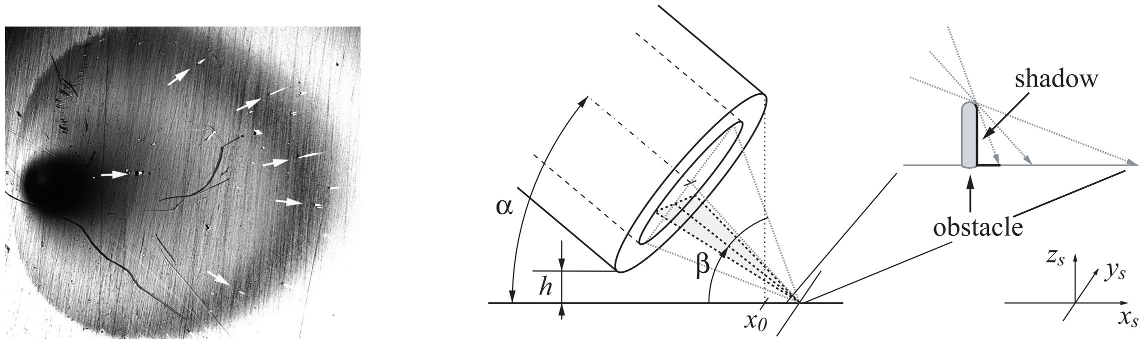

(a) (b)

Figure 6.20: *(a) Optical micrograph of a local thermal decomposition pattern produced by a tilted tube nozzle on a brass substrate using the precursor* $Co_2(CO)_8$*. Particles on the substrate produced shaded areas indicated by arrows pointing in the direction of the impinging local flux. Dark lines are due to scratches in the substrate prior to deposition. (b) Scheme of shadowing behind an obstacle on the substrate. The angle* β *defines the inclination of the direction of impinging molecules at the obstacle relative to the substrate.*

A case study of the impinging flux and shadowing effects on the substrate for the tube nozzle (Fig. 6.7) configuration was performed in molecular flow conditions. The scheme in Fig. 6.20 (b) outlines the tube nozzle including geometrical considerations to predict shading on a tip-like structure on the substrate.

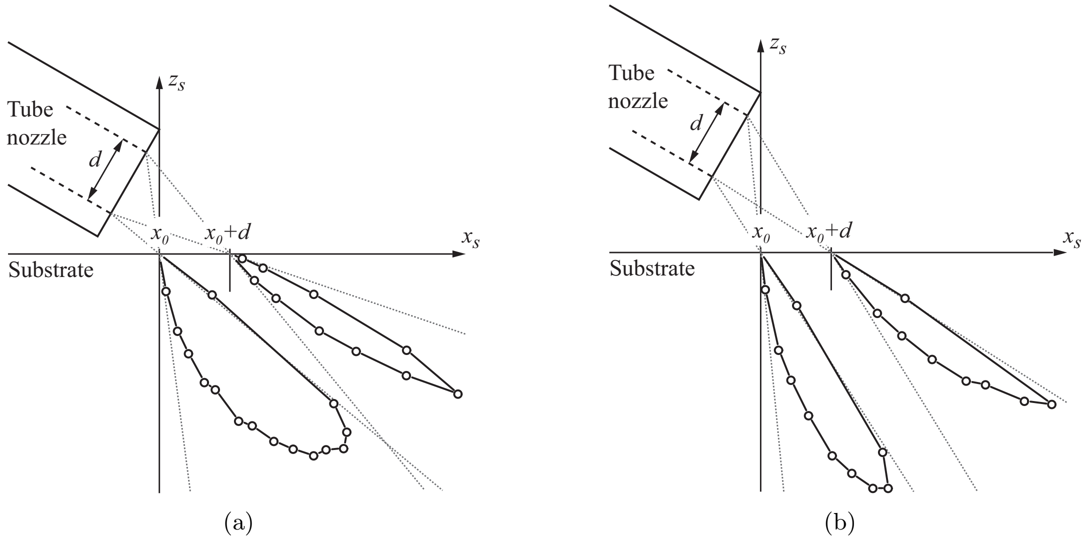

Figure 6.21: *TPMC simulation of polar probability diagram of angular distributions of molecules impinging on the substrate at* $y_s = 0$ *and at distances of* $x_s = x_0$ *and* $x_s = x_0 + d$ *from the tube upper-edge projection onto the substrate. Tube dimensions:* $L = 7.5d$, $d_a = 1.75d$, *tube incidence:* $\alpha = 30°$. *Vertical tube-substrate distance:* $h = 0.25d$, $h = 0.75d$.

Molecular TPMC simulations of the angular probability of β defined in Fig. 6.20 (b) are presented in Fig. 6.21. The results for a 30° incident tube nozzle at $h = 0.25d$ and $h = 0.75d$ is plotted for molecules impinging in a small area $0.04d^2$ on the substrate at two distances from the tube: i) at $x_s = x_0$, $y_s = 0$ defined by the tube upper-edge projected onto the substrate and ii) at $x_s = x_0 + d$, $y_s = 0$. From simple geometrical reasoning based on Fig. 6.20 (b) it is clear that the angular distribution of β is confined by two limiting angles. The simulated distributions reveal more detailed information about, e.g. the average and most probable incidence angle and allow to determine the reduced flux value behind an obscuring object on the substrate. At $x_s = x_0$ the flux arrives in average with an incidence angle β of 55° and 67° for $h = 0.25d$ and $0.75d$, respectively while at $x_s = x_0 + d$ the average angles are 33° and 41°.

For a micrometer sized obscuring substrate feature TPMC simulations in molecular flow conditions have been performed which yield a quantitative picture in terms of local impinging flux of the shadow effects on the substrate (Fig. 6.22). At an increased vertical tube-substrate distance flux shading effects are reduced.

In practice, additional precursor sources such as, i) desorption from the chamber walls (background contribution), ii) gas-phase scattering above the substrate and iii) surface diffusion will supply molecules to the area which is shaded from directly impinging flux. The background flux driven by the residual precursor pressure in the chamber is found from Eq. 3.4, e.g. for a partial background Cu(hfac)$_2$ pressure $P_b = 1\times10^{-3}$ Pa a flux $J_b = 7\times10^{14}$ cm^{-2} s^{-1} results at room temperature which is about 10% of the typical maximum local flux in our tube nozzle GIS which impinges on the substrate. For precursors with higher vapor pressures and

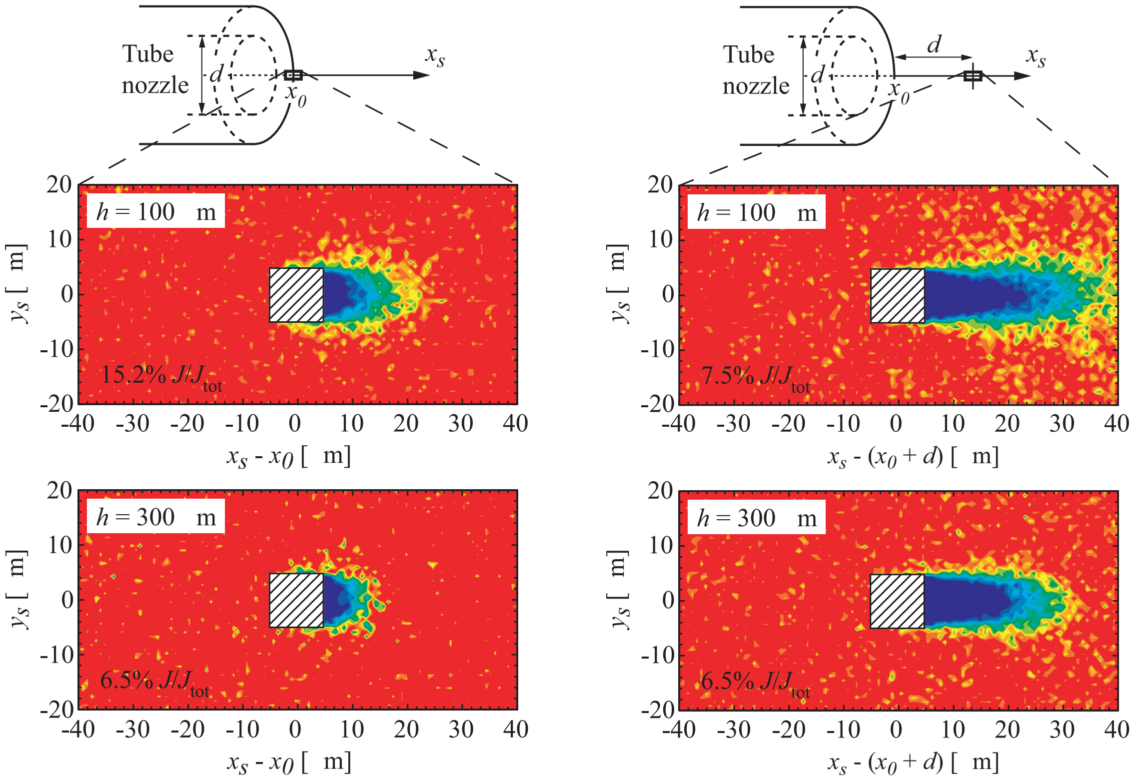

(a) (b)

Figure 6.22: *Isoflux contours of the impinging flux on the substrate (in top-view) around a cubic obstacle (shaded box) of 20 μm height and 10×10 μm^2 area centered at (a) $x_s = x_0$, $y_s = 0$ and (b) $x_s = x_0 + d$, $y_s = 0$ for nozzle-substrate height $h = 100$ μm and $h = 300$ μm and tube incidence $\alpha = 30°$. The tube nozzle dimensions are $d = 400$ μm ($d_a = 700$ μm) with a length $L = 4$ mm. The average flux values J/J_{tot} within the simulated area without obstacle are indicated; in the dark blue area no precursor impinges.*

the same GIS arrangment the background contribution tends to vanish. It is difficult to determine precisely the pressure and mean free path above the substrate and therefore the gas-phase scattering contribution. From the DSMC simulations in Fig. 6.11 it is predicted to be negligible, since the Knudsen number is $> 10 \ldots 100$ for the precursor $\mathrm{Co_2(CO)_8}$ at a total flux of 2×10^{18} $\mathrm{cm^{-2}\ s^{-1}}$ leaving the tube. Precursor supply to the shaded area by surface diffusion on the substrate *and* on the deposited structure surface are mainly responsible at the length scale of the molecular diffusion path $\sqrt{D\tau}$, where D is the diffusion coefficient and τ the residence time of adsorption on the surface. From our measurement using the mass sensor (Chapter 4) we found a typical value in the order of $\tau = 1$ ms and from model fits to experimental deposition shapes $D = 3 \times 10^{-8} \ldots 4 \times 10^{-7}$ $\mathrm{cm^2\ s^{-1}}$ for $\mathrm{Cu(hfac)_2}$ molecules (Chapter 7) which results in an estimation of the average diffusion path length of $50 \ldots 200$ nm.

6.9.2 Alternative nozzle geometries

Alternative nozzle geometries are inspired by the search for maximum J_{local}/Q, i.e. maximum impinging local flux at a tolerable pressure load. The geometries depicted in Fig. 6.23 overcome the essential limitation of the conventional tube nozzle being the relatively large distance of the exit aperture to the substrate. If shadowing effects influence the reproducibility of the FEB/FIB processing alternative nozzle geometries can also provide an isotropically directed flux from all directions.

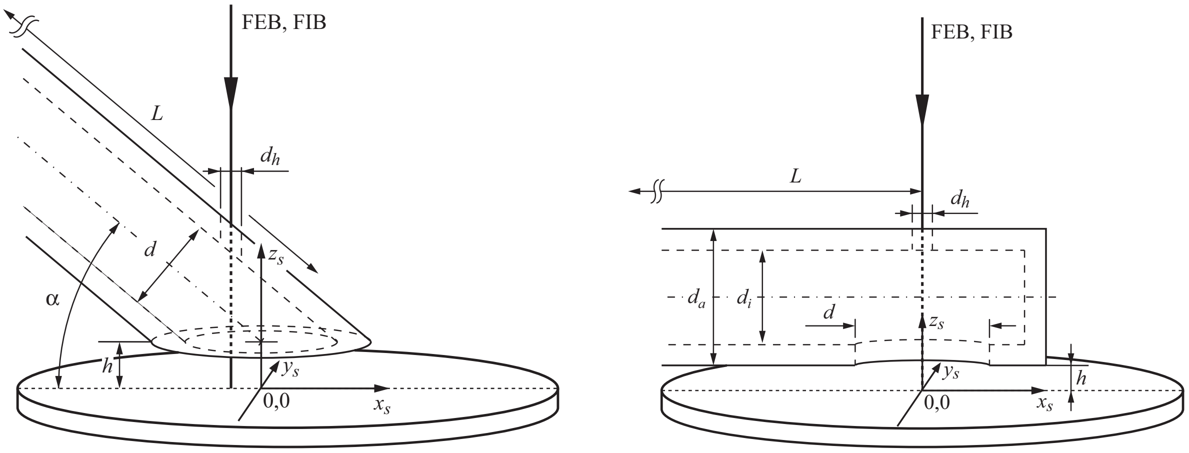

(a) (b)

Figure 6.23: *Two alternative GIS nozzle geometries. (a) Tilted nozzle with angled tube end and access hole with diameter d_h for FEB/FIB passage. (b) Horizontal nozzle with closed tube end and coaxially aligned exit aperture and access hole for FEB/FIB passage with diameter d and d_h, respectively.*

Figure 6.24 summarizes local CVD experiments with the precursor $Co_2(CO)_8$ on native polished Si substrates to characterize the flux distribution of the alternative GIS nozzles. The profile data along $y = 0$ are superposed by impinging local flux simulations by TPMC in transient conditions. The flow through the nozzle in Fig. 6.24 (a) was simulated in transient conditions, $Kn = 2.5$ uniformly along the tube, which matched well the experimental profile (Fig. 6.24 (b)). The access hole had no significant influence on the flux distribution as was confirmed from the simulations. The nozzle in Fig. 6.24 (c) was simulated as a short tube with diameter $d = 640$ μm and length 215 μm which represents the exit aperture. In the 10 mm long horizontal tube with inner diameter 1.07 mm for the $Co_2(CO)_8$ precursor roughly 80% P_{vap} is maintained up to the aperture as predicted from Eq. 6.7. Accordingly the flow conditions are strongly transient, translating in a mean free path $\lambda = 180$ μm ($Kn = 0.28$). The TPMC simulated impinging local flux matches well the experimental profiles in these conditions (Fig. 6.24 (d)). The experimentally determined flux distribution from this nozzle is circular symmetric along x_s and y_s. This geometry is advanteougous if isotropic flux to the site of processing is required, e.g. to avoid shadowing effects.

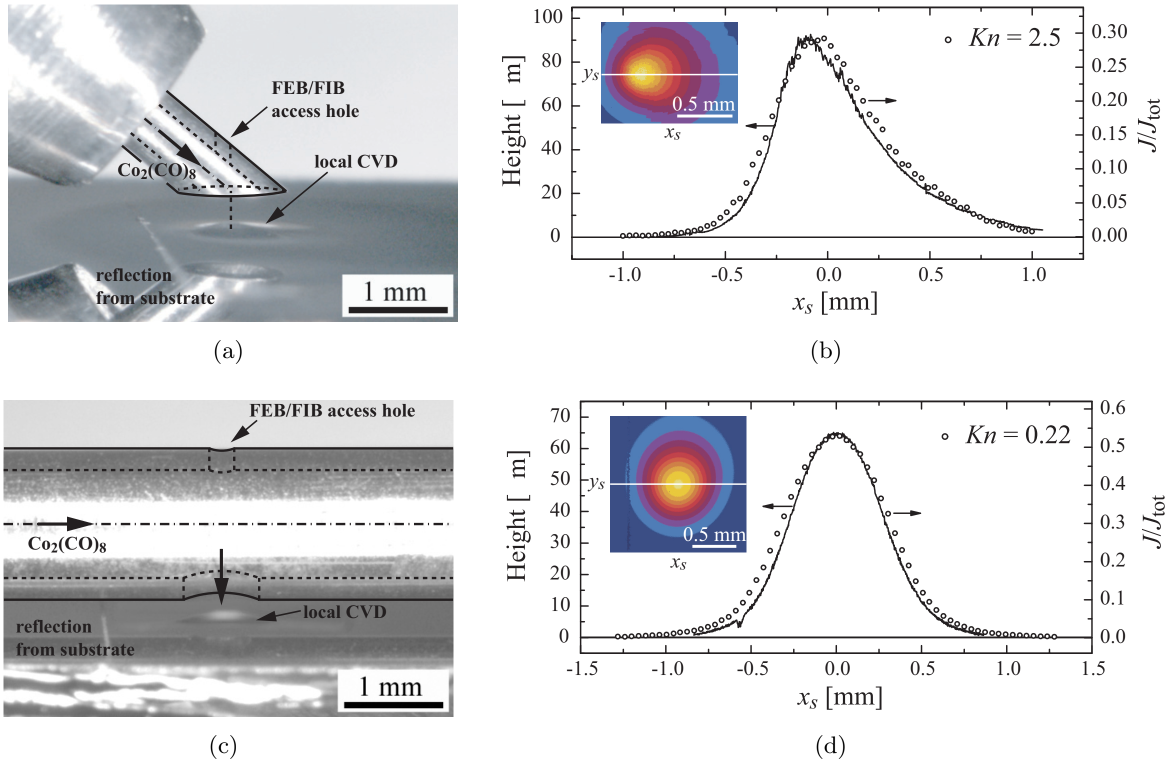

(a) (b)

(c) (d)

Figure 6.24: *Local $Co_2(CO)_8$ CVD experiments and corresponding impinging local flux simulations for two alternative GIS nozzle geometries. Microscope images show the nozzle-substrate configuration in side view. For clarity, the geometry is pointed out by an overlay. (a) Angled tube nozzle: $L = 4.16$ mm, $d = 400$ μm, $d_a = 710$ μm, $d_h = 170$ μm. Nozzle-substrate configuration: $\alpha = 40°$, $h = 287$ μm) (b) Deposit profile (red solid line) measured along $y = 0$ for the nozzle in (a). Superposed are TPMC simulations (circles) of the normalized impinging local flux $J(x)/J_{tot}$ in transient conditions, $Kn = 2.5$ uniformly along the tube. (c) Horizontal nozzle: $L = 10$ mm, $d_i = 1.07$ mm, $d_a = 1.5$ mm, $d = 640$ μm, $d_h = 160$ μm. Nozzle-substrate configuration: $h = 330$ μm. (d) Deposit profile (red solid line) measured along $y = 0$ for the nozzle in (c). Superposed are TPMC simulations (circles) of the normalized impinging local flux $J(x)/J_{tot}$ in transient conditions, $Kn = 0.22$ uniformly along the tube. Insets in (b) and (d) show the deposit topography in two-dimensions.*

In Table 6.2 the three nozzle geometries used in this work (Figs. 6.7, 6.23 (a), and 6.23 (b)) are compared based on TPMC simulated maximally accessible impinging flux values. The figure of merit is given in terms of $J_{\max}/J_{\text{tot}}$ at the same throughput $Q = J_{\text{tot}}A$ for the three nozzles, where A is the exit aperture area. The values indicated that the alternative nozzle geometries provide a 2.9×/2.2× (nozzle in Fig. 6.23 (a)) and 5.7×/4.2× (nozzle in Fig. 6.23 (b)) larger accessible flux for 100 μm/300 μm vertical nozzle-substrate distance compared to the conventional tilted tube nozzle (Fig. 6.7).

Table 6.2: *Comparison of TPMC simulated local impinging flux at a fixed nozzle-substrate distance h for i) the conventional tube nozzle (Fig. 6.7), ii) the tilted nozzle with angled tube end (Fig. 6.23 (a)) and iii) the horizontal nozzle with closed tube end and perpendicular exit aperture (Fig. 6.23 (b)).* J_{max} *is the maximal accessible local flux to a normally incident FEB/FIB. Nozzle dimensions and nozzle-substrate configuration were inspired by the actual designs used in the experiments presented in Figs. 6.15 (b), 6.23 (c) and (d). However, the exit aperture size was set to* $A = 0.126$ mm^2 *for all nozzles. The simulations were performed for the flow conditions which matched best the experiments.*

h [μm]	$J_{\text{max}}/J_{\text{tot}}$		
	i) Fig. 6.7	ii) Fig. 6.23 (a)	iii) Fig. 6.23 (b)
100	0.15	0.44	0.86
300	0.081	0.18	0.34

6.10 Summary

TPMC simulations covering the molecular and transient flow regime have been implemented and are checked against experiments. The approach is originally intended for the simulation of the conditions present in the tube and in its downstream chamber in molecular conditions, where intermolecular conditions are not relevant. For transient flows which are present at higher pressures this is more difficult to achieve using the TPMC method. However, pragmatic reasoning leads to good results. Based on a set of approximations the simulations can be used as a predictive tool to determine the local precursor flux impinging on a substrate which is located in close proximity to the tube outlet in the vacuum chamber. The DSMC method is currently the most accurate tool for the simulation of flows in transient conditions. The major advantage and motivation for TPMC simulations employed in this work is their ability to provide three-dimensional spatial flux profiles at more affordable computational costs compared to DSMC.

We found good agreement between impinging precursor distributions obtained by thermal decomposition experiments (local CVD) and TPMC simulations in molecular and transient flow conditions for three different precursor molecules: $[(PF_3)_2RhCl]_2$, (hfac)CuVTMS and, $Co_2(CO)_8$. The generalization of the results to other experimental conditions and molecular species requires some care, since at the end of this work only a limited number of experiments were performed and compared to the simulations. The results obtained from our studies, however, are encouraging to perpetuate the efficient TPMC approach in the context of gas-assisted FEB/FIB induced processing and to establish a simulative tool to predict species-dependent local gas flux distributions in the future. We believe that the restricted model employed in the TPMC simulations is sufficient to predict a wide range of rarefied flow conditions to within an accuracy of several percent. At the current state of the research, the simulations need to be “calibrated” based on experimental results.

Chapter 7

Continuum model of FEB/FIB induced processing

The key physical processes governing the rate and resolution of FEB/FIB induced deposition and etching are analyzed via an adsorption rate model.[297] We quantified how the balance of molecule depletion and replenishment determines the resolution inside the locally irradiated area. A scaling law is derived relating the resolution of the deposits to molecule dissociation, adsorption, and desorption. Experimental deposit shapes fitted well to model calculations (Sect. 7.6). From this experiment we estimated fundamental parameters of the process, such as the surface diffusion coefficient $D = 3\times10^{-8} \ldots 4\times10^{-7}$ cm^2 s^{-1} and the overall decomposition cross-section $\sigma = 0.09 \ldots 0.6$ nm^2 of Cu(hfac)$_2$ on a Si substrate irradiated by a 5 kV FEB.

7.1 Introduction

The processing regimes, or more precisely the ratio between adsorbed precursor flux and electron/ion flux at the deposition/etch area crucially determine the deposition and etch rate,[77,265,311] minimum dot dimensions at nano-scale,[281] the shape,[126] the metal content and electrical resistivity,[99] and mechanical properties[94]. Model calculations parametrize the process with the aim to determine the sensitivity of these experimental outcomes to the various process parameters. Scaling laws show at a comprehensive level the interrelation between the process resolution and the molecule depletion and replenishment.

7.2 Deposition and etching rate

The model assumes second-order kinetics of molecule dissociation by electrons. In a system with rotational symmetry the vertical FEB deposition or etch rate $R(r)$ (in units of dimension per unit time) as function of the distance r from the center of the primary electron (PE) beam is thus:[5]

$$R(r) = Vn(r)\int_0^{E_{PE}} \sigma(E)f(E,r)\mathrm{d}E \cong Vn(r)\sigma f(r) \tag{7.1}$$

Table 7.1: *Typical ranges of incident peak flux f_0 and size $FWHM_B$ of a focused electron beam (5 keV, field emission) and an ion beam (30 kV, Ga^+). Representative ranges for σ were collected from*[148,158,265] *for FEB and from*[19,171,231] *for FIB.*

	f_0 [nm^{-2} s^{-1}]	FWHM$_B$ [nm]	σ [nm^2]	σf_0 [s^{-1}]
FEB	$8 \times 10^6 \ldots 5 \times 10^7$	$2.5 \ldots 100$	$2 \times 10^{-4} \ldots 2 \times 10^{-1}$	$2 \times 10^3 \ldots 1 \times 10^7$
FIB	$2 \times 10^5 \ldots 5 \times 10^6$	$7 \ldots 100$	$10 \ldots 50$	$2 \times 10^6 \ldots 2.5 \times 10^8$

where V is the volume of the decomposed molecule or etched atom, $n(r)$ is the number of adsorbed molecules per surface unit, $\sigma(E)$ is the energy dependent electron impact dissociation cross section, E_{PE} is the energy of the PEs, and $f(E, r)$ describes the spatial flux distribution of the electron energy spectrum generated by the PEs. Since the energy integral can be solved only approximatively due to missing $\sigma(E)$ data of adsorbed molecules and uncertain parameter estimates entering in the Monte Carlo simulation of the emitted electron distribution $f(E, r)$,[5] we use the simplified expression in Eq. 7.1, where σ represents an integrated value over the energy spectrum. Such cross-sections were measured for several relevant molecules.[19,148,158,171,231,265] The spatial distribution $f(r)$ is a convolution of the Gaussian incident beam distribution $f(r) \propto exp(-r^2)$ with a peak function for the emitted spectrum which can be roughly approximated by $f(r) \propto exp(-r)$. Full widths at half maximum (FWHM) of the emitted distributions range between ~ 0.1 nm (200 keV)[114] and 2 nm (1 keV)[5]. Similar considerations apply for FIB where the spatial distribution being responsible for molecule dissociation is a convolution of the primary beam distribution with the distribution of excited surface atoms generated by the collision cascade.[70] Its range can be roughly estimated to 2 nm for 50 keV Kr^+ - ions using an approach and data in[250]. From Table 7.1, summarizing typical FWHM ranges and peak flux values f_0 of primary beams, it can be seen that in most cases the beam FWHM dominates the FWHM of the emitted secondary electrons or excited surface atoms. Thus we will not concentrate on the convolution aspect of $f(r)$ but rather derive the scaling laws for the Gaussian distribution and the exponential decay function.

Four key processes as depicted in Fig. 7.1 are considered to determine the surface density $n(r)$ of adsorbed molecules: a) Adsorption from the gas phase governed by the precursor flux J, the sticking probability s, and coverage $\Theta = n/n_0$; b) surface diffusion from the surrounding area to the irradiated area governed by the diffusion coefficient D and the concentration gradient; c) desorption of physisorbed molecules after a residence time τ; d) molecule dissociation governed by the product $\sigma f(r)$. For the molecule adsorption rate dn/dt follows:

$$\frac{\partial n}{\partial t} = \underbrace{sJ\left(1 - \frac{n}{n_0}\right)}_{\text{Adsorption}} + \underbrace{D\left(\frac{\partial^2 n}{\partial r^2} + \frac{1}{r}\frac{\partial n}{\partial r}\right)}_{\text{Diffusion}} - \underbrace{\frac{n}{\tau}}_{\text{Desorption}} - \underbrace{\sigma f n}_{\text{Decomposition}} . \tag{7.2}$$

The adsorption term in Eq. 7.2 describes a non-dissociative Langmuir adsorption, where n_0 is the maximum monolayer density given by the inverse of the molecule size. This adsorption type accounts for surface sites already occupied by non-dissociated precursor molecules and limits the coverage to n_0. All parameters other than $n = n(r,t)$ and $f = f(r,t)$ are considered constant.

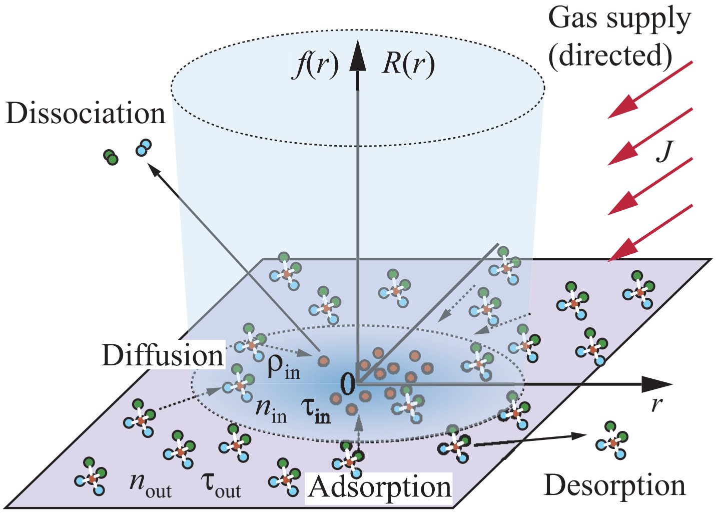

Figure 7.1: *Reference system and schematics of processes involved in FEB induced deposition. Inside the irradiated area, precursor molecules are depleted by dissociation and replenished by adsorption and surface diffusion (dashed arrows). Symbols are defined in text.*

7.3 Precursor supply from the gas phase

Solving Eq. 7.2 for steady-state ($\mathrm{d}n/\mathrm{d}t = 0$) and neglecting the diffusion term we obtain $n(r) = sJ\tau_{\text{eff}}(r)$ with the effective residence time of the molecules $\tau_{\text{eff}}(r) = (sJ/n_0 + 1/\tau + \sigma f(r))^{-1}$. The deposition or etch rate becomes

$$R(r) = sJ\tau_{\text{eff}}(r)V\sigma f(r) \tag{7.3}$$

and represents the deposit or etch shape at a given time. For any peak function $f(r)$ with a peak value $f_0 = f(r = 0)$, we can define the effective residence time in the center of the eletron beam $\tau_{\text{in}} = \tau_{\text{eff}}(0) = 1/(sJ/n_0 + 1/\tau + \sigma f_0)$ and the effective residence time far away from the electron-beam center $\tau_{\text{out}} = \tau_{\text{eff}}(r \to \infty) = 1/(sJ/n_0 + 1/\tau)$. The dimensionless ratio

$$\tilde{\tau} = \frac{\tau_{\text{out}}}{\tau_{\text{in}}} = 1 + \frac{\sigma f_0}{1/\tau + sJ/n_0} \tag{7.4}$$

represents a measure for depletion of precursor molecules due to dissociation at the center of the beam. Furthermore, we define the dimensionless deposit or etch resolution as

$$\tilde{\varphi} = \frac{\text{FWHM}_\text{D}}{\text{FWHM}_\text{B}}, \tag{7.5}$$

where $\mathrm{FWHM_D}$ and $\mathrm{FWHM_B}$ are the full widths at half maximum of $R(r)$ (the deposit or etch hole) and $f(r)$, respectively. The relation between depletion and resolution is analytically derived by solving the relation $R(\mathrm{FWHM_D}/2) = R(0)/2$ for $\mathrm{FWHM_D}$ and dividing by $\mathrm{FWHM_B}$. With a Gaussian beam $f(r) = f_0 \exp(-r^2/2a^2)$ having $\mathrm{FWHM_B} = a2\sqrt{2\ln 2}$ we find the resolution as function of depletion $\tilde{\varphi}(\tilde{\tau})$:

$$\tilde{\varphi} = \{\log_2(1+\tilde{\tau})\}^{1/2}\,. \tag{7.6}$$

For the peak function $f(r) = f_0 \exp(-ar)$, having $\mathrm{FWHM_B} = 2/a \ln 2$ the exponent in Eq. 7.6 becomes 1.

7.4 Precursor supply by surface diffusion

In the following it is shown under which conditions substantial replenishment by surface diffusion can be expected. Solving equation 7.2 numerically for steady-state ($\mathrm{d}n/\mathrm{d}t = 0$), the boundary conditions $n(r \to \infty) = n_{\mathrm{out}} = sJ\tau_{\mathrm{out}}$ and $\mathrm{d}n(r=0)/\mathrm{d}r = 0$, and with a Gaussian distribution $f(r) = f_0 \exp(-r^2/2a^2)$ we get $n(r)$ and finally $R(r)$. Fig. 7.2 shows a plot of $R(r)$ against the dimensionless variable $\tilde{r} = 2r/\mathrm{FWHM_B}$ for a given depletion. Diffusive replenishment is described by the dimensionless ratio

$$\tilde{\rho} = 2\rho_{\mathrm{in}}/\mathrm{FWHM_B}, \tag{7.7}$$

relating the molecule diffusion path in the center of the beam $\rho_{\mathrm{in}} = (D\tau_{\mathrm{in}})^{1/2}$, D being the diffusion coefficient, to the beam size. For $\tilde{\rho} = 0$, the deposit or etch shape is defined by Eq. 7.3 and its resolution by Eq. 7.6.

7.5 Process regimes

The idealized case of zero depletion, i.e. permanent monolayer coverage, corresponds to $\tilde{\tau} = 1$. Then deposition or etching proceeds in the electron-limited regime and the deposit (or etch) size corresponds to the electron-beam distribution since the logarithmic term in Eq. 7.6 becomes 1. With increasing depletion the deposit (or etch) size becomes steadily larger than the beam size. The degree of depletion strongly depends on the dissociation frequencies σf_0 summarized for FEB and FIB in Table 7.1. In order to replenish the dissociated molecules inside the continuously irradiated area by gas transport only, we need $\tilde{\tau} \to 1$, i.e. the precursor supply frequency sJ/n_0 should exceed σf_0, being equivalent to $> 2 \times 10^3$ ML s^{-1} (monolayers per second) for FEB. This corresponds to a precursor flux on the substrate of $J = 2 \times 10^{17}$ cm^{-2} s^{-1}, setting $s = 1$ and taking $n_0 = 10^{14}$ cm^{-2} as typical value. For FIB several orders of magnitude larger gas supply would be needed. Reported desorption frequencies are situated around $\tau^{-1} = 10^0 \ldots 10^3$ Hz.[76,117,171,265] Above estimations clearly suggest that most of the FEB and FIB processing experiments were performed in the precursor-limited regime.

With increasing diffusive replenishment deposits change from flat top shape to indented and round shapes, since adsorbed molecules increasingly reach the center of the irradiated area before being dissociated. Both deposition rate *and* resolution increase. The maximum

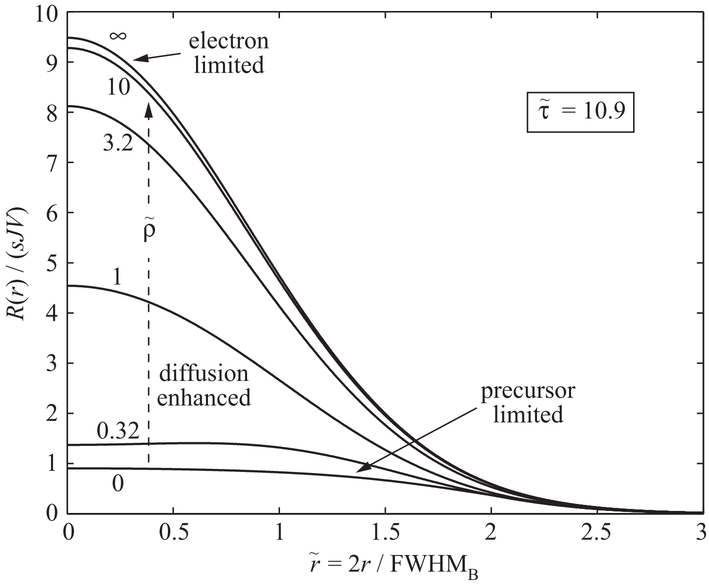

Figure 7.2: *Normalized steady-state deposition rate at indicated depletion from Eq. 7.1 representing the deposit shape. The diffusive replenishment* $\tilde{\rho} = 2\rho_{in}/FWHM_B$ *is varied. Note the shape transition from flat top,* $\tilde{\rho} = 0$*, indented,* $\tilde{\rho} = 0.32$*, to Gaussian,* $\tilde{\rho} = \infty$*.*

diffusion enhancement in deposition rate becomes $R(\tilde{\rho} = \infty)/R(\tilde{\rho} = 0) = \tilde{\tau}$ at $r = 0$. For $\tilde{\rho} \rightarrow \infty$, Eq. 7.3 simplifies to $R(r) = sJ\tau_{\mathrm{out}}V\sigma f(r)$ since any depletion is entirely compensated by diffusion and a permanent monolayer coverage provided. In this case the electron-limited regime is established and the deposit shape corresponds to the electron-beam distribution $f(r)$.

Compensation of depletion by surface diffusion requires a molecule diffusion path inside the irradiated area at least comparable to the beam size.[297] Employing pulsed beams allows to increase replenishment by diffusion and impinging precursor flux during the refresh times between pulses. This field is interesting for both, achieving maximum resolution[262] and rates[171].

7.6 Application to FEB/FIB induced deposition

Figure 7.3 presents shape measurements of FEB deposits obtained with a SEM compatible AFM operated in frequency modulation mode which is described in Sect. 3.2.4. The AFM measured topography reveals indented shapes which are difficult to resolve in SEMs due to edge effects. The deposition experiments were performed using Cu(hfac)$_2$ precursor molecules impinging on a native Si substrate with a local flux of $J/n_0 = 10$ ML s^{-1} and irradiated with a 5 keV Gaussian electron beam ($f_0 = 9 \times 10^4$ nm^{-2} s^{-1} and $\mathrm{FWHM_B} = 110$ nm). An indented shape with $\mathrm{FWHM_D} = 200$ nm is observed giving a resolution $\tilde{\varphi} = 1.8$ using Eq. 7.5. Equation 7.6 yields $\tilde{\tau} = 8.9$. Assuming as typical values $\tau = 10^{-3}$ s and $s = 1$, Eq. 7.4

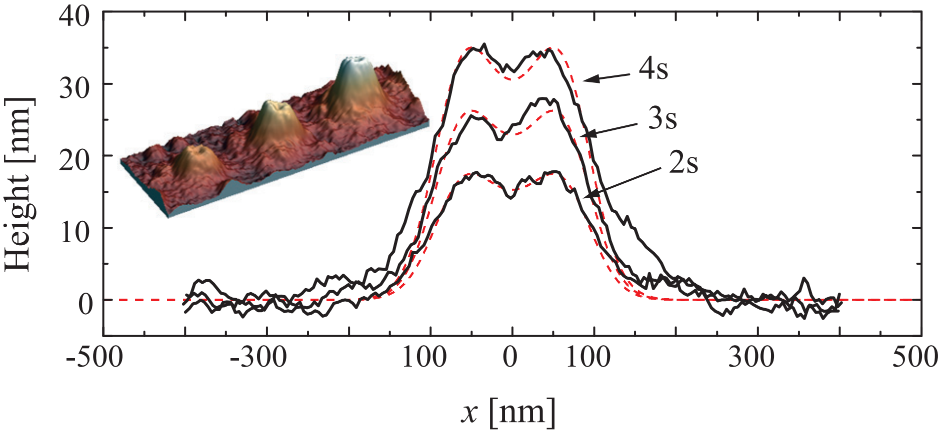

Figure 7.3: *In situ AFM image and line scans of FEB deposits from Cu(hfac)$_2$ precursor with Gaussian beam of FWHM$_B$ = 110 nm, 5 keV, $f_0 = 9 \times 10^4$ nm^{-2} s^{-1}, and $sJ/n_0 = 10$ ML s^{-1}. Exposure times are indicated. The indented apex shapes are due to depletion. Dotted lines represent fits of $R(r)$ using Eq. 7.1 with $\tau = 10^{-3}$ s (typical value), $\sigma = 0.6$ nm^{-2} (= molecule size), $V = 0.2$ nm^3, and $D = 4 \times 10^{-7}$ cm^2 s^{-1}.*

results in $\sigma \sim 0.09$ nm^2, which is a lower limit estimation since surface diffusion is neglected in Eq. 7.6. This can be illustrated by considering diffusion as a source of precursor supply to the depleted deposit center. Accordingly, replenishment by diffusion adds a "surface flux" component to J which tends to increase the resolution (Fig. 7.4) and decrease the depletion. Opposing to this, a larger cross-section increases depletion and may have compensated the diffusive replenishment.

From a scaling law describing the relation of the resolution to irradiative depletion and diffusive replenishment[297] follows $\tilde{\rho} = 0.37$, i.e. $\rho_{\text{in}} = 20$ nm. Using the relation $\rho_{\text{in}} \simeq (D/\sigma f_0)^{1/2}$ for strong depletion $\tilde{\tau} \gg 1$ results in $D \sim 3 \times 10^{-8}$ cm^2 s^{-1}. These values for the cross-section and diffusion coefficient are not unique solutions, since the same resolution can be obtained with larger depletion *and* larger diffusive replenishment. The values represent lower limit estimations. For a detailed derivation of these result see Appendix D.

Upper limit estimates can be obtained by taking as maximum dissociation cross-section the molecule size $\sigma = 0.6$ nm^2.[111] This gives $\tilde{\tau} = 60$ using Eq. 7.4. The corresponding diffusion coefficient is derived from the shape fit in Fig. 7.3 to be $D = 4 \times 10^{-7}$cm^{2}s^{-1}.

7.7 Summary

Based on a continuum model we quantified the crucial role of irradiative depletion and diffusive replenishment on deposit and etch pit shape and resolution. The presented model is applicable to FEB and FIB induced deposition and etching where precursor shadow effects, forward scattering or sidewall secondary electron emission are negligible. We demonstrated how physical parameters can be estimated from fitting experimental deposit shapes with the

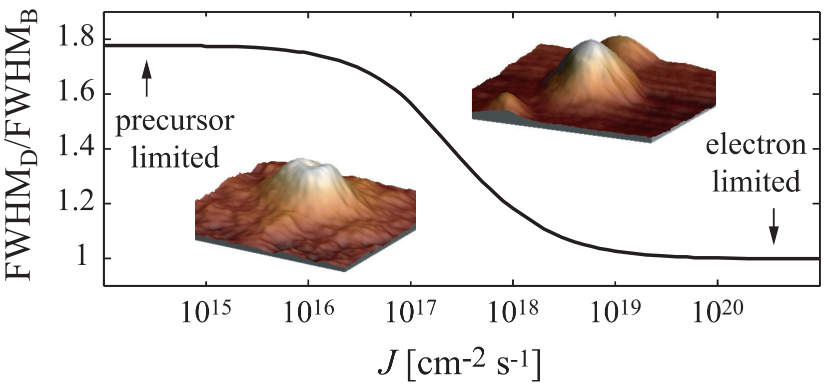

Figure 7.4: *Minimum deposit dimensions, $FWHM_D/FWHM_B$, plotted against the supplied precursor flux J. At low impinging precursor flux (precursor-limited regime) irradiative dissociation dominates the precursor supply to the deposit center which results in depletion and reduced resolution. At sufficiently high impinging precursor flux the electron-limited regime is established and $FWHM_D = FWHM_B$. The transition between the two regimes is governed by the process parameters estimated in Fig. 7.3. Insets show typical AFM measured shapes of short exposure FEB deposits from Cu(hfac)$_2$ (precursor limited) and Co$_2$(CO)$_8$ (electron limited).*

model. The predictive power of the model benefited from the process parameters which had been determined using the methods proposed in this work. Namely the impinging precursor flux, the surface residence time of precursor molecules together with the deposit shape allowed to estimate the ranges of the surface diffusion coefficient and the overall decomposition cross-section.

Chapter 8

Conclusion

In this work, surface structuring techniques using focused electron- and ion-beams (FEBs and FIBs) for high-resolution additive and subtractive nanofabrication and prototyping were studied. FEB/FIB induced deposition and etching are reactions with surface adsorbed precursor molecules. In addition, for FIB physical sputtering of surface atoms by incident ions occurs. FEB/FIB induced processes are complex mainly due to the strong interrelation of the three sub-processes involved, namely the FEB/FIB-solid interaction, the precursor supply and, the irradiation chemistry. The consumption of precursor at the beam impact region is related to the surface density of the available precursor molecules as well as the electrons or ions. In addition, the molecule surface density is affected by the irradiative decomposition by electrons or ions.

It is crucial to identify the rate-limiting process to understand experimental results, such as the process rate, the resolution, the deposit and etch pit shapes and the deposit material properties. At the current state of the art the main limitation to this is the lacking knowledge of relevant process parameters. The dearth of data is most pronounced for the cross-sections of precursor decomposition and for the characterization of surface adsorption, desorption and diffusion kinetics of precursor molecules. The predictive power of available modeling frameworks is low since this fundamental input data is missing.

To date, a large number of empirical investigations could not satisfactorily solve fundamental issues of the process. This is obvious from the literature, which reports only very few comparisons between experimental work and modeling.

This work was motivated by the rudimentary knowledge of the data required to model FEB/FIB induced processes. We tackled the problem by applying several previously unexplored methods. One approach chosen is based on the development of micromechanical tools for *in situ* real-time monitoring of the process and the *in situ* analysis of the deposited materials. Simulative and experimental approaches were chosen for the detailed characterization of the precursor supply into the vacuum chamber. The proposed methods are complementary tools to determine process parameters that are valuable input for model calculations. We aim to advance the achievement of gaining full control over the outcome of FEB/FIB induced processes.

8.1 Contributions of this thesis

A mass sensor based on a resonating cantilever was developed and integrated into the vacuum chamber of electron/ion microscopes. The working principle relies on the relation between the cantilever resonance frequency and its mass. We measured the mass removal by FIB sputtering and the mass accumulation by FEB/FIB induced deposition in real-time. Rates of FIB sputtering and FEB/FIB deposition were determined. This *in situ* mass sensing technique offered absolute measurements for three-dimensional deposit or etch pit shapes. The method does not suffer from secondary effects, such as the influence of the deposit shape and the substrate material on the monitoring signal, as is the case for the techniques based on stage current measurements or microanalysis. The mass rate evolution during depositions of thin films was revealed to be constant. Mass rate evolution measurements of stationary spot irradiation depositions confirmed the well-known correlation of the secondary and forward scattered electron yield to the deposition rate. Relating the measured values of deposit mass to the volume known from FEB imaging enabled the direct determination of the **material density**. The deposit densities gave insight to the process efficiency in terms of deposited atoms per electron/ion through the calculation of the **deposition yield**. From the measurements of the added mass of adsorbed precursor molecules we extracted further process parameters which fundamentally determine the deposition or etch rate: the **surface coverage** and **residence time** of precursor molecules. Such measurements are of great interest for FEB/FIB induced processes since they quantify the adsorption/desorption kinetics on the substrate for the actual deposition/etching conditions. Successful application of cantilever-based mass sensing was based on accurate frequency measurements at the 10 ppb level using the phase-locking technique. This corresponds to a mass resolution at the femtogram-scale. The setup temperature was stabilized which eliminated thermal drift problems being important in these experiments. At an absolute scale, the method allows to measure mass changes within the accuracy of the calibration of the sensor. We calibrated the mass response with a precision in the order of 5%-10% using conventional techniques. An *in situ* calibration method using FIB milling offering a precision $< 5\%$ was proposed and applied for the first time. Irradiation induced sensor stimuli beside mass changes have been observed as small offsets in the response.

In situ cantilever-based force sensors were used to investigate the mechanical properties of FEB deposited materials. The imaging capabilities of the hosting scanning electron microscope served as guidance to perform experiments on individual nanostructures. FEB grown pillars were subjected to bending by applying a known force at the pillar tip. From the force-deflection relation the **Young's modulus** was determined. Mechanically induced vibration revealed the pillar's fundamental resonance frequency which is related to both the Young's modulus and the material density. The proposed experimental technique is straightforward and yields amplitude *and* phase spectra acquisition at resonance based on measurements via the capabilities of the secondary electron detector of the scanning electron microscope together with phase-locking. The combination of the results from the bending and vibration experiments yielded the **material density**. We found that the carbonaceous matrix material of these deposits dominates the mechanical properties. Both, the stiffness and the density of the deposited pillars tended to increase with increasing FEB voltage. Based on a similar technique as was employed for *in situ* bending experiments, cantilever force sensing was applied for **tensile strength** measurements of thin FEB-bonds.

The methodology based on micromechanical sensing tools integrated in electron/ion microscopes extends the available diagnostic tools in the field of FEB/FIB induced deposition. The proposed experimental techniques for *in situ* monitoring and mechanical analysis overcame the severe requirements in terms of the very low amount of material removed or added and the spatial confinement down to the sub-micrometer range of the measured structures.

A simple experimental characterization method enabling the investigation of the non-uniform **precursor flux distribution** on the substrate produced by local gas injection was presented. Precursor flux distributions of several precursors were measured for the first time. The method relies on the thermal decomposition of impinging precursor molecules at substrate temperatures similar to those used in chemical vapor deposition reactors operated in the mass flow limited deposition regime. The deposition topography measured by profilometry and interference colors was related to the impinging flux pattern. A Monte Carlo simulation approach of rarefied gas flows known from vacuum science was adapted to the problem of the precursor supply in FEB/FIB processing based on tube nozzle gas injection systems. Simulations implemented in this work related well to the experimentally determined flux patterns. We identified two different regimes of rarefied flow which influence the local flux impinging on the substrate: molecular flow governed by the interaction of molecules with surfaces and transient flow governed by intermolecular collisions.

The topography of short exposure spot irradiation depositions were measured by *in situ* frequency modulation atomic force microscopy. We fitted the experimental dot shapes with continuum model calculations and extracted fundamental process parameters. With one experiment the ranges of the precursor **diffusion coefficient** and the **overall decomposition cross-section** were estimated. Several process parameters determined by the methods presented in this work, such as the impinging precursor flux, the surface coverage and residence time of the precursor molecules as well as the deposit density were the bases of the model solutions. The calculated shapes resulted from the numerically solved adsorption rate equation for Gaussian beam profiles. This realistic continuum model allowed to outline the crucial role of irradiative depletion and diffusive replenishment on deposit and etch rate and resolution.

8.2 Perspective

We think that the concept of resonant mass sensing beyond quartz crystal microbalances is well suited for further investigations related to local modifications by FEB/FIB in general. For the monitoring of FEB/FIB induced deposition this technique may allow to quantify the evolution of density during growth and the amount of halo deposition by forward scattered electrons. Specifically, for FIB milling the amount of redeposition and ion implantation could be investigated by the mass sensor. Owing to their small size, cantilever mass sensors could spatially map the FIB profile, i.e. its large background ion flux, via its sputtering action. Similarly, spatial distributions of precursor surface coverage could be determined when mapping the sensor response with respect to the precursor supply nozzle. The technique could serve as a control tool of the processing conditions to ensure reliability, e.g. by measuring the absolute processing efficiency and detect fluctuations in the precursor supply. There is currently a strong ongoing development to fabricate downscaled mass sensing devices with appropriate read-out principles. Current advances to high-frequency resonators are promising for fundamental studies in the field of FEB/FIB processing, such as the investigation of the initial nucleation mechanisms. Besides the pursuit to higher sensitivity, future device designs should allow to adapt the substrate material, e.g. by thin film depositions of the active sensor area.

With their nanofabrication capabilities focused electron- and ion-beam techniques will become more important for device prototyping applications and as assistance tools in nanomechanics in the future offering a solution for attach-and-release mechanisms in AFM based nanomanipulation. In view of these applications, to control the mechanical properties will become a major issue. Besides the stiffness and strength of these materials other aspects, such as adhesion of the FEB bonds to the substrate are proposed for future investigations. Adhesion measurements are well suited to be performed by cantilever-based *in situ* methods. The *in situ* modal analysis is a promising technique to perform investigations of the influence of post-treatments, such as FEB post-irradiation, annealing, or exposure to plasmas, on the mechanical properties and on dissipation in FEB/FIB deposited pillars.

In the future, the Monte Carlo precursor flux simulations can serve as a tool to extend FEB/FIB induced processing models including the knowledge of impinging precursor flux and shadow effects. Such simulations are a valuable tool to determine the influence from the often encountered shadow effects in experiments, e.g. the direction-depending line deposition rates or asymmetries in stationary beam vertical pillar growth. Besides the application and further development of test-particle Monte Carlo simulations, the direct simulation approach, or a combination of both, in three dimensions are proposed for future investigations where more accurate model description of the precursor gas flow are required, i.e. for investigations of the strongly rarefied flux at the scale of the fabricated structures. Sophisticated and flexible precursor supply arrangements with the ability to control the precursor flux to the substrate are of great interest in the future to tailor the processing throughput and the properties of deposited materials. Further optimization of gas injection and mixed gas flows evolving from multi-nozzle systems have to be investigated to gain a better control over gas-assisted FEB/FIB induced processing. The proposed experimental characterization approach by thermal decomposition is appropriate to conduct such studies.

To overcome the enormous lack of relevant data on adsorption, desorption, diffusion, scattering, and dissociation, future model investigations should be related to experimental results which up to now rarely was done. To adaptively model FEB/FIB induced processing it is promising to couple Monte Carlo simulations with continuum models. This hybrid approach is advantageous since continuum models allow to increase the simulative time steps which are limited in Monte Carlo simulations due to the description at the molecular level.

Appendix A

Properties of precursor molecules

Table A.1: *Summary of data for the precursors used in this work: Vapor pressure P_{vap} at temperature T, molecule diameter δ, mean free path at the vapor pressure $\lambda_{P_{vap}}$ calculated according to Eq. 6.2 and the reported chemical vapor deposition (CVD) temperature T_{CVD}.*

Precursor	P_{vap} [Pa] / T	δ [$\mathring{A}$]	$\lambda_{P_{\text{vap}}}$ [μm]	T_{CVD} [° C]
Acrylic acid: $CH_2{=}CHCOOH$ CAS: 79-10-7	380 / 25 ℃[23]	7 [a]	5	-
(Trimethyl)methylcyclo-pentadienylplatinum: $(CH)_3PtCpCH_3$ CAS: 94442-22-5	7.7[282]	7.8 [a]	199	-
Dicobalt-octacarbonyl: $Co_2(CO)_8$ CAS: 10210-68-1	13.4 / 27 ℃[101]	7 [a]	100	150-400[145]
Bis-hexafluoroacetylacetonato-Copper(II): $Cu(hfac)_2$ CAS: 14781-45-4	0.4 / 25 ℃[111]	8.1 [b]	3550	250[176]
Hexafluoroacetylacetonato-Copper(I)-vinyltrimethylsilane: (hfac)CuVTMS CAS: 139566-53-3	10 / 25 ℃[43]	8.6 [b]	124	180-280[43]
Rhodium-chloro-trifluorophosphine: $((PF_3)_2RhCl)_2$ CAS: 14876-98-3	8.6 / 25 ℃[219]	5.7 [a]	380	200[66]

---

[a] Longest dimension of molecule.

[b] Calculated from density ρ according to $\delta = 1.122(M/(\rho N_a))^{1/3}$, where M is the molecular mass and N_a Avogadro's constant.[160]

Appendix B

Distribution sampling

B.1 Cosine distribution

From the random number $Rn \in [0, 1]$ a three-dimensional cosine distribution described by an azimuthal and a polar angle, ϕ and θ, is sampled using:[110]

$$\phi = 2\pi Rn$$

$$\theta = \arcsin \sqrt{Rn}$$

A cosine-distributed molecular flow emitted from a point source located on the wall of a spherical chamber impinges uniformly onto the chamber surface.

B.2 Isotropic distribution

From the random number $Rn \in [0, 1]$ a three-dimensional isotropic distribution from 0 to 90° described by an azimuthal and a polar angle, ϕ and θ, is sampled using:

$$\phi = 2\pi Rn$$

$$\theta = \arccos Rn$$

and a three-dimensional isotropic distribution from 0 to 180° using:

$$\phi = 2\pi Rn$$

$$\theta = \arccos (2Rn - 1)$$

An isotropic molecular flow emitted from a point source located in the center of a spherical chamber impinges uniformly onto the chamber surface.

Appendix C

DS2V: Simulation parameters

A detailed exposition of the implemented DSMC method is available in the textbook by Bird[18]. However, the DS2V program takes advantage of several important developments in DSMC methodology that have occurred since that time. The parameters which specified the flow problems in the DSMC simulations in Sect. 6.7 are outlined in the following. The full capabilities of the DS2V program are described in detail in the Users Guide.[16]

Flow boundaries

The boundaries delimiting the volume of the simulation are specified as:

- **Vacuum interface**
  No molecules enter the flow and all molecules striking the boundary are removed from the flow.

- **Stream boundary**
  Molecules that are typical of the specified stream enter across the boundary. Molecules that strike stream boundaries are removed from the flow. This boundary conditions maintains a uniform flow in an empty flow field, even for a subsonic or stationary stream.

Custom gas composition

The gas is a mixture of the variable hard sphere (VHS) or the variable soft sphere (VSS) models and the cross-sections, the viscosity-temperature index (which determines the way in which the cross-section changes with the relative velocity), are set separately for every molecular species. The VHS model is adequate for simple gases. The gas species are specified using the following parameters:

- **Number of molecular species in the flow**
  This is the total number of molecules that appear in the gas that enters the specified flow entry lines.

- **Diameter of the molecular model**
  The VHS and VSS molecular models employ the hard sphere or modified hard sphere scattering model but have a diameter that varies with the collision energy. The energy for the specified diameter is characteristic of the temperature that is specified at a reference temperature.

- **Inverse of the VSS scattering parameter**
  This is set to unity if the VHS model is to be used or, for VSS molecules, to the value appropriate to the Schmidt number of the gas.

- **Viscosity-temperature power law**
  The variation in the VHS diameter is such as to produce a coefficient of viscosity that varies with temperature raised to this power. 0.5 is a hard sphere gas and 1.0 is effectively a Maxwell gas. These should be regarded as limiting values.

- **Molecular Mass**

- **Number of rotational degrees of freedom**
  A monatomic molecule has no rotational degrees of freedom and a diatomic molecule or a linear triatomic molecule has two. Non-linear and complex polyatomic molecules have three rotational degrees of freedom.

- **Rotational relaxation collision number**
  This sets the rotational relaxation rate. It may be made a constant (generally about five) or a second order polynomial in the temperature.

Gas-surface interaction

The surfaces in the flow are specified in a two-dimensional cut view and are revolved around a defined axis of rotation to provide a three-dimensional axi-symmetric geometry. A reference temperature is attributed to the solid surfaces. The classical diffuse (cosine-law) desorption model with complete accommodation of the gas to the surface temperature was used with the following options:

- **Fraction of specular reflection**
  A combination of specified fractions of specular and diffuse reflection can be used to provide an indication of non-diffuse effects.

- **Uptake at surface**
  The specified fraction of molecules that strike the surface are removed from the calculation.

Appendix D

Resolution vs. process regimes

D.1 Universal scaling graph

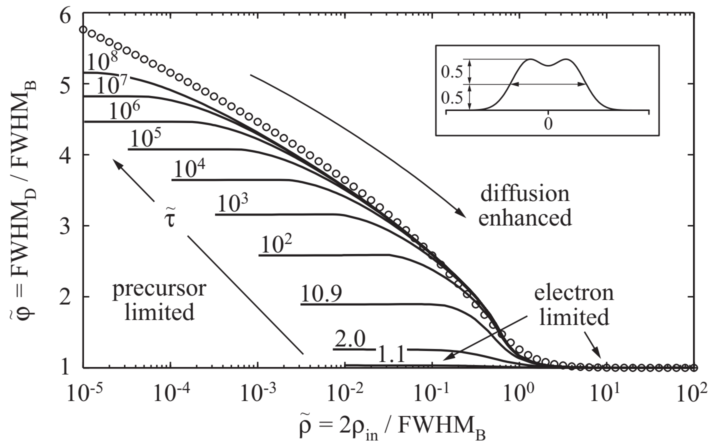

Figure D.1: *Normalized deposit size vs. normalized diffusion path for varying depletion (indicated). At $\tilde{\rho} = 2$ the diffusion path equals the beam size. The curve for $\tilde{\tau} = 10.9$ corresponds to the FWHMs of shapes in Fig. 7.2. Circles represent a scaling law of resolution as function of diffusive replenishment as given in*[297]*. The inset shows the $FWHM_D$ definition of indented deposits.*

Figure D.1 represents a graph relating the dimensionless resolution to irradiative depletion and diffusive replenishment. Evidently, when the diffusion path inside the irradiated area becomes at least comparable to the size of the electron-beam distribution $\tilde{\rho} \geq 2$, the resolution is $\tilde{\varphi} \leq 1.03$ for any depletion, i.e. the deposit size is within 3% close to $\mathrm{FWHM_B}$. The deposits become broader than the electron beam for $\tilde{\tau} > 1$ and small $\tilde{\rho}$, branching out into constant maximum size given by Eq. 7.6 at negligible diffusive replenishment $\tilde{\rho} \to 0$. Figure D.1 holds independently of how diffusive replenishment is experimentally achieved: either via the beam size $\mathrm{FWHM_B}$ (using the focus of the beam) or via the diffusion path ρ_{in} (changing precursor diffusion).

D.2 Lower limit parameter estimations

For an experimentally determined deposit resolution $\tilde{\varphi} = 1.8$ (Fig. 7.3), the depletion without diffusion is found as $\tilde{\tau} = 8.9$ (Eq. 7.6) which results for $f_0 = 9 \times 10^4$ nm^{-2} s^{-1}, $J/n_0 =$ 10 ML s^{-1}, $s = 1$ and $\tau = 10^{-3}$ s in a lower limit dissociation cross-section $\sigma \sim 0.09$ nm^2 (Eq. 7.4). The same $\tilde{\varphi}$ at $\tilde{\tau} = 8.9$ is predicted from Fig. D.1 for diffusive replenishment $\tilde{\rho} \lesssim 0.37$. The corresponding $\rho_{\text{in}} = \tilde{\rho}\ \text{FWHM}_{\text{B}}/2 = 20$ nm evaluates to a diffusion coefficient $D = \rho_{\text{in}}^2/\tau_{\text{in}} \simeq \rho_{\text{in}}^2 \sigma f_0 = 3 \times 10^{-8}$ cm^2 s^{-1} assuming strong depletion ($\tilde{\tau} \gg 1 \rightarrow \sigma f_0 \gg 1/\tau + sJ/n_0$). It is readily seen from Fig. D.1 that the derived diffusion coefficient is a lower limit value for depletions $\tilde{\tau} > 8.9$: to obtain the measured $\tilde{\varphi} = 1.8$, larger depletion will be compensated with larger diffusive replenishment and thus a larger diffusion coefficient.

Bibliography

[1] S. Adamson and J. F. McGilp. Measurement of Gas Flux Distributions from Single Capillaries Using a Modified, UHV-Compatible Ion Gauge, and Comparison with Theory. *Vacuum*, 36(4): 227–232, 1986. 97

[2] T. Akiyama, U. Staufer, N. F. de Rooij, P. Frederix, and A. Engel. Symmetrically arranged quartz tuning fork with soft cantilever for intermittent contact mode atomic force microscopy. *Rev. Sci. Instrum.*, 74(1):112–117, 2003. 29

[3] T. R. Albrecht, P. Grutter, D. Horne, and D. Rugar. Frequency-Modulation Detection Using High-Q Cantilevers for Enhanced Force Microscope Sensitivity. *J. Appl. Phys.*, 69(2):668–673, 1991. 39, 44

[4] Alicona Imaging AG, Germany. `www.alicona.com`, 2007. 31

[5] T. E. Allen, R. R. Kunz, and T. M. Mayer. Monte-Carlo Calculation of Low-Energy Electron-Emission from Surfaces. *J. Vac. Sci. Technol. B*, 6(6):2057–2060, 1988. 9, 113, 114

[6] Peter William Atkins and Julio De Paula. *Atkins' physical chemistry.* Oxford University Press, Oxford, 8th edition, 2006. 6

[7] B. Babic, J. Furer, S. Sahoo, S. Farhangfar, and C. Schonenberger. Intrinsic thermal vibrations of suspended doubly clamped single-wall carbon nanotubes. *Nano Lett.*, 3(11):1577–1580, 2003. 17

[8] J. D. Barry, M. Ervin, J. Molstad, A. Wickenden, T. Brintlinger, P. Hoffman, and J. Meingailis. Electron beam induced deposition of low resistivity platinum from Pt(PF3)4. *J. Vac. Sci. Technol. B*, 24(6):3165–3168, 2006. 10

[9] F. M. Battiston, J. P. Ramseyer, H. P. Lang, M. K. Baller, C. Gerber, J. K. Gimzewski, E. Meyer, and H. J. Guntherodt. A chemical sensor based on a microfabricated cantilever array with simultaneous resonance-frequency and bending readout. *Sensor. Actuat. B-Chem.*, 77(1-2):122–131, 2001. 34

[10] B. Bauer and R. Speidel. Reduction of Contamination Rate in STEM at a Pressure of 10-5 Torr. *Optik*, 48(2):237–246, 1977. 10

[11] S. Bauerdick, C. Burkhardt, R. Rudorf, W. Barth, V. Bucher, and W. Nisch. In-situ monitoring of electron beam induced deposition by atomic force microscopy in a scanning electron microscope. *Microelectron. Eng.*, 67-8:963–969, 2003. 29

[12] S. Bauerdick, C. Burkhardt, D. P. Kern, and W. Nisch. Addressable field emitter array: A tool for designing field emitters and a multibeam electron source. *J. Vac. Sci. Technol. B*, 22(6): 3539–3542, 2004. 11

[13] M. A. Bennett and D. J. Patmore. 4-Coordinate and 5-Coordinate Complexes of Rhodium and Iridium Containing Trigluorophosphine. *Inorg. Chem.*, 10(11):2387, 1971. 99

[14] R. Berger, E. Delamarche, H. P. Lang, C. Gerber, J. K. Gimzewski, E. Meyer, and H. J. Guntherodt. Surface stress in the self-assembly of alkanethiols on gold. *Science*, 276(5321):2021–2024, 1997. 34

[15] R. Berger, H. P. Lang, C. Gerber, J. K. Gimzewski, J. H. Fabian, L. Scandella, E. Meyer, and H. J. Guntherodt. Micromechanical thermogravimetry. *Chem. Phys. Lett.*, 294(4-5):363–369, 1998. 34, 46

[16] G. A. Bird. The DS2V Program User's Guide (availalable at `gab.com.au`). Version 3.8, 2006. 91, 129

[17] G. A. Bird. personal communication. 2007. 91

[18] G. A. Bird. *Molecular gas dynamics and the direct simulation of gas flows.* Clarendon, Oxford, 1994. 80, 87, 90, 129

[19] P. G. Blauner, J. S. Ro, Y. Butt, and J. Melngailis. Focused Ion-Beam Fabrication of Sub-Micron Gold Structures. *J. Vac. Sci. Technol. B*, 7(4):609–617, 1989. 5, 114

[20] G. Boero, I. Utke, T. Bret, N. Quack, M. Todorova, S. Mouaziz, P. Kejik, J. Brugger, R. S. Popovic, and P. Hoffmann. Submicrometer Hall devices fabricated by focused electron-beam-induced deposition. *Appl. Phys. Lett.*, 86(4):042503, 2005. 11

[21] A. Botman, J. J. L. Mulders, R. Weemaes, and S. Mentink. Purification of platinum and gold structures after electron-beam-induced deposition. *Nanotechnology*, 17(15):3779–3785, 2006. 11

[22] J. M. Breguet and P. Renaud. A 4-degrees-of-freedom microrobot with nanometer resolution. *Robotica*, 14:199–203, 1996. 26

[23] T. Bret. *Physico-chemical study of the focused electron beam induced deposition process.* PhD thesis, Ecole Polytechnique Fédérale de Lausanne, Switzerland, 2005. 9, 10, 60, 103, 104, 125

[24] T. Bret, I. Utke, A. Bachmann, and P. Hoffmann. In situ control of the focused-electron-beam-induced deposition process. *Appl. Phys. Lett.*, 83(19):4005–4007, 2003. 13, 14

[25] T. Bret, I. Utke, C. Gaillard, and P. Hoffmann. Periodic structure formation by focused electron-beam-induced deposition. *J. Vac. Sci. Technol. B*, 22(5):2504–2510, 2004. 57, 74

[26] T. Bret, S. Mauron, I. Utke, and P. Hoffmann. Characterization of focused electron beam induced carbon deposits from organic precursors. *Microelectron. Eng.*, 78-79:300–306, 2005. 10, 71

[27] T. Bret, I. Utke, and P. Hoffmann. Influence of the beam scan direction during focused electron beam induced deposition of 3D nanostructures. *Microelectron. Eng.*, 78-79:307–313, 2005. 107

[28] T. Bret, N. Utke, P. Hoffmann, M. Abourida, and P. Doppelt. Electron range effects in focused electron beam induced deposition of 3D nanostructures. *Microelectron. Eng.*, 83(4-9):1482–1486, 2006. 13, 14

[29] T. Brintlinger, M. S. Fuhrer, J. Melngailis, I. Utke, T. Bret, A. Perentes, P. Hoffmann, M. Abourida, and P. Doppelt. Electrodes for carbon nanotube devices by focused electron beam induced deposition of gold. *J. Vac. Sci. Technol. B*, 23(6):3174–3177, 2005. 10, 11

[30] S. J. Buckman, R. J. Gulley, M. Moghbelalhossein, and S. J. Bennett. Spatial Profiles of Effusive Molecular-Beams and Their Dependence on Gas Species. *Meas. Sci. Technol.*, 4(10):1143–1153, 1993. 97

[31] E. Buks and M. L. Roukes. Stiction, adhesion energy, and the Casimir effect in micromechanical systems. *Phys. Rev. B*, 63(3):033402, 2001. 66

[32] N. A. Burnham, X. Chen, C. S. Hodges, G. A. Matei, E. J. Thoreson, C. J. Roberts, M. C. Davies, and S. J. B. Tendler. Comparison of calibration methods for atomic-force microscopy cantilevers. *Nanotechnology*, 14(1):1–6, 2003. 47

[33] E. F. Burton, R. S. Sennett, and S. G. Ellis. Specimen Changes due to Electron Bombardment in the Electron Microscope. *Nature*, 160(4069):565–567, 1947. 9

[34] H. J. Butt, P. Siedle, K. Seifert, K. Fendler, T. Seeger, E. Bamberg, A. L. Weisenhorn, K. Goldie, and A. Engel. Scan Speed Limit in Atomic Force Microscopy. *J. Microsc.-Oxford*, 169:75–84, 1993. 47

[35] H. J. Butt, B. Cappella, and M. Kappl. Force measurements with the atomic force microscope: Technique, interpretation and applications. *Surf. Sci. Rep.*, 59(1-6):1–152, 2005. 17

[36] L. Calabri, N. Pugno, W. Ding, and R. S. Ruoff. Resonance of curved nanowires. *J. Phys.-Condens. Mat.*, 18(33):S2175–S2183, 2006. 67

[37] D. W. Carr, S. Evoy, L. Sekaric, H. G. Craighead, and J. M. Parpia. Measurement of mechanical resonance and losses in nanometer scale silicon wires. *Appl. Phys. Lett.*, 75(7):920–922, 1999. 72

[38] L. G. Carrascosa, M. Moreno, M. Alvarez, and L. M. Lechuga. Nanomechanical biosensors: a new sensing tool. *Trac-Trend. Anal. Chem.*, 25(3):196–206, 2006. 34

[39] M. Castagne, M. Benfedda, S. Lahimer, P. Falgayrettes, and J. P. Fillard. Near field optical behaviour of C supertips. *Ultramicroscopy*, 76(4):187–194, 1999. 11

[40] G. Y. Chen, T. Thundat, E. A. Wachter, and R. J. Warmack. Adsorption-Induced Surface Stress and Its Effects on Resonance Frequency of Microcantilevers. *J. Appl. Phys.*, 77(8):3618–3622, 1995. 34

[41] Y. X. Chen, B. L. Dorgan, D. N. McIlroy, and D. E. Aston. On the importance of boundary conditions on nanomechanical bending behavior and elastic modulus determination of silver nanowires. *J. Appl. Phys.*, 100(10):104301, 2006. 62

[42] T. P. Chiang, H. H. Sawin, and C. V. Thompson. Surface kinetic study of ion-induced chemical vapor deposition of copper for focused ion beam applications. *J. Vac. Sci. Technol. A*, 15(6): 3104–3114, 1997. 16

[43] K. K. Choi and S. W. Rhee. Effect of the neutral ligand (L) on the characteristics of hexafluoroacetylacetonate (hfac)Cu(I)-L precursor and on the copper deposition process. *Thin Solid Films*, 409(1):147–152, 2002. 99, 125

[44] R. W. Christy. Formation of Thin Polymer Films by Electron Bombardment. *J. Appl. Phys.*, 31 (9):1680–1683, 1960. 11

[45] V. Cimalla, F. Niebelschuetz, K. Tonisch, C. Foerster, K. Brueckner, I. Cimalla, T. Friedrich, J. Pezoldt, R. Stephan, M. Hein, and O. Ambacher. Nanoelectromechanical devices for sensing applications. *Sensor. Actuat. B-Chem.*, 126(1):24–34, 2007. 41

[46] Natalia Cividjian. *Electron beam induced nanometer scale deposition.* DUP Science, Delft, 2002. 9

[47] Natalia Cividjian. *Electron-beam-induced nanometer-scale deposition.* Elsevier, Amsterdam, 2006. 9

[48] P. Clausing. Flow of Highly Rarefied Gases through Tubes of Arbitrary Length. *J. Vac. Sci. Technol.*, 8(5):636, 1971. 80, 87

[49] A. N. Cleland. Thermomechanical noise limits on parametric sensing with nanomechanical resonators. *New J. Phys.*, 7:235, 2005. 40, 41

[50] A. N. Cleland and M. L. Roukes. Noise processes in nanomechanical resonators. *J. Appl. Phys.*, 92(5):2758–2769, 2002. 41

[51] J. P. Cleveland, S. Manne, D. Bocek, and P. K. Hansma. A Nondestructive Method for Determining the Spring Constant of Cantilevers for Scanning Force Microscopy. *Rev. Sci. Instrum.*, 64(2):403–405, 1993. 47

[52] C. A. Clifford and M. P. Seah. The determination of atomic force microscope cantilever spring constants via dimensional methods for nanomechanical analysis. *Nanotechnology*, 16(9):1666–1680, 2005. 47

[53] J. W. Coburn and H. F. Winters. Ion-Assisted and Electron-Assisted Gas-Surface Chemistry - Important Effect in Plasma-Etching. *J. Appl. Phys.*, 50(5):3189–3196, 1979. 11

[54] M. C. Cross and R. Lifshitz. Elastic wave transmission at an abrupt junction in a thin plate with application to heat transport and vibrations in mesoscopic systems. *Phys. Rev. B*, 64(8):085324, 2001. 71

[55] P. A. Crozier, J. Tolle, J. Kouvetakis, and C. Ritter. Synthesis of uniform GaN quantum dot arrays via electron nanolithography of D2GaN3. *Appl. Phys. Lett.*, 84(18):3441–3443, 2004. 3

[56] C. Danelon, C. Santschi, J. Brugger, and H. Vogel. Fabrication and functionalization of nanochannels by electron-beam-induced silicon oxide deposition. *Langmuir*, 22(25):10711–10715, 2006. 11

[57] N. Davidson and J. Hillier. Single Crystal Electron Diffraction by Micro-Crystalline Materials. *J. Appl. Phys.*, 18(6):499–511, 1947. 10

[58] D. H. Davis. Monte-Carlo Calculation of Molecular Flow Rates through a Cylindrical Elbow and Pipes of Other Shapes. *J. Appl. Phys.*, 31(7):1169–1176, 1960. 84

[59] B. B. Dayton. Vacuum technology as applied to continuously pumped systems. In A.H. Beck, editor, *Gases and vacua.* Pergamon, Oxford, 1965. 93

[60] A. D. Dellaratta, J. Melngailis, and C. V. Thompson. Focused-Ion Beam-Induced Deposition of Copper. *J. Vac. Sci. Technol. B*, 11(6):2195–2199, 1993. 11

[61] S. Dhara. Formation, dynamics, and characterization of nanostructures by ion beam irradiation. *Crit. Rev. Solid State*, 32(1-2):1–50, 2007. 5

[62] D. A. Dikin, X. Chen, W. Ding, G. Wagner, and R. S. Ruoff. Resonance vibration of amorphous SiO2 nanowires driven by mechanical or electrical field excitation. *J. Appl. Phys.*, 93(1):226–230, 2003. 17

[63] W. Ding, D. A. Dikin, X. Chen, R. D. Piner, R. S. Ruoff, E. Zussman, X. Wang, and X. Li. Mechanics of hydrogenated amorphous carbon deposits from electron-beam-induced deposition of a paraffin precursor. *J. Appl. Phys.*, 98(1):014905, 2005. 10, 65, 75

[64] W. Q. Ding, L. Calabri, X. Q. Chen, K. M. Kohhaas, and R. S. Ruoff. Mechanics of crystalline boron nanowires. *Compos. Sci. Technol.*, 66(9):1112–1124, 2006. 17, 67, 74

[65] S. Dohn, R. Sandberg, W. Svendsen, and A. Boisen. Enhanced functionality of cantilever based mass sensors using higher modes. *Appl. Phys. Lett.*, 86(23), 2005. 39

[66] P. Doppelt, V. Weigel, and P. Guinot. Mineral Precursor for Chemical Vapor-Deposition of Rh Metallic-Films. *Mat. Sci. Eng. B-Solid*, 17(1-3):143–146, 1993. 99, 125

[67] A. D. Dubner. *Mechanism of Ion Beam Induced Deposition.* PhD thesis, Massachusetts Institute of Technology, 1990. 16

[68] A. D. Dubner and A. Wagner. Insitu Measurement of Ion-Beam-Induced Deposition of Gold. *J. Appl. Phys.*, 65(9):3636–3643, 1989. 15

[69] A. D. Dubner and A. Wagner. The Role of Gas-Adsorption in Ion-Beam-Induced Deposition of Gold. *J. Appl. Phys.*, 66(2):870–874, 1989. 15

[70] A. D. Dubner and A. Wagner. Mechanism of Ion-Beam Induced Deposition of Gold. *J. Vac. Sci. Technol. B*, 7(6):1950–1953, 1989. 114

[71] A. D. Dubner, A. Wagner, J. Melngailis, and C. V. Thompson. The Role of the Ion-Solid Interaction in Ion-Beam-Induced Deposition of Gold. *J. Appl. Phys.*, 70(2):665–673, 1991. 16

[72] J. S. Duerr and R. E. Ogilvie. Electron-Probe Microdetermination of Carbon in Ferrous Alloys. *Anal. Chem.*, 44(14):2361, 1972. 10

[73] E. Dupas, G. Gremaud, A. Kulik, and J. L. Loubet. High-frequency mechanical spectroscopy with an atomic force microscope. *Rev. Sci. Instrum.*, 72(10):3891–3897, 2001. 39

[74] U. Durig, J. K. Gimzewski, and D. W. Pohl. Experimental-Observation of Forces Acting during Scanning Tunneling Microscopy. *Phys. Rev. Lett.*, 57(19):2403–2406, 1986. 44

[75] Saul Dushman. *Scientific foundations of vacuum technique.* Wiley, New York, second edition, 1962. 81

[76] K. Edinger and T. Kraus. Modeling of focused ion beam induced surface chemistry. *J. Vac. Sci. Technol. B*, 18(6):3190–3193, 2000. 116

[77] K. Edinger and T. Kraus. Modeling of focused ion beam induced chemistry and comparison with experimental data. *Microelectron. Eng.*, 57-8:263–268, 2001. 113

[78] K. L. Ekinci and M. L. Roukes. Nanoelectromechanical systems. *Rev. Sci. Instrum.*, 76(6): 061101, 2005. 37, 41, 71

[79] K. L. Ekinci, Y. T. Yang, and M. L. Roukes. Ultimate limits to inertial mass sensing based upon nanoelectromechanical systems. *J. Appl. Phys.*, 95(5):2682–2689, 2004. 41

[80] M. S. El-Morsi, A. C. Wei, G. F. Nellis, R. L. Engelstad, S. Sijbrandij, D. Stewart, and H. Mulders. Gas flow modeling for focused ion beam (FIB) repair processes. In W. Staud and J. T. Weed, editors, *Proceedings of SPIE - The International Society for Optical Engineering*, volume 5567 of *24th Annual BACUS Symposium on Photomask Technology*, pages 467–476, Monterey, CA, 2004. 6

[81] A. E. Ennos. The Origin of Specimen Contamination in the Electron Microscope. *Brit. J. Appl. Phys.*, 4(Apr):101–106, 1953. 10

[82] A. E. Ennos. The Sources of Electron-Induced Contamination in Kinetic Vacuum Systems. *Brit. J. Appl. Phys.*, 5(Jan):27–31, 1954. 10

[83] S. Fahlbusch, S. Mazerolle, J. M. Breguet, A. Steinecker, J. Agnus, R. Perez, and J. Michler. Nanomanipulation in a scanning electron microscope. *J. Mater. Process. Tech.*, 167(2-3):371–382, 2005. 27

[84] M. R. Falvo, G. J. Clary, R. M. Taylor, V. Chi, F. P. Brooks, S. Washburn, and R. Superfine. Bending and buckling of carbon nanotubes under large strain. *Nature*, 389(6651):582–584, 1997. 17

[85] A. Folch, J. Servat, J. Esteve, J. Tejada, and M. Seco. High-vacuum versus "environmental" electron beam deposition. *J. Vac. Sci. Technol. B*, 14(4):2609–2614, 1996. 3

[86] L. Folks, M. E. Best, P. M. Rice, B. D. Terris, D. Weller, and J. N. Chapman. Perforated tips for high-resolution in-plane magnetic force microscopy. *Appl. Phys. Lett.*, 76(7):909–911, 2000. 11

[87] J. D. Fowlkes, S. J. Randolph, and P. D. Rack. Growth and simulation of high-aspect ratio nanopillars by primary and secondary electron-induced deposition. *J. Vac. Sci. Technol. B*, 23 (6):2825–2832, 2005. 9, 12

[88] L. Frey, C. Lehrer, and H. Ryssel. Nanoscale effects in focused ion beam processing. *Appl. Phys. A-Mater.*, 76(7):1017–1023, 2003. 51

[89] V. Friedli, C. Santschi, J. Michler, P. Hoffmann, and I. Utke. Mass sensor for in situ monitoring of focused ion and electron beam induced processes. *Appl. Phys. Lett.*, 90(5):053106, 2007. 49, 50, 55, 71

[90] V. Friedli, S. Hoffmann, J. Michler, and I. Utke. AFM Sensors in Scanning Electron and Ion Microscopes: Tools for Nanomechanics, Nanoanalytics, and Nanofabrication. In B. Bhushan, H. Fuchs, and M. Tomitori, editors, *Applied Scanning Probe Methods VIII*, pages 247–288. Springer, Heidelberg, 2008 (available at `www.springer.com/978-3-540-74079-7`). 33

[91] C. R. Fritzsche. The Mechanism of Film Deposition by Particle-Beam Induced Polymerization. *J. Electrochem. Soc.*, 133(10):2131–2135, 1986. 11

[92] W. Fritzsche, K. Bohm, E. Unger, and J. M. Kohler. Making electrical contact to single molecules. *Nanotechnology*, 9(3):177–183, 1998. 11

[93] W. Fritzsche, J. M. Kohler, K. J. Bohm, E. Unger, T. Wagner, R. Kirsch, M. Mertig, and W. Pompe. Wiring of metallized microtubules by electron beam-induced structuring. *Nanotechnology*, 10(3):331–335, 1999. 11

[94] J. Fujita, M. Ishida, T. Sakamoto, Y. Ochiai, T. Kaito, and S. Matsui. Observation and characteristics of mechanical vibration in three-dimensional nanostructures and pillars grown by focused ion beam chemical vapor deposition. *J. Vac. Sci. Technol. B*, 19(6):2834–2837, 2001. 6, 17, 113

[95] J. Fujita, M. Ishida, T. Ichihashi, Y. Ochiai, T. Kaito, and S. Matsui. Growth of three-dimensional nano-structures using FIB-CVD and its mechanical properties. *Nucl. Instrum. Meth. B*, 206:472–477, 2003. 17

[96] J. Fujita, S. Okada, R. Ueki, M. Ishida, T. Kaito, and S. Matsu. Elastic double structure of amorphous carbon pillar grown by focused-ion-beam chemical vapor deposition. *Jpn. J. Appl. Phys. 1*, 46(9B):6286–6289, 2007. 18, 65

[97] L. Fustoss. Monte-Carlo Calculations for Free Molecular and near-Free Molecular-Flow through Axially-Symmetric Tubes. *Vacuum*, 31(6):243–246, 1981. 84

[98] M. Gad-el Hak. The fluid mechanics of microdevices - The Freeman Scholar Lecture. *J. Fluids Eng.-Trans. ASME*, 121(1):5–33, 1999. 91

[99] T. J. Gannon, G. Gu, J. D. Casey, C. Huynh, N. Bassom, and N. Antoniou. Focused ion beam induced deposition of low-resistivity copper material. *J. Vac. Sci. Technol. B*, 22(6):3000–3003, 2004. 113

[100] R. Garcia and R. Perez. Dynamic atomic force microscopy methods. *Surf. Sci. Rep.*, 47(6-8): 197–301, 2002. 43

[101] M. L. Garner, D. Chandra, and K. H. Lau. Low-temperature vapor pressures of W-, Cr-, and Co-carbonyls. *J. Phase Equilib.*, 16(1):24–29, 1995. 102, 125

[102] G. C. Gazzadi and S. Frabboni. Fabrication of 5 nm gap pillar electrodes by electron-beam Pt deposition. *J. Vac. Sci. Technol. B*, 23(2):L1–L3, 2005. 16

[103] GE Advanced Ceramics. `www.advceramics.com`, 2007. 25

[104] C. T. Gibson, G. S. Watson, and S. Myhra. Scanning force microscopy - Calibrative procedures for 'best practice'. *Scanning*, 19(8):564–581, 1997. 62

[105] C. T. Gibson, D. A. Smith, and C. J. Roberts. Calibration of silicon atomic force microscope cantilevers. *Nanotechnology*, 16(2):234–238, 2005. 47, 48

[106] R. F. Gibson, E. O. Ayorinde, and Y. F. Wen. Vibrations of carbon nanotubes and their composites: A review. *Compos. Sci. Technol.*, 67(1):1–28, 2007. 17

[107] A. E. Gildemeister, T. Ihn, C. Barengo, P. Studerus, and K. Ensslin. Construction of a dilution refrigerator cooled scanning force microscope. *Rev. Sci. Instrum.*, 78(1):013704, 2007. 44

[108] Joseph I. Goldstein. *Scanning electron microscopy and X-ray microanalysis.* Kluwer, New York, 3rd edition, 2003. 4

[109] V. Gopal, V. R. Radmilovic, C. Daraio, S. Jin, P. D. Yang, and E. A. Stach. Rapid prototyping of site-specific nanocontacts by electron and ion beam assisted direct-write nanolithography. *Nano Lett.*, 4(11):2059–2063, 2004. 11

[110] J. Greenwood. The correct and incorrect generation of a cosine distribution of scattered particles for Monte-Carlo modelling of vacuum systems. *Vacuum*, 67(2):217–222, 2002. 85, 127

[111] S. A. Gromilov, I. A. Baidina, P. A. Stabnikov, and G. V. Romanenko. Crystal structure of copper(II) bis-hexafluoroacetylacetonate. *J. Struct. Chem.*, 45(3):476–481, 2004. 118, 125

[112] J. M. Guevremont, S. Sheldon, and F. Zaera. Design and characterization of collimated effusive gas beam sources: Effect of source dimensions and backing pressure on total flow and beam profile. *Rev. Sci. Instrum.*, 71(10):3869–3881, 2000. 97

[113] R. A. Haefer. Addition theorem for the resistance to flow of composite systems and its relationship with the pumping speed in the region of molecular flow. *Vacuum*, 30(6):217–223, 1980. 80

[114] C. W. Hagen, N. Silvis-Cividjian, and P. Kruit. Resolution limit for electron beam-induced deposition on thick substrates. *Scanning*, 28(4):204–211, 2006. 7, 12, 114

[115] C. Hagleitner, A. Hierlemann, D. Lange, A. Kummer, N. Kerness, O. Brand, and H. Baltes. Smart single-chip gas sensor microsystem. *Nature*, 414(6861):293–296, 2001. 34

[116] O. Hansen and A. Boisen. Noise in piezoresistive atomic force microscopy. *Nanotechnology*, 10 (1):51–60, 1999. 42, 43

[117] S. Haraichi and M. Komuro. Broad-Pulsed Ga Ion-Beam-Assisted Etching of Si with Cl2. *Jpn. J. Appl. Phys. 1*, 32(12B):6168–6172, 1993. 12, 116

[118] L. R. Harriott and M. J. Vasile. Focused Ion-Beam Secondary Ion Mass-Spectrometry - Ion Images and Endpoint Detection. *J. Vac. Sci. Technol. B*, 7(2):181–187, 1989. 14

[119] L. R. Harriott, A. Wagner, and F. Fritz. Integrated-Circuit Repair Using Focused Ion-Beam Milling. *J. Vac. Sci. Technol. B*, 4(1):181–184, 1986. 14

[120] J. K. Haviland and M. L. Lavin. Application of the Monte-Carlo Method to Heat Transfer in a Rarefied Gas. *Phys. Fluids*, 5(11):1399–1405, 1962. 84

[121] P. J. Heard, J. R. A. Cleaver, and H. Ahmed. Application of a Focused Ion-Beam System to Defect Repair of VLSI Masks. *J. Vac. Sci. Technol. B*, 3(1):87–90, 1985. 14

[122] H. G. Heide. Elektronenmikroskopie: Von Objekten unter Atmosphärendruck oder unter Dr × ucken, welche ihre Austrocknung verhindern. *Naturwissenschaften*, 47(14):313–317, 1960. 10

[123] H. G. Heide. Contamination and Irradiation Effects and Their Dependence on Composition of Residual Gases in Electron Microscope. *Lab. Invest.*, 14(6P2):1134, 1965. 11, 22

[124] M. A. Henderson, R. D. Ramsier, and J. T. Yates. Minimizing Ultrahigh-Vacuum Wall Reactions of Fe(Co)5 by Chemical Pretreatment of the Dosing System. *J. Vac. Sci. Technol. A*, 9(5):2785–2787, 1991. 86

[125] Marian A. Herman and Helmut Sitter. *Molecular beam epitaxy fundamentals and current status.* Springer, Berlin etc., second, rev. and updated edition, 1996. 85, 92

[126] P. Hoffmann, I. Utke, and F. Cicoira. Limits of 3-D nanostructures fabricated by focused electron beam (FEB) induced deposition. In Z. I. Alferov and L. Esaki, editors, *Proceedings of SPIE - The International Society for Optical Engineering*, volume 5023 of *10th International Symposium on Nanostructures: Physics and Technology*, pages 4–10, St. Petersburg, 2003. 113

[127] S. Hoffmann, I. Utke, B. Moser, J. Michler, S. H. Christiansen, V. Schmidt, S. Senz, P. Werner, U. Gosele, and C. Ballif. Measurement of the bending strength of vapor-liquid-solid grown silicon nanowires. *Nano Lett.*, 6(4):622–625, 2006. 17

[128] S. Hoffmann, F. Ostlund, J. Michler, H. J. Fan, M. Zacharias, S. H. Christiansen, and C. Ballif. Fracture strength and Young's modulus of ZnO nanowires. *Nanotechnology*, 18(20):205503, 2007. 17

[129] P. C. Hoyle, J. R. A. Cleaver, and H. Ahmed. Ultralow-Energy Focused Electron-Beam-Induced Deposition. *Appl. Phys. Lett.*, 64(11):1448–1450, 1994. 11

[130] P. C. Hoyle, J. R. A. Cleaver, and H. Ahmed. Electron beam induced deposition from W(CO)6 at 2 to 20 keV and its applications. *J. Vac. Sci. Technol. B*, 14(2):662–673, 1996. 11

[131] B. Ilic, D. Czaplewski, M. Zalalutdinov, H. G. Craighead, P. Neuzil, C. Campagnolo, and C. Batt. Single cell detection with micromechanical oscillators. *J. Vac. Sci. Technol. B*, 19(6):2825–2828, 2001. 34

[132] M. Ishida, J. Fujita, and Y. Ochiai. Density estimation for amorphous carbon nanopillars grown by focused ion beam assisted chemical vapor deposition. *J. Vac. Sci. Technol. B*, 20(6):2784–2787, 2002. 18

[133] M. Ishida, J. Fujita, T. Ichihashi, Y. Ochiai, T. Kaito, and S. Matsui. Focused ion beam-induced fabrication of tungsten structures. *J. Vac. Sci. Technol. B*, 21(6):2728–2731, 2003. 17, 18

[134] H. Jiang, M. F. Yu, B. Liu, and Y. Huang. Intrinsic energy loss mechanisms in a cantilevered carbon nanotube beam oscillator. *Phys. Rev. Lett.*, 93(18):185501, 2004. 71

[135] D. C. Joy. SMART - a program to measure SEM resolution and imaging performance. *J. Microsc.-Oxford*, 208:24–34, 2002. 23

[136] D. C. Joy. D.C. Joy's "Database of Electron-Solid interactions" (available at `web.utk.edu/~srcutk/htm/interact.htm`). 2007. 56

[137] D. C. Joy. A Database on Electron-Solid Interactions. *Scanning*, 17(5):270–275, 1995. 56

[138] David C. Joy. *Monte Carlo modeling for electron microscopy and microanalysis.* Oxford University Press, New York etc., 1995. 7, 8, 57

[139] I. Jungwirthova, J. Eklund, Y. Sun, and J. M. White. System for inducing and characterizing electron beam-induced surface reactions at pressures up to 10(-4) Torr. *Rev. Sci. Instrum.*, 73 (9):3302–3305, 2002. 11

[140] Keithley Instruments Inc., USA, Model 6485 5-1/2 digit picoammeter with 10 fA resolution. `www.keithley.com`, 2007. 21

[141] A. Kis, G. Csanyi, J. P. Salvetat, T. N. Lee, E. Couteau, A. J. Kulik, W. Benoit, J. Brugger, and L. Forro. Reinforcement of single-walled carbon nanotube bundles by intertube bridging. *Nat. Mater.*, 3(3):153–157, 2004. 17

[142] Kleindiek Nanotechnik, Germany. `www.kleindiek.com`, 2007. 27

[143] B. Kloeck. Piezoresistive Sensors. In Haim H. Bau, editor, *Mechanical sensors*, pages XIII, 674. VCH, Weinheim etc., 1994. 42

[144] M. Knudsen. Molecular current of hydrogen through channels and the heat conductor manometer. *Ann. Phys.-Berlin*, 35(7):389–396, 1911. 81

[145] T. T. Kodas and M. J. Hampden-Smith. *The chemistry of metal CVD.* VCH, Weinheim etc., 1994. 102, 125

[146] K. T. Kohlmann, M. Thiemann, and W. H. Brunger. E-Beam Induced X-Ray Mask Repair with Optimized Gas Nozzle Geometry. *Microelectron. Eng.*, 13(1-4):279–282, 1991. 5

[147] K. T. Kohlmann-von Platen and W. H. Bruenger. Electron-beam induced etching of resist with water vapor as the etching medium. *J. Vac. Sci. Technol. B*, 14(6):4262–4266, 1996. 11

[148] K. T. Kohlmann-von Platen, L. M. Buchmann, H. C. Petzold, and W. H. Brunger. Electron-Beam Induced Tungsten Deposition - Growth-Rate Enhancement and Applications in Microelectronics. *J. Vac. Sci. Technol. B*, 10(6):2690–2694, 1992. 11, 114

[149] T. Komoda and N. Morito. Experimental Study on the Specimen Contamination in Electron Microscopy. *J. Electron Microsc.*, 9(2):77–80, 1960. 10

[150] H. König. Die Rolle der Kohle bei elektronenmikroskopischen Abbildungen. *Naturwissenschaften*, 35(9):261–265, 1948. 9

[151] H. Konuma. Rate of Carbon Contamination on Copper, Iron and Aluminum Targets in Gas-Flows by an Electron-Microprobe. *Mikrochim. Acta*, 2(1-2):99–108, 1983. 10

[152] H. W. P. Koops, R. Weiel, D. P. Kern, and T. H. Baum. High-Resolution Electron-Beam Induced Deposition. *J. Vac. Sci. Technol. B*, 6(1):477–481, 1988. 10, 11

[153] H. W. P. Koops, A. Reinhardt, F. Klabunde, A. Kaya, and R. Plontke. Vapour supply manifold for additive nanolithography with electron beam induced deposition. *Microelectron. Eng.*, 57-8: 909–913, 2001. 5

[154] P. Krasuski. Angular-Distribution of Flux at the Exit of Cylindrical-Tubes. *J. Vac. Sci. Technol. A*, 5(4):2488–2492, 1987. 93

[155] A. Kulik, A. Kis, G. Gremaud, S. Hengsberger, G. Luengo, P. Zysset, and L. Forró. Nanoscale Mechanical Properties - Measuring Techniques and Applications. In Bharat Bhushan, editor, *Springer handbook of nanotechnology*, pages 1107–1136. Springer, Berlin, 2004. 17

[156] A. Kumao, H. Hashimoto, and K. Shiraishi. Studies on Specimen Contamination by Transmission Electron-Microscopy. *J. Electron Microsc.*, 30(3):161–170, 1981. 10

[157] R. R. Kunz and T. M. Mayer. Electron-Beam Induced Surface Nucleation and Low-Temperature Decomposition of Metal-Carbonyls. *J. Vac. Sci. Technol. B*, 6(5):1557–1564, 1988. 15, 103

[158] D. Kunze, O. Peters, and G Sauerbrey. Polymerisation adsorbierter Kohlenwasserstoffe bei Elektronenbeschuss. *Z. Angew. Physik*, 22(2):69, 1967. 15, 114

[159] M. V. Kurepa and C. B. Lucas. The Density Gradient of Molecules Flowing Along a Tube. *J. Appl. Phys.*, 52(2):664–669, 1981. 87

[160] James M. Lafferty. *Foundations of vacuum science and technology.* Wiley, New York, 1998. 25, 78, 79, 80, 81, 82, 86, 87, 125

[161] H. P. Lang, R. Berger, C. Andreoli, J. Brugger, M. Despont, P. Vettiger, C. Gerber, J. K. Gimzewski, J. P. Ramseyer, E. Meyer, and H. J. Guntherodt. Sequential position readout from arrays of micromechanical cantilever sensors. *Appl. Phys. Lett.*, 72(3):383–385, 1998. 34, 46

[162] R. M. Langford. Focused ion beam nanofabrication: A comparison with conventional processing techniques. *J. Nanosci. Nanotechno.*, 6(3):661–668, 2006. 5

[163] N. V. Lavrik, M. J. Sepaniak, and P. G. Datskos. Cantilever transducers as a platform for chemical and biological sensors. *Rev. Sci. Instrum.*, 75(7):2229–2253, 2004. 34

[164] Leica Microsystems GmbH, Switzerland. `www.leica-microsystems.com`, 2007. 25

[165] H. J. Lezec, A. Degiron, E. Devaux, R. A. Linke, L. Martin-Moreno, F. J. Garcia-Vidal, and T. W. Ebbesen. Beaming light from a subwavelength aperture. *Science*, 297(5582):820–822, 2002. 11

[166] W. Li and D. C. Joy. Study of temperature influence on electron beam induced deposition. *J. Vac. Sci. Technol. A*, 24(3):431–436, 2006. 9

[167] J. Ling. An Approximate Expression for Growth Rate of Surface Contamination on Electron Microscope Specimens. *Brit. J. Appl. Phys.*, 17(4):565, 1966. 11

[168] R. Linnemann, T. Gotszalk, L. Hadjiiski, and I. W. Rangelow. Characterization of a Cantilever with an Integrated Deflection Sensor. *Thin Solid Films*, 264(2):159–164, 1995. 42

[169] R. Linnemann, T. Gotszalk, I. W. Rangelow, P. Dumania, and E. Oesterschulze. Atomic force microscopy and lateral force microscopy using piezoresistive cantilevers. *J. Vac. Sci. Technol. B*, 14(2):856–860, 1996. 42

[170] S. Lipp, L. Frey, C. Lehrer, E. Demm, S. Pauthner, and H. Ryssel. A comparison of focused ion beam and electron beam induced deposition processes. *Microelectron. Reliab.*, 36(11-12): 1779–1782, 1996. 57

[171] S. Lipp, L. Frey, C. Lehrer, B. Frank, E. Demm, S. Pauthner, and H. Ryssel. Tetramethoxysilane as a precursor for focused ion beam and electron beam assisted insulator (SiOx) deposition. *J. Vac. Sci. Technol. B*, 14(6):3920–3923, 1996. 11, 114, 116, 117

[172] K. H. Liu, W. L. Wang, Z. Xu, L. Liao, X. D. Bai, and E. G. Wang. In situ probing mechanical properties of individual tungsten oxide nanowires directly grown on tungsten tips inside transmission electron microscope. *Appl. Phys. Lett.*, 89(22):3, 2006. 17

[173] Z. Q. Liu, K. Mitsuishi, and K. Furuya. Modeling the process of electron-beam-induced deposition by dynamic Monte Carlo simulation. *Jpn. J. Appl. Phys. 1*, 44(7B):5659–5663, 2005. 12

[174] Z. Q. Liu, K. Mitsuishi, and K. Furuya. A dynamic Monte Carlo study of the in situ growth of a substance deposited using electron-beam-induced deposition. *Nanotechnology*, 17(15):3832–3837, 2006. 12

[175] R. G. Livesey. Solution methods for gas flow in ducts through the whole pressure regime. *Vacuum*, 76(1):101–107, 2004. 82

[176] A. Luisier, I. Utke, T. Bret, F. Cicoira, R. Hauert, S. W. Rhee, P. Doppelt, and P. Hoffmann. Comparative study of Cu precursors for 3D focused electron beam induced deposition. *J. Electrochem. Soc.*, 151(8):C535–C537, 2004. 10, 125

[177] L. M. Lund and A. S. Berman. Flow and Self-Diffusion of Gases in Capillaries I. *J. Appl. Phys.*, 37(6):2489, 1966. 81

[178] L. M. Lund and A. S. Berman. Flow and Self-Diffusion of Gases in Capillaries II. *J. Appl. Phys.*, 37(6):2496, 1966. 81

[179] T. E. Madey. Electron-Stimulated and Photon-Stimulated Desorption - Probes of Structure and Bonding at Surfaces. *Science*, 234(4774):316–322, 1986. 9

[180] Marc J. Madou. *Fundamentals of microfabrication: the science of miniaturization.* CRC Press, Boca Raton, FL, 2nd edition, 2002. 42, 46, 56

[181] D. N. Madsen, K. Molhave, R. Mateiu, A. M. Rasmussen, M. Brorson, C. J. H. Jacobsen, and P. Boggild. Soldering of nanotubes onto microelectrodes. *Nano Lett.*, 3(1):47–49, 2003. 11

[182] E. Majorana and Y. Ogawa. Mechanical thermal noise in coupled oscillators. *Phys. Lett. A*, 233 (3):162–168, 1997. 37

[183] S. Matsui and M. Mito. Si Deposition by Electron-Beam Induced Surface-Reaction. *Appl. Phys. Lett.*, 53(16):1492–1494, 1988. 14

[184] S. Matsui and K. Mori. New Selective Deposition Technology by Electron-Beam Induced Surface-Reaction. *Jpn. J. Appl. Phys. 2*, 23(9):L706–L708, 1984. 5, 9

[185] S. Matsui and K. Mori. New Selective Deposition Technology by Electron-Beam Induced Surface-Reaction. *J. Vac. Sci. Technol. B*, 4(1):299–304, 1986. 3

[186] S. Matsui and K. Mori. Insitu Observation on Electron-Beam Induced Chemical Vapor-Deposition by Auger-Electron Spectroscopy. *Appl. Phys. Lett.*, 51(9):646–648, 1987. 14

[187] S. Mazerolle, R. Rabe, T. Varidel, A. Bergander, and J. M. Breguet. High thrust force linear actuators. In *Proceedings of the International Symposium on Robotics*, pages 23–26, Paris - France, 2004. 27

[188] A. W. McFarland, M. A. Poggi, M. J. Doyle, L. A. Bottomley, and J. S. Colton. Influence of surface stress on the resonance behavior of microcantilevers. *Appl. Phys. Lett.*, 87(5):053505, 2005. 34

[189] D. McMullan. Scanning Electron-Microscopy 1928-1965. *Scanning*, 17(3):175–185, 1995. 9

[190] Megatron AG, Switzerland. `www.megatron.ch`, 2007. 28, 67

[191] R. Melamud, B. Kim, S. A. Chandorkar, M. A. Hopcroft, M. Agarwal, C. M. Jha, and T. W. Kenny. Temperature-compensated high-stability silicon resonators. *Appl. Phys. Lett.*, 90(24): 244107, 2007. 46

[192] J. Merhaut. *Theory of electroacoustics.* McGraw-Hill, New York a.o., 1981. 39

[193] G. Meyer and N. M. Amer. Novel Optical Approach to Atomic Force Microscopy. *Appl. Phys. Lett.*, 53(12):1045–1047, 1988. 41

[194] K. Mitsuishi, Z. Q. Liu, M. Shimojo, M. Han, and K. Furuya. Dynamic profile calculation of deposition resolution by high-energy electrons in electron-beam-induced deposition. *Ultramicroscopy*, 103(1):17–22, 2005. 12

[195] K. Mitsuishi, M. Shimojo, M. Takeguchi, M. Tanaka, and K. Furuya. Proximity effect in electron-beam-induced deposition. *Jpn. J. Appl. Phys. 1*, 45(6B):5517–5521, 2006. 60

[196] K. Molhave. *Tools for In-situ Manipulation and Characterization of Nanostructures.* PhD thesis, Technical University of Denmark, 2004. 29

[197] K. Molhave, D. N. Madsen, A. M. Rasmussen, A. Carlsson, C. C. Appel, M. Brorson, C. J. H. Jacobsen, and P. Boggild. Solid gold nanostructures fabricated by electron beam deposition. *Nano Lett.*, 3(11):1499–1503, 2003. 10

[198] B. C. Moore. Gas Flux Patterns in Cylindrical Vacuum-Systems. *J. Vac. Sci. Technol.*, 9(3): 1090, 1972. 91

[199] B. Moser, K. Wasmer, L. Barbieri, and J. Michler. Strength and fracture of Si micropillars: A new scanning electron microscopy-based micro-compression test. *J. Mater. Res.*, 22(4):1004–1011, 2007. 10

[200] J. J. L. Mulders, D. A. M. de Winter, and W. J. H. C. P. Duinkerken. Measures and calculations of FIB milling yield of bulk metals. *Microelectron. Eng.*, 84(5-8):1540–1543, 2007. 50

[201] K. H. Müller. Elektronen-Mikroschreiber mit geschwindigkeitsgesteuerter Strahlführung. I. *Optik*, 33(3):296–311, 1971. 11

[202] T. Nagata, P. Ahmet, Y. Sakuma, T. Sekiguchi, and T. Chikyow. GaN nanostructure fabrication by focused-ion-beam-assisted chemical vapor deposition. *Appl. Phys. Lett.*, 87(1):013103, 2005. 11

[203] K. Nakamatsu, M. Nagase, J. Y. Igaki, H. Namatsu, and S. Matsui. Mechanical characteristics and its annealing effect of diamondlike-carbon nanosprings fabricated by focused-ion-beam chemical vapor deposition. *J. Vac. Sci. Technol. B*, 23(6):2801–2805, 2005. 17

[204] Nanonis GmbH, Switzerland. `www.nanonis.com`, 2007. 30, 68

[205] Nanosensors™ (Nano World AG, Switzerland). `www.nanosensors.com`, 2007. 29

[206] Nanosurf AG, Switzerland. `www.nanosurf.com`, 2007. 30

[207] Nanotools GmbH, Germany. `www.nano-tools.com`, 2007. 11

[208] Nascatec GmbH, Germany. `www.nascatec.com`, 2007. 29, 43

[209] NaWoTec GmbH, Germany. `www.nawotec.com`, 2007. 11

[210] P. M. Nellen and R. Bronnimann. Milling micro-structures using focused ion beams and its application to photonic components. *Meas. Sci. Technol.*, 17(5):943–948, 2006. 5

[211] P. M. Nellen, V. Callegari, and R. Bronnimann. FIB-milling of photonic structures and sputtering simulation. *Microelectron. Eng.*, 83(4-9):1805–1808, 2006. 11

[212] J. Nilsson, J. R. I. Lee, T. V. Ratto, and S. E. Letant. Localized functionalization of single nanopores. *Adv. Mater.*, 18(4):427, 2006. 11

[213] M. Nishio, S. Sawaya, S. Akita, and Y. Nakayama. Carbon nanotube oscillators toward zeptogram detection. *Appl. Phys. Lett.*, 86(13):133111, 2005. 19

[214] M. Nishio, S. Sawaya, S. Akita, and Y. Nakayama. Density of electron-beam-induced amorphous carbon deposits. *J. Vac. Sci. Technol. B*, 23(5):1975–1979, 2005. 19

[215] A. Noy, D. V. Vezenov, and C. M. Lieber. Chemical force microscopy. *Annu. Rev. Mater. Sci.*, 27:381–421, 1997. 17

[216] C. W. Oatley. The Early History of the Scanning Electron-Microscope. *J. Appl. Phys.*, 53(2): R1–R13, 1982. 9

[217] Y. Ochiai, K. Shihoyama, T. Shiokawa, K. Toyoda, A. Masuyama, K. Gamo, and S. Namba. Characteristics of Maskless Ion-Beam Assisted Etching of Silicon Using Focused Ion-Beams. *J. Vac. Sci. Technol. B*, 4(1):333–336, 1986. 5

[218] Milton Ohring. *Materials science of thin films deposition and structure.* Academic Press, San Diego, 2nd edition, 2002. 9

[219] T. Ohta, F. Cicoira, P. Doppelt, L. Beitone, and P. Hofmann. Static vapor pressure measurement of low volatility precursors for molecular vapor deposition below ambient temperature. *Chem. Vapor Depos.*, 7(1):33–37, 2001. 125

[220] S. Okada, T. Mukawa, R. Kobayashi, J. Fujita, M. Ishida, T. Ichihashi, Y. Ochiai, T. Kaito, and S. Matsui. Growth manner and mechanical characteristics of amorphous carbon nanopillars grown by electron-beam-induced chemical vapor deposition. *Jpn. J. Appl. Phys. 1*, 44(7B):5646–5650, 2005. 6

[221] S. Okada, T. Mukawa, R. Kobayashi, M. Ishida, Y. Ochiai, T. Kaito, S. Matsui, and J. Fujita. Comparison of Young's modulus dependency on beam accelerating voltage between electron-beam- and focused ion-beam-induced chemical vapor deposition pillars. *Jpn. J. Appl. Phys. 1*, 45(6B):5556–5559, 2006. 18, 65

[222] Jon Orloff. *Handbook of charged particle optics.* CRC Press, Boca Raton, Florida etc., 1997. 5

[223] I. Palaci, S. Fedrigo, H. Brune, C. Klinke, M. Chen, and E. Riedo. Radial elasticity of multiwalled carbon nanotubes. *Phys. Rev. Lett.*, 94(17):–, 2005. 17

[224] J. G. Pellerin, G. M. Shedd, D. P. Griffis, and P. E. Russell. Characterization of Focused Ion-Beam Micromachined Features. *J. Vac. Sci. Technol. B*, 7(6):1810–1812, 1989. 49

[225] A. Perentes and P. Hoffmann. Focused electron beam induced deposition of Si-based materials from SiOxCy to stoichiometric SiO2: Chemical compositions, chemical-etch rates, and deep ultraviolet optical transmissions. *Chem. Vapor Depos.*, 13(4):176–184, 2007. 10, 11

[226] A. Perentes, A. Bachmann, M. Leutenegger, I. Utke, C. Sandu, and P. Hoffmann. Focused electron beam induced deposition of a periodic transparent nano-optic pattern. *Microelectron. Eng.*, 73-74:412–416, 2004. 11

[227] A. Perentes, T. Bret, I. Utke, P. Hoffmann, and M. Vaupel. Real-time reflectometry-controlled focused-electron-beam-induced deposition of transparent materials. *J. Vac. Sci. Technol. B*, 24 (2):587–591, 2006. 15

[228] A. Perentes, G. Sinocco, G. Boero, B. Dwir, and P. Hoffman. Focused electron beam induced deposition of Nickel. *J. Vac. Sci. Technol. B*, 25(6):2228, 2007. 10

[229] S. Perisanu, P. Vincent, A. Ayari, M. Choueib, D. Guillot, M. Bechelany, D. Cornu, P. Miele, and S. T. Purcell. Ultra high sensitive detection of mechanical resonances of nanowires by field emission microscopy. *Phys. Status Solidi. A*, 204(6):1645–1652, 2007. 69

[230] S. Perisanu, P. Vincent, A. Ayari, M. Choueib, S. T. Purcell, M. Bechelany, and D. Cornu. High Q factor for mechanical resonances of batch-fabricated SiC nanowires. *Appl. Phys. Lett.*, 90(4): 043113, 2007. 72

[231] H. C. Petzold and P. J. Heard. Ion-Induced Deposition for X-Ray Mask Repair - Rate Optimization Using a Time-Dependent Model. *J. Vac. Sci. Technol. B*, 9(5):2664–2669, 1991. 114

[232] D. M. Photiadis and J. A. Judge. Attachment losses of high Q oscillators. *Appl. Phys. Lett.*, 85 (3):482–484, 2004. 71

[233] Physik Instrumente (PI), Germany. `www.physikinstrumente.com`, 2007. 26, 62

[234] W. G. Pollard and R. D. Present. On Gaseous Self-Diffusion in Long Capillary Tubes. *Phys. Rev.*, 73(7):762–774, 1948. 81

[235] P. Poncharal, Z. L. Wang, D. Ugarte, and W. A. de Heer. Electrostatic deflections and electromechanical resonances of carbon nanotubes. *Science*, 283(5407):1513–1516, 1999. 17

[236] W. H. Press, S. A. Teulkolsky, W. T. Vetterling, and B. P. Flannery. *Numerical Recipes in C: The Art of Scientific Computing.* Cambridge University Press, 2007. 89

[237] BC Prorok, Y Zhu, HD Espinosa, Z Guo, ZP Bazant, Y Zhao, and BI Yakobson. *Micro- and Nanomechanics*, volume 5 of *Encyclopedia of Nanoscience and Nanotechnology.* American Scientific Publishers, 2004. 16

[238] S. T. Purcell, P. Vincent, C. Journet, and V. T. Binh. Tuning of nanotube mechanical resonances by electric field pulling. *Phys. Rev. Lett.*, 89(27):4, 2002. 17

[239] U. Rabe, J. Turner, and W. Arnold. Analysis of the high-frequency response of atomic force microscope cantilevers. *Appl. Phys. A-Mater.*, 66:S277–S282, 1998. 36, 39

[240] P. D. Rack. In situ probing of the growth and morphology in electron-beam-induced deposited nanostructures. *Nanotechnology*, 18(46):465602, 2007. 14, 60

[241] P. D. Rack, S. Randolph, Y. Deng, J. Fowlkes, Y. Choi, and D. C. Joy. Nanoscale electron-beam-stimulated processing. *Appl. Phys. Lett.*, 82(14):2326–2328, 2003. 14

[242] G. M. Rackham and J. A. Eades. Specimen Contamination in Electron-Microscope When Small Probes Are Used. *Optik*, 47(2):227–232, 1977. 10

[243] R. D. Ramsier and J. T. Yates. Electron-Stimulated Desorption - Principles and Applications. *Surf. Sci. Rep.*, 12(6-8):243–378, 1991. 9

[244] S. J. Randolph, J. D. Fowlkes, and P. D. Rack. Focused, nanoscale electron-bearn-induced deposition and etching. *Crit. Rev. Solid State*, 31(3):55–89, 2006. 9, 11, 57

[245] V. Ray. Gas delivery and virtual process chamber concept for gas-assisted material processing in a focused ion beam system. *J. Vac. Sci. Technol. B*, 22(6):3008–3011, 2004. 6

[246] Ludwig Reimer. *Scanning electron microscopy physics of image formation and microanalysis.* Springer, Berlin [etc.], second completely rev. and updated edition, 1998. 3, 4, 8, 14, 21, 56, 57

[247] S. Reyntjens and R. Puers. A review of focused ion beam applications in microsystem technology. *J. Micromech. Microeng.*, 11(4):287–300, 2001. 5, 51

[248] H. S. Rhee and B. T. Ahn. Cobalt metallorganic chemical vapor deposition and formation of epitaxial CoSi2 layer on Si(100) substrate. *J. Electrochem. Soc.*, 146(7):2720–2724, 1999. 102

[249] S. A. Rishton, S. P. Beaumont, and C. D. W. Wilkinson. Measurement of the Profile of Finely Focused Electron-Beams in a Scanning Electron-Microscope. *J. Phys. E Sci. Instrum.*, 17(4): 296–303, 1984. 21

[250] J. S. Ro, C. V. Thompson, and J. Melngailis. Mechanism of Ion-Beam-Induced Deposition of Gold. *J. Vac. Sci. Technol. B*, 12(1):73–77, 1994. 114

[251] J. Robertson. Diamond-like amorphous carbon. *Mat. Sci. Eng. R*, 37(4-6):129–281, 2002. 75

[252] Sheldon M. Ross. *Simulation.* Elsevier Academic Press, Burlington, 4th edition, 2006. 89

[253] S. Roy, R. Raju, H. F. Chuang, B. A. Cruden, and M. Meyyappan. Modeling gas flow through microchannels and nanopores. *J. Appl. Phys.*, 93(8):4870–4879, 2003. 79

[254] F. Rugamas, D. Roundy, G. Mikaelian, G. Vitug, M. Rudner, J. Shih, D. Smith, J. Segura, and M. A. Khakoo. Angular profiles of molecular beams from effusive tube sources: I. Experiment. *Meas. Sci. Technol.*, 11(12):1750–1765, 2000. 94, 97

[255] K. Rykaczewski, W. B. White, and A. G. Fedorov. Analysis of electron beam induced deposition (EBID) of residual hydrocarbons in electron microscopy. *J. Appl. Phys.*, 101(5):054307, 2007. 12

[256] J. E. Sader. Atomic Force Microscopy: Cantilever Calibration. In A. T. Hubbard, editor, *Encyclopedia of surface and colloid science*, page 846. Dekker, New York, 2002. 47, 48

[257] J. E. Sader, I. Larson, P. Mulvaney, and L. R. White. Method for the Calibration of Atomic-Force Microscope Cantilevers. *Rev. Sci. Instrum.*, 66(7):3789–3798, 1995. 37, 39, 47, 48, 53

[258] E. J. Sanchez, J. T. Krug, and X. S. Xie. Ion and electron beam assisted growth of nanometric SimOn structures for near-field microscopy. *Rev. Sci. Instrum.*, 73(11):3901–3907, 2002. 11

[259] R. Sandberg, K. Molhave, A. Boisen, and W. Svendsen. Effect of gold coating on the Q-factor of a resonant cantilever. *J. Micromech. Microeng.*, 15(12):2249–2253, 2005. 46

[260] D. Santamore, K. Edinger, J. Orloff, and J. Melngailis. Focused ion beam sputter yield change as a function of scan speed. *J. Vac. Sci. Technol. B*, 15(6):2346–2349, 1997. 50

[261] D. J. Santeler. New Concepts in Molecular Gas-Flow. *J. Vac. Sci. Technol. A*, 4(3):338–343, 1986. 80

[262] C. Santschi, M. Jenke, P. Hoffmann, and J. Brugger. Interdigitated 50 nm Ti electrode arrays fabricated using XeF2 enhanced focused ion beam etching. *Nanotechnology*, 17(11):2722–2729, 2006. 117

[263] G. Sauerbrey. Verwendung von Schwingquarzen zur Wägung dünner Schichten und zur Mikrowägung. *Z. Phys.*, 155(2):206–222, 1959. 15, 38

[264] S. Sawaya, S. Akita, and Y. Nakayama. In situ mass measurement of electron-beam-induced nanometer-sized W-related deposits using a carbon nanotube cantilever. *Appl. Phys. Lett.*, 89 (19):193115, 2006. 19

[265] V. Scheuer, H. Koops, and T. Tschudi. Electron beam decomposition of carbonyls on silicon. *Microelectron. Eng.*, 5(1-4):423–430, 1986. 6, 113, 114, 116

[266] K. I. Schiffmann. Investigation of fabrication parameters for the electron-beam-induced deposition of contamination tips used in atomic force microscopy. *Nanotechnology*, 4(3):163–169, 1993. 57

[267] M. P. Seah and W. A. Dench. Quantitative electron spectroscopy of surfaces: A standard data base for electron inelastic mean free paths in solids. *Surf. Interface Anal.*, 1(1):2–11, 1979. 7

[268] G. M. Shedd, H. Lezec, A. D. Dubner, and J. Melngailis. Focused Ion-Beam Induced Deposition of Gold. *Appl. Phys. Lett.*, 49(23):1584–1586, 1986. 5

[269] Ching Shen. *Rarefied gas dynamics fundamentals, simulations and micro flows.* Springer, Berlin, 2005. 79

[270] Z. Y. Shen, W. Y. Shih, and W. H. Shih. Mass detection sensitivity of piezoelectric cantilevers with a nonpiezoelectric extension. *Rev. Sci. Instrum.*, 77(6):065101, 2006. 39

[271] Y. Shi, C. Q. Chen, Y. S. Zhang, J. Zhu, and Y. J. Yan. Determination of the natural frequency of a cantilevered ZnO nanowire resonantly excited by a sinusoidal electric field. *Nanotechnology*, 18(7):6, 2007. 17

[272] M. Shimojo, K. Mitsuishi, M. Tanaka, M. Han, and K. Furuya. Application of transmission electron microscopes to nanometre-sized fabrication by means of electron beam-induced deposition. *J. Microsc.-Oxford*, 214:76–79, 2004. 3

[273] N. Silvis-Cividjian, C. W. Hagen, L. H. A. Leunissen, and P. Kruit. The role of secondary electrons in electron-beam-induced-deposition spatial resolution. *Microelectron. Eng.*, 61-2:693–699, 2002. 12

[274] N. Silvis-Cividjian, C. W. Hagen, P. Kruit, M. A. J. Van der Stam, and H. B. Groen. Direct fabrication of nanowires in an electron microscope. *Appl. Phys. Lett.*, 82(20):3514–3516, 2003. 3

[275] N. Silvis-Cividjian, C. W. Hagen, and P. Kruit. Spatial resolution limits in electron-beam-induced deposition. *J. Appl. Phys.*, 98(8):084905, 2005. 9, 12

[276] SmarAct GmbH, Germany. `www.smaract.de`, 2007. 24

[277] C. G. Smith and G. Lewin. Free Molecular Conductance of a Cylindrical Tube with Wall Sorption. *J. Vac. Sci. Technol.*, 3(3):92, 1966. 86

[278] D. A. Smith, J. D. Fowlkes, and P. D. Rack. A nanoscale three-dimensional Monte Carlo simulation of electron-beam induced deposition with gas dynamics. *Nanotechnology*, 18(26):265308, 2007. 12

[279] G. Stemme. Resonant silicon sensors. *J. Micromech. Microeng.*, 1(2):113, 1991. 34

[280] R. E. Stickney, R. F. Keating, S. Yamamoto, and W. J. Hastings. Angular Distribution of Flow from Orifices and Tubes at High Knudsen Numbers. *J. Vac. Sci. Technol.*, 4(1):10, 1967. 93, 94

[281] M. Tanaka, M. Shimojo, K. Mitsuishi, and K. Furuya. The size dependence of the nano-dots formed by electron-beam-induced deposition on the partial pressure of the precursor. *Appl. Phys. A-Mater.*, 78(4):543–546, 2004. 113

[282] T. Tao, J. S. Ro, J. Melngailis, Z. L. Xue, and H. D. Kaesz. Focused Ion-Beam Induced Deposition of Platinum. *J. Vac. Sci. Technol. B*, 8(6):1826–1829, 1990. 54, 125

[283] S. L. Thomson and W. R. Owens. Survey of Flow at Low-Pressures. *Vacuum*, 25(4):151–156, 1975. 86

[284] T. Thundat, E. A. Wachter, S. L. Sharp, and R. J. Warmack. Detection of Mercury-Vapor Using Resonating Microcantilevers. *Appl. Phys. Lett.*, 66(13):1695–1697, 1995. 34

[285] T. Thundat, P. I. Oden, and R. J. Warmack. Microcantilever sensors. *Microscale Therm. Eng.*, 1(3):185–199, 1997. 34

[286] M. Tortonese, R. C. Barrett, and C. F. Quate. Atomic Resolution with an Atomic Force Microscope Using Piezoresistive Detection. *Appl. Phys. Lett.*, 62(8):834–836, 1993. 42

[287] M. Toth, C. J. Lobo, G. Hartigan, and W. R. Knowles. Electron flux controlled switching between electron beam induced etching and deposition. *J. Appl. Phys.*, 101(5):6, 2007. 12

[288] M. M. J. Treacy, T. W. Ebbesen, and J. M. Gibson. Exceptionally high Young's modulus observed for individual carbon nanotubes. *Nature*, 381(6584):678–680, 1996. 17

[289] A. A. Tseng. Recent developments in nanofabrication using focused ion beams. *Small*, 1(10): 924–939, 2005. 5

[290] Unimed SA, Switzerland. `www.unimed.ch`, 2007. 23

[291] I. Utke, P. Hoffmann, B. Dwir, K. Leifer, E. Kapon, and P. Doppelt. Focused electron beam induced deposition of gold. *J. Vac. Sci. Technol. B*, 18(6):3168–3171, 2000. 10

[292] I. Utke, P. Hoffmann, R. Berger, and L. Scandella. High-resolution magnetic Co supertips grown by a focused electron beam. *Appl. Phys. Lett.*, 80(25):4792–4794, 2002. 10, 11

[293] I. Utke, T. Bret, D. Laub, P. Buffat, L. Scandella, and P. Hoffmann. Thermal effects during focused electron beam induced deposition of nanocomposite magnetic-cobalt-containing tips. *Microelectron. Eng.*, 73-74:553–558, 2004. 10, 11

[294] I. Utke, J. Michler, P. Gasser, C. Santschi, D. Laub, M. Cantoni, P. A. Buffat, C. Jiao, and P. Hoffmann. Cross section investigations of compositions and sub-structures of tips obtained by focused electron beam induced deposition. *Adv. Eng. Mater.*, 7(5):323–331, 2005. 11

[295] I. Utke, V. Friedli, S. Amorosi, J. Michler, and P. Hoffmann. Measurement and simulation of impinging precursor molecule distribution in focused particle beam deposition/etch systems. *Microelectron. Eng.*, 83(4-9):1499–1502, 2006. 99, 100

[296] I. Utke, V. Friedli, J. Michler, T. Bret, X. Multone, and P. Hoffmann. Density determination of focused-electron-beam-induced deposits with simple cantilever-based method. *Appl. Phys. Lett.*, 88(3):031906, 2006. 18, 19, 54, 57, 71

[297] I. Utke, V. Friedli, M. Purrucker, and J. Michler. Resolution in focused electron- and ion-beam induced processing. *J. Vac. Sci. Technol. B*, 25(6):2219–2223, 2007. 12, 113, 117, 118, 131

[298] I. Utke, P. Hoffmann, and J. Melngailis. Gas assisted focused electron beam and ion beam processing and fabrication. *J. Vac. Sci. Technol. B*, (submitted), 2008. 9

[299] W. F. van Dorp, B. van Someren, C. W. Hagen, and P. Kruit. Approaching the resolution limit of nanometer-scale electron beam-induced deposition. *Nano Lett.*, 5(7):1303–1307, 2005. 34

[300] W. F. Van Dorp, C. W. Hagen, P. A. Crozier, and P. Kruit. In situ monitoring and control of material growth for high resolution electron beam induced deposition. *J. Vac. Sci. Technol. B*, 26(6):2210, 2007. 15

[301] Veeco Instruments Inc. `www.veeco.com`, 2007. 31

[302] E. A. Wachter and T. Thundat. Micromechanical Sensors for Chemical and Physical Measurements. *Rev. Sci. Instrum.*, 66(6):3662–3667, 1995. 34

[303] P. S. Waggoner and H. G. Craighead. Micro- and nanomechanical sensors for environmental, chemical, and biological detection. *Lab Chip*, 7(10):1238–1255, 2007. 34

[304] D. A. Walters, J. P. Cleveland, N. H. Thomson, P. K. Hansma, M. A. Wendman, G. Gurley, and V. Elings. Short cantilevers for atomic force microscopy. *Rev. Sci. Instrum.*, 67(10):3583–3590, 1996. 47

[305] D. Wang, P. C. Hoyle, J. R. A. Cleaver, G. A. Porkolab, and N. C. Macdonald. Lithography Using Electron-Beam-Induced Etching of a Carbon-Film. *J. Vac. Sci. Technol. B*, 13(5):1984–1987, 1995. 10

[306] Y. Wang, J. A. Henry, A. T. Zehnder, and M. A. Hines. Surface chemical control of mechanical energy losses in micromachined silicon structures. *J. Phys. Chem. B*, 107(51):14270–14277, 2003. 71

[307] J. H. L. Watson. An Effect of Electron Bombardment Upon Carbon Black. *J. Appl. Phys.*, 18 (2):153–161, 1947. 9

[308] W. Weaver, Stephen Prokofevich Timoshenko, and D. H. Young. *Vibration problems in engineering.* Wiley, New York [etc.], fifth edition, 1990. 35, 61

[309] M. Weber, H. W. P. Koops, and W. Gortz. Scanning Probe Microscopy of Deposits Employed to Image the Current-Density Distribution of Electron-Beams. *J. Vac. Sci. Technol. B*, 10(6): 3116–3119, 1992. 29

[310] G. A. West and K. W. Beeson. Chemical Vapor-Deposition of Cobalt Silicide. *Appl. Phys. Lett.*, 53(9):740–742, 1988. 102

[311] W. B. White, K. Rykaczewski, and A. G. Fedorov. What controls deposition rate in electron-beam chemical vapor deposition? *Phys. Rev. Lett.*, 97(8):086101, 2006. 113

[312] XENOS™ Nano-Lithography System, Germany. `www.xenos-semi.com`, 2007. 21

[313] H. Yamaguchi, A. Shimase, S. Haraichi, and T. Miyauchi. Characteristics of Silicon Removal by Fine Focused Gallium Ion-Beam. *J. Vac. Sci. Technol. B*, 3(1):71–74, 1985. 50

[314] J. L. Yang, T. Ono, and M. Esashi. Surface effects and high quality factors in ultrathin single-crystal silicon cantilevers. *Appl. Phys. Lett.*, 77(23):3860–3862, 2000. 71

[315] J. L. Yang, T. Ono, and M. Esashi. Investigating surface stress: Surface loss in ultrathin single-crystal silicon cantilevers. *J. Vac. Sci. Technol. B*, 19(2):551–556, 2001. 71

[316] Y. T. Yang, C. Callegari, X. L. Feng, K. L. Ekinci, and M. L. Roukes. Zeptogram-scale nanomechanical mass sensing. *Nano Lett.*, 6(4):583–586, 2006. 41

[317] K. Y. Yasumura, T. D. Stowe, E. M. Chow, T. Pfafman, T. W. Kenny, B. C. Stipe, and D. Rugar. Quality factors in micron- and submicron-thick cantilevers. *J. Microelectromech. S.*, 9(1):117–125, 2000. 37, 71

[318] E. Yoda and B. M. Siegel. Reduction of Contamination in Reflection Electron Diffraction. *J. Appl. Phys.*, 33(4):1419, 1962. 10

[319] N. Yoshimura, H. Hirano, and T. Etoh. Mechanism of Contamination Buildup Induced by Fine Electron-Probe Irradiation. *Vacuum*, 33(7):391–395, 1983. 10

[320] Warren C. Young and Richard G. Budynas. *Roark's formulas for stress and strain.* McGraw-Hill, New York, 7th edition, 2002. 61

[321] M. F. Yu, O. Lourie, M. J. Dyer, K. Moloni, T. F. Kelly, and R. S. Ruoff. Strength and breaking mechanism of multiwalled carbon nanotubes under tensile load. *Science*, 287(5453):637–640, 2000. 11

[322] M. F. Yu, G. J. Wagner, R. S. Ruoff, and M. J. Dyer. Realization of parametric resonances in a nanowire mechanical system with nanomanipulation inside a scanning electron microscope. *Phys. Rev. B*, 66(7):073406, 2002. 17

[323] X. M. Yu, J. Thaysen, O. Hansen, and A. Boisen. Optimization of sensitivity and noise in piezoresistive cantilevers. *J. Appl. Phys.*, 92(10):6296–6301, 2002. 42

[324] T. D. Yuzvinsky, A. M. Fennimore, W. Mickelson, C. Esquivias, and A. Zettl. Precision cutting of nanotubes with a low-energy electron beam. *Appl. Phys. Lett.*, 86(5):053109, 2005. 11

[325] G. S. Zhdanov and V. N. Vertsner. Mechanism Behind Formation of Hydrocarbon Impurities Upon Surfaces Irradiated by a Narrow Electron Beam. *Dokl. Akad. Nauk SSSR*, 176(5):1040, 1967. 11

[326] G. S. Zhdanov and V. N. Vertsner. Study of Mechanism of Formation of Hydrocarbon Contaminants on Electron-Bombarded Objects. *Izv. An. SSSR Fiz.*, 32(6):1091, 1968. 11

[327] C. Ziegler. Cantilever-based biosensors. *Anal. Bioanal. Chem.*, 379(7-8):946–959, 2004. 34

[328] J. F. Ziegler, J. P. Biersack, and U. Littmark. *The stopping and range of ions in solids.* Pergamon Press, New York etc., 1985. 51

[329] E. Zussman, X. Chen, W. Ding, L. Calabri, D. A. Dikin, J. P. Quintana, and R. S. Ruoff. Mechanical and structural characterization of electrospun PAN-derived carbon nanofibers. *Carbon*, 43(10):2175–2185, 2005. 75

Nomenclature

Abbreviations

AE	Auger electron
ADF	Annular dark field
AES	Auger electron spectroscopy
AFM	Atomic force microscope
BSE	Backscattered electron
CNT	Carbon nanotube
CVD	Chemical vapor deposition
DSMC	Direct simulation Monte Carlo (simulations)
EDX	Energy-dispersive X-ray (spectroscopy)
ESEM	Environmental scanning electron microscope
FEB	Focused electron beam
FIB	Focused ion beam
FSE	Forward scattered electron
FWHM	Full width at half maximum
GIS	Gas injection system
HV	High vacuum
NEMS	Nanoelectromechanical system
NW	Nanowire
MEMS	Microelectromechanical system
PE	Primary electron
PLL	Phase-locked-loop
QCM	Quartz crystal microbalance
SE	Secondary electron
SEM	Scanning electron microscope
SIM	Scanning ion microscope
SPM	Scanning probe microscope
STEM	Scanning transmission electron microscope

TEM	Transmission electron microscope
TPMC	Test-particle Monte Carlo (simulations)
UHV	Ultrahigh vacuum
VHS	Variable hard sphere (model)
VSS	Variable soft sphere (model)

List of puplications

Book chapter

- V. Friedli, S. Hoffmann, J. Michler, and I. Utke. AFM Sensors in Scanning Electron and Ion Microscopes: Tools for Nanomechanics, Nanoanalytics, and Nanofabrication. In B. Bhushan, H. Fuchs, and M. Tomitori, editors, *Applied Scanning Probe Methods VIII.* Springer, Heidelberg, 2008 (Online version available at `www.springer.com/978-3-540-74079-7`)

Journal articles

- V. Friedli, J. Michler, and I. Utke. Optimization of nozzle-based gas injection systems for focused electron- and ion-beam induced processing. *article in preparation*, 2008
- V. Friedli, J. Michler, and I. Utke. Stiffness, density and quality of high aspect ratio Cu/C nanostructures produced by focused electron-beam induced deposition. *article in preparation*, 2008
- I. Utke, V. Friedli, M. Purrucker, and J. Michler. Resolution in focused electron- and ion-beam induced processing. *J. Vac. Sci. Technol. B*, 25(6): 2219-2223, 2007
- V. Friedli, Ch. Santschi, J. Michler, P. Hoffmann, and I. Utke. Mass sensor for in situ monitoring of focused ion and electron beam induced processes, *Appl. Phys. Lett.*, 90(5):053106, 2007
- I. Utke, V. Friedli, J. Michler, T. Bret, X. Multone, and P. Hoffmann. Density determination of focused-electron-beam-induced deposits with simple cantilever-based method. *Appl. Phys. Lett.*, 88(3):031906, 2006
- I. Utke, V. Friedli, S. Amorosi, J. Michler, and P. Hoffmann. Measurement and simulation of impinging precursor molecule distribution in focused particle beam deposition/etch systems. *Microelectron. Eng.*, 83(4-9):1499-1502, 2006
- I. Utke, V. Friedli, S. Fahlbusch, S. Hoffmann, P. Hoffmann, and J. Michler, Tensile strengths of metal-containing joints fabricated by focused electron beam induced deposition. *Adv. Eng. Mater.*, 8(3):155-157, 2006

- P. Kern, C. Jaeggi, I. Utke, V. Friedli, and J. Michler, Local electron beam induced reduction and crystallization of amorphous titania films, *Appl. Phys. Lett.*, 89(2):02102, 2006

Curriculum Vitae

Personal Data

Name:	Vinzenz FRIEDLI
Date of Birth:	24.07.1978
Place of Birth:	Bern
Nationality:	Swiss

Professional activities

2004-2008	Swiss Federal Laboratories for Materials Testing and Research (EMPA), Thun Ph.D. project at the Laboratory for Mechanics of Materials and Nanostructures
2003	Ecole Polytechnique Fédérale de Lausanne (EPFL) Research engineer at the Advanced Photonics Laboratory (8 months)
2001	Internship at Helbling Technik AG, Bern (3 months)

Education

1998-2003	Ecole Polytechnique Fédérale de Lausanne (EPFL) Master of Science in Microengineering, specialization in Applied Photonics, Diploma thesis awarded with two prizes
2000-2001	Royal Institute of Technology (KTH), Stockholm, Sweden Exchange Student (ERASMUS)
1993-1998	Gymnasium Bern-Kirchenfeld Matura Typus E (economics)